Patient-Specific Blood Flow Modelling in Diagnosis of Coronary Artery Disease

by

Alena Uus, MSc (Eng) London

Research Centre for Biomedical Engineering

Department of Electrical and Electronic Engineering

City University London

May 2016

Declaration

The author grants powers of discretion to the University Librarian to allow this thesis to be copied in whole or in part without further reference to the author. This permission covers only single copies made for study purposes, subject to normal conditions of acknowledgement.

Abstract

This thesis presents the approach for development of patient-specific coronary blood flow models in 3D and 0D domains based on coronary artery geometries reconstructed from Coronary Computed Tomography Angiography datasets (CCTA). The computed flow patterns extend the diagnostic value of CCTA, which, being noninvasive imaging modality, provides only static information on the anatomy of epicardial arteries. The clinical indices extracted from the virtual blood flow can be potentially employed in the assessment of the haemodynamic severity of Coronary Artery Disease (CAD) lesions as well at the analysis of the underlying mechanisms of formation and localisation of atherosclerotic plaques.

However, the existing patient-specific coronary blood flow modelling approaches are generally characterised by relatively high levels of uncertainty and instability due to a number of unknown factors and modelling assumptions. Analysis and comparison of the impact of various modelling assumptions has the potential to reduce this uncertainty. The overarching contributions of this thesis are the thorough analysis and investigation of the existing issues in patient-specific coronary blood flow simulations and the provision of the guidelines for the design and implementation of blood flow models in order to improve and ensure the reliability and accuracy of the numerical results.

In addition, a novel approach for the implementation of spatially extended patient-specific 0D blood flow models was proposed, which significantly decreases the high computational costs generally associated with 3D blood flow simulations. While the classical 0D models based on the electrical–hydraulic analogy use the lumped-parameter representation of major vessel tree structures and are thus characterised by limited spatial characteristics, the proposed method for modelling of individual vessel tree branches through a series of 0D elements provides the means for correlation of the computed flow with the precise location along a vessel. Therefore, this extends the applicability of 0D modelling in patient-specific blood flow simulations for the assessment of functional stenosis severity.

Acknowledgements

I would like to gratefully and sincerely thank my mentor and supervisor Professor Panos Liatsis for his guidance and support. His knowledge and wisdom motivated me. He also patiently corrected my academic writing. This thesis would have not been possible without him.

I want to thank Doctor Ronak Rajani for helping me on exploring the potential of application for blood flow simulations in diagnosis of coronary artery diseases and Doctor Efstathios Milonidis for his general support during my academic life at City.

I would also like to thank my parents, who believed in me, inspired me, and supported me throughout the hardest times of this research. Special thanks to my dear friend Natasha for her encouragement, coffee breaks and laughs.

Contents

List of Tables

List of Figures

Abbreviations

ALE	Arbitrarily Lagrangian-Eulerian
ANS	Autonomic Nervous System
AP	Aortic Pressure
AS	Area of Stenosis
BC	Boundary Conditions
CABG	Coronary Artery Bypass Graft
CAD	Coronary Artery Disease
CCTA	Coronary Computed Tomography Angiography
CFD	Computational Fluid Dynamics
CFR	Fractional Flow Reserve
CHD	Coronary Heart Disease
CMM	Coupled Momentum Method
cMPR	Curved Multiplanar Reconstruction
CO	Cardiac Output
CTA	Computed Tomography Angiography
CVS	Cardiovascular System
DICOM	Digital Imaging and Communications in Medicine
DS	Diameter of Stenosis
ECG	Electrocardiogram
ESS	Endothelial Shear Stress
FE	Finite Element

FEM	Finite Element Method
FFR	Fractional Flow Reserve
FSI	Fluid Structure Interactions
FVM	Finite Volume Method
HU	Hounsfield Unit
ICA	Invasive Coronary Angiography
IVUS	Intravascular Ultrasound
LAD	Left Anterior Descending
LCA	Left Coronary Artery
LCx	Left Circumflex
LDL	Low-Density Lipoprotein
LMCA	Left Main Coronary Artery
LVP	Left Ventricular Pressure
LV	Left Ventricle
KD	Kawasaki disease
N-S	Navier-Stokes
NURBS	Non-Uniform Rational Basis Spline
OCT	Optical Coherence Tomography
OSI	Oscillatory Shear Index
PCI	Percutaneous Coronary Intervention
PDA	Posterior Descending Artery
PDE	Partial Differential Equation
QCA	Quantitative Invasive Angiography

RCA	Right Coronary Artery
RRT	Relative Residence Time
SCCT	Society of Cardiovascular Computed Tomography
SN	Sinoatrial Node
SV	Stroke Volume
TAWSS	Time Averaged Wall Shear Stress
UDF	User Defined Function
VPG	Ventricular Pressure Generator
WK	Windkessel
WSS	Wall Shear Stress
WSSG	Wall Shear Stress Gradient

Chapter 1

Introduction

This thesis presents the approach for the development of image-based coronary blood flow models in the 3D and 0D domains based on coronary artery geometries reconstructed from Coronary Computed Tomography Angiography (CCTA) datasets. The computed flow patterns extend the diagnostic value of CCTA, which, being noninvasive imaging modality, provides only static information on the anatomy of epicardial arteries. The clinical indices extracted from the virtual blood flow can be potentially employed in the assessment of the haemodynamic severity of Coronary Artery Disease (CAD) lesions as well at the analysis of the underlying mechanisms of formation and localisation of atherosclerotic lesions.

At first, this chapter gives an introduction into the clinical background associated with the research area and the problem domain including: (i) the anatomy and function of the coronary blood circulation system; (ii) clinical diagnosis indices used in the detection and gradation of CAD severity; and (iii) the specifics of medical imaging modalities employed in diagnosis of cardiovascular diseases. Next, Section 1.2 defines the research objectives and the contributions of the thesis with respect to the application of image-based coronary blood flow simulations in clinical decision support. Finally, the thesis outline is presented in Section 1.3.

1.1 Clinical Diagnostic Technologies of Coronary Artery Disease

1.1.1. Anatomy and Function of the Coronary Blood Circulation System

The coronary blood circulation loop is a part of the cardiovascular system (CVS) and is responsible for the supply of blood to the heart, which distributes blood to the rest of the body (Figure 1.1.a). Therefore, the coronary circulation system is one of the central elements with regards to the entire CVS functionality. The coronary vascular system consists of the coronary arterial tree, the capillary bed and the coronary venous tree. The left and right coronary arteries (LCA and RCA, respectively), also known as epicardial arteries, run on the surface of the heart and prove oxygenated blood to the myocardium and other heart components (Figure 1.1.b).

Both arteries originate from the root of the aorta from openings called the coronary ostia located behind the aortic valve leaflets. The LCA distributes blood to the left side of the heart and bifurcates into the left anterior descending artery (LAD) and the left circumflex artery (LCx) [1]. The part that is between the aorta and the main bifurcation is the left main coronary artery (LMCA). Sometimes, an additional artery, known as ramus or intermediate artery, arises at the LCA bifurcation, thus forming a trifurcation. The RCA distributes blood to the right atrium and both ventricles and branches into the posterior descending artery (PDA) and the right marginal artery. However, in approximately 10% of general population, the PDA is supplied from the LCx artery and in this case, the coronary circulation is classified as "left-dominant". In other cases, circulation is either right-dominant with the PDA originating from the RCA (approximately 70% of the general population) or a combination, known as co-dominant, which occurs in 20% of the population [1].

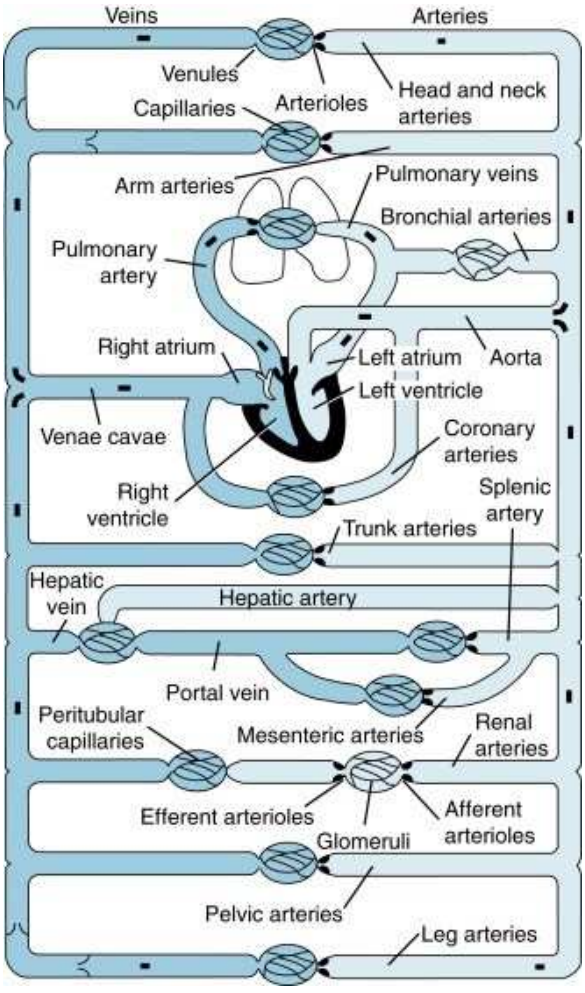

a. Schematic diagram of CVS [2]

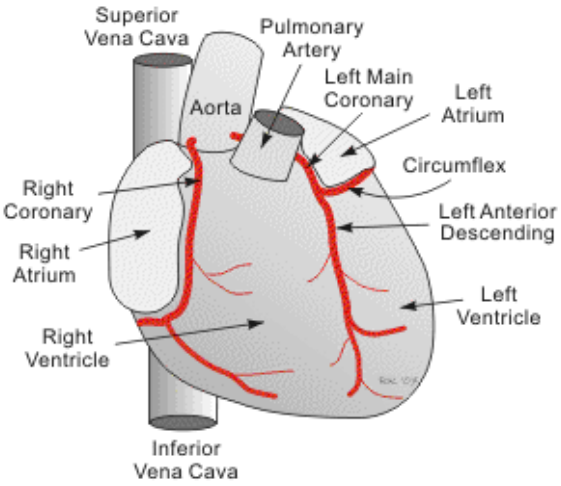

b. Epicardial coronary arteries [3]

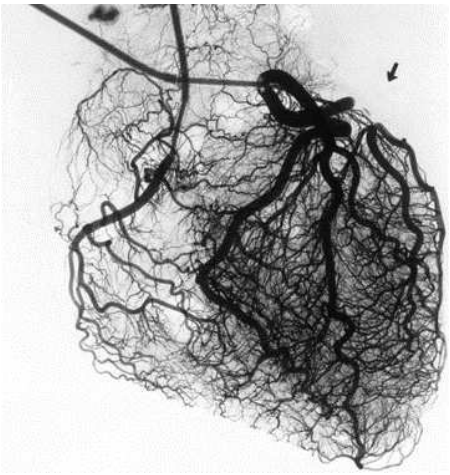

c. Ex vivo heart arteriogram [4]

Figure 1.1 Coronary circulation

The exact anatomy of the coronary arteries is highly patient-specific and could exhibit a wide range of variation [1]. Taking into account the general interpatient variations, the average proximal diameters are 4.5±0.5 mm for the LMCA and 3.7±0.4 mm for the LAD artery. Depending on the anatomical dominance, diameter vary between 3.9±0.6 and 2.8±0.5 mm for LCx artery and between 3.4±0.5 and 4.2±0.6 for RCA [5].

Following the morphometry laws of vascular trees, the main coronary arteries branch into a network of small arteries and arterioles ending in capillary vascular bed (Figure 1.1.c). The capillaries deliver oxygen to the cardiomyocytes (cardiac muscle cells) along with the removal of metabolic waste products. Capillary blood flow enters the coronary venules further forming cardiac veins ending into the right atrium.

During the short-term metabolic autoregulation processes, depending on the oxygen demands and CO_2 content of the heart muscle, the vasodilation or vasoconstriction of the coronary vasculature is regulated by a baroreceptor reflex mechanism. Under the exercise condition, the sympathetic activation to the heart results in coronary vasodilation, which corresponds to higher blood flow. In other words, dilation of blood vessels decreases the vascular resistance, thus resulting in an increase in the blood flow rate, which in turn leads to a decrease in pressure. This relation is described as $\Delta P = R \cdot Q$, where ΔP is the change in pressure, R is the vascular resistance, and Q is the blood flow rate through the vascular tree [1]. The vascular resistance is defined from the vascular tree geometry and blood viscosity and can be represented through an adapted form of the Hagen–Poiseuille equation: $R = 8 \cdot L \cdot \mu / (\pi \cdot r^4)$, where L is the vessel length, r is the vessel radius, and μ is the blood viscosity [1]. While the vessel length is generally not subjected to change, the vascular resistance is regulated by regulation of the vessel radius. Being narrower than the main arteries, small arteries and arterioles are the primary sites of vascular resistance and are responsible for the majority of the pressure drop. This is due to the fact that the vascular resistance is inversely proportional to the fourth power of the vessel radius. Age and lifestyle-related conditions along with arterial hypertension and cardiovascular disease are associated with elevated vascular resistance [1]. While healthy coronary arteries supply an adequate amount of blood flow to the myocardium at all levels of cardiac activity in accordance with oxygen demands, diseased arteries are characterised by higher resistance resulting in a decrease in blood flow which becomes more pronounced under exercise. Figure 1.2.b. illustrates the autoregulation in coronary vasculature and the effect of metabolic activity on the position of the autoregulatory region with the changes in coronary flow rate are caused mainly by changes of the coronary resistance in

response to variations in metabolic activity. Pharmacologically-induced vasodilation is widely employed in the stress testing for the assessment of the degree of severity of coronary artery disease corresponding to the amount of decrease in myocardial perfusion. The condition of maximum hyperaemia (increased coronary blood flow) is simulated by administering of adenosine (a vasodilator), thus resulting in maximum vasodilation of the peripheral vascular bed.

One of the specifics of coronary blood flow is that, unlike the rest of the CVS, its flow rate phase is shifted with respect to the driving pressure wave due to the impact of extravascular compression caused by the high pressure of contraction of ventricular myocardium (Figure 1.2.a). Consequently, the left coronary flow rate becomes low during the systole (isovolumetric contraction and ejection) and most myocardial perfusion occurs during the diastole (heart relaxation), when the pressure on the vessels is low. Since the right ventricular pressure is lower than the left ventricular (LV) pressure, the RCA flow rate does not decrease to zero. In addition, because of the impact of extravascular compression, the endocardium is more susceptible to ischemia and tachycardia episodes, which lower the blood flow due to the shorter diastole [18].

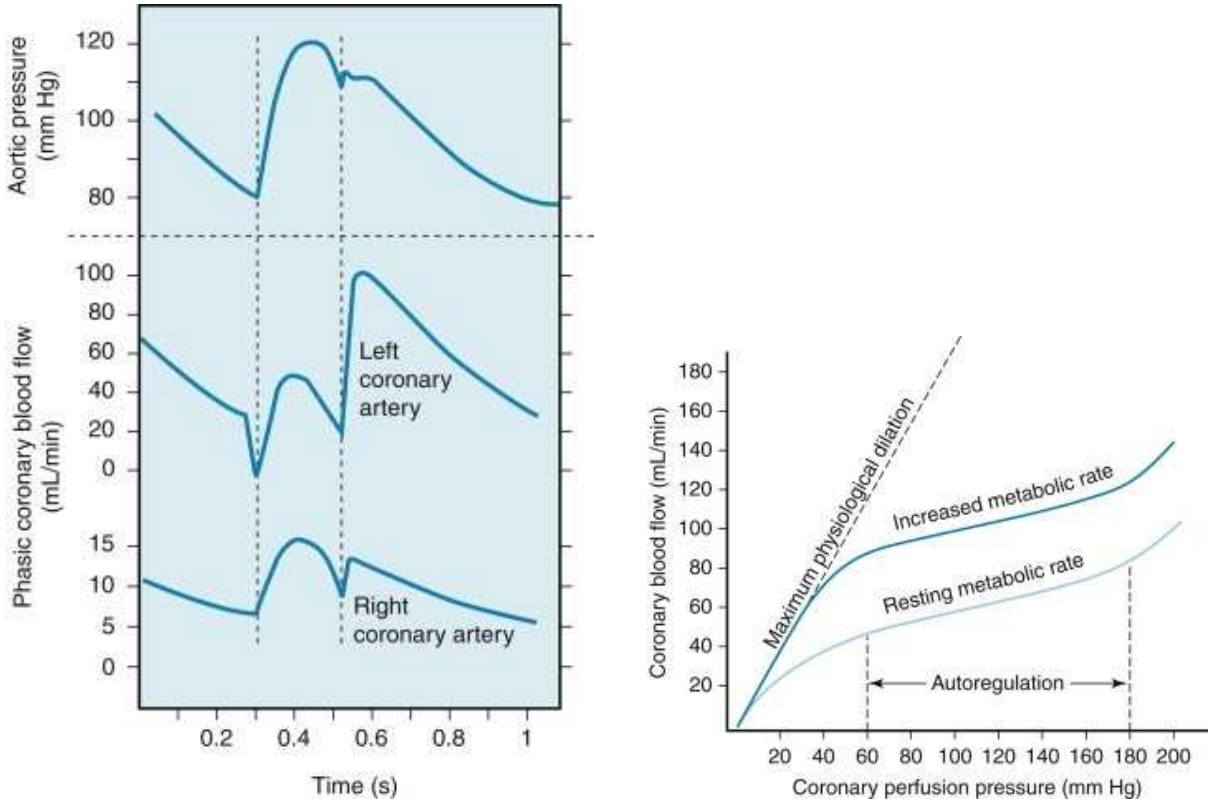

a. Coronary pressure and flow rate [2] b. Coronary autoregulation [2]

Figure 1.2 Characteristics of coronary blood flow

Since coronary arteries represent the only source of blood supply to the heart muscle, the reduced coronary blood flow or blockage of artery lumen will lead to oxygen deficiency (ischemia) and eventually heart tissue damage. Depending on the severity of the ischemia, it can be accompanied with intense chest pain episodes (angina) or result in myocardial infarction, when the heart muscle dies from hypoxia, in the case of total blockage of one of the main arterial branches. Chronic ischemia causes gradual weakening of the heart muscle leading to myocardial hibernation [6]. Because the heart supplies blood to the rest of the body, the irreversible damage on the heart function affects the entire CVS. This is the reason why coronary artery disease is one of the major causes of death in the developed world [6].

1.1.2. Coronary Artery Disease

Coronary artery disease (CAD) is characterised by changes in both structure and function of the epicardial arteries including increased arterial stiffness and formation of atherosclerotic plaques. Atherosclerosis is the gradual deposition of cholesterol, fibrous tissue and calcium within the artery wall accompanied by inflammation and resulting in the formation of atherosclerotic plaques. Figure 1.3 illustrates the stages of plaque formation beginning from fatty streak and fibrous atheromas to complicated lesions leading to critical stenosis or plaque rupture-induced thrombosis.

Atherogenesis is a complex process, which involves vascular wall injury and atheroma formation due to multiple local and systemic factors. It is associated with high levels of LDL-cholesterol, inflammation, vascular calcification, hypertension, endothelial dysfunction, and other factors [6]. The endothelium layer of the vessel wall acts as a barrier function between the vessel lumen and surrounding tissue that controls the biological transfer function in and out of the bloodstream together with regulating the balance between vasoconstriction and vasodilation and immune function [7]. Being in direct contact with the circulating blood, endothelial cells are exposed to the tangential drag force produced by blood moving across the lumen surface, which is referred as wall shear stress (WSS). WSS is a function of the velocity gradient and its magnitude is proportional to the blood flow and viscosity and inversely proportional to the cube of the vessel radius [8]. Therefore, even small variations in the lumen diameter caused by the tortuosity, bifurcation or the presence of atherosclerotic lesions will lead to different WSS patterns. Variations in WSS are correlated with a modulation of the cellular structure and function including, the barrier function, vascular homeostasis, and thromboresistance [7]. In the cases of complex geometries resulting in low or oscillatory shear

stress regions, WSS is thought to play an important role in the process of atherosclerotic plaque development and localisation [7].

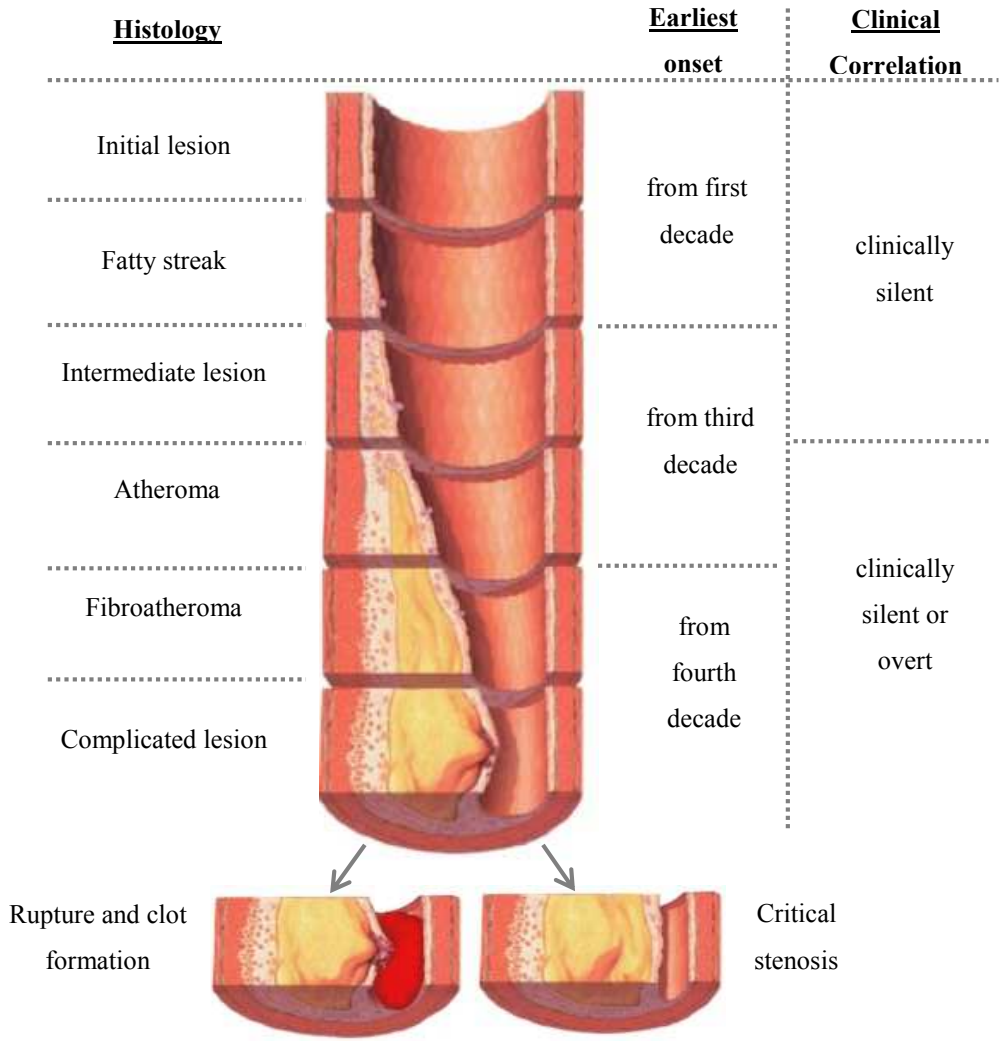

Figure 1.3 Sequences in the progression of atherosclerosis (reproduced from [9])

Gradual plaque formation leads to the narrowing of arterial lumen, which increasingly restricts blood flow, thus resulting in ischemia. The stenosis becomes critical when it causes a significant reduction in maximal blood flow to the peripheral vascular bed. Generally, this is correlated with a $\geq$ 70% lumen diameter reduction [17]. Until becoming critical, coronary artery stenoses generally do not decrease the resting flow due to the development of collateral blood flow or the long-term autoregulation of vasodilation mechanism of the downstream vascular bed [18]. Thus, atherosclerosis may remain asymptomatic for decades until the condition becomes severe with multivessel disease exhausting the autoregulation mechanism or in the case where a plaque rupture results in myocardial infarction [6]. The CAD lesions are

classified with respect to the presence and volume of the lipid core, fibrous layers, calcifications, haemorrhage, and stenosis area [10].

Unstable plaques prone to rupture, also known as vulnerable plaques, are referred to as “thin-cap fibroatheroma” [11]. Some of the prominent characteristics of unstable plaques include a large necrotic lipid core, thin fibrous cap, active inflammation, calcium deposit, intraplaque haemorrhage, positive vascular remodelling, etc. [11]. Plaque rupture exposes highly thrombogenic material to the flowing blood, which results in the formation of blood clots that may cause occlusion of one of the coronary artery branches or localised chronic inflammation. Factors contributing to the rupture mechanism include weakening and erosion of the fibrous cap, inflammation, and increased local mechanical stresses [12].

Depending on the diagnosis outcome of CAD severity, the treatment strategy may be limited to medication treatment or require surgical intervention such as balloon angioplasty, stenting, or coronary artery bypass graft (CABG).

1.1.3. Clinical Diagnostic Indices for Coronary Artery Disease Diagnosis

The characteristics by which the severity of CAD lesions can be quantified are divided into two groups, geometry-derived and haemodynamic indices. The associated value are extracted from performed medical imaging tests such as coronary angiography, computed tomography angiography (CTA), intravascular ultrasound (IVUS), myocardial perfusion scan, etc. [23].

The commonly used indices describing the significance of anatomical stenosis are the percentage decrease in the lumen diameter and area (DS and AS) in the artery lumen cross-section [13]. The DS and DA values are computed as $DS = 1 - D_1/D_2$ and $AS = 1 - A_1/A_2$ [13], where D_1 and D_2 are the minimal stenosis and reference “healthy” vessel diameters, respectively and A_1 and A_2 are the lumen cross-sectional area with and without stenosis (Figure 1.4). In some cases, AS can also be computed as $AS = 1 - (D_1/D_2)^2$. At the same time, taking into account the irregular geometries of atherosclerotic lesions and the resolution limitations of medical images, the severity of the stenosis can be either over- or under-estimated (e.g., if the D_3 and D_4 values were used instead or if the A_2 area was not accurately approximated). In addition, these parameters of the stenosis anatomy only partially reflect the impact it produces on the blood flow in the artery. Other factors that affect the stenosis flow-limiting action include the length of the lesion, the location in the arterial tree, exit angle, tortuosity, etc. [5,13,15].

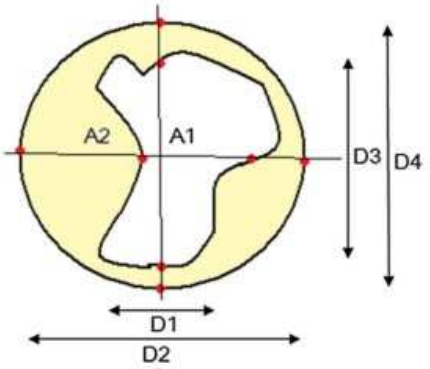

Figure 1.4 - Geometry-derived characteristics of a stenosis in cross-section [14]

Based on the quantification of the diameter and area reduction, the severity of the stenosis is diagnosed in accordance with recommended guidelines. For instance, the assessment scheme for CCTA stenosis severity has the following gradations [16]: (0) Normal: Absence of plaque and no luminal stenosis; (1) Minimal: Plaque with <25% stenosis; (2) Mild: 25%–49% stenosis; (3) Moderate: 50%–69% stenosis; (4) Severe: 70%–99% stenosis; (5) Occluded: 100%.

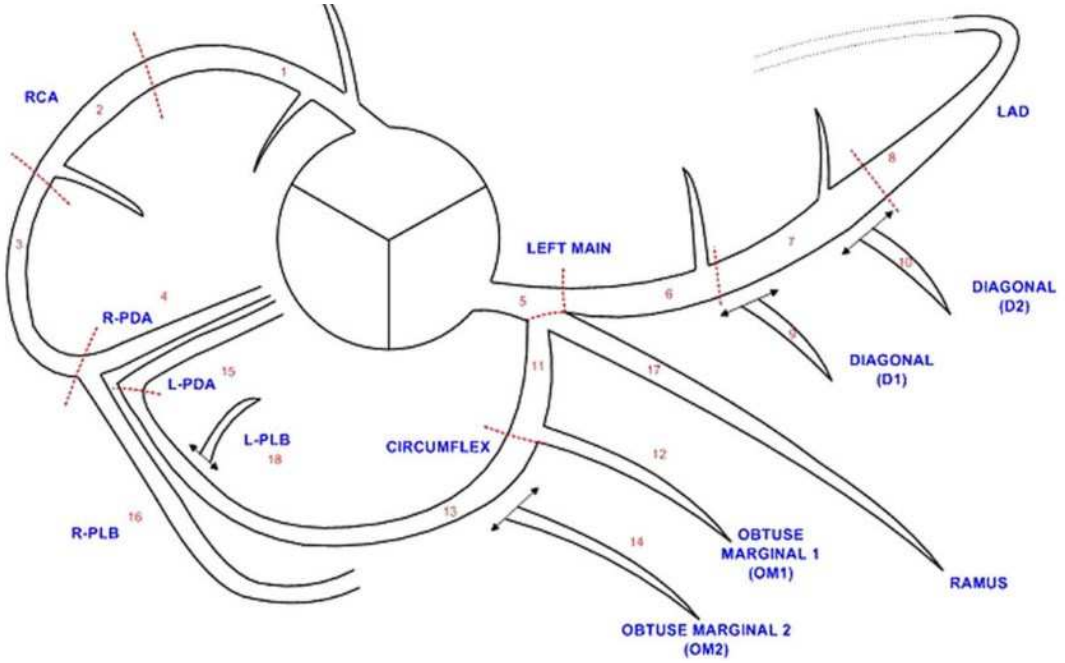

Figure 1.5 SCCT Coronary Segmentation Diagram [16]

In many cases, precise grading to a single percentage value is difficult due to lumen irregularities and thus, a range of values is used, for instance, 50-75% stenosis. Figure 1.5 shows the CCTA Coronary Segmentation Diagram used for referencing of the detected CAD lesions with respect to a specific segment of the coronary artery. Another index widely used in

CAD diagnosis is the total coronary artery calcium score, or Agatston score, which represents the amount of calcified atherosclerotic lesions [16].

The second group of diagnostic indices is based on the haemodynamic characteristics of CAD lesions, associated with the limited supply of oxygenated blood to the myocardial tissue. This includes the coronary flow reserve (CFR) and the fractional flow reserve (FFR). CFR is defined as the maximum increase of the total coronary flow under hyperaemia with respect to the baseline flow under resting conditions, where the condition of hyperaemia (maximum achievable flow) is pharmacologically induced by vasodilation [18,19]. Abnormal CFR values, lower than 2.0 cut-off threshold, correspond to myocardial perfusion defects caused by CAD (including both epicardial stenoses and microvascular dysfunction). On the other hand, FFR provides information on the functional severity of individual lesions in epicardial arteries in terms of the degree to which they limits oxygen delivery to the myocardium. It is computed as a ratio P_d/P_a, where P_d is the pressure distal to the lesion and P_a is the pressure proximal to the lesion at the root of the coronary artery [18]. The cut-off value defining a critical stenosis varies between 0.75 - 0.8, and accounts for the resulting 25 - 20% drop in the blood pressure under hyperaemia. In general, FFR-guided cardiac intervention procedures are associated with a lower level of follow-up coronary events than DS and CFR [20,21]. However, at the present time, the anatomy-based characteristics remain the main indices used in the diagnosis of CAD, since they can be directly derived from medical imaging tests [22].

1.1.4. Medical Imaging Technologies for Diagnosis of Coronary Artery Disease

The initial choice of medical technologies in the diagnosis of CAD depends on the patient state and the history of the disease. In patients suffering from angina, however not presently experiencing chest pain episodes and without CVD symptoms in the past, rest and exercise electrocardiogram (ECG) tests are generally performed along with the associated blood tests. In the case of any documented changes in the ECG characteristics, the test is considered diagnostic for CAD. The exercise test also provides information on other markers of myocardial ischaemia such as blood pressure response and dysrhythmia [6]. The alternative noninvasive tests include stress echocardiography, myocardial perfusion scan, or cardiac magnetic resonance (CMR) scan for noninvasive assessment of CFR [23].

In cases where the diagnosis outcome of these noninvasive tests shows medium to high risk acute coronary syndrome, invasive coronary angiography (ICA) is generally

prescribed in order to specify the nature and extent of the coronary lesions. The procedure of coronary angiography involves the transmission of a catheter to the root of the coronary arteries, followed by the injection of contrast medium into the coronary bloodstream, which is visible under the performed X-ray examination. Figure 1.6.a shows an example of the 2D ICA scan of the coronary artery with the performed quantiative assessment of the detected stenosis including DS, reference diameter, and length of the stenosed segment. Being the gold standard technique in CAD diagnosis [6,23], ICA provides visual information that can be used to recognise lesions such as stenosis, restenosis occlusion, thrombosis, aneurysms together with the myocardium contraction function and measured coronary artery pressure. The obtained information is further analysed for identification of a treatment strategy, such as coronary intervention or coronary bypass surgery. The decision on the required surgical intervention is normally based on angiographic results alone. However, in the case of multiple medium-severity epicardial artery stenoses, the decision on which of the lesions is the main cause of ischemia and thus requires stenting cannot be completely clear from the angiography data alone. ICA visualises only the blood inside a vessel replicating luminal changes but not the actual atherosclerotic lesions and can either underestimate or overestimate the lesion burden.

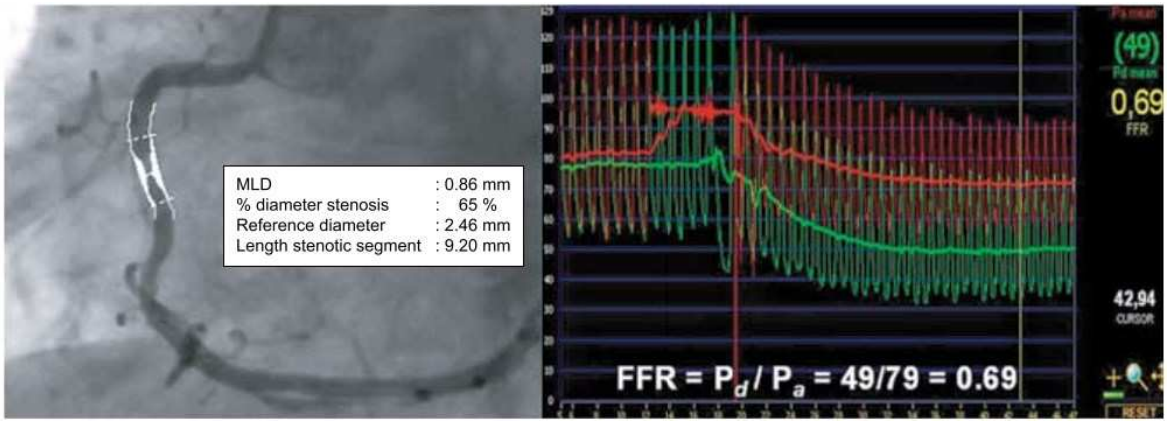

a. ICA scan with quantiative assessment of the stenosis anatomy

b. FFR index measured along the artery with functionally critical stenosis

Figure 1.6 Coronary angiography and FFR measurement: severe CAD [24]

The gold standard procedure for quantitative evaluation of the functional severity of individual stenosis lesions is the measurement of Fractional Flow Reserve (FFR) index. The FFR procedure is performed invasively during coronary catheterisation (ICA) through the measurement of the pressure drop along the stenosis that may cause myocardial ischemia. The measurement is performed under the simulated hyperaemia condition with a pressure sensor wire, which is pulled along the vessel. Maximum vasodilation of the peripheral vasculature is

induced by an intravenous adenosine injection (140 μg/kg/min) [23]. The FFR index is then computed from the measured pressure and visualised in real time with the values below the 0.75-0.8 threshold indicating the presence of ischemia-causing lesions.

Figure 1.6.b shows of an example of ICA-guided FFR acquisition in a critical flow-limiting stenosis case. The measured instantaneous pressure at the root of the coronary artery P_a (red) and distal along the artery P_d (green) is visualised on the screen along with the computed heart-cycle mean values. In can be observed that after the pharmacologically-induced hyperaemia there is a significant drop in the measured distal pressure from 78 mmHg to 49 mmHg, which results in FFR = P_d/P_a = 0.69 being below the critical threshold value. The Fractional Flow Reserve versus Angiography for Multivessel Evaluation (FAME) study demonstrated that in comparison to the anatomy-only treatment strategy, the FFR-guided coronary revascularization strategy allows to avoid stenting of functionally non-significant stenoses thus reducing the associated costs and risks [25]. At the same time, being an invasive procedure it is associated with a small risk of severe complications.

CT coronary angiography (CCTA) is a noninvasive alternative to the ICA. The ECG-gated acquisition of tomographic images of the heart is performed on single or dual source CT scanners with high temporal resolution [13,17]. The resulting image volume is the 3D representation of the heart and coronary arteries. Intravenous blood contrast-enhancing agents are used for high resolution imaging of the artery lumen as well as detection of the vulnerable plaques, while non-contrast CCTA is used for identification of the presence of calcified lesions for the assessment of the total calcium score [16]. However, a significant limitation of CCTA is that it provides only anatomy-based information for diagnosis of CAD (i.e., DS and AS) and, although characterised by high sensitivity and high negative predictive value, the positive predictive value of CCTA is lower than that of coronary angiography [13,26]. Consequently, since the positive CAD results are generally less conclusive, it is generally used for low to intermediate severity patients with suspected CAD in order to either eliminate the presence of critical stenoses or provide the guidance for further catheterisation tests.

In addition, CCTA provides information on the ventricle and atrium volume and dimensions and can be employed in follow-up of the CABG procedure and evaluation of valvular heart disease or the presence of cardiac masses. One of the advantages of CCTA is that it is able to identify the characteristics and global extent of CAD together with providing data for the straightforward reconstruction of the entire arterial tree lumen. Since CCTA

produces 3D datasets, such techniques as curved multiplanar reformations (cMPR) and 3D volume rendering are generally employed to facilitate the diagnosis accuracy [16].

Case I: detected vulnerable plaque with <50% stenosis in LAD

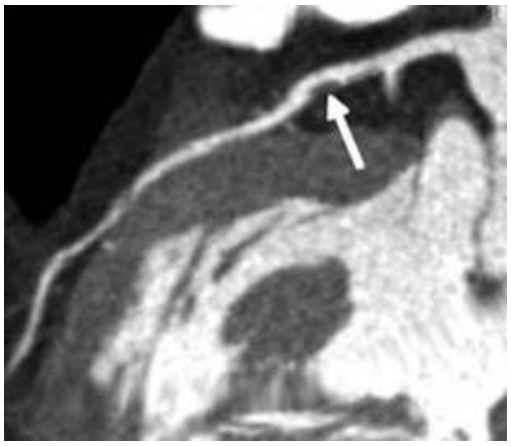

a. Curved multiplanar reformation view

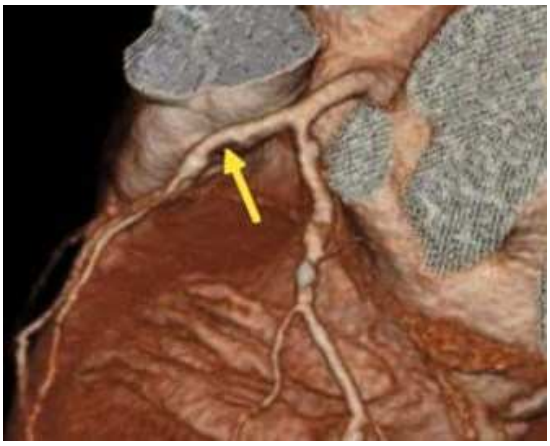

b. 3D volume rendering representation

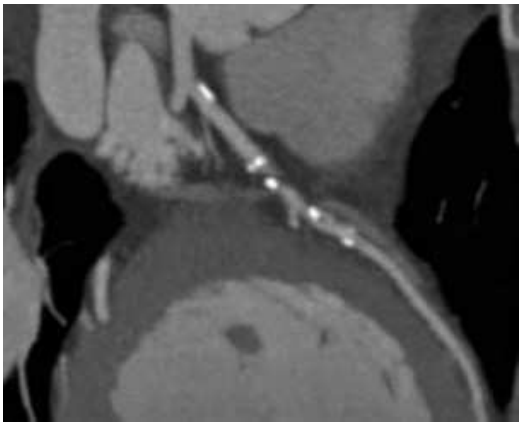

c. Case II: Severe stenosis with multiple calcified plaques in LAD

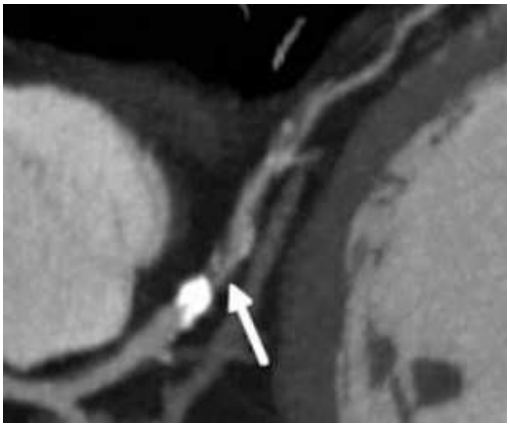

d. Case III: Severe stenosis with calcified and multiple soft plaques in LAD

Figure 1.7 CCTA examples of medium to severe stenosis cases [17]

Three examples of CCTA scans with detected atherosclerotic plaques in the left coronary artery are given in Figure 1.7. In the first case, Figures 1.7.a-b present the cMPR and volume rendering of the LAD artery. The difference between the HU (Hounsfield units) grey intensity values of the contrast-enhanced blood and the surrounding tissue clearly shows the reduction in the vessel lumen with approximately 50% stenosis degree. At the same time, it is also possible to distinguish the plaque composition since its fibrous cap and lipid core have lower HU intensity. The stenosis is also visible in the 3D representation. In the second case (Figure 1.7.c), a high degree stenosis with multiple plaques was detected in LAD. Due to the high HU intensity, the calcified plaques are plainly seen within the artery lumen. On the other

hand, as can be observed from the third example (Figure 1.7.d), due to the blooming effect of calcium, the presence of large calcium deposits can result in artefacts in CCTA data. This significantly affects the accuracy of 3D lumen reconstruction and stenosis gradation [16-17].

Since the main cause of myocardial infarction is not ischemia but the rupture of vulnerable plaques, which are normally characterised by intermediate stenoses [11], detection and categorisation of the atheroma structure and its component materials as well as the underlying formation mechanisms constitutes another focus area in CAD diagnosis. While providing general information on the presence of atherosclerotic plaques and their type, resolution of the CCTA is generally insufficient for the precise assessment of plaque composition due to the low difference in HU intensities for soft tissue. The gold standard for characterisation of plaque vulnerability is invasive inspection of epicardial arteries with a catheter-guided ultrasound transducer known as intravascular ultrasound (IVUS). Ultrasound provides high resolution information on the plaque components along the vessel cross-section and, in addition to information on the stenosis degree, it also can detect and measure the dimensions of the characteristics of vulnerable plaques such as fibrous cap thickness, lipid core volume, calcified nodules, etc. [23]. The IVUS procedure is performed together with ICA, which is used for guiding of the ultrasound catheter.

1.2. Motivation and Contributions of the Thesis

1.2.1. Research Objective

The main aim of patient-specific image-based blood flow simulations is the computation of flow patterns that are physiologically realistic (i.e., the flow parameters are within the defined interpatient range) and accurate for a particular patient taking into account the corresponding individual CVS characteristics. The underlying principle is based on the application of the universal methods of computational fluid dynamics (CFD) for the solution of flow-governing Navier-Stokes equations defined over the blood volume within the 3D vessel lumen of coronary artery geometries reconstructed from medical images.

The emergence of modern technologies in CFD solvers and efficient methods for accurate vessel segmentation make the development of patient-specific coronary blood flow models an achievable and relatively straightforward task. However, the high complexity and scale of the system together with the limited information on coronary circulation that can be acquired with medical imaging can affect the accuracy of the computed flow patterns. The

computational resource requirements for the solution of a system with many interrelated processes also play an important role in the model development process. Therefore, the majority of the implemented coronary blood flow models focus on a particular problem domain rather than construction of a global model that comprises all fundamental processes of coronary circulation. The application areas of blood flow modelling in coronary arteries can be summarised into three main groups: (i) investigation of haemodynamic-related mechanisms of CAD formation in correlation with WSS-derived parameters; (ii) estimation of CAD severity with haemodynamic FFR and CFR indices; and (iii) planning of surgical intervention procedures through optimisation of stent, angioplasty and bypass design.

During the process of clinical decision-making in CAD diagnosis, clinicians face a number of options with respect to various diagnostic techniques. The choice is based on the balance between safety and cost of the medical imaging procedures together with the reliability of the corresponding diagnostic value and the patient's risk group. Being a non-invasive technique, CCTA-based diagnosis relies only on the analysis of the anatomical features of atherosclerosis lesions and the situations when the cumulative effect of multiple medium severity stenoses contributes to ischemia can be left undetected. On the other hand, it can also overestimate the significance of stenoses with respect to their real flow-limiting impact. In general, CCTA is characterised by high true negative prognosis and is generally used for intermediate-risk patients [13,26].

The application of virtual blood flow simulation methods to patient-specific coronary artery geometries reconstructed from 3D CCTA datasets will provide additional haemodynamic information such as FFR and WSS patterns, which potentially improve the diagnostic value of CCTA (e.g., the assessment of the functional severity of stenoses). This, in turn, will aid in the treatment planning as a part of the clinical decision support system. At the same time, the existing patient-specific coronary blood flow modelling approaches are generally characterised by relatively high levels of uncertainty and instability due to a number of unknown factors and modelling assumptions. Investigation and comparison of the impact of various modelling assumptions and approaches has the potential to reduce this uncertainty. The baseline guidelines for design and implementation of image-based coronary blood flow models have to be established in order to improve and ensure the reliability and accuracy of the numerical results.

While the majority of the patient-specific blood flow models are implemented in 3D domain, since it provides the extensive information on local flow features, the application of the reduced order modelling approach has an advantage of the significantly lower computational costs. This is especially relevant in the case of blood flow simulations in complex vascular geometries with multiple branches, for which a CFD-based solution of blood equations can take up to 12 hours. The reduction of the dimension of the computational domain to 1D or 0D geometry representation significantly decreases the time and computational resources required for solution of the corresponding blood flow model. Although it was not yet implemented, in the case of 0D modelling based on the electrical–hydraulic analogy with the lumped-parameter representation of major vessel tree structures, the associated deficiency of spatial flow features can be partially resolved through the extension of the initial model with spatial information. Consequently, this extension could potentially make patient-specific 0D blood flow models to be an alternative to the classical 3D blood flow simulations.

The overall research objective of this thesis is to develop a methodology for the assessment of functional CAD severity in the context of non-invasive prediction of FFR, providing the evidence that it offers a reliable and robust computational solution of patient-specific blood flow fields in comparison to the established modelling approaches. The development and implementation of patient-specific coronary blood flow model in 0D and 3D domains will be followed by the thorough analysis of the influence of various modelling assumptions and factors directly related to the computation of physiologically accurate FFR and WSS patterns. This will result in a new set of design guidelines on the aspects of geometry reconstruction requirements and specification of flow boundary conditions representing the rest of cardiovascular system. In addition, the comparability and correlation between multiscale blood flow models will be investigated in order to assess the relevance of application of spatially extended 0D blood flow simulations in functional stenosis severity assessment for patient-specific cases.

1.2.2. Contribution

The overarching contributions of this thesis are the thorough analysis and investigation of the existing issues in multidimensional patient-specific coronary blood flow simulations and the provision of the guidelines for the design and implementation of blood flow models with the specific task of non-invasive assessment of haemodynamic clinical indices. Specifically, the contributions of this thesis are summarised as follows:

- Based on the defined modelling requirements and specifics of the problem domain with respect to the CAD diagnosis, the universal approach for the design of 3D coronary blood flow models and its implementation in a CFD solver was proposed and formalised. The computed blood flow patterns are used for the assessment of FFR and WSS clinical indices considered to be the most relevant for the prediction and estimation of CAD severity. In addition, a novel approach for the straightforward approximation of parameters of 0D peripheral vasculature models was derived from the classical morphometric laws defining the geometry of vascular trees.
- A series of experiments were performed for the assessment of the stability and accuracy of image-based coronary blood flow simulations based on the investigation of the impact of the modelling assumptions and parameters on the computed blood flow patterns. The FFR and TAWSS (time averaged WSS) indices were used as the solution quality metrics. In particular, this involved the investigation of the various aspects of boundary conditions (BC) models used for the modelling of the interaction of the coronary blood flow with the rest of the CVS. This includes: (i) the differences between various outlet 0D BC models generally employed in the 3D coronary blood flow modelling for the representation of the peripheral vascular bed, (ii) the influence of the adjustment of the corresponding 0D parameters that replicate the impedance of the peripheral vasculature, and (iii) the impact of regulation of the peripheral resistance for modelling of hyperaemia induced by vasodilation. This was followed by the assessment of the influence of interpatient variations in the model parameter values, such as viscosity, inlet coronary flow rate, aortic and LV pressure, and the geometry of peripheral vascular tree. In addition, the performed investigations of the impact of variations in the vessel tree lumen geometry reconstruction parameters such as blood segmentation threshold, side branch truncation level, and degree of surface smoothing showed to produce a significant influence on the computed FFR and TAWSS patterns. The results of this analysis were summarised in a set of guidelines regarding the optimal coronary blood flow modelling strategy.
- Taking into account the fact that one of the major limitations of CFD blood flow modelling is related to the high computational costs and long time required for one simulation, the feasibility of the application of reduced-order models was investigated since they are significantly less time consuming. A novel approach for the implementation of spatially extended patient-specific 0D blood flow models was proposed. While the classical lumped-parameter 0D models use electric circuits for representation of the entire vascular trees and

thus are characterised by limited spatial characteristics, the proposed method for modelling of individual vessel tree branches through a series of 0D elements provides the means for correlation of the computed flow with the corresponding locations along a vessel. The corresponding flow resistance values are extracted from the vessel lumen geometry reconstructed from the CCTA dataset. Therefore, this extends the application of 0D modelling in patient-specific blood flow simulations for FFR assessment. The patient-specific 0D model of left coronary artery was developed and implemented together with the 0D model of the CVS, which is required for the modelling of physiologically realistic flow boundary condition. The 0D CVS loop model generates physiologically realistic haemodynamics and can be adjusted with patient-specific parameters such as CO and heart rate. The performed experiments showed high correlation between the equivalent 0D and 3D computed flow fields of the patient-specific LCA. This validated the proposed approach for extraction of flow resistance from vascular geometries and the extension of the classical 0D modelling for computation of spatially distributed characteristics of computed blood flow such as FFR.

1.3. Thesis Outline

Chapter 1 presented the general introduction into the physiology of coronary circulation and the mechanisms of coronary artery disease formation along with the clinical diagnostic indices and medical imaging technologies employed in CAD diagnosis. Following the identified motivation and research objectives, the thesis proceeds by exploring the state-of-the-art developments in image-based coronary blood flow modelling in Chapter 2. Firstly, in Section 2.1, a review of the existing image-based coronary blood flow models is presented with respect to the application areas of computed haemodynamic parameters in the prediction of CAD formation, estimation of CAD severity, and optimisation of coronary intervention. Section 2.2 presents the definition and modelling requirement of multiscale blood flow models. Current progress, existing limitations and possible future research directions are summarised in Sections 2.3-4 thus defining the basis for the implementation of the proposed blood flow modelling approach.

The stages of the proposed framework for implementation of 3D image-based coronary blood flow model using the ANSYS® Fluent CFD solver are described in Chapter 3. In Section 3.2, the essential steps required in the preparation of the 3D patient-specific domain are described including reconstruction of coronary artery geometries from CCTA and

discretisation of the 3D blood volume. The identified optimal blood flow modelling assumptions are listed in Section 3.3. Next, the inlet and outlet flow BC models are described in Section 3.4 including the type of BC models of peripheral vasculature, the proposed method for approximation of the corresponding patient-specific parameters, and the approach for simulation of hyperaemia. Sections 3.5-6 describe the process of blood flow model setup in the CFD solver and the extraction of haemodynamics parameters from the computed flow fields. The limitations of the proposed modelling approach and future research directions are summarised in Section 3.7.

Chapter 4 presents the proposed novel approach for spatially extended 0D image-based coronary blood flow simulations. Section 4.2 describes the developed framework for extraction of the spatially-distributed 0D parameters from the vessel lumen geometry, where the patient-specific arterial tree geometry reconstructed from CCTA datasets is processed branch by branch for the computation of flow resistance. Implementation of the 0D coronary blood flow model in MATLAB® Simulink also included the development of the 0D CVS model producing the essential flow boundary conditions at the inlet and outlets of the coronary arterial tree, as described in Sections 4.3-6.

Chapter 5 presents the results of a series of blood flow simulations targeting the analysis of the various aspects in the development of patient-specific coronary blood flow models with respect to the accuracy of the computed haemodynamic indices employed in CAD diagnosis. Section 5.2 investigates variations in the blood flow modelling assumptions and the essential parameters of flow boundary condition models. Next, the assessment of the impact of variations in the arterial lumen geometry reconstruction parameters is presented in Section 5.3. The analysis of the correlation between the equivalent 0D and 3D coronary blood flow models is presented in Section 5.4. The chapter is concluded with the summary guidelines for development and implementation of image-based coronary blood flow models with respect to the quality of reconstruction of vascular geometries and the choice of modelling assumptions.

Chapter 6 concludes this thesis and provides a list of recommendations for the potential future research directions and improvements to the presented work. The list of references is available at the end of the thesis.

Chapter 2

State-of-the-art in Coronary Blood Flow Modelling

In recent years, the advancement of computational sciences and resources led to the extensive employment of CFD methods in blood flow simulations in 3D patient-specific vascular geometries. Specifically, taking into account the difficulties associated with measurement of haemodynamic parameters in coronary arteries, the use of blood flow modelling techniques for the assessment of CAD pathophysiology has a direct practical application. At the same time, the high complexity and scale of the coronary circulation system together with the limited information on coronary vascular geometries that can be acquired with medical imaging significantly affect the accuracy of the computed flow patterns. The required computational resources for the solution of a system with many interrelated factors also play an important role with respect to the model implementation and solution process. For instance, the dynamic motion of the myocardium contraction and fluid-structure interaction (FSI) with the surrounding tissue introduce increased computational challenges for blood flow modelling. Therefore, the majority of existing coronary blood flow models focus on a particular problem domain rather than constructing a global model that comprises all fundamental processes of coronary circulation.

As described in Section 1.2, the main aim of image-based blood flow simulations is the computation of flow patterns that are physiologically realistic (i.e., flow parameters are within the defined interpatient range) and accurate for a particular patient taking into account the individual CVS characteristics. The underlying principle is based on the application of CFD methods to the solution of the flow governing Navier-Stokes equations defined over the 3D computational domain. The computational domain is represented by the blood volume within the 3D vessel lumen of the coronary artery geometry, reconstructed from medical images. The main haemodynamic parameters that can be extracted from the computed flow fields are pressure, velocity, flow rate, WSS, and WSS-derived parameters.

The application areas of blood flow modelling in coronary arteries are generally classified into three main groups: (i) investigation of haemodynamic-related mechanisms of CAD formation in correlation with WSS-derived parameters; (ii) estimation of CAD severity using the haemodynamic FFR and CFR indices; and (iii) planning of surgical intervention

procedures through optimisation of stent, angioplasty and bypass design. In addition, CFD simulations can be used for visualisation of velocity streamline patterns in bifurcations and regions with slow recirculation associated with aneurisms and simulation of dye injection. Consequently, the choice of the problem domain defines the scale of the model, specific requirements and acceptable modelling assumptions. 3D blood flow models are characterised by the chosen approaches to: (i) reconstruction of vascular geometries from medical image datasets and meshing of the computational domain; (ii) the choice of flow boundary condition (BC) models and their parameters; (iii) the assumption of rigid or compliant vessel wall; (iv) the choice of the CFD solver and the specification of the solution methods and associated settings; (v) simulation of various physiological conditions; and (vi) the extraction and quantification of haemodynamic parameters and their analysis.

The scale of the model defines the extent of incorporation of the CVS elements into the models representing the flow conditions on the boundaries of the computational domain. Since the information extracted from medical image datasets (e.g., CCTA, ICA) is generally limited to the 3D lumen geometry of epicardial arteries, information on the upstream and downstream flow conditions as well as the interactions between the computational domain and other parts of the CVS is unknown. And although, in the case of ICA, the velocity at the root of the coronary artery is measured invasively and can be directly used as the inlet BC representing the blood flow from the aorta, the impact of the peripheral vasculature defined by the microcirculation resistance and the extravascular pressure cannot be measured but only approximated. One of the solutions to this uncertainty is the use of multiscale modelling with the reduced-order models representing the idealised elements of the CVS being coupled to the boundaries of the 3D coronary artery tree. For instance, a 0D model of the heart and the aorta will provide both pressure and flow rate conditions at the coronary artery inlet, while 0D and 1D models of the peripheral vasculature will approximate the total downstream impedance for the coronary tree outlets. At the same time, the requirement for the use of complex BC models depends on the specifics of the problem domain and which of the haemodynamic parameters have to be extracted for further analysis.

This chapter addresses the task of providing the basis for the development of the proposed modelling approach for non-invasive assessment of FFR in patient-specific coronary arteries through an overview of the state-of-the-art developments in image-based coronary blood flow simulations. At first, recent research findings in coronary blood flow models with respect to the practical application areas in CAD diagnosis are presented in Section 2.1. The

essential aspects of the process of developing blood flow models are defined in Section 2.2, including multiscale models of the entire cardiovascular system. Section 2.3 discusses the current progress and issues in coronary blood flow simulations with respect to the main stages of model implementation. Finally, the general recommendations regarding the modelling assumptions with respect to the specifics of the problem domain are summarised in Section 2.4. This overview primarily focuses on coronary blood flow models, since, as mentioned above, one of the factors that makes a difference in blood flow modelling in coronary arteries from the similar models in other vascular regions (e.g., carotid arteries) is the impact of extravascular pressure on myocardium contraction. In addition, because the epicardial arteries are significantly narrower and have lower wall compliance than other major arteries, the rigid vessel wall assumption is generally considered to be appropriate in the task of assessing the major characteristics of coronary flow.

2.1 Application Areas of Image-Based Coronary Blood Flow Modelling

2.1.1 Prediction of CAD Formation with Haemodynamic Parameters

Investigation of the haemodynamics-related factors associated with the initial CAD formation and progression mechanisms, as well as restenosis after stenting or angioplasty is generally based on the correlation between the computed WSS patterns and plaque locations in in-vivo CAD cases. As described in Section 1.2.1, the explosion of the endothelium to low and oscillatory WSS is considered to be one of the factors leading to the vessel wall remodelling such as stenosis or aneurism. Another theory is based on the hypothesis that a longer recirculation time of blood particles is associated with a higher concentration of LDL (low-density lipoprotein), which consequently leads to formation of atherosclerotic plaques [6]. At the later stages of the disease, the local areas of maximum vessel wall pressure might be associated with rupture of vulnerable atherosclerotic plaques. These theories can be potentially used in CAD diagnosis for indication “critical areas”.

However, proof of the reliability and sensitivity of these parameters requires thorough validation, especially when considering the level of uncertainty in blood flow modelling. One of the related difficulties is that the WSS patterns cannot be directly obtained from invasive flow measurements and thus the blood simulation results can only be validated indirectly.

The study of Olgac et al. [27] investigated the process of transport and accumulation of LDL through the interface between the blood flow and the arterial wall. The blood flow simulations were performed on a reconstructed LCA bifurcation with the detected plaque being "virtually" removed to replicate the healthy state of the artery (prior to plaque formation). The vessel wall related to the endothelium was represented through a dedicated homogeneous three-pore model based on the mechanism of transportation of LDL and blood plasma though normal junctions, leaky junctions, and the vesicular pathway. The LDL concentration associated with plaque formation was estimated as a function of the local WSS. The "healthy case" simulation results showed a high-LDL concentration in the location of the developed plaque, while in the "diseased state", the LDL concentration region shifted below the plaque (Figure 2.1). The simulated hypertension state further increased the number of high-LDL concentration regions.

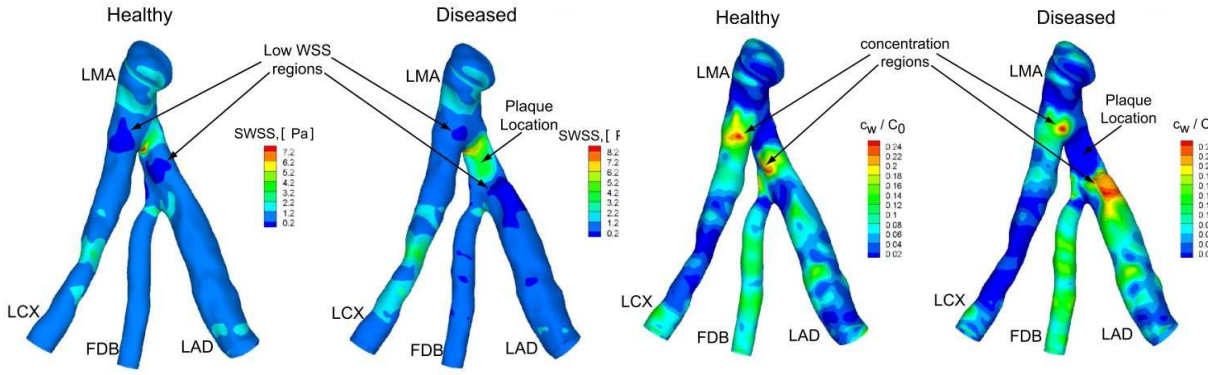

a. Computed WSS patterns b. Computed LDL-concentration patterns

Figure 2.1 Computed WSS (a) and LDL (b) for healthy and diseased LCA cases [27]

In their further study, Olgac et al. investigated haemodynamics in atherosclerotic plaque locations in CCTA-reconstructed coronary arteries of 60 CAD patients [28]. The results of simulations showed that in the artificially removed plaque regions, the LDL concentration is 45% in the RCA and 187% in the LCA, higher than the average concentrations. However, one of the major assumptions of the study was that the initial arterial lumen is obtained through the virtual removal of plaques, which consequently can either under- or over-estimate the geometry of the artery. In a similar study involving 30 CCTA-reconstructed left and right coronary arteries of CAD patients with plaques being virtually removed, Knight et al. [29,30] investigated the relationship between the locations of atherosclerotic plaques and various local WSS-derived haemodynamic indices. The statistical analysis showed that TAWSS had the highest sensitivity in the prediction of future plaque locations, but produced more false positives than RRT (relative residence time) and OSI (Oscillatory Shear Index). In addition,

the results indicated that the choice of haemodynamic indices for LCA differs from RCA due to its multiple branching and higher degree of tortuosity.

In [31], Stone et al. investigated the role of endothelial shear stress (ESS or WSS) in the progression of atherosclerosis and in-stent restenosis in 8 CAD patients in a 6 month follow-up study. The geometries of 12 stenosed and/or stented coronary arteries were reconstructed from IVUS and ICA scans. The results showed correlation between low ESS and the increase in intima-medial thickness and de novo plaque development, while regions with high ESS led to the increased outward remodelling in the stented segments. Further development of the concept led to the PREDICTION (Prediction of Progression of Coronary Artery Disease and Clinical Outcome Using Vascular Profiling of Shear Stress and Wall Morphology) study, which involved healthy and diseased 3D vessels reconstructed from ICA and IVUS of 374 CAD patients at baseline and a 6–10 months follow-up [32]. In disease-free regions, baseline low ESS magnitude and heterogeneity were associated with an increased probability of formation of the de novo eccentric plaques at follow-up. In diseased vessel regions, baseline low and large plaque dimensions were independent predictors of significantly increasing plaque localisation index together with the increasing of the stenosis degree.

A positive correlation between regions of low WSS and coronary plaque phenotype (necrotic core and calcium) was demonstrated by Eshtehardi et al. in a 27 CAD patient study involving CFD simulations in IVUS reconstructed coronary arteries [33].

Sengupta et al. used a multiscale model of patient-specific coronary circulation to investigate the haemodynamics in coronary artery aneurysms of Kawasaki disease (KD) patients in comparison to the normal coronary vasculature modelled for the same case [34]. The computed blood flow showed that the influence of aneurysms in the proximal LCA and RCA leads to significantly lower WSS and higher OSI in the aneurismal region as well as high localised stress at the aneurism neck due to flow recirculation and stagnation. Flow recirculation resulted in that after a cardiac cycle approximately 30% of the blood flow particles remained in the diseased LCA and RCA in comparison to approximately 10% in the “healthy” arteries. All these factors are associated with an increased risk of thrombosis [35]. In their follow-on research [36], Sengupta et al. performed blood flow simulations on five KD and one healthy cases, which confirmed that low WSS, high OSI, and flow stagnation are associated with aneurisms.

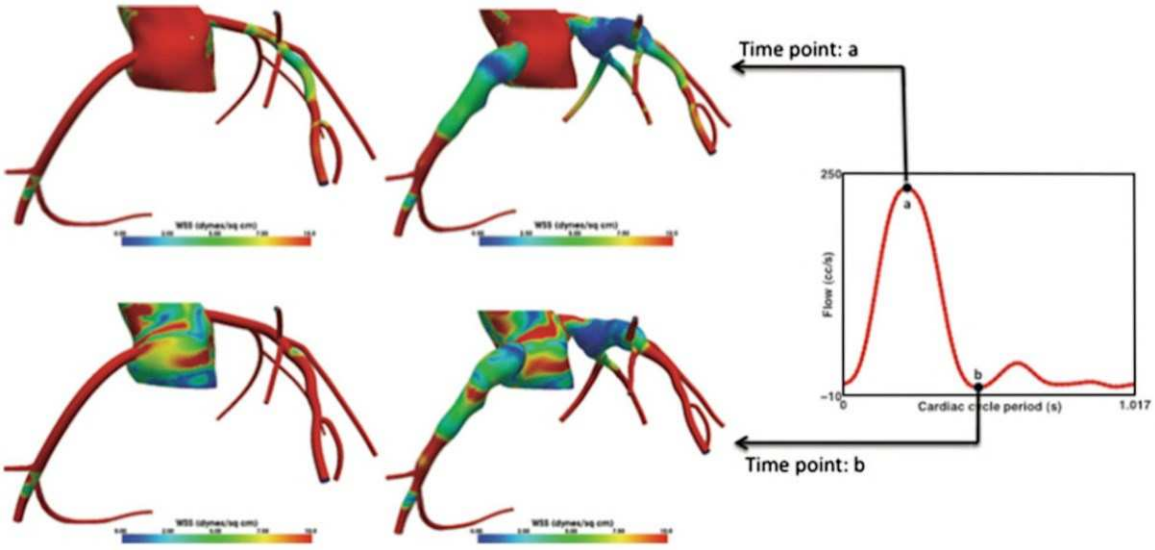

Figure 2.2 Comparison of WSS distribution for reconstructed KD patient coronary arteries and modelled healthy case at diastole and systole [35]

Taking into account that atherosclerotic plaque rupture is the primary cause of infarction and stroke, another research direction is devoted to the mechanics of plaque rupture and vulnerability with FSI modelling methods. These studies investigate mechanical plaque wall stress/ strain conditions and flow shear stress. However, the general lack of "gold standard" validation data (measurements before/after rupture events) limits the potential research impact.

Following the hypothesis associated with an increased risk of atherosclerotic plaque rupture at local maxima stress regions, Tang et al. proposed a stress-based computational plaque vulnerability index (CPVI) for estimation of plaque vulnerability in terms of the critical sites and stress conditions [37]. The reported ex-vivo simulation results for 14 human coronary plaque samples showed good agreement of the CPVI with histopathological data of rupture [38]. This hypothesis was further investigated by Huang et al. [39], who demonstrated that critical plaque wall stress is related to plaque rupture on 12 ex vivo cases of coronary plaques reconstructed from MRI. The cases of patients who died from CAD showed higher plaque wall stress than those with non-CAD related death causes. Although there is a number of limitations to this study (including the number of cases), the results indicated that estimates of wall stress distributions can provide additional diagnostic value in the assessment of plaque vulnerability. In [40], Liu et al. showed positive correlation between wall thickness and wall pressure in patient-specific stenosed coronary artery segments. Furthermore, Fan et al. [41] showed positive correlation between coronary plaque wall thickness and flow shear stress in a 10

patient study for the mechanical analysis for human coronary atherosclerotic plaques. The coronary artery geometry and vessel wall morphology were reconstructed from combined IVUS and coronary angiography scans. The proposed FSI modeling approach also incorporated cyclic bending motion, representing the impact of cardiac contraction. The calculated flow shear stress distribution showed positive correlation with vessel wall thickness, while plaque wall stress showed negative correlation. It was also reported that cyclic bending changed the stress/strain distribution patterns. In [42], Tang et al. summarised recent morphological and mechanical risk factors of atherosclerotic plaque progression and rupture mechanisms.

Rambhia et al. investigated the influence of microcalcifications on plaque vulnerability in patient-specific FSI simulations [42]. The geometry and plaque morphology (the fibrous cap with microcalcifications and the atheroma's lipid core) were reconstructed from a high resolution post-mortem micro-CT scan of the coronary artery. The inclusion of microcalcifications into the fibrous cap resulted in a 2.15 increase in mean circumferential stress and localisation of maximum stress around the micro-Ca regions. Both these factors are associated with an increased risk of plaque rupture. It was also reported that the phase shift between the coronary pressure and flow produces prolonged duration of high WSS.

2.1.2 Estimation of CAD Indices with Haemodynamic Parameters

The second application area of coronary blood flow simulations is the diagnosis of CAD severity with respect to the flow-limiting impact of an individual stenosis or a series of stenoses. Recently, a number of research projects performed investigations in terms of the correlation between CFD-computed ("virtual") and invasively measured FFR index values in CAD affected arteries. In these projects, the coronary artery geometries were reconstructed from either ICA or CCTA. In the latter case, computation of FFR is particularly useful since it extends the anatomical characteristics of stenosis with haemodynamical parameters, thus improving the diagnostic value of CCTA. The NXT Trial (Analysis of Coronary Blood Flow Using CT Angiography: Next Steps) investigated the correlation between the diagnostic performance of invasive FFR, CCTA, and virtual FFR_{CT}, computed using the HeartFlow® CFD coronary blood flow modelling system [43]. The HeartFlow® system was originally developed in the Cardiovascular Biomechanics Research Lab at Stanford University by Taylor et al. [44]. An example of the system performance is given in Figure 2.3 with a computed FFR_{CT} value of 0.64 being below the critical threshold (i.e., 0.75), with an invasive FFR measurement of 0.72. The comparison was performed on FFR, ICA and CCTA datasets acquired for 251 CAD

patients with 30-90% stenoses in vessels with diameters greater than 2 mm. The computed results reported high per-patient and per-vessel correlation with the invasive measurements. The diagnostic accuracy, sensitivity, specificity, positive predictive value, and negative predictive value for FFR_{CT} on a per-patient basis were 81%, 86%, 79%, 65%, and 93%, respectively. On a per-vessel basis, these values were 86%, 84%, 86%, 61%, and 95%, respectively [43]. In summary, these findings demonstrated that the computed haemodynamic characteristics in the form of FFR_{CT} increase the diagnostic accuracy of CCTA through a reduction in the number of false-positives (i.e., ≥ 50% stenoses that are not haemodynamically significant).

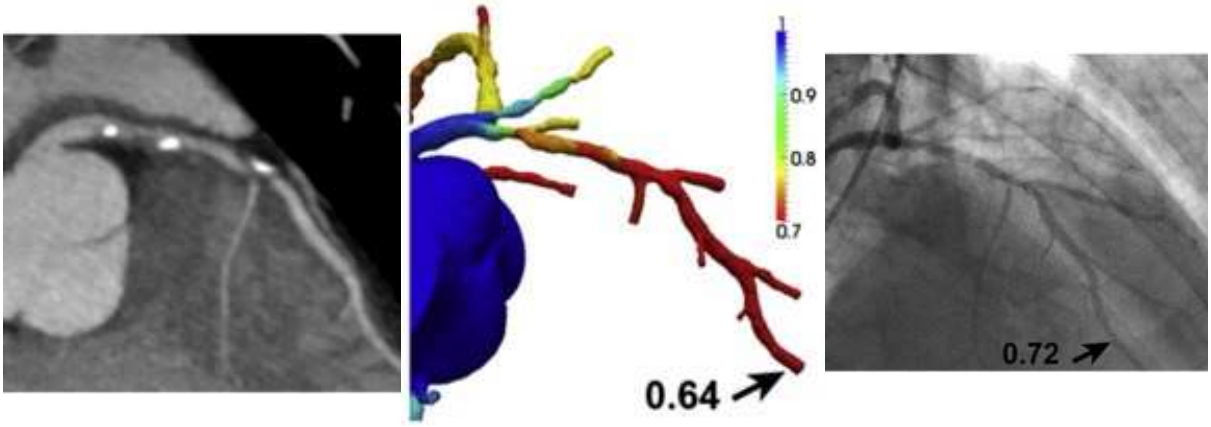

a. CCTA: LAD artery b. Computed FFR_{CT} c. ICA and FFR

Figure 2.3 HeartFlow® FFR_{CT} results for a multivessel CAD case [45]

In accordance with these results, the CFD model specifications for non-invasive FFR_{CT} assessment were summarised as [45]: (i) the 3D luminal surface of the major vessels and the branches of coronary arteries are segmented from CCTA; (ii) hyperaemia is simulated by vasodilation of the peripheral vasculature; (iii) the peripheral microcirculation vascular resistance is approximated as being proportional to the vessel diameter; (iv) the mean aortic pressure is derived from the mean brachial artery pressure; (v) the total coronary flow rate is derived from the myocardial mass; (vi) blood is approximated as a Newtonian fluid; and (vii) FFR is computed as the ratio of the mean pressure distal to coronary stenosis relative to the mean aortic pressure. The main limitations of FFR_{CT} are related to the modelling assumptions in the physiological models, which include average population-specific as well as patient-specific data, such as the degree of reduction of microvascular resistance in response to adenosine-induced hyperaemia and the relation between the total coronary flow and myocardial mass [46].

The results of an earlier FFR_{CT} study, the DeFACTO Trial (Determination of Fractional Flow Reserve by Anatomic Computed TOmographic Angiography) demonstrated that the accuracy of the reconstructed 3D lumen boundary directly affects the blood flow simulation results. These findings also emphasised the importance of the CCTA acquisition guidelines in order to avoid artifacts that may affect CTA interpretability [47]. The presence of calcifications challenges the diagnostic performance of coronary CTA by lowering its diagnostic specificity, due to limited spatial resolution because of partial volume and beam-hardening related artifacts. Accordingly, this also affects FFR_{CT} due to the resulting inaccuracies in lumen reconstruction. In [63], Nørgaard et al. investigated the influence of calcifications on FFR_{CT} performance based on the findings of the NXT trial [43]. It was reported that in patient vessels with a high Agatston score, FFR_{CT} provided high and superior diagnostic performance compared to CCTA interpretation alone [63]. In addition, the use of machine-learning methods was proposed for the assessment of the sensitivity of FFR_{CT} to geometric uncertainties and the computation of associated confidence intervals [45,53]. With respect to the assessment of FFR_{CT} in CAD patients who underwent PCI (Percutaneous Coronary Intervention), the reported high correlation between FFR_{CT} and invasive FFR in stented arteries demonstrated the potential feasibility of the application of FFR_{CT} in "virtual" stenting, thus predicting the effect of this type of surgical intervention [65].

There is also a number of similar research studies devoted to the investigation of the application of blood flow simulations in the task of virtual FFR assessment. In [48], Baumann et al. demonstrated the preliminary results of the performance of an on-site Siemens cFFR software (Siemens Healthcare) for FFR prediction from CCTA. In this 28 patient study, both per-vessel and per-patient analyses for the identification of haemodynamically-significant lesions showed good correlation with invasive FFR. Further results of investigation of cFFR performance were reported by Renker et al. in a 53 patient study [55]. For FFR measured on a per-lesion and per-patient basis, the CT-derived FFR resulted in a sensitivity of 85% and 94%, a specificity of 85% and 84%, a positive predictive value of 71% and 71%, and a negative predictive value of 93% and 97%, respectively [55]. Figure 2.4 shows an example of (computed) cFFR of 0.76 for a CCTA, where an intermediate to severe stenosis was detected, compared to an invasive FFR measure of 0.76, indicating a haemodynamically significant stenosis.

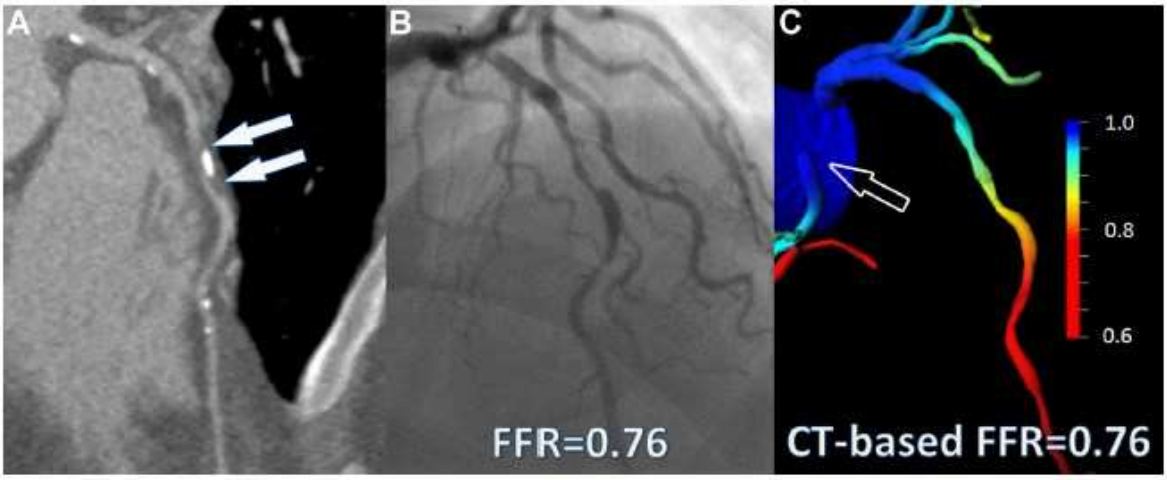

a. CCTA detected plaque b. ICA and FFR c. Computed cFFR

Figure 2.4 Siemens cFFR® computed FFR for a multivessel CAD case [55]

The outcomes of another clinical study VIRTU-1 (VIRTUal Fractional Flow Reserve From Coronary Angiography) were reported by Morris et al. in [49]. The virtual FFR was computed in 22 coronary arteries reconstructed from ICA and showed a high correlation with invasive FFR measurements, thus proving the feasibility of the proposed approach that allows the replacement of fully invasive FFR measurements and also reduces the cost of the FFR procedure. In [50], Tu et al. presented an approach for computation of FFR on the basis of 3D quantitative coronary angiography (QCA) acquired under hyperaemia, which was successfully validated with invasive FFR with a diagnostic accuracy of 88.3% in 77 vessels. In this case, one of the advantages is that the coronary flow rate at hyperaemia can be directly extracted from ICA data, thus eliminating potential inaccuracies related to various modelling assumptions. In addition, ICA generally results in more accurate vessel segmentation than CCTA, since it visualises only the vessel lumen and does not include plaques. Both works, [49] and [50], employed professional CFD solvers, ANSYS® FLUENT and CFX (ANSYS Inc., Canonsburg, Pennsylvania), respectively.

It can be summarised that all these findings demonstrated the feasibility of the application of CFD methods for virtual assessment of FFR so as to enhance anatomic features of detected stenoses with the computed degree of hemodynamic significance. A series of clinical trials under the ADVANCE (Assessing Diagnostic Value of Non-invasive FFRCT in Coronary Care) multicenter registry are planned for evaluation of the clinical and economic impacts of FFR_{CT} [45].

Other research investigated the influence of the stenosis position, length and degree on FFR values calculated in the LAD branch with multiple outlets [51], the feasibility of FFR assessment from IVUS/ICA reconstructed coronary arteries [52], the relation between vessel geometry and estimated pressure drop [54], and the application of reduced-order 1D and 0D blood flow modelling in FFR assessment [56,57,94].

For instance, Schrauwen et al. performed a series of CFD simulations in 22 coronary arteries with medium severity stenoses for estimation of geometry-related pressure drop. Based on the simulation results and information on the tapering angle, stenosis area, and centreline characteristics, they generated a geometry-based model for ΔP prediction (i.e., FFR), which showed good correlation between FFR_{CFD} and $FFR_{estimation}$. It was also suggested that this approach can be used for estimation of BC for other models and the advantages of steady-state simulations over transient were investigated. Characterised by lower computational costs, steady-state simulations do not require the use of the deformable vessel wall assumption and can be used for estimation of mean flow parameters such as FFR and TAWSS.

2.1.3 Optimisation of Coronary Intervention Strategies

In combination with CFD blood flow simulations, geometrical modelling methods also provide a means for virtual planning of surgical interventions based on patient-specific geometries or prediction of potential benefits of alternative treatment strategies. In terms of the application to coronary blood flow modelling, this generally involves optimisation of stent and coronary artery bypass graft (CABG) design based on the computed haemodynamic indices.

In a recent study, Sankaran et al. developed a multiscale computational framework for surgical modelling and blood flow simulations for the assessment of haemodynamics in various patient-specific CABG models [58]. They investigated the relationship between the graft geometry, such as anastomosis angles, length and radius, with the post-CABG complications, such as restenosis, graft occlusion, and plaque rupture that are reportedly associated with local hemodynamics (WSS, WSSG, OSI). The results showed that both coronary perfusion and local hemodynamics near the anastomosis region differ substantially in pre- and post- bypass graft surgery models, while the various bypass graft (BG) shapes and anastomosis angles also affect the flow fields. For instance, a 70% anastomosis angle provides better results in terms of higher WSS and lower OSI (Figure 2.5). At the same time, higher angles cause larger flow separation regions and reduced energy efficiency. Based on the analysis of the simulation results, a specific cost function was proposed for optimisation of CABG parameter design [58]. It is

based on a combination of risk factors and the computed haemodynamics indices. According to the authors, the main limitations of the proposed framework are the lack of validation data and the rigid vessel wall assumption, due to controversial reports on the FSI-computed WSS fields.

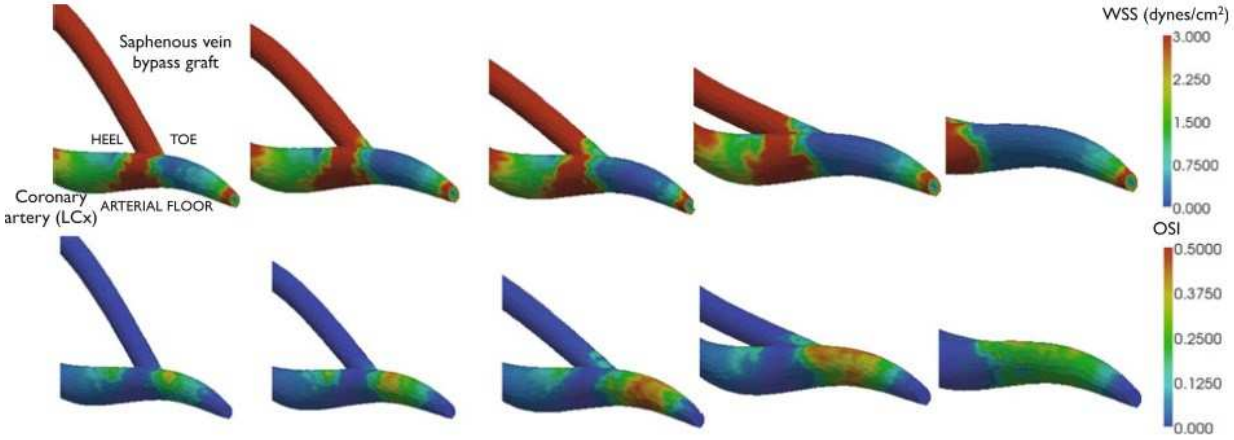

Figure 2.5 Impact of CABG anastomosis angles on the computed WSS and OSI [58]

In [59], Kabinejadian et al. demonstrated the beneficial impact of the coupled sequential CABG design on computed coronary blood flow patterns and WSS fields in comparison to the conventional end-to-side configuration. It was also reported that although the FSI and non-Newtonian rheology modelling assumptions do not affect the computed velocity patterns despite the relatively large wall deformations, it results in reduced TAWSS (by up to 32% in the junction regions) and elevated OSI patterns.

With respect to the optimisation of stent design, LaDisa et al. investigated the effect of coronary stent implantation on WSS at rest and maximum vasodilation conditions [60]. The reported results indicate a significance reduction of WSS (75%) in the stent area, which might potentially lead to restenosis in the future. The same research group pursued studies in the assessment of WSS produced by stents in the in vivo case of post-stent and follow-up LCx artery reconstructed from optical coherence tomography (OCT) [61]. The comparison of immediate post-stenting and follow-up CFD results showed that the areas of low stent-induced WSS returned to physiological levels after 6 months. At the same time, the CFD studies of Dehlaghi et al. showed that the analysis of the WSS profile between stent struts, and in pre-stent and post-stent regions is essential in stent design, since the optimal strut spacing, strut profile, and number of struts vary between the different with respect to the resulting WSS patterns [62].

In [64], Martin et al. reported the significance of the modelling of stent and vessel wall deformation in accurate prediction of the haemodynamic parameters in coronary arteries by comparison of WSS, TAWSS, and OSI results in FSI and CFD simulations. The vessel wall was represented through three layers, namely, intima, media, and adventitia, using isotropic hyperplastic material models. Three types of stainless steel stents were constructed and their deformations were modelled by the defined elastic response. An example of the TAWSS patterns computed under rigid and deformable vessel wall assumptions in stented coronary arteries is given in Figure 2.6 demonstrating the lower WSS magnitudes and non-uniform distribution in the CFD results. On the other hand, in the work presented by Chiastra et al., the results of the comparison of FSI and CFD simulations in a stented coronary artery indicated that, for idealised models, the rigid-wall assumption is adequate in the analysis of haemodynamic parameters, such as WSS [66].

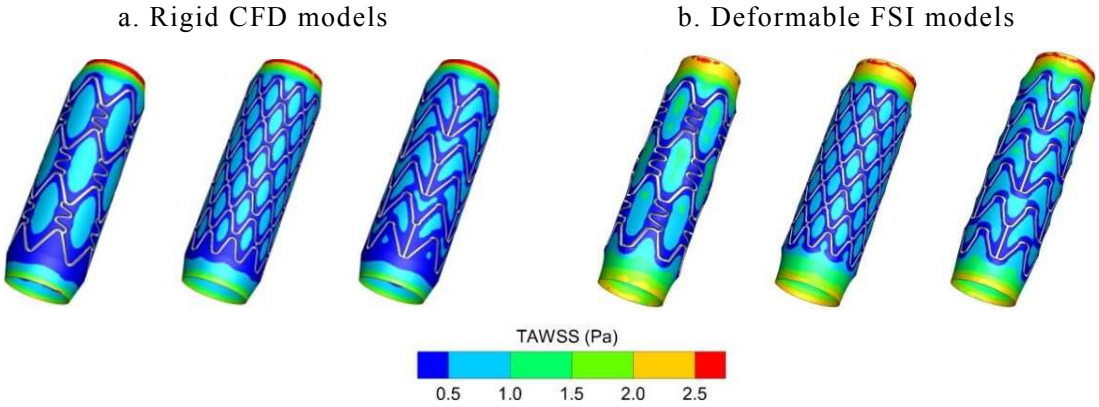

Figure 2.6 Computed TAWSS patters on the lumen surface of a stented coronary artery for rigid CFD and deformable FSI models [64]

In general, there is a plethora of research works on optimisation of stent and bypass design and surgical intervention for aneurism treatment applied to other regions of CVS that can also be applied to coronary arteries with appropriate adjustments, such as scaling, wall compliance modelling, and boundary conditions. With respect to the more complex surgical procedures, the notable works of Migliavacca et al. and Baretta et al. [67-69] successfully demonstrated the application of multiscale blood flow simulations in preoperative planning and quantitative evaluation of surgical outcomes in congenital heart disease (CHD).

2.2 Definition of Blood Flow Modelling Methodology

While 3D CFD modelling is the classical approach in patient-specific blood flow simulations since it provides the highest degree of information on the computed local flow

fields, reduced order 0D and 1D models are also employed for simulation of blood flow on a wider scale and as boundary conditions for 3D blood flow models. The most common examples include the global flow behaviour in the entire 0D CVS model and flow patterns in the idealised 1D vessel tree, which includes all levels of vasculature from the large arteries to the capillary bed.

2.2.1 3D Blood Flow Modelling

In recent years, 3D simulations of blood flow emerged as a powerful tool for both research and patient-specific assessment of haemodynamics in the cardiovascular system. 3D blood flow models can be divided into two categories on the basis of the modelling assumptions of the vessel wall properties, i.e., rigid and compliant vessel walls. Classical CFD models assume the vessel wall to be rigid and unaffected by pulsatile flow and heart movement. The no-slip condition is assigned to the rigid wall of the vessel lumen and blood flow simulations are performed through the numerical CFD solution of the flow governing Navier-Stokes (N-S) equations defined over the discretised computational domain [70]:

$$\begin{aligned} &\nabla \cdot \mathbf{v} = 0 \\ &\rho \cdot \frac{\partial \mathbf{v}}{\partial t} + \rho \mathbf{v} \cdot \nabla \mathbf{v} = -\nabla P + \nabla \cdot (\mu \nabla \mathbf{v}) \end{aligned} \quad , \tag{2.1}$$

where v is the velocity, P is the pressure and ρ and μ are the fluid density and viscosity, respectively.

The N-S equations describe the motion of viscous fluid substances through the pressure and velocity variables and, under the general modelling assumption of incompressible Newtonian fluid flow, are represented in the form of the continuity and momentum equations (2.1). The computational domain is the blood volume within the lumen discretised into elementary cell elements and is also known as the volume mesh. The volume mesh resolution and discretisation strategy directly affect the quality of the numerical solution with respect to both local and global flow features. The numerical solution of the N-S equations over the volume mesh is performed by classical CFD approaches, specifically Finite Element Modelling (FEM) and Finite Volume Modelling (FVM). The choice of the numerical solution method and the corresponding parameter settings have more influence on the simulation results than the choice of CFD solvers. This mainly depends on the specifics of the problem domain and the required precision for the solution of the specified question (e.g., FFR prediction) [71].

As mentioned in the introduction of this chapter, due to the limited extent of the extracted 3D vascular geometries from medical image datasets, the flow conditions (i.e., pressure, flow rate, or velocity) on the boundaries of the coronary arteries tree have to be assigned based on the measured patient-specific data, average interpatient values, or idealised modelling assumptions. The choice of the BC type and parameters directly defines the computed flow patterns but the complexity of the BC model generally depends on the problem domain. In the cases that require blood flow to be solved taking into account the influence of the interactions between the computational domain and the rest of the CVS, the multidomain modelling approach is generally employed with 0D and 1D reduced-order models representing the essential CVS elements, implicitly coupled to the inlet and outlet boundaries. For instance, this approach is employed in the models for virtual FFR assessment in CCTA reconstructed coronary artery geometries with multiple branches due to the lack of invasively measured flow conditions [44, 48]. At the same time, the assessment of WSS patterns in a single vessel study does not require complex BC models and simple assignment of outlet pressure or outflow BC is generally used. The common approaches for the choice of flow BC models in the specific task of coronary blood flow simulations are discussed in Section 2.3.2.

Under the baseline condition, blood flow in major epicardial arteries is laminar. However, flow can become weakly turbulent under high flow conditions and recirculation induced by the complex stenosis geometries. At the same time, it was reported that Reynolds-averaged turbulence models, commonly available in commercial CFD solvers, are unsuitable for pulsatile, relaminarising physiologically realistic blood flow models [72].

The assumption of blood being a Newtonian fluid is considered acceptable for the flow in large arteries with high shear rate and is used in the majority of coronary blood flow models. However, in small arteries, arterioles, and capillaries, non-Newtonian effects should be considered in solving blood flow and pressure [72]. Non-Newtonian blood models with dynamic viscosity are generally employed in the studies of WSS fields associated with plaque formation and restenosis after stenting. An overview of research employing various blood rheology models in coronary blood flow simulations is given in Section 2.3.4.

Since the rigid wall assumption does not represent realistic vessel wall properties, CFD solutions provide a general approximation of the blood flow behaviour and cannot be considered to be fully physiologically realistic. This is especially true in terms of wave propagation, which is significantly prominent in large arteries characterised by high

compliance, such as the aorta, the carotid and femoral arteries [73]. The modelling assumption of deformable wall requires the incorporation of interactions between the flow and the vessel walls into the system of PDEs defining the blood flow model.

Taking into account the high computational costs associated with the solution of FSI models, there are several existing approaches to the formulation of fluid-solid interaction, depending on the strategy for the coupling of the N-S and the elastodynamic equations of the vessel walls. In the classical Arbitrarily Lagrangian-Eulerian (ALE) formulation, the equations governing mesh movement involving flow in a moving domain and accounting for the elastodynamics of the wall are solved using either a fully-coupled or a staggered approach [74]. An alternative to the ALE approach is the Coupled Momentum Method (CMM) proposed by Figueroa et al. [75]. In this approach, the following simplifications are employed: (i) wall motion is assumed to be small, thus the fluid mesh is not updated; (ii) the vessel wall is represented through a membrane model; and (iii) node-on-node compatibility between the lateral surface of the fluid volume mesh and the vessel wall is enforced. These simplifications enable the elastodynamic equations for the wall to be embedded within the fluid dynamics equations, thus significantly decreasing computational costs. In the cases with underlying modelling assumptions of thin walls and small deformation (<10%), the CMM is highly efficient for large scale FSI simulations and the resolution of wave propagation phenomena.

Similarly to the blood viscosity modelling assumption, the choice of the FSI modelling approach is defined by the problem domain. For instance, the incorporation of the myocardial contraction induced movement of coronary arteries requires the application of the ALE formulation. The use of FSI is also required in the modelling of WSS-related studies of stent optimisation and plaque rupture mechanisms. An overview of the recent progress and findings in coronary FSI modelling is presented in Section 2.3.3.

In general, the predominant reason for the choice of the rigid vessel wall assumption and CFD methods in coronary blood flow simulations is related to the high computational expenses for the incorporation of the elastodynamic equations through FSI into the model. At the same time, since the epicardial arteries are relatively narrow and have significantly lower wall compliance than the large arteries, the rigid vessel wall assumption is generally considered to be appropriate in the assessment of the major characteristics of coronary blood flow [44,49,55,58]. Other reasons limiting the use of coronary FSI models include the lack of patient-specific information regarding the properties of vessel wall materials and spatial

variations along the vessel wall and as well the uncertainties related to the incorporation of the myocardium contraction mechanics [76].

2.2.2 Multidomain Blood Flow Modelling

Reduced order blood flow modelling is based on the simplification of the computational domain, thus resulting in significantly lower computational costs. An example of the representation of vascular structures in 3D, 1D and 0D domains is given in Figure 2.7. Fractal-like 1D structural trees (Figure 2.7.b) are based on the morphometry scaling laws of vascular branching and, with respect to the reduced model dimension, vessel segments are represented as either rigid or elastic tubes characterised by length and radius parameters [77]. In the 0D domain (Figure 2.7.c), the lumped-parameter model of vascular structures is based on the classical electrical–hydraulic analogy with the geometry-induced flow resistance and vessel wall compliance represented through R and C elements, respectively [73].

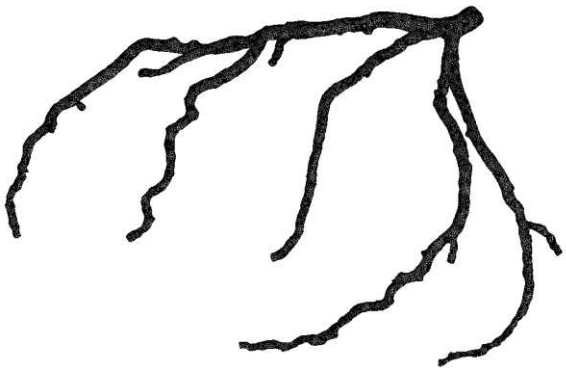

a. Patient-specific 3D vascular tree

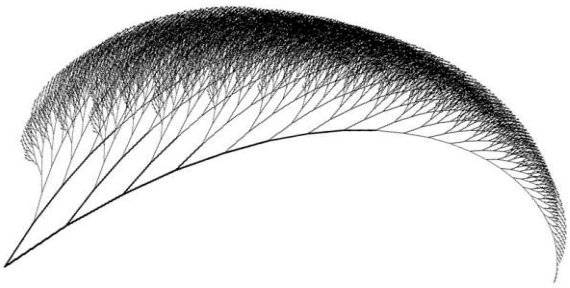

b. 1D structural vascular tree

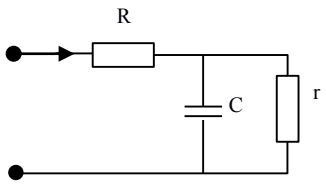

c. 0D WK model of a vascular tree

Figure 2.7 Vascular tree representation in the 3D, 1D and 0D domains

1D blood flow model equations are derived from the Navier-Stokes equations with the assumptions that the dominant component of blood flow velocity is along the vessel axis and that the pressure is constant over the cross-section of the vessel [77]. Thus, the 1D

equations of blood flow integrate the velocity and pressure over the cross-section and solve a system of nonlinear partial differential equations in a single spatial variable and time.

Although being widely employed as either BC models [77] or for the representation of systemic arterial trees [78,81], the 1D approach is not generally used in patient-specific coronary blood flow simulations with a notable exception of the anatomy-based 1D coronary model implemented by Smith et al. [79,80]. The topology of the model, shown in Figure 2.8, is based on the largest six generations of the coronary arterial vasculature. The effect of vessel elasticity was modelled through a specific pressure-radius relationship, which provided the means for simulation of the deformation of vascular networks under the pressure of heart contraction, while the microcirculation network was implemented using 0D models.

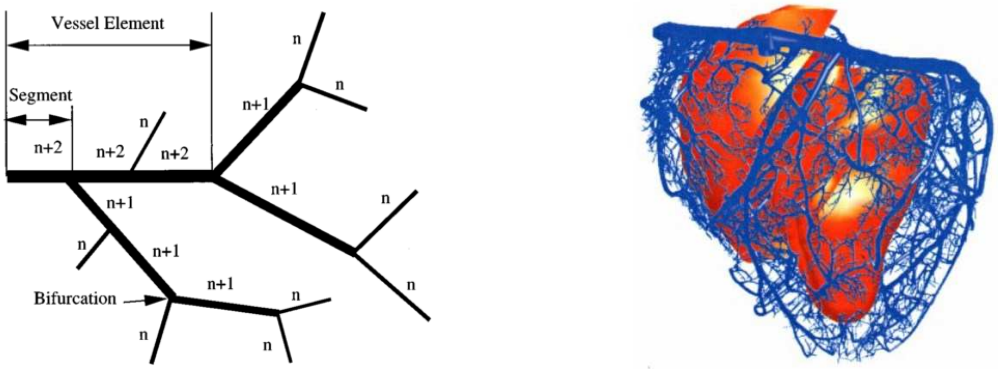

a. 1D tree topology features b. Generated 1D tree model

Figure 2.8 Anatomically-based 1D model of coronary vasculature [80]

Other 1D models of coronary circulation include the histology-based structured tree model of the entire porcine coronary arterial tree implemented by Mittal et al. [82] and the approach for the assessment of FFR in 1D patient-specific coronary arteries proposed by Itu et al. [56]. The latter model employed the 0D CVS model for representation of boundary conditions.

Based on the electrical analogy, in 0D models, voltage in an electrical circuit system corresponds to the pressure difference ΔP in the equivalent vascular system and the electric current along a conductor corresponds to the flow rate Q along a vascular tree. It allows the straightforward representation of either individual vessels, an entire vascular tree, or a heart chamber as an electric circuit consisting of the basic elements of resistance, capacitance, and inductance. The parameter values of these elements can be derived from the vascular tree geometry and are generally used in the description of physiological characteristics of the

cardiovascular system (i.e., vascular resistance and compliance) [2]. Figure 2.7.c demonstrates an example of the classical 3-element RCR Windkessel (WK) model considered to be the optimal configuration for modelling of the global features of the vascular network with physiologically derived parameters [77,87]. Many studies have utilised 0D models to simulate complex blood flow and pressure waveforms of the cardiovascular processes resulting in the foundation of classical 0D CVS loop models and the guidelines for the adjustment of their parameters and simulation of various pathological conditions [83-86].

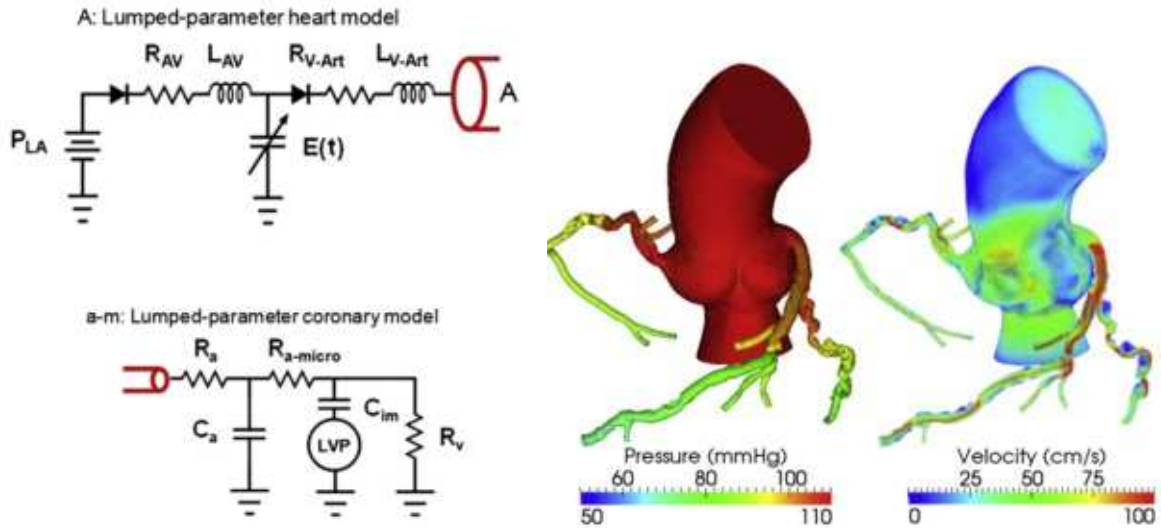

a. 0D models of left ventricle and downstream coronary vasculature

b. Computed pressure and velocity fields

Figure 2.9 HeartFlow® system: 0D boundary condition models [44]

Being useful in modelling of the global characteristics of the CVS and representation of haemodynamics of elements such as venous circulation and capillary beds, the main limitation of lumped parameter models is the lack of spatial characteristics of the computed blood flow. Therefore, they are mainly employed as BC for either 3D or 1D models in multiscale blood flow simulations. In coronary blood flow models, 0D BC were used for representation of the CVS and coronary peripheral vasculature in the models for prediction of FFR in CCTA-reconstructed geometries [44,55] as well as in the model for CABG surgery planning [58]. For instance, Figure 2.9 shows the 0D BC models used in the HeartFlow® system along with an example of the computed pressure and velocity fields in the 3D domain.

Based on the approach originally established by Mantero et al. [88], patient-specific 0D models of coronary blood flow represent separate branches through RLC WK models, which are suitably interconnected for the construction of the arterial tree [57,89,90]. The R, L,

C parameter values are derived from the branch geometry and the downstream impedance Z values are approximated from the outlet diameters. An example of the 0D model for evaluation of the haemodynamics of different coronary bypass configurations is presented in Figure 2.10. It consists of the LCA tree model constructed from RLC circuits representing the sections of the major artery branches (i.e., LCx_1, LAD_1, etc.) incorporated into the 0D CVS loop model.

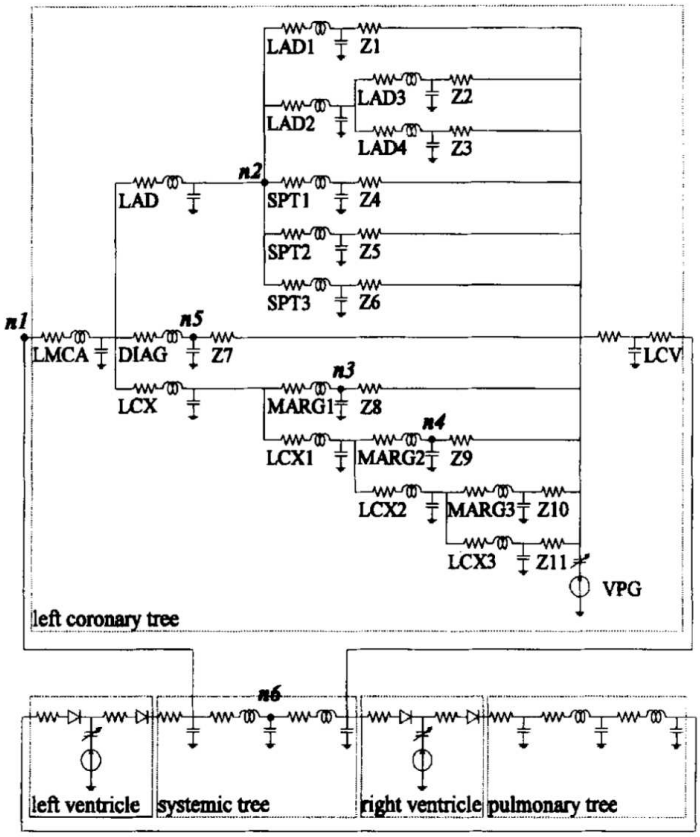

Figure 2.10 0D model of the LCA for evaluation of CABG fluid dynamics [89]

Other examples of application areas of 0D coronary blood flow simulations include sensitivity analysis of the impact of myocardial parameters on coronary flow rate [92] and investigation of the correlation between the computed 0D coronary flow and time intensity curves extracted from angiograms under rest and hyperaemia conditions [93]. In a recent study, Nickisch et al. employed lumped-parameter modelling in the task of FFR from patient-specific coronary geometries based on the assessment of the coefficients balancing the local nonlinear hydraulic effects from a training set of precomputed 3D FEM simulations [94]. The evaluation of the proposed approach in a 41 patient study showed good correlation with the invasive FFR measurements.

Global multiscale models provide the means for modelling of the entire CVS with the ability to incorporate local flow features through 3D patient-specific vascular tree segments. In

[95], Larrabide et al. described the developed HeMoLab frameworks for 3D/1D/0D coupled blood flow simulations in patient-specific vascular segments such as the abdominal aorta and vertebral arteries. Blanco et al. proposed a multiscale closed loop CVS model with 3D FSI models of patient-specific arteries, a 1D systemic tree with 128 segments of large arteries, and a 0D model of the heart, pulmonary tree and peripheral vasculature [96-97]. The model also incorporates a baroreflex control mechanism for regulation of the system haemodynamics in order to assess the baroreflex response to pathologies such as haemorrhage in the abdominal aorta and regurgitating aortic valve.

2.3 Current Progress and Issues in 3D Coronary Blood Flow Modelling

Depending on the problem domain, the employed medical imaging modalities and the availability of invasively measured flow boundary conditions, 3D blood flow models can be characterised with respect to: (i) preparation of the computational domain; (ii) modelling of flow BC; (iii) selection of modelling assumptions: rigid or compliant vessel walls and blood as a Newtonian or non-Newtonian fluid; and (iv) simulation of various physiological conditions.

2.3.1 Geometry of the Computational Domain

Preparation of the computational domain involves reconstruction of the vessel lumen geometry from medical image datasets, definition of the inlet and outlet boundaries, and discretisation of the volume mesh. Since the lumen boundary of the computational domain defines the computed flow patterns, the optimisation of vessel segmentation methods plays an important role in the physiological accuracy of blood flow simulations [98]. Medical imaging modalities commonly employed in clinical practice that have sufficient spatial resolution for extraction of coronary artery geometries include ICA, CCTA, and IVUS. While the ICA limitations are mainly related to the reconstruction of the vessel lumen from 2D image datasets, extraction of coronary artery geometries from 3D CCTA is relatively straightforward but the accuracy of segmentation is highly affected by the quality of data acquisition and artefacts due to presence of calcified plaques [53, 63]. One of the optimal approaches is considered to be the level set method, which balances image- and shape-based characteristics to define the lumen boundary. Recent developments in CCTA segmentation methods can be found in the standardised framework for evaluating coronary artery stenosis detection, stenosis quantification and lumen segmentation algorithms in CCTA, implemented by Kirisli et al. [99] (Figure 2.11).

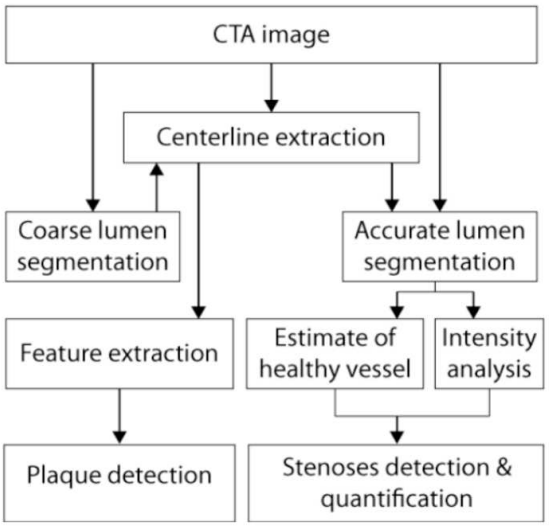

Figure 2.11 Framework for plaque and stenosis detection and quantification in CCTA[98]

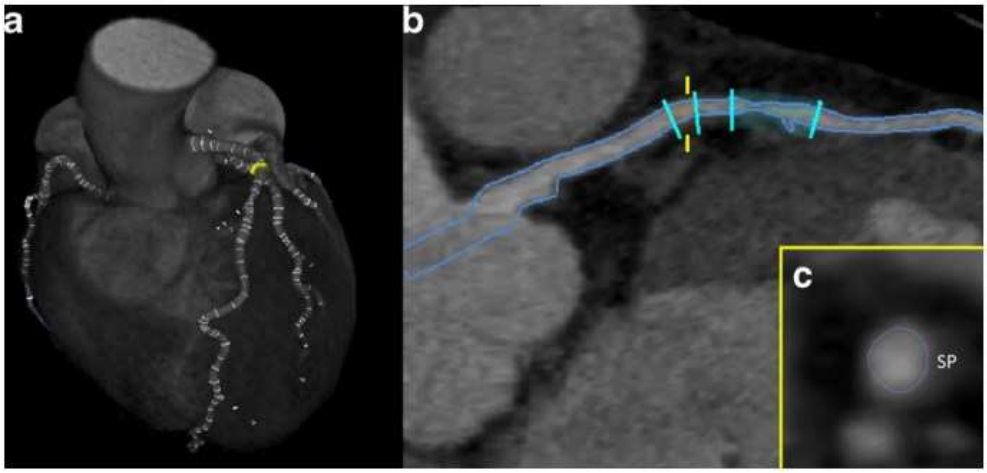

Figure 2.12 Segmentation of coronary arteries from CCTA [48]

An example of segmentation of coronary arteries from CCTA with the Siemens Healthcare system, which is further used for cFFR assessment [48] is given in Figure 2.12. It includes volume rendering (A), cMPR (B), and lumen cross-sectional (C) views of the segment with a vulnerable plaque. In combination with ICA, IVUS provides information on the vessel wall structure and plaque composition, which are essential in FSI simulations for the assessment of plaque rupture related factors [41]. Taking into account the interpatient variations in the geometries of epicardial arteries, there is no completely reliable, fully automated solution for vessel segmentation or universal parameter settings. Consequently, the accuracy of vessel segmentation has to be verified before the next step of volume mesh generation especially with respect to the detection and quantification of stenosis regions.

The general blood flow modelling guidelines formalised in [71] are based on the analysis of different commercial CFD solvers, volume meshing strategies and solution methods. With respect to the strategy for discretisation of the computational domain, the general recommendation is to employ tetrahedral meshing with multiple boundary layers for complex vascular geometries [71], even though hexahedral meshes provide higher accuracy. In order to optimise computational costs and ensure that the volumetric mesh is not under-resolved, sensitivity analysis has to performed through extensive simulations with increasingly finer meshes in order to determine the appropriate mesh density, so as the solution does not vary by more than 1-5%. Adaptive refinement of the regions of interest such as stenoses or bifurcations also improves the accuracy of blood flow simulations. For instance, in [100], Sahni et al. proposed a method for anisotoropic adaptive meshing based on feedback posteriori flow error estimation. It was demonstrated that adapted boundary layer meshing provides more accurate solutions in comparison to similar size globally uniform meshes, which is essential in the prediction of WSS distributions.

With respect to the definition of the boundaries of the computational domain and variations in the lumen geometry, Wellnhofer et al. demonstrated that the inclusion of side branches has significant impact on the computed blood flow and WSS profile on 17 patient-specific RCA cases, including healthy, stenosed, and aneurysmatic [101]. The impact of side branches on the WSS distribution was shown to be non-linear and highly influenced by the vessel tree geometry.

In a recent study, Chaichana et al. investigated the haemodynamic impact of stenosis location and severity in patient-specific LCA bifurcations of 17 patients [102]. It was reported that a combination of LCX and LAD stenoses results in higher WSS and TAWSS changes than a single stenosis or either type (with stenosis >30%), while the WSS change in stenoses of >70% degree is significantly different from 30% stenosis. The same research group also investigated the haemodynamic impact of variable angulations in idealised and four image-based LCA cases [103]. The results showed that there is a direct correlation between LCA angulations and haemodynamic parameters, i.e., wider angles (e.g. > 100^{o}) are associated with lower WSS. In [104], Su et al. investigated the effect of a modelled stenosis of varying degree on blood flow in a 3D porcine LAD artery. The results demonstrated that only significant stenoses (≥75%) considerably altered the pressure drop. However, the computed OSI fields and relative flow stagnation showed that stenoses of lower degrees may potentially induce localisation of CAD.

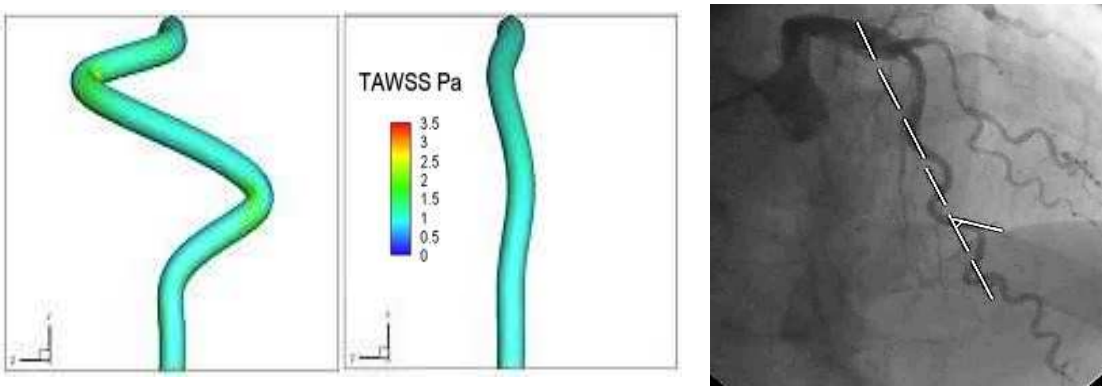

a. Computed TAWSS depending on the bend angle b. Coronary tortuosity

Figure 2.13 Correlation between coronary tortuosity and haemodynamics [105,106]

The impact of coronary artery tortuosity on the computed haemodynamics was investigated by Xie et al. in [105]. The results showed strong correlation between the tortuosity of vascular geometries and alternations in flow and WSS. For instance for bend angles >120°, high OSI and low WSS regions were observed downstream of the bent region, while due to the increase in driving pressure, the flow resistance increased by up to 96% under the simulated exercise condition (Figure 2.13). In accordance with the outcomes of the related clinical studies [106], Xie et al. concluded that tortuosity of the arteries may be associated with localisation of CAD.

2.3.2 Flow Boundary Conditions

In 3D blood flow simulations, boundary conditions play an important role because they represent the interaction of the computational domain with the upstream and downstream parts of the CVS. The choice of BC type and parameter values affects the computed flow distribution, the pressure range, reflection and attenuation of the pressure wave, as well as the shape of the flow and pressure waveforms.

There are two approaches to the definition of flow conditions at the inlet and outlet boundaries, explicit and implicit. In the former, constant values or transient waveforms of pressure, flow rate, or velocity are prescribed. The corresponding waveform shape magnitudes are either obtained from the literature, in vitro or in vivo measurements. The implicit coupling is based on the reduced order models representing the upstream and downstream vasculature.

The majority of the implemented coronary blood flow models employed explicit BC with average or measured velocity prescribed at the inlet and zero pressure or outflow ratio at the outlets based on Murray's law [73]. However, models based on explicit BC are not capable

of predicting physiologically realistic pressure distributions and, indeed, it can be observed that the related studies presented the analysis of only velocity and WSS-related haemodynamic parameters. For instance, Frauenfelder et al. performed blood flow simulations and evaluated the effect of CAD on blood flow in CCTA reconstructed coronary arteries of five patients [107]. The employed boundary conditions included average transient velocity at the inlet and zero pressure at the outlets.

In other words, the explicit assignment of constant or time-varying pressure, zero traction or velocity at outlet boundaries has limitations due to the fact that they do not accurately replicate the fluid impedance of the downstream vasculature. Particularly, with constant pressure and zero traction as outlet boundary conditions, the flow distribution is solely determined by the resistance of the artery tree geometry and not by the flow demand of the downstream vasculature. Even in a hypothetical case, when the measured pressure waveforms for each boundary are available, another issue of explicit BC is related to the synchronisation of the transient inlet and outlet waveforms. An example of an exception to this is the work of Torii et al. [125,126], where the transient inlet velocity and outlet pressure, simultaneously acquired with IVUS in the RCA, are prescribed at the vessel boundaries.

On the other hand, under the implicit coupling, the outlet boundary conditions are derived naturally through the interactions between the computational domain and the reduced order BC models. Reduced order models are based on either 1D wave theory or the lumped-parameter approach, thus resulting in physiologically realistic flow rate and pressure fields. In [108], Vignon-Clementel et al. compared the performance of various outlet BC types on an example of a rigid stenosed bifurcation model including constant pressure, resistance R, and 1D impedance. The results showed that, in terms of pressure field and flow distribution, implicit coupling produces the most realistic results and improves solution convergence in the case of multiple outlet vascular tree models. Pure resistance BC relates pressure and flow rate as $\Delta P = Q\ R$ and tends to overestimate the predicted pressure, while the 3-element RCR WK model incorporates the transient factor and provides more physiologically accurate solutions.

In 3D models with multiple outlets that require accurate computation of pressure patterns (e.g., for FFR assessment or predicting outcomes of interventions) and with the lack of patient-specific data, 0D models of peripheral vasculature are the optimal BC choice [71,109]. At the same time, in single vessel models developed for the assessment of velocity and WSS fields [60-62,64,66], simple explicit BC models are considered to be acceptable.

Figure 2.14 shows the 0D/3D coupled model proposed in a landmark study by Kim et al. [110] with the inflow boundary condition (A) supplied by a lumped-parameter heart model and the outlets coupled with 0D models of downstream vasculature. While 3-element WK models are used for the aorta and the upper branch vessel outlets (B-H), the coronary artery outlets (a-k) are coupled to a 5-element RCRCR circuit connected to the P_{im} pressure source, representing the extravascular pressure of myocardium contraction. As discussed in Section 2.2.2, models for virtual FFR assessment and CABG planning in CCTA-derived geometries also employ 0D CVS loop BC [44,48,58]. In addition, 0D BC models allow for simulation of exercise and hyperaemia conditions, which are required for FFR assessment [44,110].

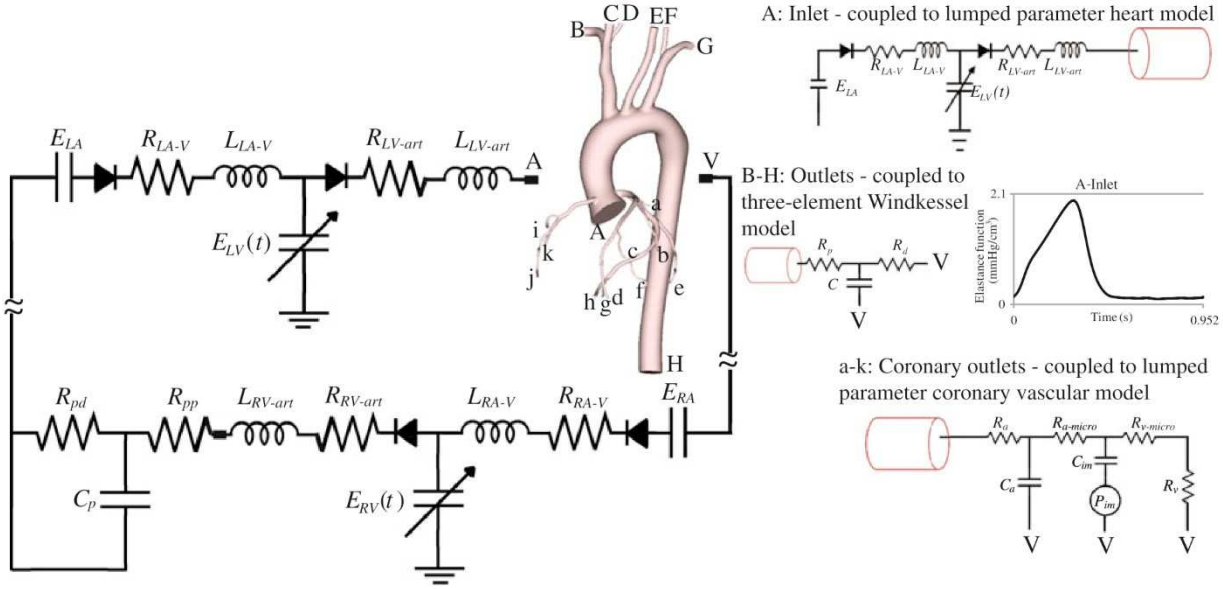

Figure 2.14 3D model of the aorta and coronary arteries coupled to a 0D CVS loop [110]

With respect to the flow distribution requirements derived from the artery structure, Van der Giessen et al. investigated the influence of various outlet BC types on WSS distribution in 6 patient-specific coronary arteries [111]. It was proposed the use of Doriot's fit for the estimation of the flow ratio. It relates local geometry to flow rates through the main and side branches, in contrast to the generally employed Murray's morphometric law [73], which relates the flow ratio to the third power of the outlet diameter. Doriot's fit results in lower average WSS and flow in the main branch and more extent regions of low WSS near bifurcations, when compared to the outputs of the Murray's Law based BC.

It also has to be emphasized that although implicit models provide more stable solutions, they are also characterised by a more complex coupling procedure, which requires

the adjustment of the flow governing equation [112,133]. For instance, in the case of 3D/0D coupling, the interface matching requires PDE-ODE coupling.

2.3.3 Impedance of Downstream Vasculature

Similarly to the explicit method, implicit BC models require the assignment of patient-specific parameters to the peripheral vascular network. In 0D models, they include the vascular resistance and compliance and for 1D models, it is the branching topology, length, diameter, and material properties of vessel segments.

In [114], Olufsen proposed a 1D structured tree outflow BC representing the peripheral impedance for blood flow simulations in large systemic arteries. This model is capable of predicting blood flow at any level of the arterial vascular network, which generally consists of up to 20 generations before the level of the precapillary arterioles. An example of an asymmetric binary structured tree, which defines the peripheral network of smaller systemic arteries is given in Figure 2.15.a. At each bifurcation, the daughter vessel radii are scaled by factors α and β (where $0 < \alpha, \beta < 1$) and the branching terminates at a specified minimum radius. Other factors determining the vascular tree geometry are length, wall thickness, and Young's modulus. The morphometric parameters of 1D structured trees can be summarised as follows:

- The scaling law for daughter and parent vessel radii is defined through the scaling parameters ζ and η as: $r_p^{\zeta} = r_{d1}^{\zeta} + r_{d2}^{\zeta}$, $\eta = (r_{d1}/r_{d2})^2$, where r_p , r_{d1}, r_{d2} are the parent and two daughter radii, respectively, ζ is the radius exponent, and η is the ratio of the daughter vessel cross-sectional areas.
- Correspondingly, the daughter vessel radii r_{d1}, r_{d2} can be expressed through r_p : $r_{d1} = \alpha \cdot r_p$ and $r_{d2} = \beta \cdot r_p$, where the ratios are given by $\alpha = (1+\eta^{\zeta/2})^{-1/\zeta}$ and $\beta = \alpha \cdot \sqrt{\eta}$.
- The radius exponent ζ can vary in the range of 2.33 – 3 depending on the flow assumption (i.e., 2.33 for turbulent flow or 3 for laminar flow in accordance with Murray's law) with 2.76 suggested as the optimal value for the branching structure peripheral vasculature.
- The vessel length is defined though the constant ratio λ of its radius.
- The vascular tree terminates at a minimum radius r_{min} .

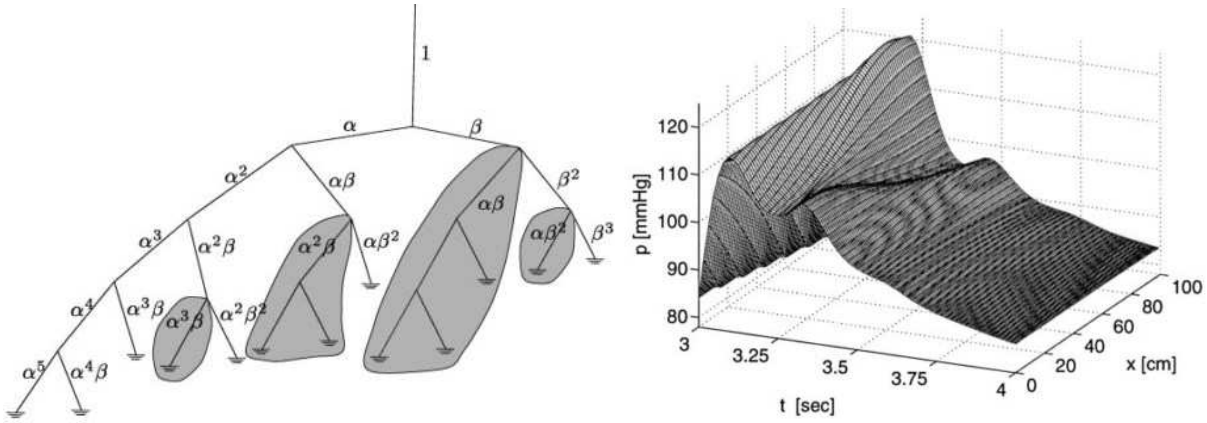

a. Asymmetric structured tree model for systemic arteries

b. Pressure in a single vessel with 1D BC as a function of time and vessel length x

Figure 2.15 1D structured tree for outflow BC models [114]

One of the major advantages of 1D over 0D models is the ability to model pulsatile flow wave propagation and reflection phenomena. The comparison of 0D RCR WK and 1D BC models demonstrated that although WK models produce similar results, they cannot implement the high-frequency oscillations associated with physiologically realistic flow waveforms. In both the 0D and 1D domains, vasodilation and vasoconstriction are modelled through changing the radius and elasticity of the vessels. In their further research, Olufsen et al. described a method for estimation of the root impedance of the structured tree, which represents the peripheral vasculature and its application as outflow BC for large arteries [115]. The method was successfully validated with in-vivo MRI-measured aortic and peripheral flow rates. Next, Olufsen and Nadim investigated the use of the 1D axisymmetric N-S equations defining the blood flow model for derivation of RCR parameters for the equivalent 0D models [116]. This method is based on the Laplace transform and is capable of producing a 0D model of the downstream vasculature impedance for a given outlet radius. It was also reported that for an outlet vessel radius < 20 mm, pressure can be considered to be proportional to flow and the effects of inertia can be neglected. Further development of the concept led to an algorithm for computation of the root impedance of the structured trees for small arteries [77]. It is based on the computation of the zero impedance of the N-generation vascular network by the recursive solution of Z(0,w) for each vessel. It requires the specification of the root radius r_{root}, the bifurcation condition through the scaling parameters α and β, the terminal boundary condition as the terminal resistance Z_t , and the radius r_{min}, at which the vessels are truncated. A comparison between the 0D R, and 0D RCR WK, and 1D BC models showed that while the pure resistance BC affects the overall shape of the curve, the results of the RCR WK and the

structured tree models are similar, except for the lag between the flow rate and pressure in the 1D results.

In [117], Sommer et al. investigated the impact of different outlet BC on the computed blood flow and the corresponding arterial input function (AIF) in a patient-specific LAD with multiple outlets. Knowledge of the AIF is required for estimation of the contrast agent bolus dispersion (i.e., contrast agent transport) in MRI-based quantification of myocardial blood flow (MBF). The types of outlet BC investigated included zero/constant pressure, 0D downstream model, 1D structured tree model, and radius-dependent flow distribution. The fractal-based 1D tree was constructed with the minimum downstream radius r_{min} = 100μm in accordance with [77]. The RCR parameters for the 0D WK models were estimated as the zero impedance of the 1D structural tree [115]. In the flow distribution BC cases, the outflow ratio was derived from the outlet radius in accordance with Murray's law $q_i \sim r_i^{\zeta}$, where ζ=2.76. The results showed that the choice outlet BC significantly affects the computed flow fields and may result in different reactions on artificially introduced stenoses and simulated hyperaemia. The general conclusion is that constant pressure can be reasonable only for single outlet models as it produces erroneous flow distribution between the outlets (by more than 100%) otherwise. Under the resting condition, the resulting flow distributions were relatively similar for resistance and flow distribution BC (20% difference) and RCR WK and 1D BC (maximum difference of 7.9%). However, in the case of the stenosed branch, the radius-dependent flow distribution BC results in the same flow distribution, which is inconsistent with clinical observations. At the same time, the computed blood flow distributions under the 0D WK and 1D BC models were very similar. Additionally, compensation of the stenosis by arteriolar vasodilation was modelled in accordance with the long-term autoregulation mechanisms. With respect to the non-Newtonian viscosity assumption, it was reported that although the velocity pattern did not change there was a decrease in the velocity magnitude during the systole. Still, this can be considered as having negligible effects on the estimation of mean velocities.

Stergiopulos et al. proposed a pulse pressure method for evaluation of the arterial tree compliance for the 2-element WK model, based on the fitting of the RC predicted pressure pulse to the measured flow and pressure waveforms [118]. The model was successfully tested in the estimation of the mean compliance of the major systemic tree arteries (ascending aorta, thoracic aorta, common carotid, and iliac arteries). In the follow-up study, Stergiopulos et al. further evaluated the proposed method in estimating the total arterial compliance from in vivo

measured aortic pressure and flow data in 7 anesthetised dog studies [119]. It was reported that the proximal aorta constitutes for 60% of the total arterial compliance.

In the case of the coronary blood flow simulations, tuning of the R and C patient-specific parameters is required to replicate the long-term autoregulation processes. In [120], Spilker and Taylor proposed a method for iterative tuning of 0D and 1D downstream impedance models based on the feedback of the 3D computed haemodynamics to control pressure and flow rate waveforms in a physiologically realistic range. This method was formalised as the solution of an inverse problem in the form of a nonlinear system of equations of RCR WK parameters and the corresponding 3D computed blood flow features. The tuning function is defined through the flow feature requirements, i.e., min/max values and shape of the pressure waveform, and mean, amplitude, and mean diastolic values of the flow rate waveform. The feasibility of employing coarse meshes and reduced order models for temporal 3D domain representation was also demonstrated. This reduces the computational cost of the tuning procedure, which requires multiple simulations. The application of this method was successfully shown in the idealised carotid bifurcation, the iliac arterial bifurcation, and patient-specific abdominal aorta models, as well as in their later works [44].

2.3.4 Fluid Structure Interactions

This section presents a summary of the recent research studies devoted to investigation of the influence of vessel wall compliance and myocardial contraction in patient-specific coronary blood flow simulations. As discussed in Section 2.2.1, the decision on the vessel wall modelling assumption and the corresponding choice of the FSI approach depends on the specifics of the application area. For instance, the majority of the existing coronary blood flow models for FFR assessment employ the rigid vessel wall modelling assumption [44,48-50]. This is due to the fact that the epicardial arteries are relatively narrow and have significantly lower wall compliance than the large arteries. In addition, CFD simulations have significantly lower computational cost in comparison to the analogical FSI solutions. At the same time, there is a divergence in the reported findings regarding the impact of the deformable vessel wall assumption on the WSS-derived parameters in the context of the investigation of both CAD formation prediction and stent design [64,66].

In [121], Zeng et al. investigated the impact of myocardium contraction on simulated blood flow patterns and WSS in patient-specific RCA reconstructed from biplane cineangiograms. Reconstruction of the RCA geometry motion was based on the moving

contour set being incorporated into the model (only global geometric changes were considered, without information about the lumen deformation). The reported results showed that although arterial movement did not appreciably affected the TAWSS patterns, it did create large temporal variations in WSS magnitudes (more than 100%). Correspondingly, it was concluded that if only the TAWSS distribution is required, static models can provide sufficiently accurate results. In their further study, Zeng et al. integrated the effect of local deformations into the earlier RCA model through the imposed spatially averaged temporal variation of the cross-sectional luminal area [122]. The results of the performed simulations under physiologically realistic inlet BC and the impact of myocardium contraction suggested that the imposed coronary compliance significantly affects WSS only in the distal region of the RCA.

In [123], Dong et al. investigated the correlation between LCA bifurcation angulation and local mechanical forces and also compared the WSS distribution in compliant and rigid vessel wall models. The results demonstrated decreased WSS and greater localised mechanical deformations (principal stress) in the LCx and LAD route regions for greater branch angle values. The computed WSS for rigid and deformable vessel wall cases had similar distributions but different magnitude. In [124], by analysing the impact of myocardial motion on the blood flow simulations in patient-specific stenosed LAD, Theodorakakos et al. concluded that this modelling assumption has a relatively low influence on the flow distribution within the arterial tree in comparison with the effect of the outlet BC choice.

Torii et al. investigated the impact of the vessel wall compliance modelling assumption on the computed blood flow in patient-specific stenosed RCA [125]. They showed that in the FSI model (based on Mooney–Rivlin hyperelastic materials), the instant WSS distribution was significantly affected by vessel dilation and contraction during the cardiac cycle in comparison to the rigid CFD model results. However, the differences in the computed TAWSS and OSI patterns were insignificant between these two models. In the further research, Torii et al. developed a patient-specific FSI RCA model that incorporated MRA-measured dynamic vessel motion [126]. The FSI simulation results showed that ventricle contraction has a significant impact on the instantaneous WSS and OSI distributions, however the TAWSS fields for both the dynamic and static cases have similar patterns and magnitudes. In addition, in the dynamic case, the relative particle residence time is notably higher (Figure 2.16).

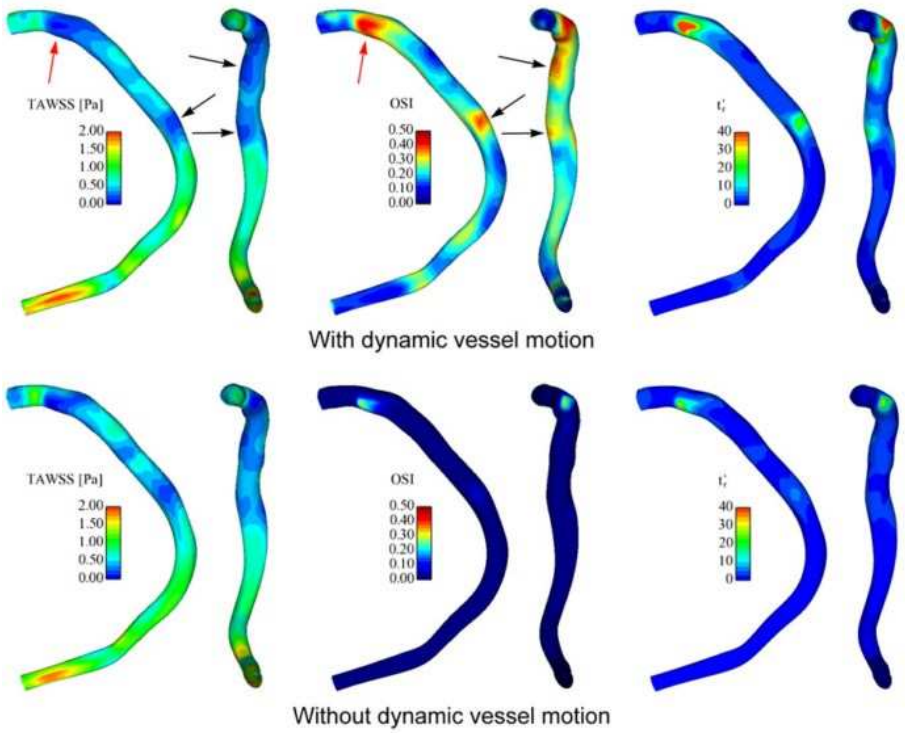

Figure 2.16 FSI RCA simulations with and without dynamic motion: TAWSS, OSI, and particle residence time [126]

In [127,128], Kung et al. in vitro validated FEM blood flow modelling on a deformable stenosed phantom vessel with 4-element WK BC and RCA with aneurysms caused by Kawasaki disease. The comparison of pressure and flow waveforms showed good agreement between the experimental measurements and FEM FSI simulation results for the deformable phantom vessel with an average difference of 1.8% in mean pressure. Figure 2.17 shows the 3D model and the physical phantom of the RCA aneurism. The results for resting and exercise conditions demonstrated a difference of 5-18% between the PCMRI measured and computed blood flow velocities. It was also observed that under the exercise condition, the difference in velocities increased. In summary, this study validated the use of blood flow methods for the assessment of haemodynamics in coronary artery aneurisms under various physiological conditions. Since the velocity errors occur mainly in the centre of the lumen, they should not affect WSS and consequently blood flow modelling can be considered to be feasible for the assessment of the risk of thrombosis. It was also reported that the comparison of the deformable and rigid RCA aneurism models showed lower WSS in the simulation results for the deformable case [128].

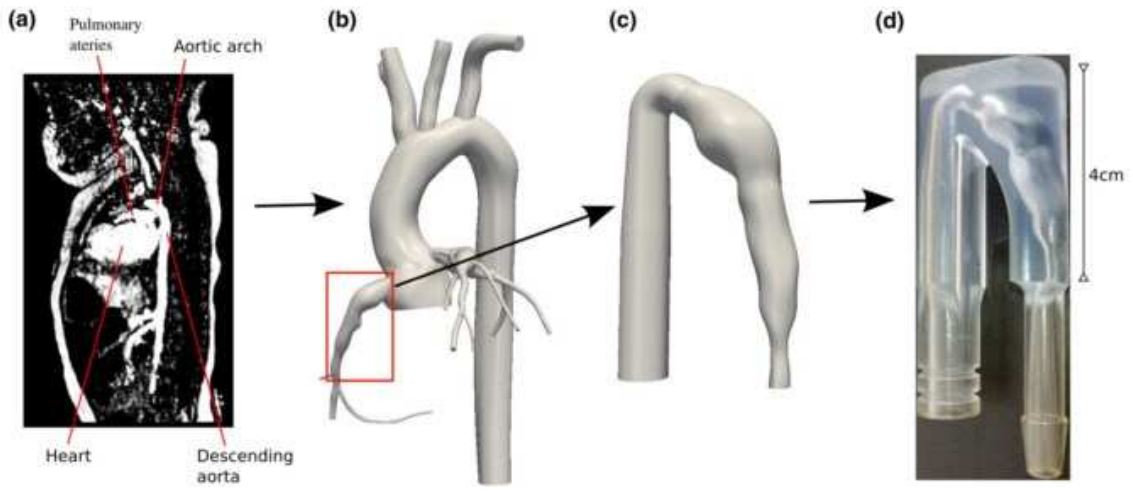

Figure 2.17 Construction of image-based phantom of coronary aneurism for in-vitro validation: (a) CCTA scan, (b) image-based 3D coronary geometry, (c) 3D model of the RCA aneurism, d) phantom of the RCA aneurism [127]

2.3.5 Application-Specific Modelling Assumptions

Other essential modelling assumptions employed depending on the specifics of the problem domain include the blood viscosity model and an approach for simulation of various physiological conditions.

In [129], Soulis et al. investigated the impact of various non-Newtonian blood viscosity models on the computed haemodynamics in patient-specific LCA bifurcations. The simulation results of Newtonian and seven non-Newtonian models (Power Law, Generalized Power Law, Carreau and Casson, and Modified Cross) were compared in terms of molecular viscosity, WSS, and WSS gradient. The Power Law and Generalized Power Law blood viscosity models produced the best approximations for molecular viscosity and WSS. Johnston et al. compared the results of transient CFD simulations in four patient-specific RCAs for Newtonian and non-Newtonian blood viscosity models [130]. The results showed that the Newtonian blood viscosity model provides an adequate approximation with the most significant differences in WSS magnitudes during the part of the cardiac cycle when blood flow is slow or reversed (≈ 30%). However, for the problem-specific blood flow simulations (e.g., coronary stent design [64]), a non-Newtonian model would be more appropriate.

In [131], Kim et al. described the process of incorporating autoregulatory mechanisms (systemic arterial baroreceptors) into the previously developed multiscale 3D/0D CVS model [110]. These baroreflex mechanisms regulate the heart rate, ventricle contractility, peripheral

arterial resistance, and venous compliance and are controlled by the CNS (Central Nervous System) signals with respect to the measured CVS physiological conditions, as shown in Figure 2.18. In other words, they provide a means for accommodate for temporal changes in metabolic demands under various physiological states (e.g., exercise, hyperaemia, etc.).

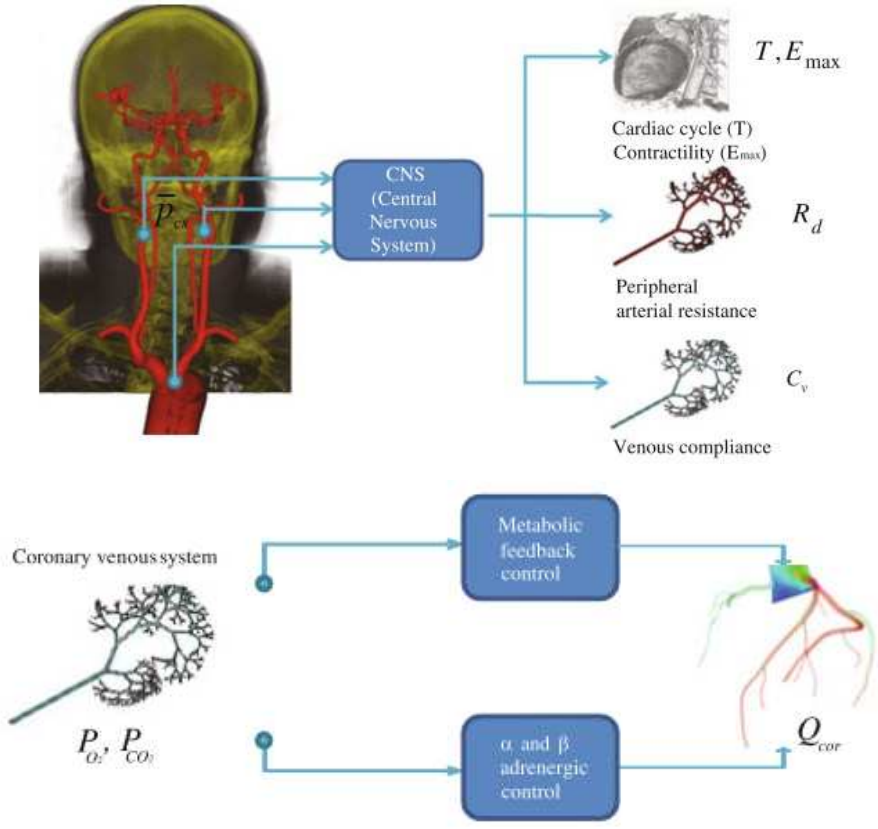

Figure 2.18 Models of systemic arterial baroreflex and coronary flow regulation system incorporated into a multidomain blood simulation model [131]

The proposed coronary flow regulation system is based on the feedback control loop that dilates the downstream vasculature by reducing the arteriolar resistance $R_{a\text{-}micro}$ in response to metabolic demands (oxygen), which corresponds to an increased coronary blood flow Q_{cor} demand [110]. The mathematical formalisation of the autoregulation model of systemic arterial baroreflex is based on the model proposed by Ottesen et al. in [77] with the compensatory mechanisms of cardiac contractility, heart rate, peripheral arterial resistance, and venous compliance were described with a system of ODEs. In other research studies specifically focused on the virtual FFR assessment [44,49,50,56], the condition of pharmacologically induced hyperaemia was straightforwardly modelled as a reduction of downstream vascular resistance to 0.2 - 0.25 of the original resting state value in accordance with the clinical findings [370].

2.4 Conclusions

This literature review outlined a number of promising studies and results in coronary blood flow simulations with regards to the analysis of the mechanisms associated with CAD formation and diagnosis of CAD severity through virtual FFR assessment. Although limited by the lack of direct validation data, the results of the extensive studies on the underlying processes of CAD formation demonstrated high correlation between the WSS-derived parameter patterns and lesion localisation [28-33]. The findings of the CFD/FSI studies in the analysis of the plaque rupture related factors and Kawasaki disease cases also provided an insight into the associated haemodynamic characteristics [34, 37-42]. A series of clinical trials and studies involving in the range of 50-200 patients showed high correlation between the computed and invasively measured FFR patterns, thus emphasising the high potential for practical application of CFD methods in CAD diagnosis [43,47-50,55]. While the FFR_{CT} prediction system developed by HeartFlow® is the most advanced in terms of the existing solutions [44], the alternative cFFR system developed by Siemens Healthcare has the advantage of on-site virtual assessment without the need for external data processing [48]. Other studies demonstrated the potential of CFD models in improving the diagnostic sensitivity of ICA by identification of ischemia causing lesions [49,50,52]. In addition to providing the means for modelling of physiologically realistic boundary conditions, 0D and 1D multiscale coronary blood flow models also showed promising results in virtual FFR assessment and surgery planning [56,57,94]. Another promising research direction employs CFD modelling for optimisation of surgical intervention, such as CABG and stent design, with respect to the assessment of variations in WSS-derived parameters associated with a high probability of restenosis [58-62,64].

Next, based on the general overview of existing coronary blood flow models, it was identified that the accuracy of the blood flow simulations is directly affected by the employed modelling assumptions and the quality of reconstruction of vessel lumen from medical image datasets. This includes the choice of boundary condition model type, the approach for approximation of the downstream vascular impedance, the rigid/compliant vessel wall assumption, and the Newtonian/non-Newtonian fluid assumption. Taking into account the associated high computational costs, the level of complexity of the blood flow model should be defined with respect to the problem domain and available information extracted from medical image datasets. For instance, estimation of FFR and CABG planning generally require

integration of the 3D domain with the 0D CVS loop for the accurate solution of pressure patterns, while single vessel stent design or plaque cap stress distribution assessment can be limited to the simple explicit BC case. The same applies to the assumptions of the deformable vessel wall and non-Newtonian blood viscosity model or the extension of the BC model for simulation of hyperaemia, which should be used in the solution of specific tasks. With respect to the non-invasive FFR assessment characterised by high sensitivity to the accuracy of the computed pressure fields, the general recommendations for future research in 3D blood flow modelling include the following critical factors: (i) the use of 0D models of peripheral vasculature or integration into the 0D CVS loop; (ii) validation of the accuracy of vessel segmentation; (iii) optimisation of the choice of 1D tree scaling parameters used for the approximation of the peripheral vascular resistance and compliance of the downstream 0D models; (iv) optimisation of the approach for modelling of various physiological conditions. Application of lumped-parameter modelling in the assessment of virtual FFR in patient-specific coronary arteries also has a high potential considering the significantly lower computational costs and the general flexibility of the 0D modelling approach.

Chapter 3

Design and Implementation of 3D Image-Based Coronary Blood Flow Model

3.1 Introduction

This chapter describes the implemented methodology for patient-specific 3D coronary blood flow modelling. As shown in Figures 3.1-2, the corresponding essential development stages include: (i) preparation of the computational domain representing the blood volume within a CCTA-reconstructed coronary artery lumen; (ii) specification of the modelling assumptions for the blood flow model; (iii) definition of boundary conditions representing the remaining parts of the CVS on the inlet and outlet boundaries of the coronary artery; (iv) setup of blood flow model and solution of the Navier-Stokes equations over the defined computational domain in the CFD solver; (v) analysis and interpretation of the results by extracting various haemodynamic indices (e.g., FFR and TAWSS) and other parameters from the computed blood flow fields. The proposed model development procedure employs the MATLAB® and ANSYS® engineering frameworks including the ICEM meshing software and the Fluent FVM CFD solver.

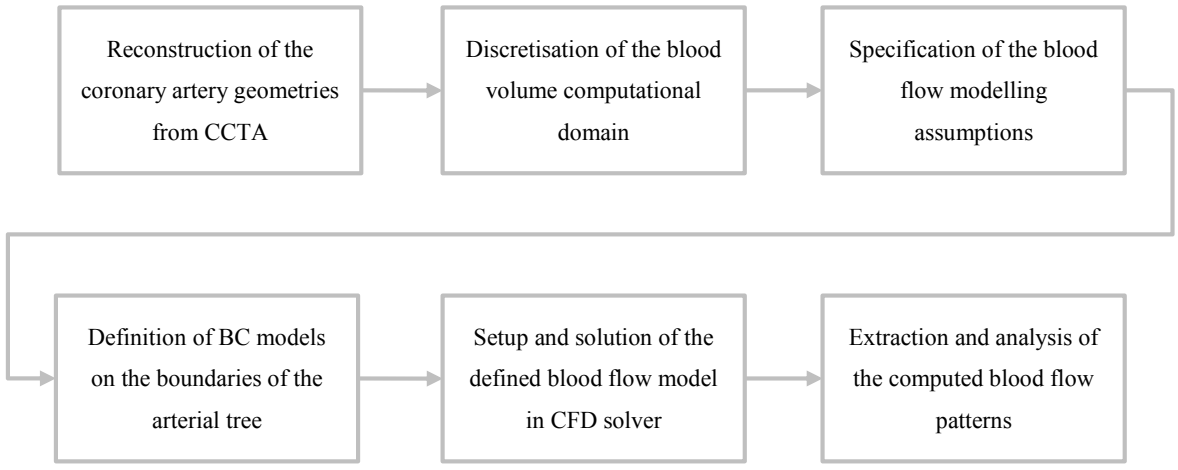

Figure 3.1 Development of 3D image-based coronary blood flow models: essential steps

As described in Chapter 2, there is a number of research works describing application of blood flow modelling in the analysis of various pathologies, investigating such aspects as

the choice of BC type, blood viscosity model, FSI modelling approach, or focusing on correlation and validation of the computed flow variables with either invasive measurements or disease progression outcomes. However, there is no defined guidelines for image-based coronary blood flow simulations that explain the step-by-step procedure of model setup together with the corresponding limitations, requirements and factors that affect the accuracy of the computed flow patterns.

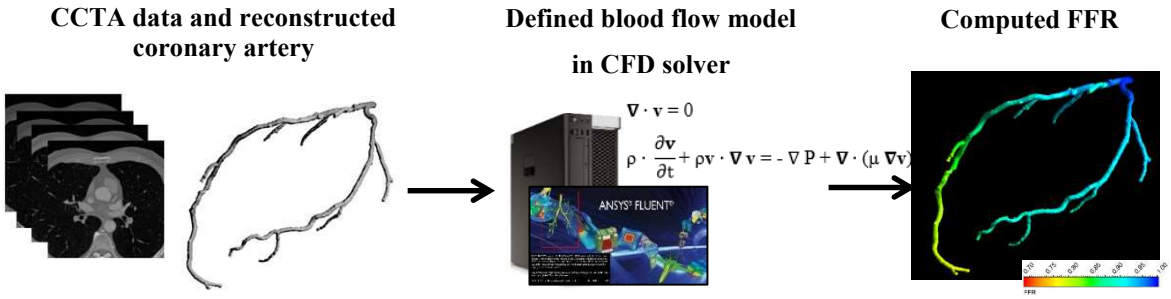

Figure 3.2 Development of 3D image-based coronary blood flow models: data flowchart

Since even small variations in the model parameter values or various modelling assumptions can potentially produce a significant change in the computed haemodynamics, it is also essential to be aware of which of the model parameters or factors have to be controlled in order to ensure that the solution is accurate and robust. Thus, in addition to the general steps that have to be performed for implementation of a patient-specific coronary blood flow model, this chapter focuses on the various modelling aspects that can affect the simulation results (i.e., FFR) including: (i) variations in blood segmentation threshold; (ii) choice of side branch truncation level; (iii) level of surface smoothing; (iv) variations in blood viscosity; (v) transient vs. steady state simulations for the assessment of the heartbeat-averaged values such as FFR and TAWSS; (vi) BC model type and identification of its parameter values; (vii) interpatient variations in average pressure and flow rate values in the BC models; and (viii) choice of maximum vasodilation degree for modelling of hyperaemia. These modelling assumptions are investigated along with the formalisation of the corresponding stages of the model implementation described in the following sections. The essential steps for preparation of the model geometry and volumetric computational domain are defined in Section 3.2. Next, Section 3.3 summarises the modelling assumptions defining the blood flow model. Various aspects of the flow BC models are presented in Section 3.4 followed the description of the implementation and numerical solution of the blood flow model in the CFD solver. Section 3.5 addresses the procedure for extraction of haemodynamic parameters from the simulation

results. Finally, Section 3.6 addresses limitations of the developed model and potential future research directions.

3.2 Preparation of 3D Patient-Specific Computational Domain

Patient-specific blood flow simulations require high quality reconstruction of vascular geometries from medical image volumes that amongst other factors constitute the basis for accurate estimates of the computed blood flow fields. In this particular case, the 3D coronary artery lumen is extracted from the CCTA DICOM dataset, since the key focus of the research is enhancement of non-invasive CCTA diagnosis information through the computed haemodynamic parameters. Preparation of the geometrical domain comprises a number of steps such as: (i) reconstruction of the coronary arteries from CCTA datasets; (ii) truncation of side branches for definition of inlet and outlet boundaries; and (iii) discretisation of the blood volume within the lumen, which represents the computational domain of the blood flow model.

3.2.1 Reconstruction of Coronary Arteries from CCTA

The procedure for reconstruction of patient-specific coronary artery geometries from ECG-gated Contrast CCTA dataset is based on a set of functions for automatic segmentation and quantification of the coronary arteries, developed by the Medical Image Processing research group at City University London [132,133]. The vascular geometries of interest include the internal lumen boundaries of the major epicardial arteries with side branches reconstructed up to the limits of CCTA resolution and left ventricle (LV) volume for assessment of cardiac output (CO).

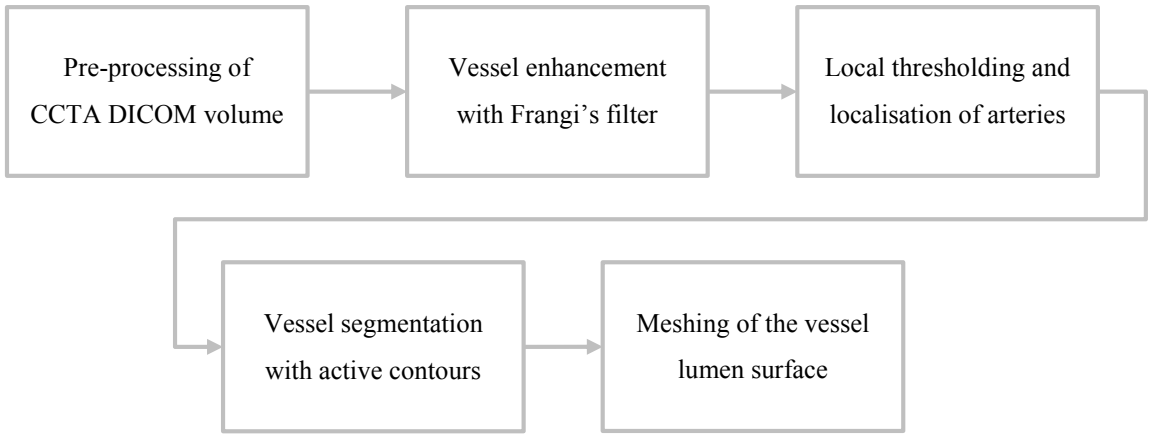

Figure 3.3 Reconstruction of 3D coronary artery lumen from CCTA: essential steps

The corresponding processing steps include (see Figure 3.3): (i) heart segmentation from CCTA volume; (ii) vessel enhancement with Frangi's filter; (iii) local blood thresholding and localization of coronary arteries; (iv) centreline extraction; (v) vessel segmentation with active contours; (vi) generation of the surface mesh of the arterial lumen. The illustration of the data level flowchart for this procedure is given in Figure 3.4, where the LCA is extracted from the CCTA volume of an intermediate severity CAD subject. After the performed segmentation, the extracted vessel lumen surface is used to generate the surface mesh, which is then used as an input to the CFD volume meshing software for further processing.

a. Segmentation the coronary arteries from CCTA

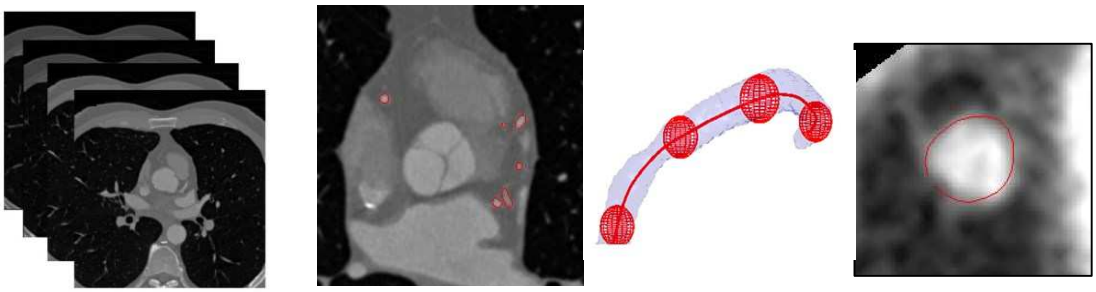

CCTA volume **Vessel Segmentation** **Extracted centreline and cross-sections**

b. Reconstructed LCA lumen surface c. Preliminary surface mesh

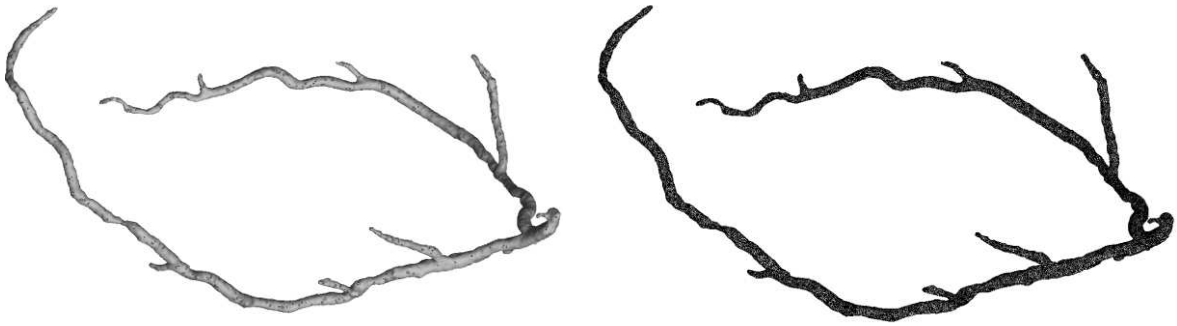

Figure 3.4 Reconstruction of 3D coronary artery lumen from CCTA: implemented framework

As can be observed from the active contour fitted lumen crossection, the limitations of CCTA resolution is a potential source of segmentation errors especially in the case of automatic processing software. In addition to the calcified plaque or stent caused artefacts and other patient-/acquisition-specific variations, one of the factors that can significantly affect the vessel segmentation results is the choice of threshold of contrast-enhanced blood intensity, which can vary within the 200 – 400 HU range [134] and constitutes a challenge for automatic vessel segmentation algorithm. Besides the development of more advanced methods based on

the local intensity analysis, one of the solutions is to use manual user input during the segmentation process further, which is further followed by the validation of the accuracy of the extracted vessel lumen by an expert.

For instance, Figure 3.5 shows curved multiplanar reconstruction (cMPR) of the segmentation results for a LAD artery segment with multiple atherosclerotic lesions. The difference between the 210 and 350 HU threshold results is clearly seen in the reduced lumen diameter in the stenosed areas with the removed components of the lumen surrounding tissue and the fibrous plaque tissue, while the vessel lumen geometry is being preserved.

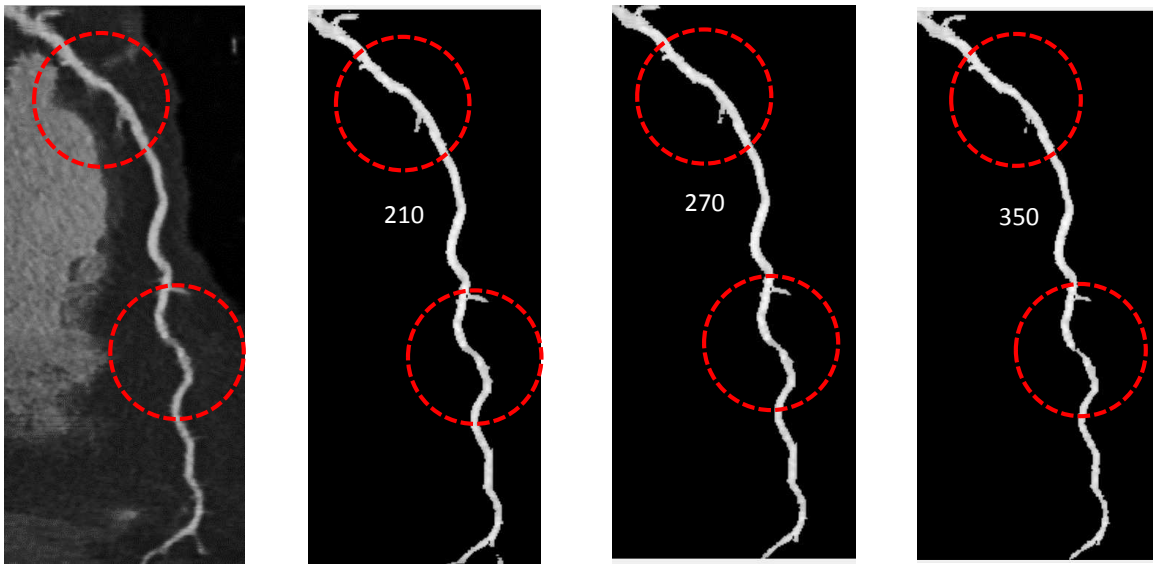

a. CCTA volume b. Threshold = 210 c. Threshold = 270 d. Threshold = 350

Figure 3.5 cMPR of the LAD artery in the stenosis region: the CCTA volume and segmented lumen

The corresponding generated surface meshes of the LAD stenosis region are given in Figure 3.6 with the stenosis being “revealed” in terms of a in diameter reduction from 15% to 75% in the case of a threshold of 210 and 350 HU, respectively. Therefore, since the results of segmentation represent the actual boundaries of the computational domain, investigation of the influence of the blood threshold choice is essential for verification of accuracy of blood flow simulations. In this particular case, a threshold of 350 HU threshold was identified as optimal, based on the comparison with manual segmentation data, however this value will differ depending on the amount and type of contrast agent and interpatient variations.

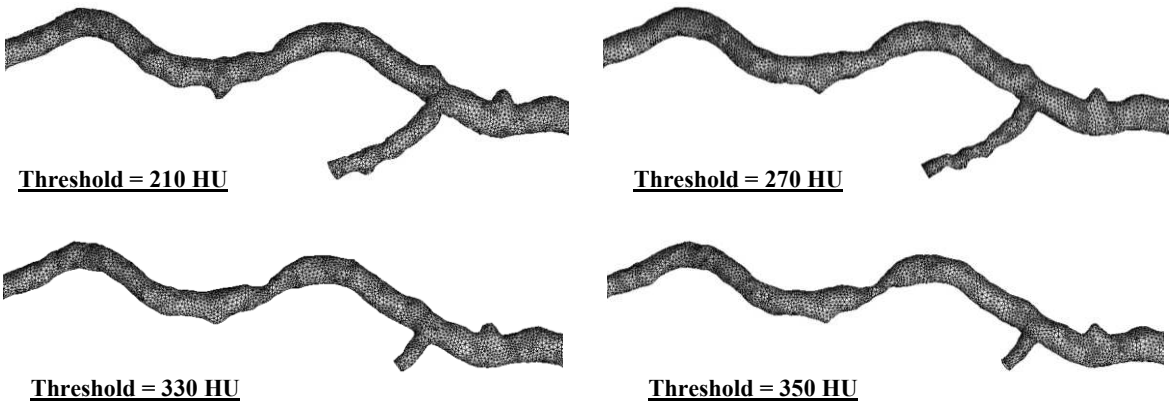

Figure 3.6 Reconstructed LCA surface mesh in the LAD stenosis region under 210 – 350 HU blood segmentation thresholds

Next, the generated lumen surface mesh is imported into the ANSYS® ICEM CFD meshing software for further refinement with respect to the required mesh quality and truncation of side branches for definition of the outlet boundaries. The inlet boundary is defined at the root of the coronary artery. The side branches can be truncated either up to the maximum reconstructed branch length or with respect to the specified level of lumen diameter, as shown in Figure 3.7. Optimally, a diameters of 2 mm should be the optimal truncation level since, in accordance with the SCCTA guidelines, the clinicians do not generally investigate vessel branches of lower diameters during CCTA interpretation [16]. In addition, taking into account the relatively low CCTA resolution and variations in contrast agent distribution along a coronary tree due to dissipation [134], segmentation of narrow branches might not be sufficiently accurate. In order to avoid this, the general strategy should be to crop narrow side branches close to the main branch. As described in Section 3.4.4, the choice of branch truncation level also defines the parameter values of the outlet BC models representing the impedance of peripheral vasculature, since flow distribution between the outlets has to be proportional to the corresponding outlet diameters in accordance to the Murray's law.

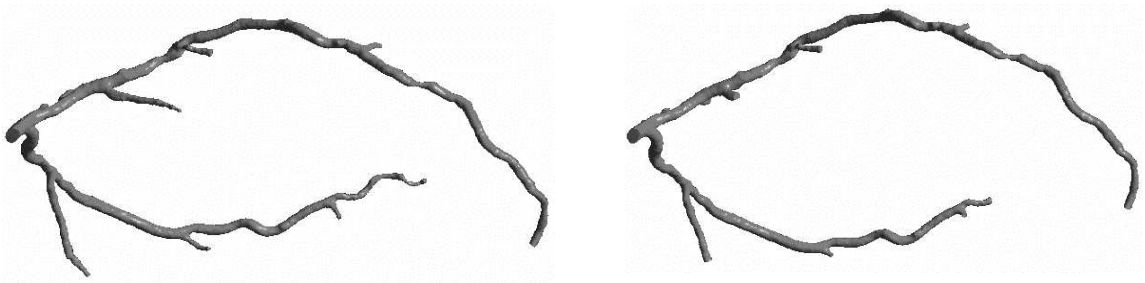

a. Truncation on the maximum branch length

b. Truncation up to 2 mm branch diameter level

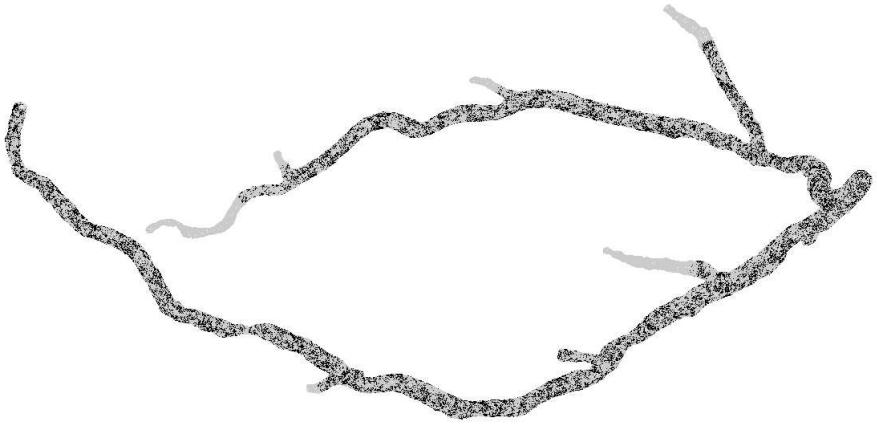

c. Overlapped meshes with different truncation strategies

Figure 3.7 Reconstructed LCA surface mesh with the defined inlet and outlet boundaries under different side branch truncation levels

Another aspect of the reconstruction of vascular geometry that can affect the accuracy of the computed blood flow is the level of smoothing of the lumen surface. Smoothing is generally used in order to remove small irregularities in the reconstructed surfaces introduced by the buildup of fatty deposits on the arterial walls as well as low image resolution and low level segmentation algorithms. Although it was demonstrated that the introduced surface roughness produces a difference in the computed TAWSS even in the case of employed volume-preserving mesh smoothing [135], in theory, this should not affect the computed pressure fields and FFR, unless a high amount of Laplacian smoothing is used thus changing the actual lumen geometry. Examples of the application of varying degree of Laplacian smoothing are shown in Figure 3.8.

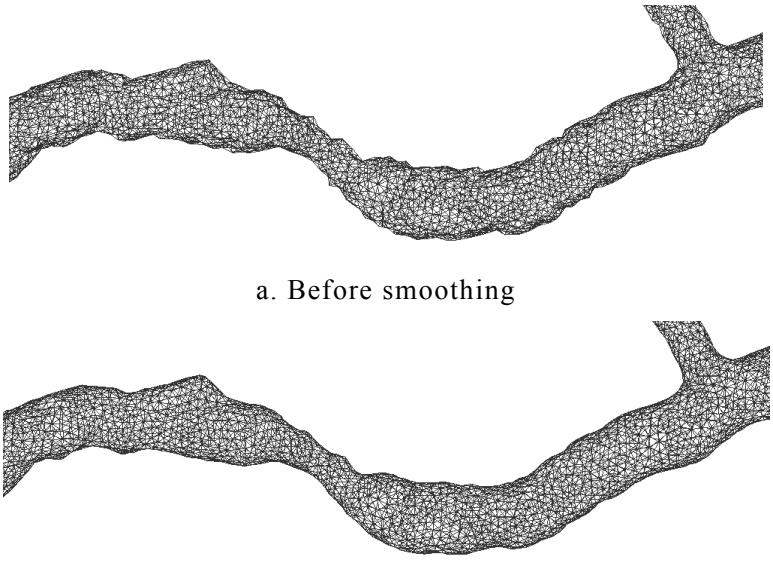

a. Before smoothing

b. After medium level smoothing

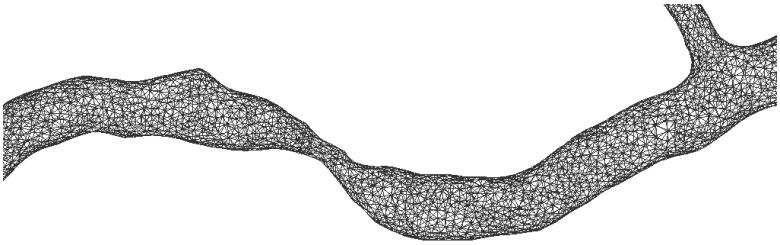

b. After high level smoothing

Figure 3.8 Reconstructed LCA surface mesh in the stenosis region before and after smoothing

The corresponding experimental results for these three parameters (blood segmentation threshold, side branch truncation level, and level of surface smoothing) of coronary artery geometry reconstruction for blood flow simulations are presented in Section 5.3 together with the identified general recommendations.

3.1.1 Discretisation of the 3D blood flow computational domain

Discretisation of the fluid domain within the vessel lumen and generation of volume meshes is performed in the ANSYS® ICEM that produces high quality meshes specifically optimised for the ANSYS® Fluent CFD solver. Although structural meshes provide more efficient solution of flow problems, unstructured tetrahedral meshing was chosen due to the high complexity of patient-specific vascular geometries and related difficulties in generation of NURBS surfaces that can hide surface features [71]. Prism layers along the lumen boundary were added for accurate computation of velocity fields near the vessel wall. The optimal mesh resolution and number of prism boundary layers were determined through the analysis of the computed flow fields in the performed mesh sensitivity study. Mesh quality was assessed in terms of the aspect ratio and mesh-independence of the solution with the quality criteria cut-off value being 1-5% difference in the computed pressure fields. An example of the generated unstructured tetrahedral mesh of an LCA with the inner tetrahedral volume and five prism boundary layers is shown in Figure 3.9.

Based on the analysis of a series of reconstructed coronary artery geometries, it was identified that the optimal volume mesh size normally varies within the 0.9 – 1.5 mln elements range, depending on the size and type of coronary arteries. This range is comparable to similar studies with a higher number of elements normally leading to a longer time required for the numerical solution, while not significantly affecting the accuracy of the computed pressure fields [71].

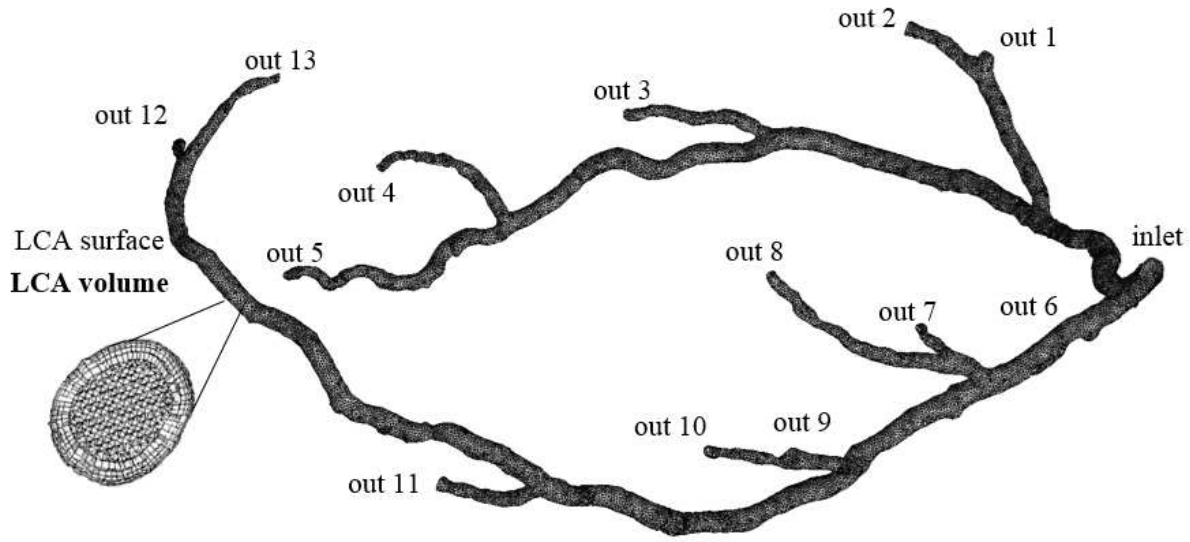

Figure 3.9 Discretisation of the computational domain: the LCA surface and fluid volume meshes and the defined inlet and outlet boundaries

3.2 Blood Flow Modelling Assumptions

A classical 3D blood flow model is represented through the fluid motion governing equations defined over the discretised computational domain, which are then numerically solved with CFD methods. The type and various parameters of the model are defined based on the chosen modelling assumptions, which depends on the specifics of the problem domain and the balance between the level of physiological accuracy of the computed flow, and computational efficiency. Taking into account the general level of complexity of coronary blood flow models and the required number of modelling assumptions, introduction of the additional features such as heart motion, vessel wall compliance or non-Newtonian blood viscosity generally increases the number of degrees of freedom thus increasing the level of uncertainty of the simulation results. The following list summarises the modelling assumptions identified as optimal based on the existing blood flow models for the specific task of computation of virtual FFR in patient-specific coronary arteries (Sections 2.1.2 and 2.3.2):

– Blood is assumed to be a Newtonian fluid with the average values for density of 1060 kg/m^3 and dynamic viscosity of $3.5 \cdot 10^{-3}$ kg/m·s [130]. Variations in blood rheology properties are considered to be of the less importance in this specific problem domain, although the choice of blood viscosity models produces changes in computed WSS and OSI patterns as was

shown in [130]. The influence of variations in blood viscosity value on computed FFR fields is investigated in Section 5.2.6.

- Blood flow is assumed to be incompressible and laminar and consequently the blood flow model is defined through the N-S equations for incompressible Newtonian fluids [70].
- Blood vessel walls are assumed to be rigid (non-deformable) and immovable under the impact of ventricle contraction. Since the coronary arteries are significantly narrower than the carotid artery or aorta and accordingly are less elastic, the rigid vessel wall assumption can be considered as feasible when the aim is calculation of cardiac cycle average values such as FFR and TAWSS as was shown in [44,48-50,125-126]. The no-slip condition is applied at the vessel lumen surface similarly to the majority of coronary blood flow simulation models.
- The flow boundary condition on the inlet is represented through the aortic pressure waveform since this does not require preliminary knowledge of the inlet flow rate and removes limitations for simulation of hyperaemia and exercise conditions. Being essential for physiologically realistic estimation of pressure fields, 0D BC models representing peripheral vasculature and the pressure of ventricle contraction are implicitly assigned to the outlet boundaries. Three types of outlet BC models of different complexity are considered in order to quantify the difference introduced by the additional downstream impedance elements and compare the corresponding computational costs. The inlet and outlet BC models are described in Section 3.4 together with the proposed approach for estimation of the peripheral vasculature parameters and approach for simulation of hyperaemia.
- Both transient and steady state blood flow simulation modes are considered and investigated in Section 5.2.2 in order to assess the differences between these two options and how they affect the accuracy of computed blood flow patterns. Although transient simulations provide more information they are also significantly more time consuming in comparison to the steady-state simulations. Moreover, steady state simulations with average flow and pressure values (over a cardiac cycle) used in the BC models are applicable in this particular case of FFR assessment.

In the next step, the defined blood flow model has to be implemented in a CFD solver software for numerical solution of the N-S equations over the generated volume mesh of the coronary artery. The chosen CFD solver and identified optimal solution settings are described in Section 3.5.

3.3 Boundary Conditions

As described in Section 2.5, computation of physiologically accurate blood flow fields (and in particular, pressure estimates) requires physiologically relevant boundary conditions defining the cardiovascular system behaviour outside the reconstructed 3D computational domain. Sections 3.4.1-6 describe the BC models assigned at the inlet and outlets of the 3D coronary artery mesh along with the approaches employed for estimation of peripheral vascular resistance and capacitance values and simulation of the hyperaemia condition required for FFR assessment. More information on the 0D blood flow modelling approach can be found in Section 2.2.2 and Chapter 4.

3.3.1 Inlet Flow Boundary Conditions

In order to decrease the computational cost of simulations and limit the number of the factors introducing additional modelling uncertainties, the inlet pressure BC is defined as a waveform representing pressure at the root of the aorta and prescribed at the inlet boundary of the coronary artery instead of implicit coupling of the 0D model of the left ventricle as in [44,48,58,110]. This approach significantly simplifies the whole model and does not set any restrictions on modelling of hyperaemia, since the aortic pressure (AP) is not affected by pharmacologically induced hyperaemia in coronary arteries and remains the same.

While in this particular case the central aortic blood pressure waveform measured at the root of the aorta in the 0D CVS model (Chapter 4) is used in order to be able to compare 3D and 0D simulation results, it is also possible to use patient-specific measured waveforms as they can be easily interpolated and further incorporated into the BC model. Figure 3.10 shows the waveform of the measured $P_{LMCA}(t)$ pressure (AP) along with the waveform of the downstream $P_d(t)$ pressure used in the 0D outlet BC models. Being the combination of the extravascular pressure of left ventricle contraction (LVP) and the downstream venous pressure, $P_d(t)$ is naturally synchronised with $P_{LMCA}(t)$. In order to avoid the backflow problem in simulations (negative flow rate at the inlet), $P_d(t)$ was regulated be to lower than the AP ($0.75 \cdot LVP + 15$) during systole taking into account the resistance of myocardium and capillary level pressure. This difference can be observed by comparison with the Wiggers diagram in Figure 3.11.

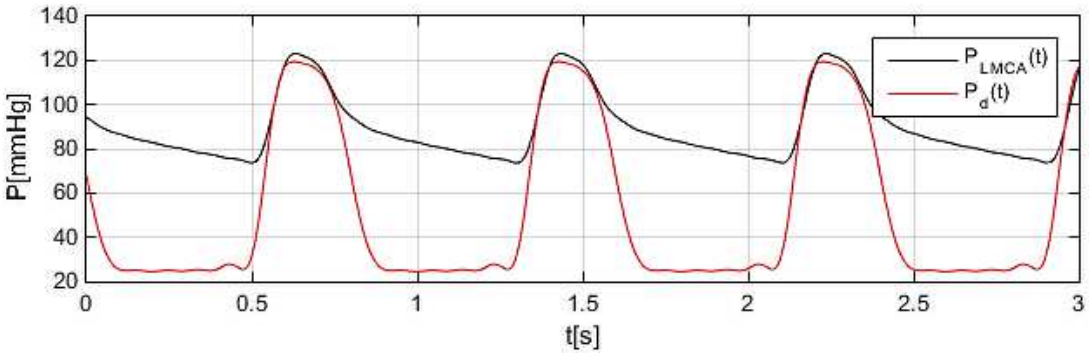

Figure 3.10 BC model pressure waveforms measured in the 0D CVS model

In order to preserve the periodic character of the measured waveforms so that they can be easily used in transient simulations with multiple cardiac cycles and synchronised with respect to each other, trigonometric interpolation is employed. An example of the 8th order Fourier polynomial representation of $P_{LMCA}(t)$ with the coefficients computed from the interpolated pressure waveform in Figure 3.10 is given below:

$$P_{LMCA}(t)= a_0+a_1\cdot\cos(t\cdot\omega)+b_1\cdot\sin(t\cdot\omega)+a_2\cdot\cos(2\cdot t\cdot\omega)+b_2\cdot\sin(2\cdot t\cdot\omega)+ a_3\cdot\cos(3\cdot t\cdot\omega)+b_3\cdot\sin(3\cdot t\cdot\omega)+a_4\cdot\cos(4\cdot t\cdot\omega)+b_4\cdot\sin(4\cdot t\cdot\omega)+a_5\cdot\cos(5\cdot t\cdot\omega)+ b_5\cdot\sin(5\cdot t\cdot\omega)+a_6\cdot\cos(6\cdot t\cdot\omega)+b_6\cdot\sin(6\cdot t\cdot\omega)+a_7\cdot\cos(7\cdot t\cdot\omega)+ b_7\cdot\sin(7\cdot t\cdot\omega)+a_8\cdot\cos(8\cdot t\cdot\omega)+b_8\cdot\sin(8\cdot t\cdot\omega)\,, \quad (3.1)$$

where, $a_0 = 52.71$; $a_1 = 23.59$; $b_1 = -39.31$; $a_2 = -10.88$; $b_2 = -18.67$; $a_3 = -2.35$; $b_3 = 2.36$; $a_4 = 4.63$; $b_4 = -3.14$; $a_5 = -1.89$; $b_5 = -3.46$; $a_6 = -0.63$; $b_6 = 1.43$; $a_7 = 1.02$; $b_7 = -0.38$; $a_8 = -0.47$; $b_8 = -0.23$; $\omega = 7.85$;

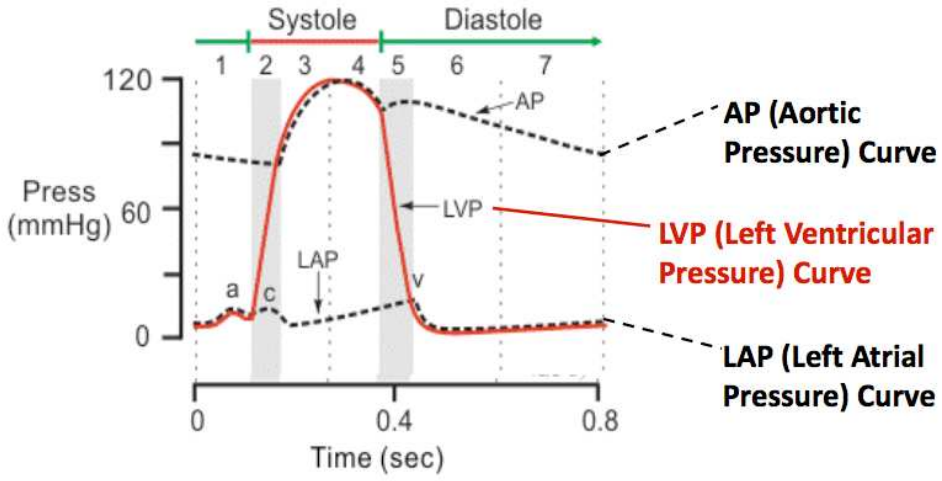

Figure 3.11 Wiggers diagram: AP, LVP and LAP waveforms [3]

As mentioned above, this approach allows incorporating any changes in the BC pressure waveforms (especially since they govern transient simulations) as well as modelling

various pathological conditions such as hypertension or aortic regurgitation [83]. The impact of variations in the aortic and LV pressure waveforms, as well as the inlet flow rate on the computed FFR fields is investigated in Section 5.2.6.

3.3.2 0D Models for Outlet Flow Boundary Conditions

In blood flow modelling, the choice of the outlet boundary conditions is defined by the problem domain. Taking into account that the primary aim is the prediction of the pressure fields, explicit prescription of either pressure or outflow ratio at the outlets is not appropriate as it will not produce meaningful results since these values are not known a priori. The alternative BC types imply implicit coupling of either the 0D or 1D model representing the impedance of the downstream vasculature for each of the outlets (Sections 2.3.2). Besides the fact that 0D BC models are generally used for representation of peripheral vascular networks, the 0D BC type was also chosen as the optimal for this particular problem domain because of the straightforward solution for modelling of the hyperaemia condition by vasodilation of the total peripheral resistance and the 3D-0D implicit coupling procedure [44,110].

Figure 3.12 presents three types of 0D downstream BC models of various degree of complexity, where P(t) and Q(t) are the pressure and flow rate at the outlet (3D-0D coupling boundary), $P_d(t)$ is the downstream pressure at the capillary level combination of the extravascular pressure of left ventricle contraction and the downstream venous pressure. The P(t) and Q(t) values are unknown a priori and are computed during the simulation with P(t) being the product of the 0D model impedance in response to the flow Q(t) from the upstream 3D domain. The pressure $P_d(t)$ is represented as a waveform (Figure 3.10) and incorporated into the 0D BC model. The rest of the elements of the 0D electric circuit models replicate physiology of the peripheral vasculature with respect to its impact on the computed blood flow. The simple R (resistance) model represents the vascular flow resistance of the downstream coronary tree comprising the network of arteries and arterioles. The 3-element RCR Windkessel model in addition to the arterial resistance R_a also incorporates the impact of arterial compliance through the capacitor C_a followed by the R_{am} resistance of arterioles [77]. The RCRCR model proposed specifically for coronary blood flow simulations [44,110], in addition to R_a , C_a and R_{am}, also incorporates the myocardium tissue compliance C_{im}, and the coronary capillary resistance R_c. More complex models can be simplified to the R resistance by removal of the capacitor elements and capillary resitance.

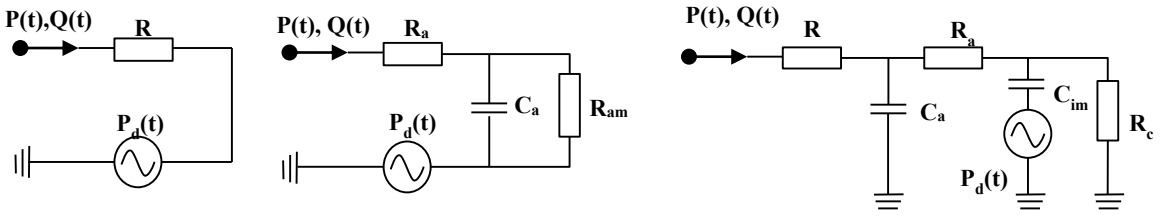

a. R model b. RCR model c. RCRCR model

Figure 3.12 0D outlet BC models of downstream vasculature

The corresponding ODEs for these models are given below:

$$P(t) = R \cdot Q(t) + P_d(t) \tag{3.2}$$

$$P(t) = P_d(t) + (R_{am} + R_a) \cdot Q(t) + R_{am} \cdot C_a \cdot \left(\frac{dP_d(t)}{dt} - \frac{dP(t)}{dt} + R_a \cdot \frac{dQ(t)}{dt}\right) \tag{3.3}$$

$$\begin{aligned} P(t) = {} & Q(t) \cdot (R_{am} + R_a + R_c) + \frac{dP(t)}{dt} \cdot (-C_a \cdot R_{am} - C_a \cdot R_c - C_{im} \cdot R_v) + \\ & \frac{dQ(t)}{dt} \cdot (C_a \cdot R_a \cdot R_{am} + C_a \cdot R_a \cdot R_c + C_{im} \cdot R_a \cdot R_{am} + C_{im} \cdot R_a \cdot R_c) + \frac{dP_d(t)}{dt} \cdot \\ & C_{im} \cdot R_c + \frac{d^2(-P(t)+R_a \cdot Q(t))}{dt^2} \cdot C_{im} \cdot C_a \cdot R_{am} \cdot R_c \,, \end{aligned} \tag{3.4}$$

where P(t) is the pressure at the outlet, Q(t) is the flow rate at the outlet, $P_d(t)$ is the downstream pressure, and the R and C elements are the resistance and capacitance values of the corresponding elements in Figure 3.12.

An example of simulation results for each of these 0D peripheral vasculature models is given in Figure 3.13.a-b in the form of the blood flow rate and pressure waveforms at the inlet and outlets. As described in Section 1.1.1, unlike the blood flow within the rest of the body, the phase of the coronary flow rate is shifted with respect to the pressure being lower during the systole (LV contraction and ejection) and higher during the diastole due to the extravascular compression. The similarity between the computed flow rates and pressure waveforms in the R and RCR models is caused by the low C_a compliance values corresponding to narrow coronary arteries, which introduce only a small difference during systole. At the same time, while generally remaining within the similar ranges for average pressure and flow rate values the shape of the flow rate waveform produced by the RCRCR model is the closest to the shape of the idealised left coronary blood flow velocity waveform (Figure 3.13.c). Specifically, while the resistance values control the magnitude of the flow rate and pressure along a cardiac cycle, C elements define the shape of the flow waveform. On the other hand, introduction of time-dependent C elements requires longer simulation times with 3-4 cardiac

cycles being the minimum for the RCRCR model in order to achieve conversion of the solution with respect to the intra-cardiac cycle difference between the computed flow fields. From this point of view, the major advantage of the R model is that it can be reduced to a steady state simulation for calculation the FFR and TAWSS values averaged over a cardiac cycle, thus further reducing the computational costs.

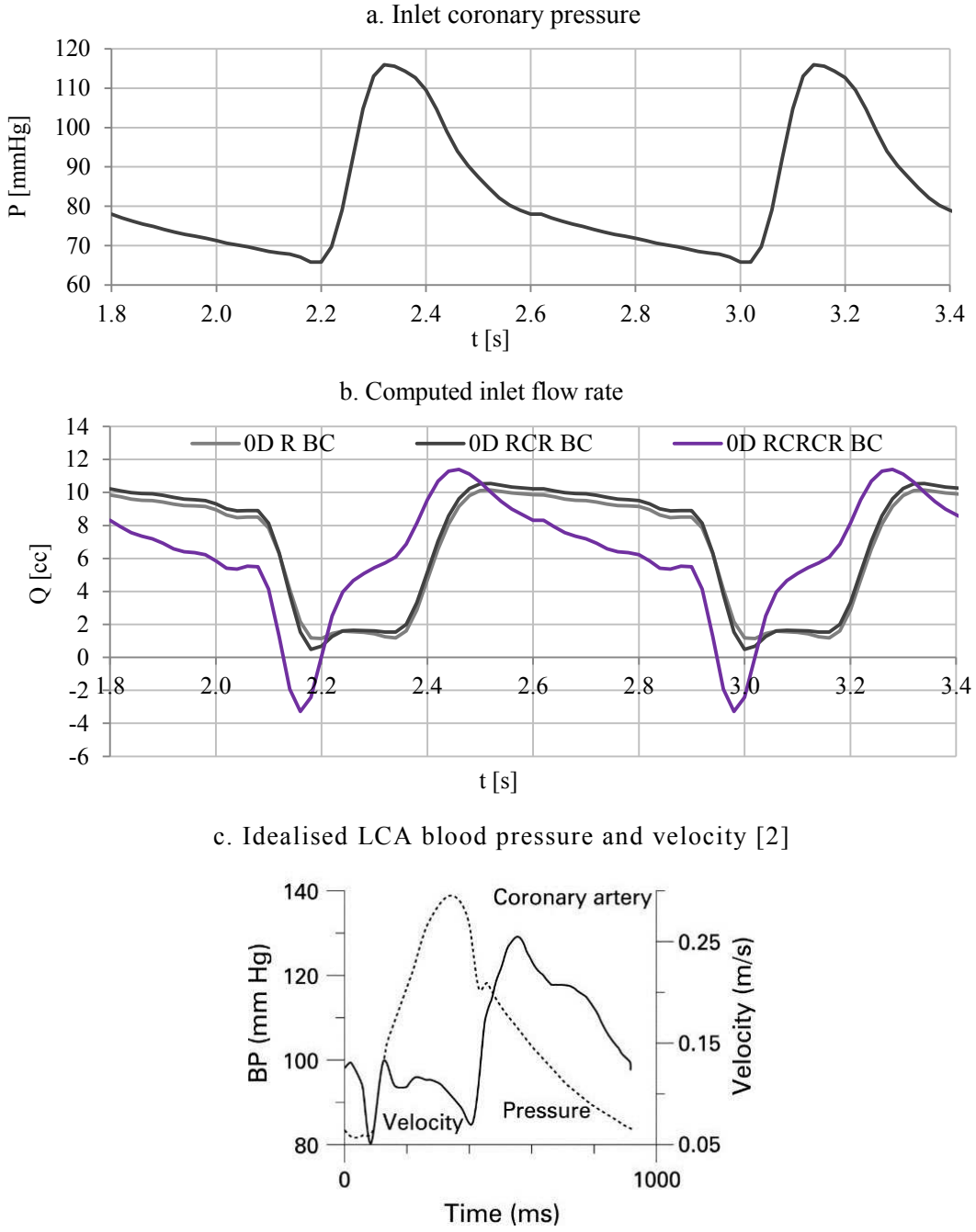

Figure 3.13 Computed LCA blood flow rate and pressure waveforms for three 0D models of downstream vasculature vs. idealised coronary pressure and velocity waveforms

Consequently, the question behind the choice of the outlet BC type is how the waveform shape affects the simulation results taking into account the level of modelling

assumptions and associated computational costs. Comparison of the computed flow fields under these three BC models including the steady state simulation mode for the pure resistance BC is presented in Sections 5.2.1-5.2.2.

The values of the downstream coronary microvascular resistance are calculated based on the Murray's morphometric law in the form $Q_{out} \sim d_{out}^{k}$, which relates flow distribution between the vessel branches to their diameters [73]. In other words, Murray's law reflects the adaptive behaviour of blood vessels when they remodel in response to variations in shear stress levels, which in turn corresponds to changes in flow rates. The morphometric exponent k is a constant derived empirically with the value of 3 proposed to be the optimal for arteries. Next, since the flow rate is inversely proportional to the resistance, the relative downstream resistance can be estimated as $R \sim d^{-k}$ with narrower branches having higher downstream vascular resistance. Consequently, prescription of the relevant resistance values for each outlet is essential for accurate computation of 3D blood flow fields.

3.3.3 Calculation of Peripheral Vascular Resistance

The proposed approach for estimation of the downstream 0D BC model parameter values is based on the generation of idealised 1D vascular trees that represent the peripheral vascular network for each of the outlets that are then used for deriving of the vascular resistance and capacitance values. As demonstrated in Figure 3.14.b, the fractal-like structure of a 1D vascular tree is based on the morphometry laws of vascular branching in accordance with the approach proposed by Olufsen [77]. Originating at the outlet of the 3D artery segment, the radii of the daughter vessel branches are scaled by factors α and β at each bifurcation with the branch length derived from the length/diameter ratio and the branching end defined by the terminal vascular diameter level.

The 1D fractal tree of the downstream vasculature (Figure 3.14.a) is generated by a recursive function initiating a new sub-tree branching process until the terminal level is reached. For each generated branch segment, the corresponding resistance R and C capacitance values are derived from Poiseuille's Law as [77,89]:

$$R = \frac{128 \cdot \mu \cdot l}{\pi \cdot D^4} \qquad C = \frac{\pi \cdot D^3 \cdot l}{4 \cdot E \cdot h} \quad , \tag{3.5-6}$$

where $\mu = 3.5 \cdot 10^{-3}$ Pa·s is blood viscosity, $E = 2 \cdot 10^{5}$ Pa is the vessel wall Young's modulus, D and l are the vessel segment diameter and length, and $h = 0.08 \cdot D$ is the estimated vessel thickness [89].

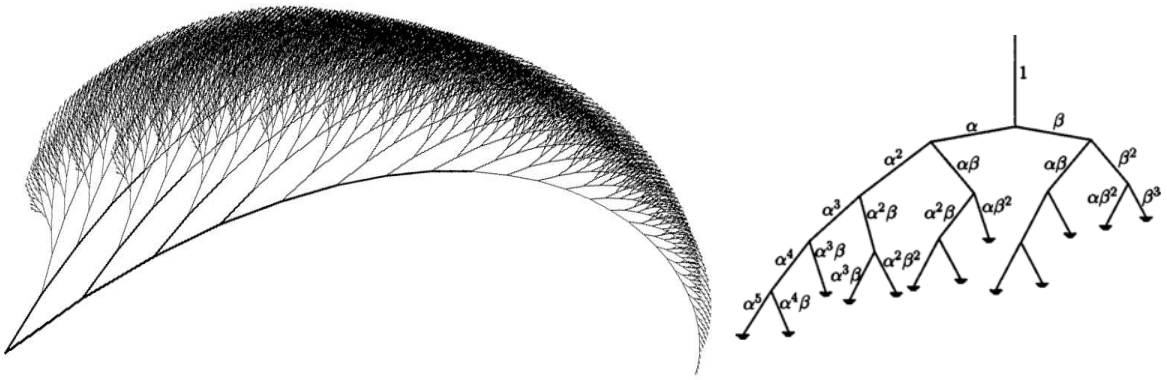

a. An example of the generated 1D vascular tree b. Structure of 1D tree [77]

Figure 3.14 1D fractal tree representing the peripheral vasculature downstream the outlet

At the final stage, the values of the total tree resistance and capacitance are derived as the summary over the corresponding circuit elements represented by 1D elementary segments. Taking into account the parallel structure of tree branching and Ohm's law the total peripheral resistance R will be lower for the outlets with wider diameter and larger peripheral vascular tree. The downstream impedance is the combination of the influence of R and C values on the blood flow from the outlet.

The flowchart of the developed recursive function [R, C] = ComputeRC (D_p, α, β, LD, D_{min}) is given in Figure 3.15, where R and C are the computed total capacitance and resistance volume, D_o is the outlet diameter, α and β are the bifurcation scaling factors, LD is the length/diameter ratio, and D_{min} is the terminal vascular level. The corresponding function implemented in MATLAB® provides a straightforward calculation of the 0D model parameters for the specified array of outlet diameters. While the computed downstream impedance directly depends on the outlet radius, the values of the scaling law parameters strongly affect the R and C values and they have to be estimated based on the modelling assumptions of the idealised vascular tree structure.

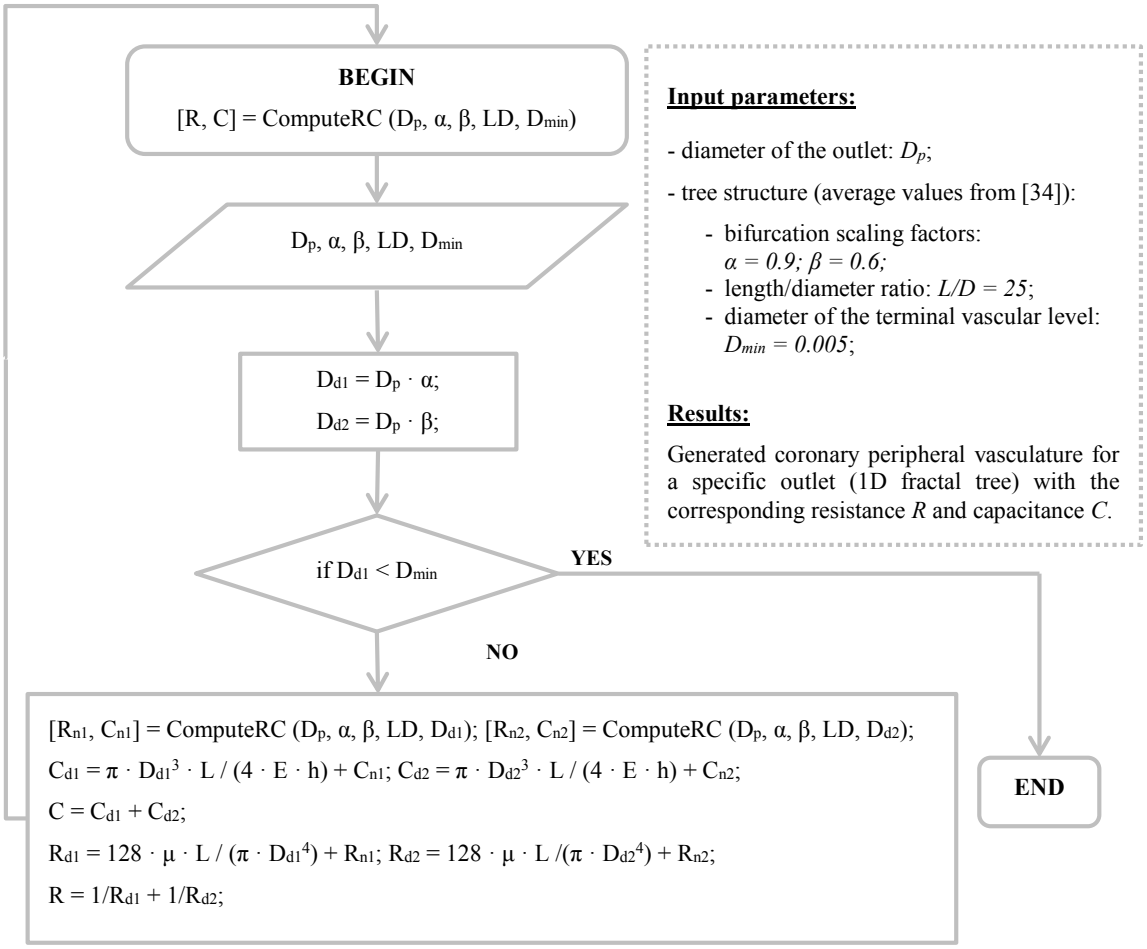

Figure 3.15 Flowchart of the recursive function for computation of the R and C values of the peripheral vascular tree

After investigation of the existing 1D vascular model parameters [73,79,110,117,136], coronary vascular structure [1,4] and sensitivity analysis (Table 3.1) the average parameters proposed by Olufsen [114] were chosen as optimal for peripheral coronary vasculature (0.6/0.9 asymmetry ratio and 20 length/diameter ratio) with 5 μm for the terminal vessel level. Another guiding factor towards this choice was the fact that the resulting computed R_a, C_a, and R_{am} together with C_{im} and R_c values lie within the range of related studies of 0D downstream BC models for coronary blood flow simulations [89,110].

Table 3.1 1D vascular tree structure parameters

Parameter	Zamir [73]	Olufsen [110]	Yang et al. [136]	Investigated range	Chosen values
Asymmetry ratio d_2/d_1	0.2 - 1	0.6/0.9	1	0.4 - 1.0	0.6/0.9
Length/diameter ratio	10-35	20-30	3.0	10 - 30	20
Terminal level diameter	-	-	10 μm	5 - 20 μm	5 μm

For instance, Figure 3.16 shows how the total peripheral resistance and capacitance depends on the diameter of the terminal vascular level for various outlet diameters. The vertical dash lines represent the idealised separation between the vascular layers for terminal levels at: 200 μm for arteries (R_a), 50 μm for arterioles (R_{am}), and 5μm for the capillary vascular bed (R_c). This classification of the vascular levels is broadly based on the anatomical data found in the literature. Since this dependence demonstrates a linear character it was decided to interpolate it and represent as a separate function thus avoiding the need to generate 1D trees every time, thus reducing the computational cost. The corresponding interpolated functions for R_a, R_{am}, C_a, and R_c are given below:

$$R_a = 2464 \cdot D^{-2.122} - 7931 \qquad R_{am} = 2901 \cdot D^{-2.463} - 9461 - R_a$$
$$C_a = 4.959e^{-05} \cdot D^{3.708} - 6.806e^{-09} \qquad R_c = 4708 \cdot D^{-2.627} - 4381 - R_{am} - R_a \tag{3.7-10}$$

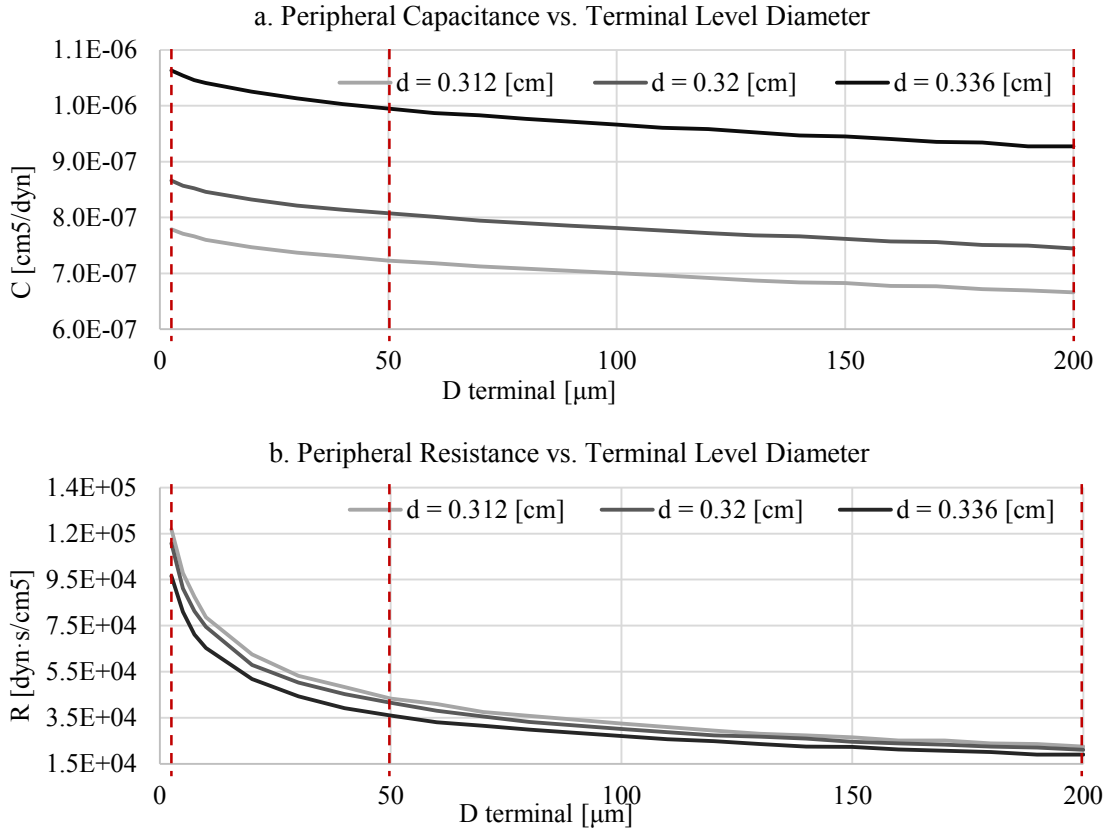

Figure 3.16 Computed downstream R and C vs. diameter of the terminal vascular level

As can be seen from the graphs in Figure 3.17, the computed resistance and capacitance values show nearly linear dependency of the length/diameter ratio. The L/D ratio value of 20 was chosen as the optimal for coronary vasculature models since the series of 3D

simulations resulted in the total inlet coronary flow being within the normal physiological range for coronary circulation as well as complying with the findings of the related studies [110].

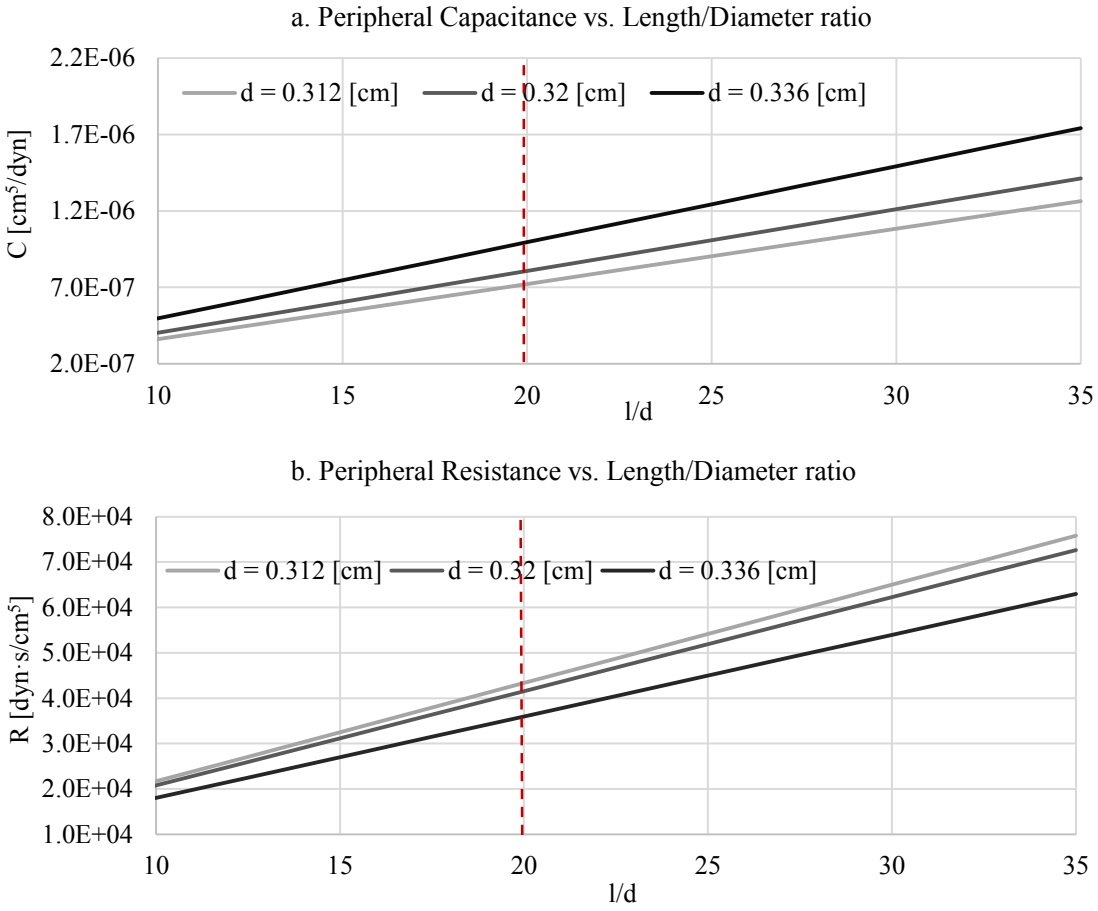

Figure 3.17 Computed downstream resistance and capacitance vs. length/diameter ratio

Further increase of the length/diameter ratio will lead to higher downstream resistance and capacitance values, which will decrease computed inlet flow rate. The results of the sensitivity study of the influence of the variations of the 0D BC model parameters on the computed blood flow fields are presented in Section 5.2.5.

Examples of the computed resistance and capacitance values for the 0D R, RCR and RCRCR models for the LCA tree (Figure 3.9) are given in Tables 3.2-4. The proximal arterial resistance R_a and compliance C_a are computed from the outlet diameter for small arteries with diameters above 200 μm vascular level, R_{am} is the resistance of arterioles with diameters between 200 and 50 μm, and R_c is the distal resistance of microcirculation vascular level with diameters between 50 and 5 μm. The C_{im} value is directly related to the myocardium surface coverage by the peripheral vascular tree and the optimal value was estimated to be $30 \cdot C_a$, based on the flow rate waveform fitting study (Figure 3.13).

Table 3.2 Computed parameter values for 0D R outlet BC model

Outlet #	Diameter [cm]	$10^5 \cdot R$ [dyn·s/cm^5]
1	0.197	1.4247
2	0.112	5.9084
3	0.133	3.8099
4	0.168	2.1115
5	0.191	1.5494
6	0.193	1.5137
7	0.167	2.1497
8	0.137	3.5026
9	0.216	1.1323

Table 3.3 Computed parameter values for 0D RCR outlet BC model

Outlet #	Diameter [cm]	$10^5 \cdot R_a$ [dyn·s/cm^5]	$10^{-6} \cdot C_a$ [cm^5/dyn]	$10^5 \cdot R_{am}$ [dyn·s/cm^5]
1	0.197	0.6996	1.0630	0.7251
2	0.112	2.4540	0.1210	3.4544
3	0.133	1.7420	0.2310	2.0679
4	0.168	0.9896	0.5640	1.1219
5	0.191	0.7200	0.9380	0.8294
6	0.193	0.7206	0.9800	0.7931
7	0.167	1.0075	0.5510	1.1422
8	0.137	1.5938	0.2570	1.9088
9	0.216	0.5533	1.5440	0.5790

Table 3.4 Computed parameter values for 0D RCRCR outlet BC model

Outlet #	Diameter [cm]	$10^5 \cdot R_a$ [dyn·s/cm^5]	$10^{-6} \cdot C_a$ [cm^5/dyn]	$10^5 \cdot R_{am}$ [dyn·s/cm^5]	$10^{-6} \cdot C_{im}$ [cm^5/dyn]	$10^5 \cdot R_c$ [dyn·s/cm^5]
1	0.197	0.6996	1.9263	0.7251	31.8900	1.9263
2	0.112	2.4540	8.6956	3.4544	3.6300	8.6956
3	0.133	1.7420	5.6031	2.0679	6.9300	5.6031
4	0.168	0.9896	2.9235	1.1219	16.9200	2.9235
5	0.191	0.7200	2.0396	0.8294	28.1400	2.0396
6	0.193	0.7206	2.0163	0.7931	29.4000	2.0163
7	0.167	1.0075	2.9763	1.1422	16.5300	2.9763
8	0.137	1.5938	5.1124	1.9088	7.7100	5.1124
9	0.216	0.5533	1.4837	0.5790	46.3200	1.4837

One of the advantages of the proposed method for estimation of the 0D model parameters is that the derived parameter values are physiologically realistic since they replicate the impedance of 1D vascular structure. As shown in [77,115] the outputs of 0D and 1D models

with similar characteristics are nearly identical. In addition, in the cases of healthy arteries, the application of these 0D model parameters directly results in the computed blood flow rate distribution to be proportionate to the outlet diameter $dQ_{out}^3 \sim d_{out}$ for healthy artery cases with the inlet flow rate also being close to the geometry-extracted requirement (4-5% of the CO [110,137]). However, this method still requires additional tuning of the 0D model parameters in the case of the presence of stenoses, which affect blood flow patterns. This requirement can be explained by the processes of long term compensatory mechanisms of adaptation of the vessel lumen diameter in response to the stenosis formation [1,2], which in its turn changes the total peripheral vascular resistance by regulation of the vasodilation degree of the downstream vasculature. Section 3.4.4 presents the proposed approach for the adjustment of the peripheral resistance, which provides the means to ensure that the computed flow rate through a specific branch (even in the case of the presence of stenosis) is proportional to its outlet radius under the rest physiological condition. It also provides a means to regulate the inlet flow rate value so that is lies within the limits of 4% from the geometry-extracted CO [137].

3.3.4 Adjustment of Peripheral Vascular Resistance

Following the preliminary computation of the blood flow under the initial boundary conditions (i.e., computed downstream resistance values) further adjustment of the downstream BC model parameters is required in order to achieve physiologically accurate computed blood flow fields. This accuracy is defined with respect to the coronary artery inlet flow rate and flow distribution between the outlets, since both of these values cannot be directly assigned under the inlet pressure BC.

In accordance with the relation defined in [110,137], the total coronary flow rate is approximately 4-5% of the CO, where the patient-specific CO can be computed from the reconstructed LV volume [110]. The compliance with the patient-specific inlet flow rate requirement is essential since it directly affects the predicted stenosis severity with higher flow rates enhancing the impact of stenosis on the pressure drop. Under the pressure inlet BC, the computed inlet flow rate can be regulated by the degree of vasodilation of the downstream vasculature. In addition, as mentioned in the previous section, although the proposed method of estimation of the downstream peripheral resistance directly produces the flow rate distributions being $dQ_{out}^3 \sim d_{out}$ for healthy coronary artery cases, it does result in lower flow rates for stenosed arteries. In its turn, the lower flow rate decreases the corresponding pressure

drop along a stenosis and the corresponding estimated haemodynamic significance becomes lower. However, this is not physiologically correct because of the long-term autoregulation mechanism that increases the degree of vasodilation of the peripheral vasculature along with the formation of a stenosis or results in the development of collateral circulation [2,4]. Thus, additional adjustment of the downstream resistance is required for CAD vessel cases.

In the method proposed in [120], this issue is resolved by the feedback function that adjusts the downstream model parameters such as resistance and capacitance based on the difference between the computed flow fields and the setup flow waveform requirements. This function controls several parameters including inlet flow rate, pressure waveform shape and flow rate distribution between the outlets. Since this involves performing transient 3D blood flow simulations between the adjustments, this approach is considerably time consuming, even when taking into account the low resolution of the employed meshes.

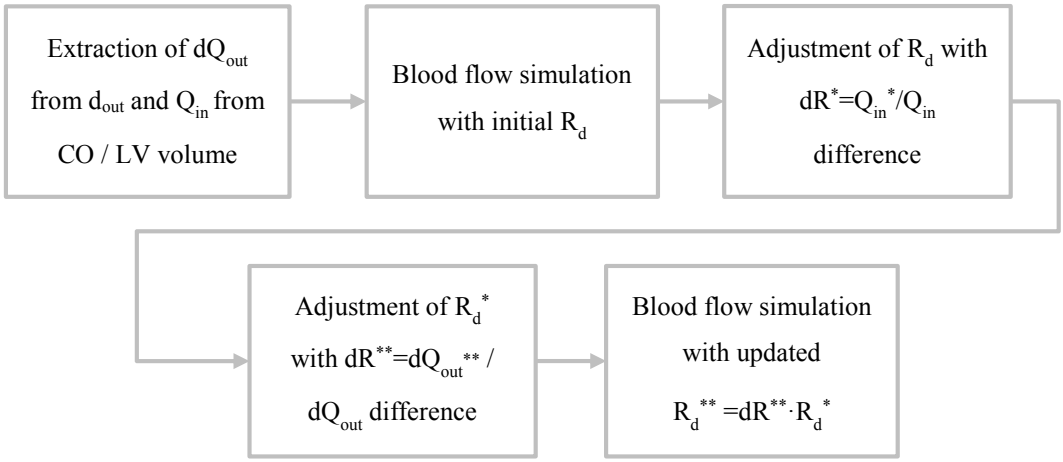

Figure 3.18 Proposed procedure for adjustment of the downstream peripheral resistance

In the case of a simple downstream resistance model in steady state blood flow simulations, this method can be implemented in a straightforward way. As shown in Figure 3.18, the proposed sequence of steps that have to be performed in order to obtain the required inlet flow rate Q_{in} and flow distribution dQ_{out} includes:

- Extraction of the system flow requirements: calculation of the modelling requirement for dQ_{out} from d_{out} and Q_{in} from the CO / LV volume and approximation of R_d from d_{out} for the 0D downstream BC;
- Blood flow simulation #I: preliminary blood flow simulation with the initial R_d resulting in the computed Q_{in}^{*} and dQ_{out}^{*}, which might be different from the required Q_{in};

- Parameter adjustment #I: adjustment of the downstream resistances R_d with $dR^* = Q_{in}^*/Q_{in}$ for regulation of the inlet flow rate by changing the general vasodilation degree $R_d^* = dR^* \cdot R_d$;
- Parameter adjustment #II: adjustment of the downstream resistances R_d with $dR^{**} = dQ_{out}^*/dQ_{out}$ for regulation of the flow distribution between the outlets $R_d^{**} = dR^{**} \cdot R_d^*$;
- Blood flow simulation #II: simulation with the adjusted R_d^{**} resulting in the computed Q_{in}^{**} and dQ_{out}^{**}.

The outputs of the second round simulation: Q_{in}^{**} and dQ_{out}^{**} are comparable with the originally calculated requirements for Q_{in} and dQ_{out} as demonstrated in the experiment results described in Section 5.2.4.

3.3.5 Modelling of Various Physiological Conditions

As described in Sections 1.1.3-4, besides the application of general static geometry CAD indices, the assessment of functional stenosis severity from non-invasive CCTA data involves computation of the virtual FFR under the simulated hyperaemia condition corresponding to maximal coronary peripheral vasodilation. The FFR index is computed as $FFR = {P_{distal}}/{P_{proximal}}$ [18], where P_{distal} is the mean distal coronary pressure and $P_{proximal}$ is the mean proximal pressure at the root of the coronary artery tree. A stenosis or a series of stenoses causing the FFR drop below the 0.75-0.8 threshold is considered as causing ischemia and a critical CAD indicator [18]. Similarly to the invasive FFR measurement procedure, in "virtual" blood flow simulations, hyperaemia is modelled by vasodilation through a decrease of peripheral vascular resistance, which it turn increases the coronary flow rate thus enhancing the flow limiting impact of stenoses on the FFR drop. According to the findings by Gould et al. [19], although the degree of vasodilation is of the patient-specific nature, the average value of total coronary resistance reduction can be taken as 24% of the original resting value as, theoretically, it represents the upper limit for achievable vasodilation corresponding to 140 mg/kg/min intravenous adenosine injection. At the same time, while the FFR_{CT} system assumes 0.24 as upper limit for achievable vasodilation in all HeartFlow® trials [47, 43,44], other models also used value of 0.2 and 0.25 [49,50,56].

In the proposed modelling approach, the degree of vasodilation dR corresponding to hyperaemia was chosen to vary within the 0.2 – 0.25 range in order to estimate the impact of

choice of dR choice on the computed FFR. Examples in Figures 3.19-20 show how the computed inlet flow rate, FFR and dQ at the outlets are changing as dR goes from one to zero. Although this representation of the results requires approximately seven simulations instead of just two solution rounds corresponding to two dR values, it provides additional information for the analysis, particularly when taking into account the patient-specific nature of vascular tree geometries and haemodynamics.

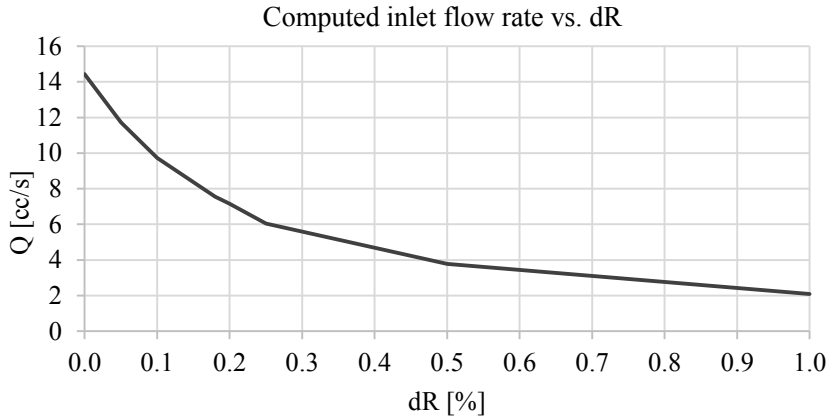

Figure 3.19 An example of changes in the computed inlet flow rate in response to modelled peripheral vasodilation (dR = 0.0:1.0)

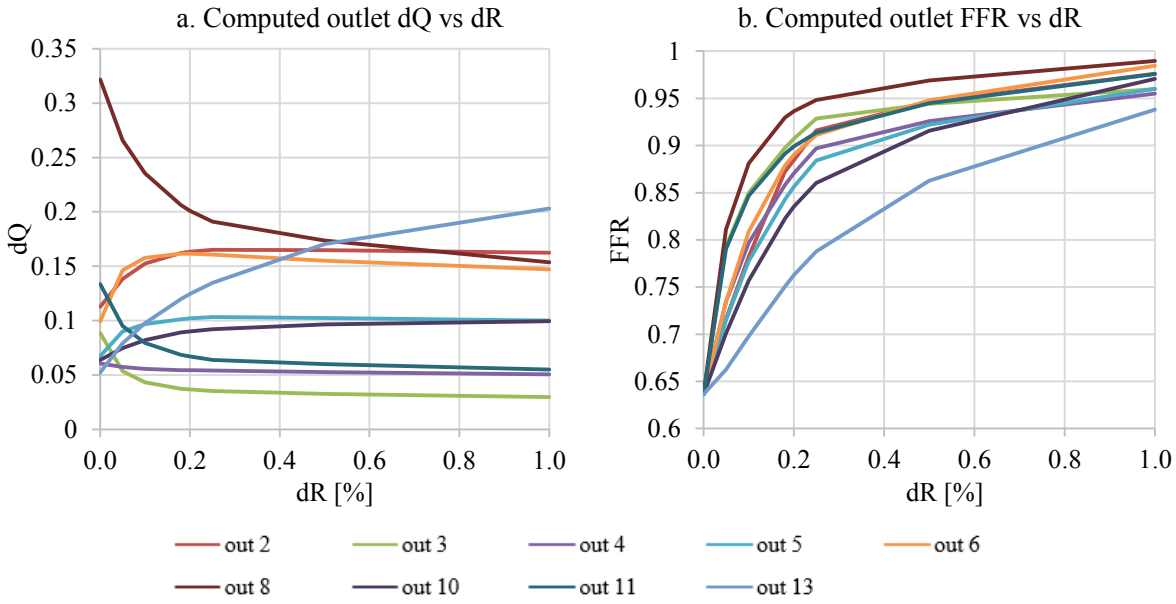

Figure 3.20 An example of changes in the computed FFR and dQ at the outlets in response to modelled peripheral vasodilation (dR = 0.0:1.0)

3.3.6 3D-0D Implicit Coupling

Assignment of the defined 0D models to the boundaries of the 3D computational domain requires the application of a specific coupling procedure due the differences in the model dimensions [112]. In the case of the inlet BC, the aortic pressure waveform has to be simply prescribed at all elements of the inlet boundary of the 3D coronary artery as the t_i timestep-specific pressure value $P_{aorta}(t_i)$ (3.1). However, in the case of 0D downstream models, both 3D and 0D models require inputs from each other in order for the flow fields to be computed and thus two-way implicit coupling is required at the outlet boundaries. Since the chosen downstream 0D models are relatively simple and do not require numerical solution, the coupling procedure consists in time discretisation of the corresponding ODEs of the 0D BC models and the direct solution at every timestep.

R resistance 0D model:

$$P_{out}(t) = P_d(t) + R \cdot Q^*_{out}(t) \tag{3.11}$$

RCR Windkessel 0D model:

$$P_{out}(t) = (P_d(t) \cdot (\tau + \Delta t) + Q^*_{out}(t) \cdot (\Delta t \cdot (R_a + R_{am}) + \tau \cdot R_a) + \tau \cdot \tag{3.12}$$
$$(P_{out}(t - \Delta t) - P_d(t - \Delta t) - R_a \cdot Q_{out}(t - \Delta t))/(\tau + \Delta t) \ ,$$
where $\tau = R_{am} \cdot C_a$.

RCRCR 0D model of coronary vasculature:

$$P_{out}(t) = (I \cdot Q^*_{out}(t) + K \cdot P_d(t) + M \cdot Q_{out}(t - \Delta t) + L \cdot P_{out}(t - \Delta t) + \tag{3.13}$$
$$+N \cdot P_d(t - \Delta t) + O \cdot P_{out}(t - 2 \cdot \Delta t) + S \cdot Q_{out}(t - 2 \cdot \Delta t))/H \ ,$$
where the corresponding coefficients are expressed as:

$$H = 1 - {}^{A}/_{\Delta t} - {}^{D}/_{\Delta t^2} \ ; \quad I = G + {}^{B}/_{\Delta t} + {}^{F}/_{\Delta t^2} \ ;$$

$$K = {}^{E}/_{\Delta t} \ ; \quad L = -{}^{A}/_{\Delta t} - 2 \cdot {}^{D}/_{\Delta t^2} \ ; \quad M = -{}^{B}/_{\Delta t} - 2 \cdot {}^{F}/_{\Delta t^2} \ ;$$

$$N = -{}^{E}/_{\Delta t} \ ; \quad O = {}^{D}/_{\Delta t^2} \ ; \quad S = {}^{F}/_{\Delta t^2}$$

$$A = -R_V \cdot C_a - R_{am} \cdot C_a - R_v \cdot C_{im} \ ;$$

$$B = R_a \cdot R_v \cdot C_a + R_a \cdot R_{am} \cdot C_a + R_a \cdot R_v \cdot C_{im} + R_{am} \cdot R_v \cdot C_{im} \ ;$$

$$D = -R_{am} \cdot R_v \cdot C_a \cdot C_{im} \ ; \quad E = R_v \cdot C_{im} \ ; \quad F = R_a \cdot R_{am} \cdot R_v \cdot C_a \cdot C_{im} \ ;$$

$$G = R_a + R_V + R_v \ ;$$

During the numerical CFD solution, at each iteration of a timestep at a simulation time t_i, the equations representing 0D R, RCR, and RCRCR 0D BC models (3.2-4) for calculation of the outlet-specific downstream pressure $P_{out}(t)$ are solved with the measured 3D-computed outlet flow rate $Q_{out}^{*}(t)$ as an input from the 3D model. The discretisation of these equations is given in (3.11-13).

These BC models have to be incorporated into the CFD solver in order to get access to the 3D model solution variables. In the case of the ANSYS® Fluent CFD solver, the BC models have to be represented as special user-defined .c functions (UDF) and compiled into a UDF library, which is then can be integrated into the blood flow model defined in the solver. The process of the adjustment of the 0D BC model parameter values described in Section 3.4.4 is also implemented as a UDF. It provides a means for automatic uninterrupted blood flow simulation thus eliminating the need for manual adjustment of parameters after the preliminary simulation results. The degree of vasodilation is also user-controlled and, in the case of steady state flow simulations, can be set to an array of dR values with the final CFD solution resulting in the computed flow fields for the required dR range.

3.4 Blood Flow Model Setup and Solution in CFD Solver

Following the preparation of the computational domain and definition of the modelling assumptions together with the patient-specific BC models, the blood flow model has to be implemented in a CFD solver. A recent study by Kim et al. [71] demonstrated that the choice of a CFD solver or specific solution settings does not significantly affect the solution accuracy in comparison to mesh resolution or variations in BC parameter settings.

The proposed modelling approach employs professional ANSYS® Fluent FVM CFD solver for numerical solution the Navier-Stokes equations (2.1) discretised over the coronary artery volume mesh under the defined modelling assumptions with the implicitly coupled BC models in the UDF form.

The optimal FVM CFD Solver settings were identified based on the general guidelines and sensitivity study regarding the required accuracy and computational cost. The pressure-based algorithm was chosen for solution of the N-S equations with the use of the control-volume-based technique applied for discretisation of the transport equation [139]. In this method, the transport equation is integrated for each control volume with the resulting discrete

equation representing the conservation law on a control-volume basis. The N-S equations are discretized using a second-order upwind scheme and the first-order fully implicit backward Euler time differencing scheme [139]. The numerical solution is performed via the SIMPLE velocity-pressure coupling algorithm [139] with a specified number of uniform time steps per second.

Taking into account the convergence requirements of the implicitly coupled 0D BC models of peripheral vasculature, low solution control under-relaxation factors were defined as optimal with the values set to 0.1 for pressure and 0.15 for momentum. The solution convergence is controlled through the solution residuals convergence criteria values of 10^{-5} for continuity and velocity and approximately 300-700 iterations per timestep depending on the outlet BC type. For transient simulations, the time step size was chosen to be 0.01 s, which is optimal from the point of view of the solution accuracy and the use of computational resources. Considering the computed flow fields, further decreasing of the time step did not affect the results visibly. In addition, the virtual FFR is computed from the mean pressure values and thus the higher precision is not required while being more computationally expensive. A duration of two heartbeats was determined as being the optimal for the numerical simulation for the 0D R BC type in order to ensure a stable solution with respect to the time-dependent downstream BC model. The results showed that the computed relative pressure and velocity did not differ by more than 3% for the 0D R BC cases. However, the 0D RCR and RCRCR BC models with the time-dependent components require four to five heartbeats to achieve sufficient repeatability.

Taking into account the high computational cost of transient CFD simulations, the numerical solution process should employ parallel CFD solver settings, which also adds a requirement to the UDF design. Depending on the BC type, the volume mesh size and the number of heartbeats, duration of one two to four heartbeats transient simulation can take approximately 8 to 30 hours on a 16-core processor engineering workstation, while the results of steady state simulation are ready for the analysis within 1 hour. After the numerical solution, the computed flow patterns are exported for further processing and analysis.

3.5 Metrics and Extraction of Computed Haemodynamics

The results of blood flow simulations are generally analysed through evaluation of the global and local changes in haemodynamic variables in response to variations in vascular

geometries such as stenoses, aneurisms atherosclerotic plaque, and stents. In 3D domain, this generally includes pressure, velocity, flow rate, WSS derived values, and FFR.

In the proposed modelling approach, the CFD simulation results are visualised and analysed in ANSYS® CFD-Post post-processing software compatible with Fluent CFD Solver. Figure 3.21 shows an example of the computed pressure, velocity, and WSS patterns averaged over a cardiac cycle represented in magnitude colour scale.

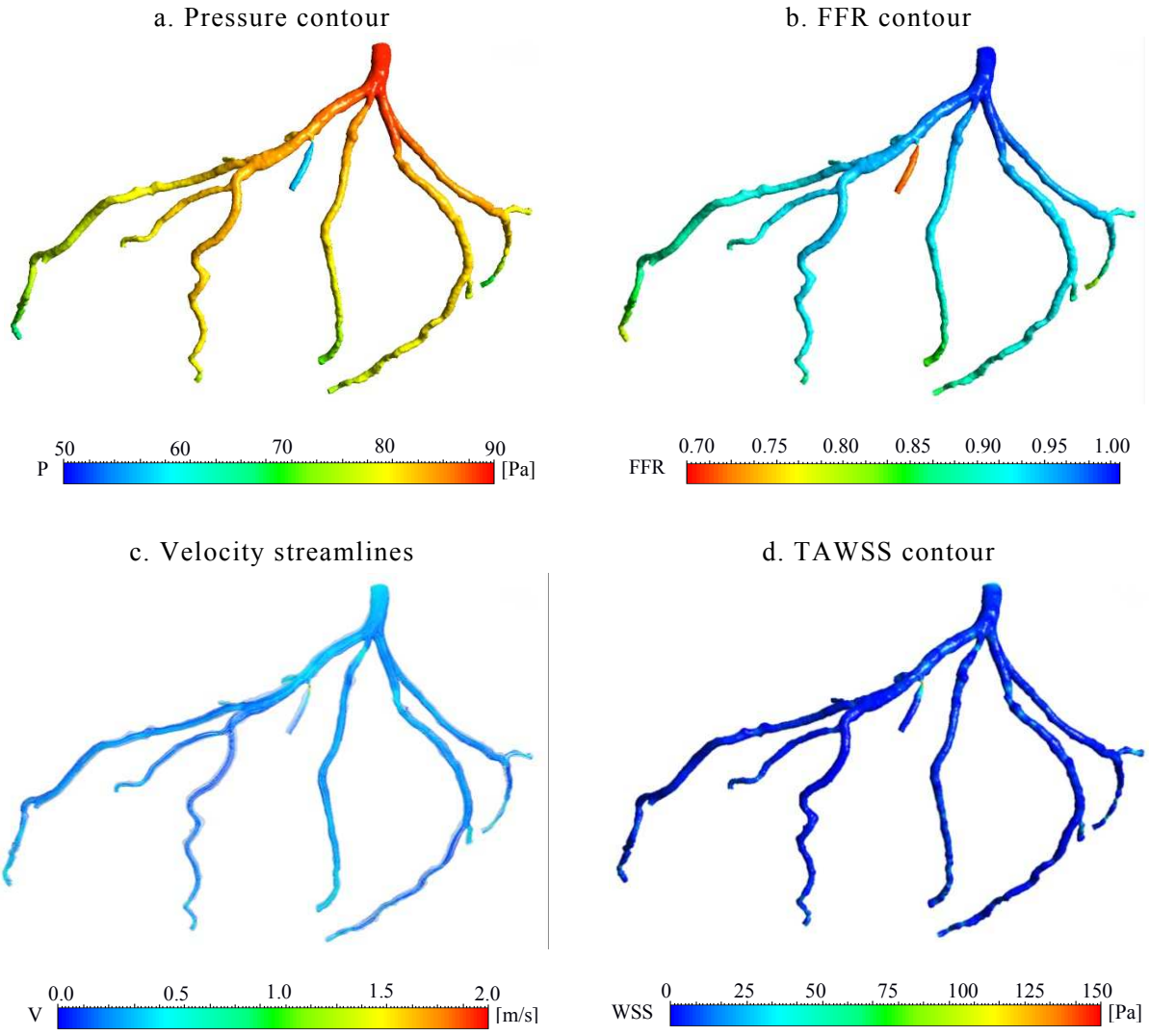

Figure 3.21 Visualisation of the computed blood flow fields in 3D colourscale form

Similarly, the virtual FFR index is computed over a heart cycle as a ratio of the mean hyperaemic pressure over the mean LMCA hyperaemic pressure. Following the established practice [44,48], computed 3D FFR is visualised in 0.7 – 1 scale as demonstrated in Figure 3.21.b. For instance, it can be observed that FFR drops below the critical 0.75 threshold for one of the side branches due to the presence of a stenosis. In addition, the pressure and flow rate

waveforms measured at the inlet and outlets at every timestep can be plotted for further analysis together with the derived flow distribution dQ(t) and FFR(t) values. The example in Figure 3.22.e shows how FFR in the branch with the outlet #13 drops below the critical threshold value.

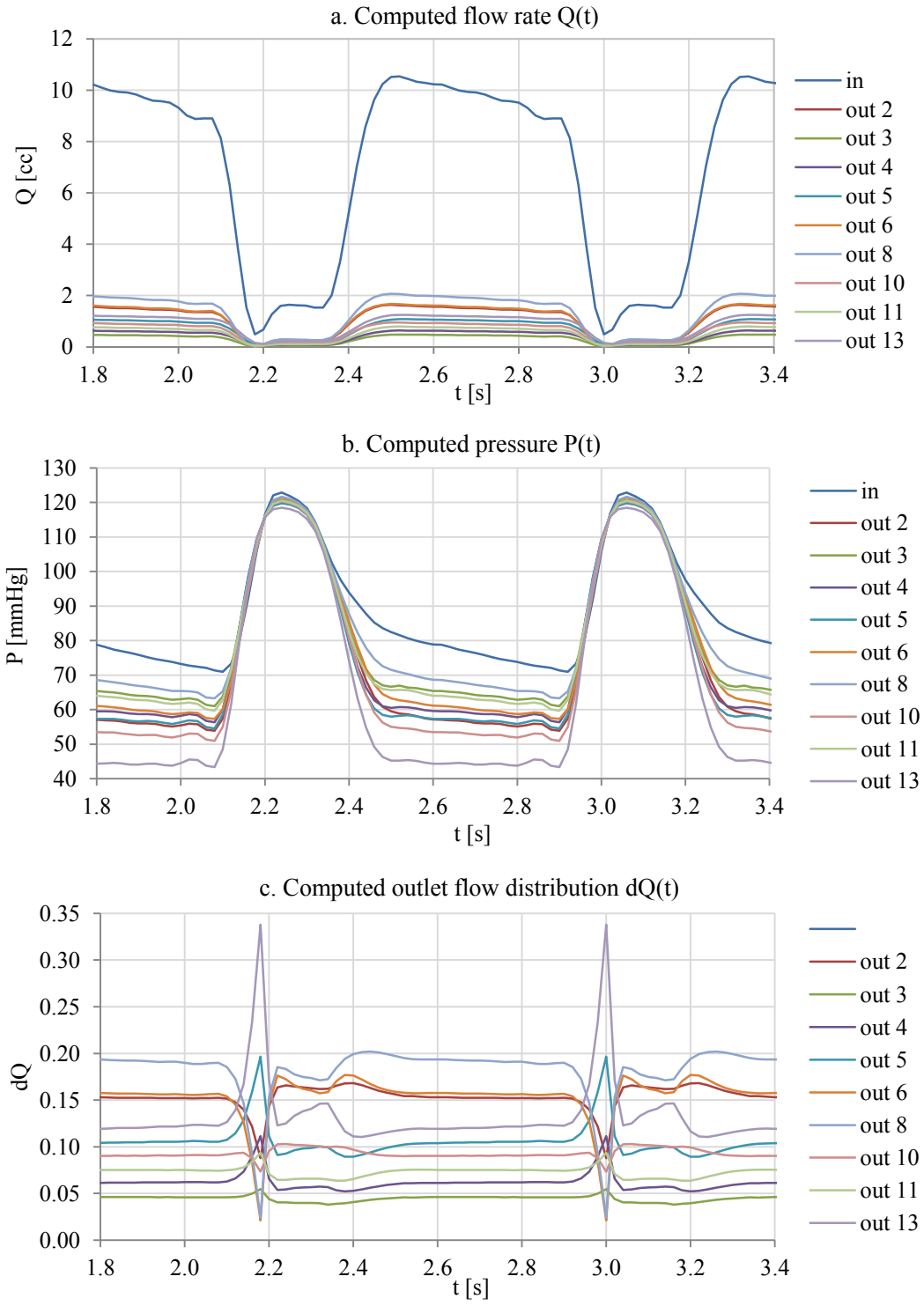

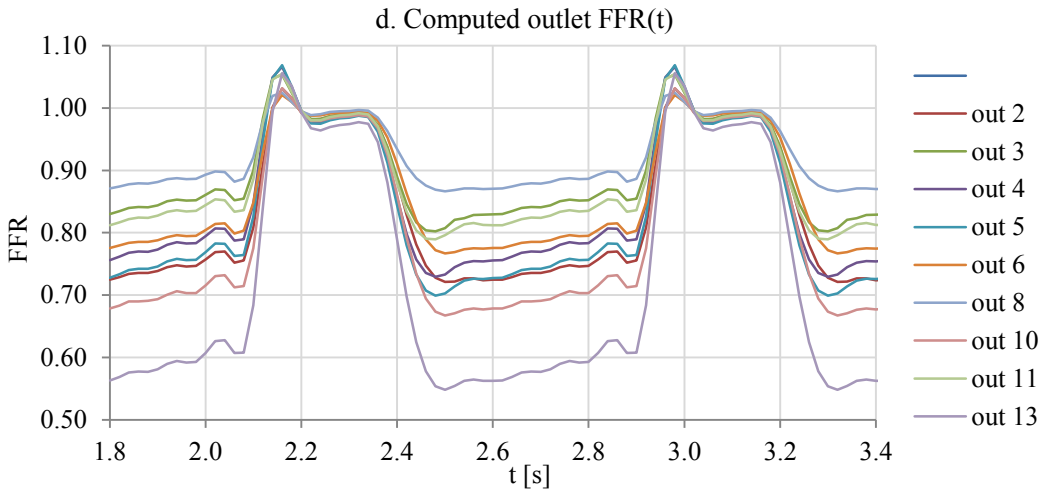

Figure 3.22 Visualisation of the computed blood flow waveforms at the inlet and outlets

3.6 Limitations and Future Research Directions

Taking into account the level of complexity of the problem domain, there is a number of limitations of the proposed patient-specific blood flow modelling approach and its application to virtual FFR assessment. The main causes are related to the introduced modelling assumptions, lack of in-depth patient-specific information that can be obtained only invasively but is required for both modelling input and validation, and the general 3D CFD model complexity due to a great number of interrelated factors and associated computational costs. Similarly to the majority of the existing 3D blood flow models and, particularly, the virtual FFR models presented in [49,50], another limitation of the implemented modelling approach is the use of the commercial CFD solver software that requires importing and exporting of data and appropriate engineering skills to operate it. On the other hand, it provides robust and time-efficient solution of blood flow models together with the set of professional tools required for preparation of high quality computational domain.

The physiological accuracy of the computed blood flow may be affected by the following factors:

– The anatomical accuracy of the geometrical reconstruction of the lumen surface may be limited by the presence of artefacts (calcifications, motion, etc.) and erroneous soft plaque detection due to low intensity variations. Furthermore, the presence of plaques is modelled as a lumen reduction (stenosis) and the plaque material is not considered (neither calcified nor soft plaques). The same can be said with respect to the models with stented arteries and bypass grafts.

- Certain physiological parameters such as blood viscosity, inlet coronary pressure, and LV pressure are set to the average population-specific rather than patient-specific values.
- The downstream impedance is represented by the idealised 0D models. Although the corresponding resistances and capacitances are computed from the measured outlet diameters, the structure of the generated 1D peripheral vascular trees is defined through the average values of the vascular network structure parameters. Hence, variations in these values may produce different R and C values. In addition, for the cases of severe stenoses with the exhaustion of the downstream autoregulation mechanism or peripheral CAD associated with vasoconstriction, the computed BC parameters may not be sufficiently accurate.
- With respect to virtual FFR assessment, the reduction of peripheral resistance corresponding to maximal hyperaemia generally varies among patients. As showed by Taylor et al. [44], for the patients with microvascular dysfunction, the computed FFR values may be lower than the invasive FFR due to the problem of overestimated peripheral vasodilation.
- Although the rigid vessel wall assumption is considered to be acceptable in coronary blood flow models [44,48-50] and the fact that the FFR index is an cardiac cycle averaged value, incorporation of elasticity of epicardial arteries and their movement due to ventricle contraction may improve the physiological accuracy of the results. This, however, will introduce additional levels of complexity and uncertainly into the model since it requires the precise knowledge of vessel wall thickness distribution and elastic moduli, as well as the ventricle contraction trajectory.

3.7 Conclusions

This chapter described the steps required for the design and implementation of the proposed patient-specific 3D coronary blood flow modelling framework with the specific purpose of assessment of haemodynamic stenosis severity in the form of virtual FFR. In addition, a number of factors that may potentially affect the accuracy of the computed flow fields were presented and analysed. The steps of the framework can be summarised as follows:

- The modelling begins with the reconstruction of the coronary artery lumen geometry from a CCTA volume, which is then pre-processed and the blood volume within the lumen is discretised into the volume mesh representing computational domain.

- The blood flow model is defined in the CFD solver including the modelling assumptions and the specification of boundary conditions on the inlet and outlets of the coronary artery tree.
- Taking into account that the computed blood flow fields are directly defined by the BC, the impedance of the downstream vasculature is implemented through the analogical 0D vascular tree models implicitly coupled at the outlets. The corresponding resistance and capacitance values are derived from the patient-specific 1D model of peripheral vascular trees and further adjusted in order to achieve the geometry extracted BC requirements to the coronary flow rate being 4% of the CO and the outlet flow rate distribution between the vascular branches being proportional to the outlet diameters.
- The blood flow governing N-S equations are numerically solved over the computational domain in the ANSYS® Fluent CFD solver. The computed results including pressure, velocity and WSS patterns are plotted and analysed. The 3D FFR patterns are computed as the average value over a heart cycle.

The developed modelling approach provides robust and physiologically realistic solution of blood flow through coronary arteries reconstructed from CCTA volumes. In addition, the implemented BC models are suitable for modelling hyperaemia, which is essential for FFR assessment. The computed virtual FFR can be used for the assessment of functional stenosis severity, which can be further used as an additional diagnostic input in CCTA interpretation. Moreover, the implemented method for calculation of resistance and capacitance of the downstream vasculature provides a robust solution ensuring that the flow rate distribution is being proportional to the outlet diameter.

The results of application of this modelling approach to the CCTA volume of a CAD patient for the assessment of virtual FFR are presented in Chapter V together with the investigation of the influence of BC model type, modelling assumptions, geometry reconstruction procedure and interpatient variations in the CVS parameters. Following the analysis of the performed parametric study, validation of the model is planned to be carried out by comparison of the simulation results with the corresponding HeartFlow® FFR_{CT} outputs for a number of CCTA volumes.

Chapter 4

Design and Implementation of 0D Image-Based Coronary Blood Flow Model

4.1 Introduction

This chapter describes the proposed novel approach for spatially extended 0D image-based coronary blood flow modelling that can be used as either additional tool for verification for the equivalent 3D blood flow models or a as standalone solution.

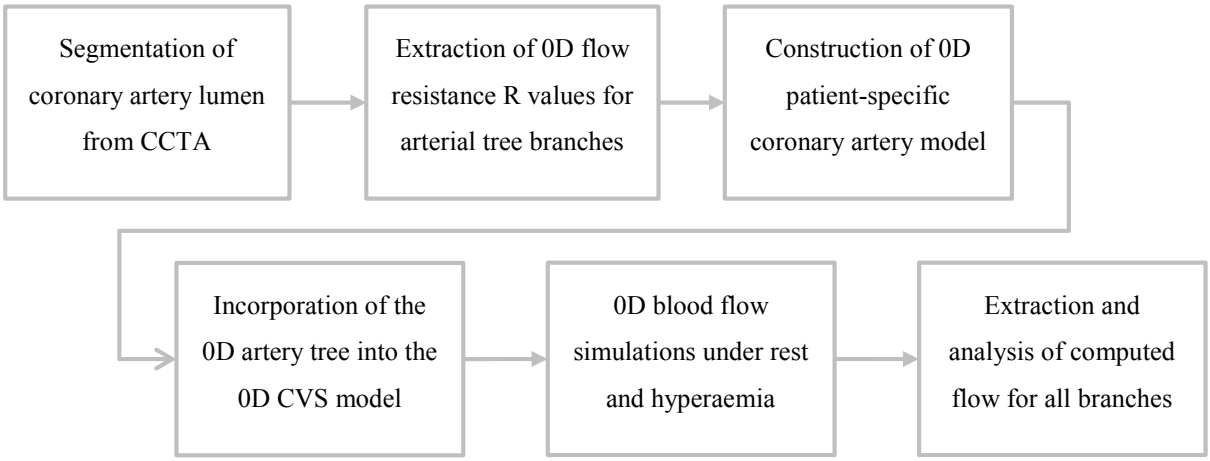

Figure 4.1 Development of 0D patient-specific coronary blood flow models: functional flowchart

As demonstrated in Figure 4.1, the implementation of the 0D coronary blood flow model includes the following steps:

(i) Extraction of spatially distributed 0D model parameter values such as flow resistance and vessel wall compliance from 3D artery lumen reconstructed from medical image volumes (in this case, CCTA), followed by the construction of the patient-specific coronary arterial tree model in 0D domain.

The initial stages of reconstruction of coronary arteries from CCTA are the same as in 3D modelling together with similar considerations with respect to the blood segmentation threshold and side branch truncation levels (Section 3.2.1). Next, the extraction of the 0D model parameter values also requires localisation of the vessel tree branches along the detected

centreline and their subdivision into elementary segments, for each of which flow resistance R values (and, if required, vessel wall compliance C and inertia L) are computed from the segment geometry. As a result, every branch is represented as a circuit of a series of resistor or RCR elements. The 0D model of the coronary tree is then constructed as an integrated electrical circuit consisting of the interconnected 0D branches.

(ii) Incorporation of the patient-specific 0D coronary artery into the 0D CVS loop model.

The CVS model provides flow boundary conditions on the inlet and outlets of the 0D coronary arterial tree and allows straightforward control of the CVS flow governing parameters for simulation of various physiological conditions such as hyperaemia or exercise. Similarly to the proposed 3D blood flow model (Section 3.3), the coronary arterial tree inlet is coupled to the root of the aorta while the outlets are coupled to the 0D BC models of the peripheral vasculature, which are also incorporated into the CVS loop. Both 0D and 3D models use the same patient-specific 0D downstream BC in order to ensure comparability of their results. Implementation of the CVS model comprising both ventricles and systemic and pulmonary circulation loops is based on the classical lumped-parameter CVS modelling approach formalised in [83].

(iii) Performing of 0D blood flow simulations and correlation of the extracted flow variables such as pressure, flow rate and FFR in the corresponding locations in 3D geometries of the coronary arterial tree and mapping of low FFR regions associated with CAD.

This stage is especially important in the context of investigating the "practical application" of 0D modelling, since its main drawback is related to the lack of spatial information on the computed blood flow. Unlike the existing 0D vascular models that represent the entire vessel tree branches by a single WK circuit [57,89,90,93] thus losing the essential geometry referencing, the proposed approach allows the extraction of the computed flow values along a vessel branch by its subdivision into a series of elementary circuit segments. The corresponding precision of the spatial registration is defined by the elementary segment length. Comparison of 0D simulation results with the equivalent 3D computed flow fields (Section 5.4) will provide the validation basis required for further development of the proposed approach along with the definition of the factors that might affect the accuracy of 0D blood flow modelling. Segmentation of coronary arteries and construction of the 0D tree model are implemented as a series of functions in the MATLAB® engineering framework, while the 0D

CVS model with the incorporated coronary tree is implemented in the MATLAB® Simulink SimElectronics toolbox.

This chapter is organised as follows: (i) Section 4.2 describes the 0D coronary arterial tree model development; (ii) Section 4.3 describes the 0D CVS model development; (iii) Section 4.4 explains the scheme for incorporation of the coronary arterial tree into the CVS loop; (iv) Section 4.5 defines the list of modelling assumptions; (v) Section 4.6 describes the implementation of the integrated model in the MATLAB® Simulink environment; (vi) Section 4.7 describes the process of extraction and analysis of the computed blood flow parameters; (vii) Section 4.8 lists the limitations of the proposed modelling approach and the implemented solution together with future research directions.

4.2 0D Patient-Specific Coronary Blood Flow Model

The process of generating the 0D patient-specific coronary arterial tree is based on the transition from 3D artery lumen geometries, reconstructed from CCTA, into the 0D domain by means of lumped-parameter modelling. The steps of the proposed method are presented in Figure 4.2 beginning from segmentation of the coronary arteries and detection of the tree branches, which are subsequently subdivided into small 3D elementary segments. Each of these segments is represented in the 0D domain with the corresponding 0D element values, derived from the segment geometry.

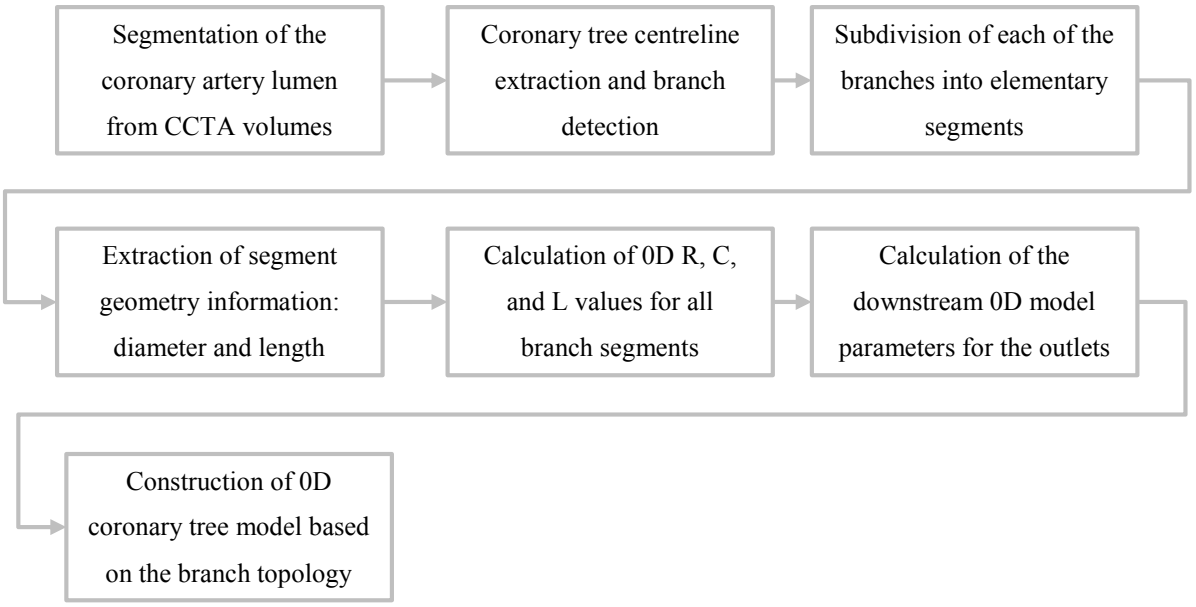

Figure 4.2 Development of the 0D patient-specific coronary blood flow model

Finally, the coronary tree is constructed from the 0D branches together with the computation of the 0D downstream vasculature model parameters. Implementation of the software for each of these steps was based on the existing set of functions for automatic segmentation and quantification of the coronary arteries, developed by the Medical Image Processing research group at City University London [132,133].

The preliminary stage of the reconstruction of the coronary artery lumen from CCTA dataset for 0D blood flow simulations is performed similarly to the preparation of the computational domain for the 3D CFD blood flow model described in Section 3.2.1. It includes: (i) vessel enhancement with Frangi's filter; (ii) local thresholding and localization of coronary arteries; (iii) vessel segmentation using active contour models. This is followed by the extraction of the arterial centreline and branch detection with the Fast Marching method [140], resulting in the vessel tree geometry being represented through its branches as shown in Figure 4.3.c, which is essential for incorporation of spatial information in the 0D domain.

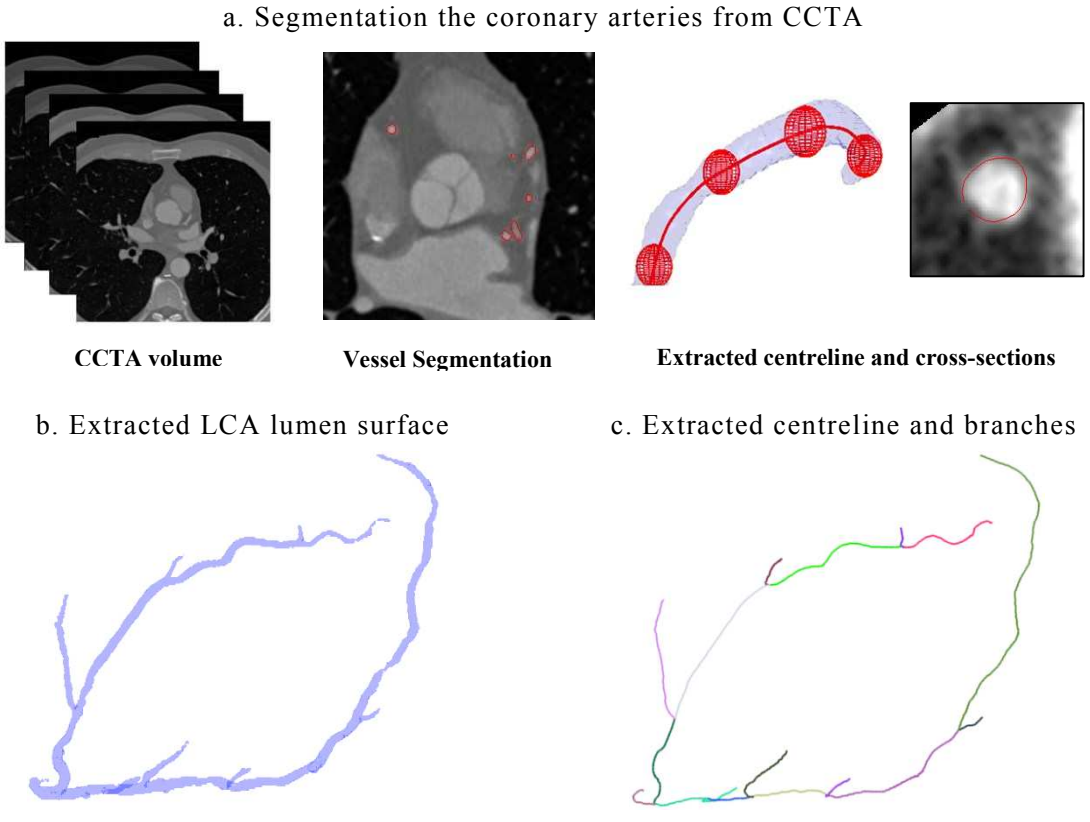

Figure 4.3 Extraction of coronary artery lumen from CCTA volume

At the next step, each of the detected arterial tree branches is processed individually. The branch centreline points are resampled to ensure that each of the elementary vessel segments has identical length l, and the cross-sectional planes are extracted through the normal

vectors (Figure 4.4.a). The mean diameters of the obtained cross-sectional contours are derived as $D = (4 \cdot A / \cdot \pi)^{1/2}$, where A is the measured cross-section area.

Each of the extracted branches is considered as a series of elementary segments represented as 0D vessel models in Figure 4.4.b. The circuit resistance (R), capacitance (C) and inductance (L) element values are derived from the segment length and cross-sectional diameters. The corresponding expressions given in (4.1-3) are derived from Poiseuille's Law for laminar incompressible flow [73,89]:

$$R = \frac{128 \cdot \mu \cdot l}{\pi \cdot D^4} \qquad C = \frac{\pi \cdot D^3 \cdot l}{4 \cdot E \cdot h} \qquad L = \frac{4 \cdot \rho \cdot l}{\pi \cdot D^2} \quad , \tag{4.1-3}$$

where $\mu = 3.5 \cdot 10^{-3}$ kg/m·s is the blood viscosity, $\rho = 1060$ kg/m^3 is the blood density, $E = 2 \cdot 10^5$ Pa is the vessel wall Young's modulus, D and l are the vessel segment diameter and length, respectively, and $h = 0.08 \cdot D$ is the estimated vessel thickness.

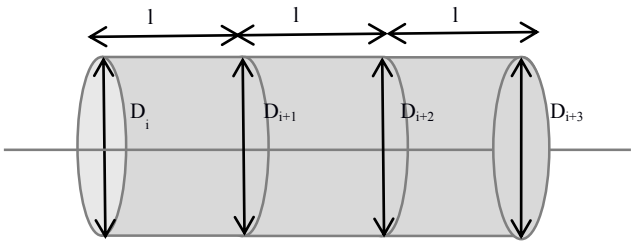

a. Idealised vessel divided into elementary segments of length l

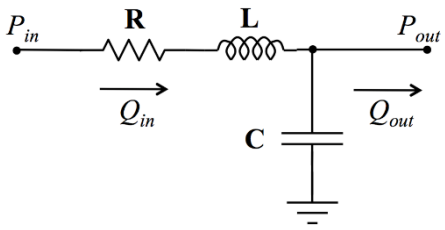

b. 0D model of a vessel segment

Figure 4.4 Representation of coronary vessels in terms of elementary parameters

Consequently, the resulting 0D vessel tree model preserves the spatial information of local variations in the vascular geometries and the computed flow fields can be associated with a specific location along a vessel with an accuracy defined by the elementary segment length.

The following subsections present two examples of generated 0D models of a single vessel and the entire left coronary artery. In order to be able to compare the 0D simulation results with 3D computed flow fields, the vessel wall is assumed rigid and the vascular geometries are represented only with the flow resistance elements. The 0D BC models representing the peripheral vasculature together with the method for derivation of their parameters are identical to the models employed in the 3D model (Section 3.4).

4.2.1 Single artery branch model

This section considers an example of a single branch of a coronary arterial tree reconstructed from CCTA. Figure 4.5 presents the selected LAD branch highlighted in red on the LCA tree centreline and the corresponding cMPR representation before and after vessel segmentation.

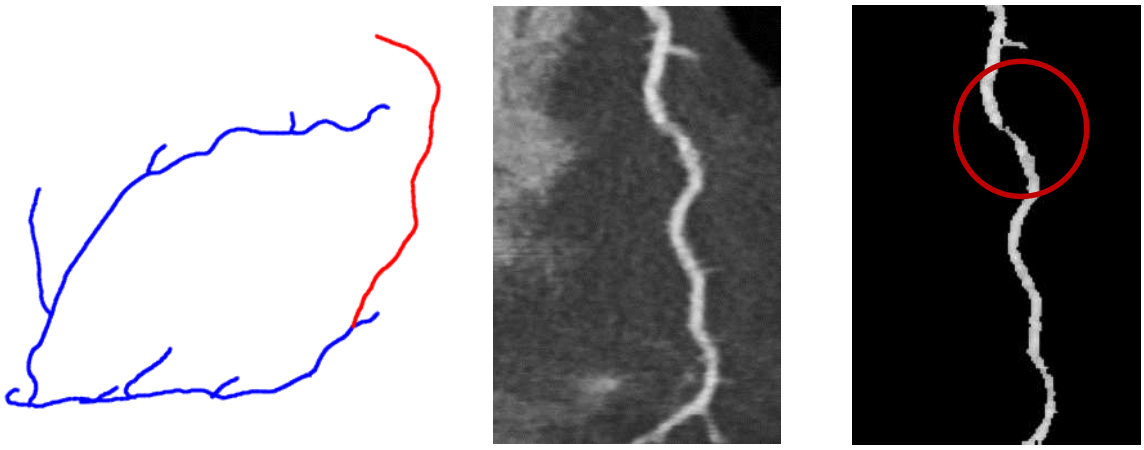

a. Extracted centrelines and the selected LAD branch

b. cMPR of the selected LAD [HU]

c. cMPR of the segmented LAD [HU]

Figure 4.5 Extracted LCA centreline and cMPR for a stenosed vessel branch

As shown in Figure 4.6.a, the extracted LAD branch in 3D has a medium-to-high severity stenosis with the maximum being approximately 70% in diameter reduction. The second stenosis is located close to the outlet is of low severity being less than 50%. The vessel lumen and centreline are divided into 160 elementary segments of l = 0.55 mm length each. The corresponding measured diameter variations along the centreline and the computed resistance values are given in Figures 4.6.b-c.

The observed fluctuations in the measured vessel diameter are mainly caused by lumen irregularities and the roughness of the extracted surface since no smoothing was applied. In addition, it might be due to the lack of sufficiently optimised parameters for vessel segmentation, which further emphasises the need for optimisation of the proposed methodology for 0D parameter extraction at a future stage of the research. The influence of the level of smoothing on the computed flow fields along with the other geometry reconstruction parameters is investigated in Section 5.3.

a. Surface of the LAD branch with a stenosis in 3D

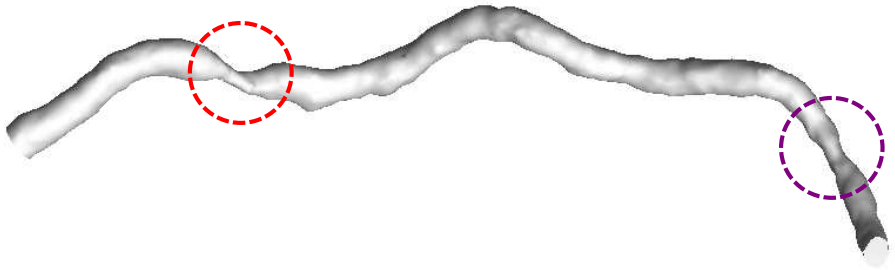

b. Extracted diameter along the vessel

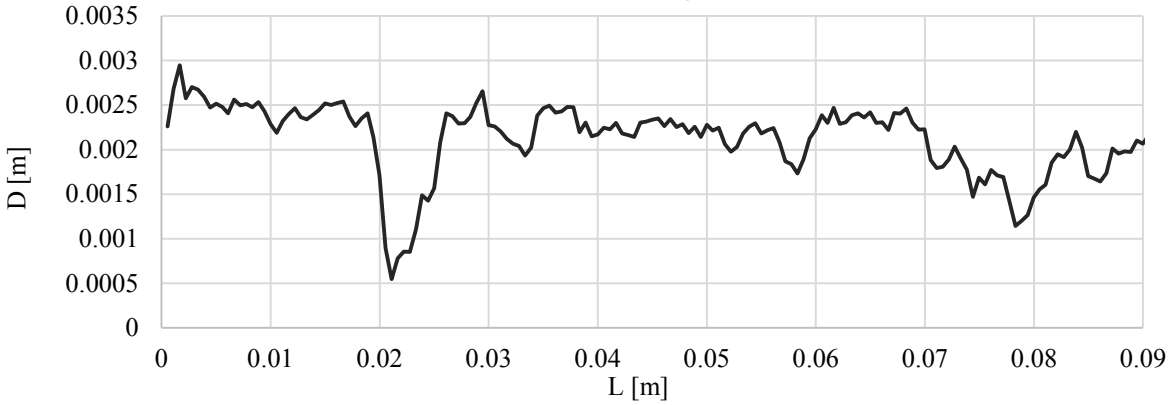

c. Computed flow resistance along the vessel

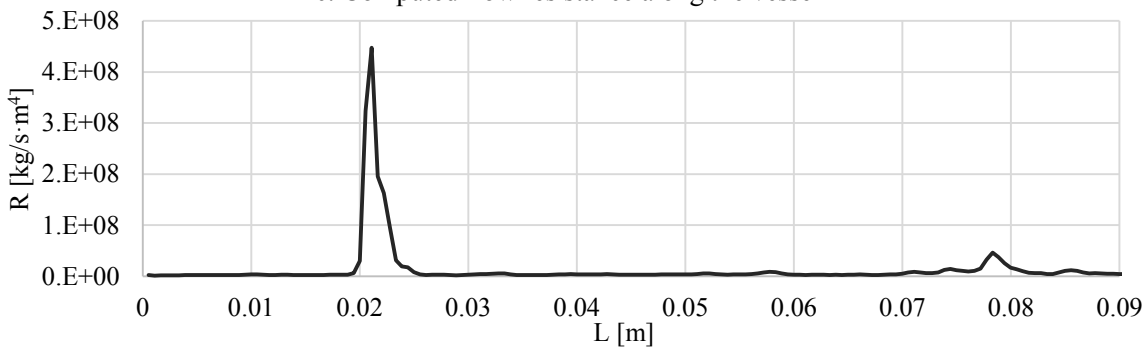

d. Vessel representation in 0D domain as a series of elementary resistance elements

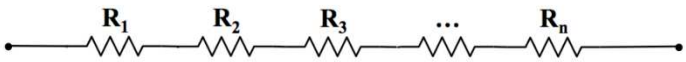

Figure 4.6 Extraction of flow resistance for a single 0D vessel branch model

The peak in the computed flow resistance (Figure 4.6.c) in the stenosis area is explained by the $R \sim D^{-4}$ relation in (4.1). Thus, flow resistance is highly sensitive to the changes in vessel geometry and is a means of detecting the presence of stenosed regions. Next, by assuming that the vessel branch is divided into elementary segments and that the vessel wall is rigid, it can be represented through a series of resistor elements, as shown in Figure 4.6.d.

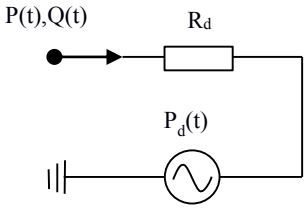

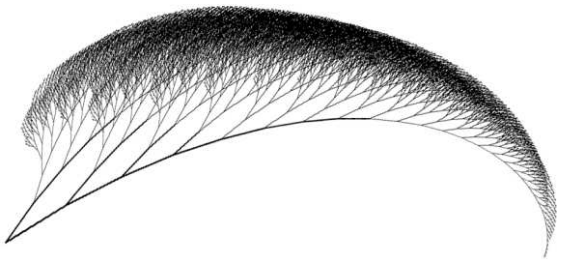

a. Resistance 0D outlet BC model b. idealised 1D tree model

Figure 4.7 0D model of peripheral vasculature for coronary tree outlets

The definition of a 0D blood flow model for an individual vessel represented through a series of n resistors R_i also requires the specification of the flow conditions on the inlet and outlet boundaries as well as the approximation of the value Z_i of the downstream impedance from the peripheral vasculature.

As shown in Figure 4.8, in the case of the terminal coronary artery branch that has to be coupled to the 0D peripheral vasculature (Figure 4.7), the definition of the corresponding 0D blood flow model will include the pressure at the inlet $P_{in}(t)$ from the upstream of the vascular tree and the downstream pressure $P_d(t)$ (representing the impact of LV contraction) coupled after the Z_i and modelled as a simple resistance BC with the resistor value derived from the generated idealised 1D peripheral vascular tree (Section 3.4.3).

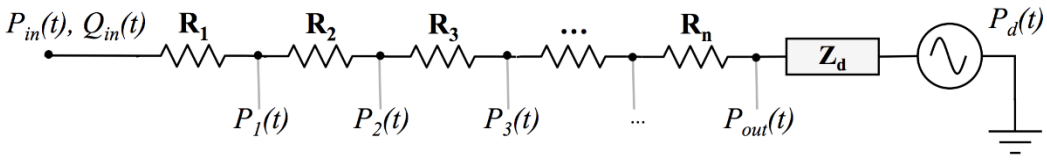

Figure 4.8 0D blood flow model in a single 0D vessel branch model

In this case, the actual 0D blood flow simulation will involve the solution of Ohm's law equation for every segment along the vessel as given in (4.4). The solution outputs are the flow rate at the inlet $Q_{in}(t)$ and the computed pressure after every segment $P^{i}_{out}(t)$:

$$P^{i}_{out}(t) = P_{in}(t) - Q_{in}(t) \cdot \sum_{i} R_i \qquad R_{total} = \sum_{i=1}^{n} R_i$$

$$Q_{in}(t) = \frac{P_{in}(t) - P_d(t)}{(R_{total} + Z)} \tag{4.4}$$

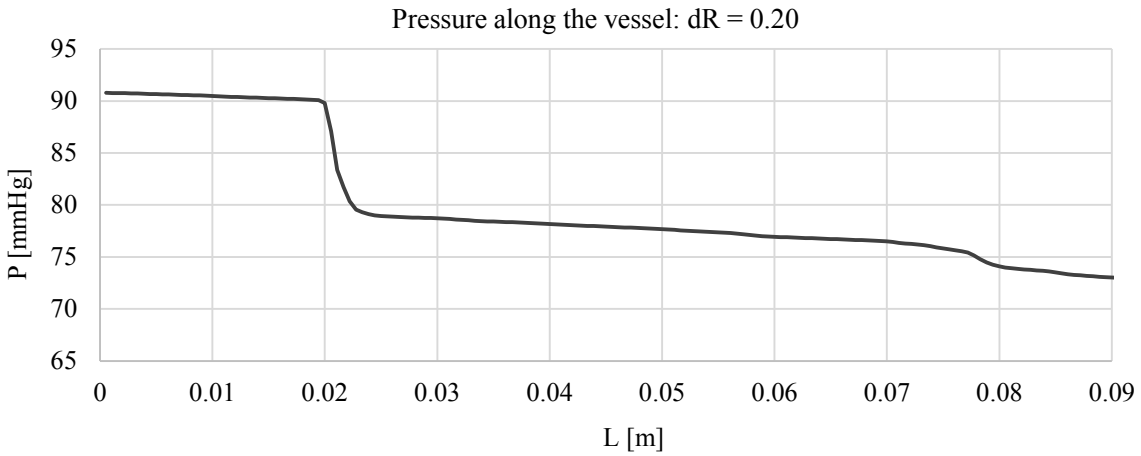

Figure 4.9 Computed pressure along a single 0D vessel branch model

An example of the mean pressure computed along the vessel is presented in Figure 4.9 with a steep pressure drop clearly observed in both stenosed regions. The hyperaemia state required for FFR assessment is simulated by vasodilation of peripheral vasculature in accordance with the approach described in Section 3.4.6.

4.2.2 Arterial tree model

Figures 4.10-11 show an example of a 3D LCA lumen reconstructed from CCTA and its representation in the 0D domain. It has a series of low to medium severity stenoses in the LAD. The red lines indicate how the artery is divided into branches at the bifurcation points based on the localised branches in the extracted centreline tree (Figure 4.3). The LCA is divided into a total of 17 branches of the LMCA, LAD, and LCx, each of which is represented through the R1-17 resistor elements in 0D domain.

In accordance with the proposed approach, each branch of the 3D tree is modelled as a total flow resistance element with the corresponding R distribution values computed from the vessel geometries. In addition, the total branch flow resistance can be expanded into a series of elementary segment resistors, thus providing the detailed information for spatial referencing of the computed flow values (4.1). As mentioned above, while normally 0D vascular models also include C and L elements [89], the present model consists only of resistances due to the specified rigid vessel wall modelling assumption.

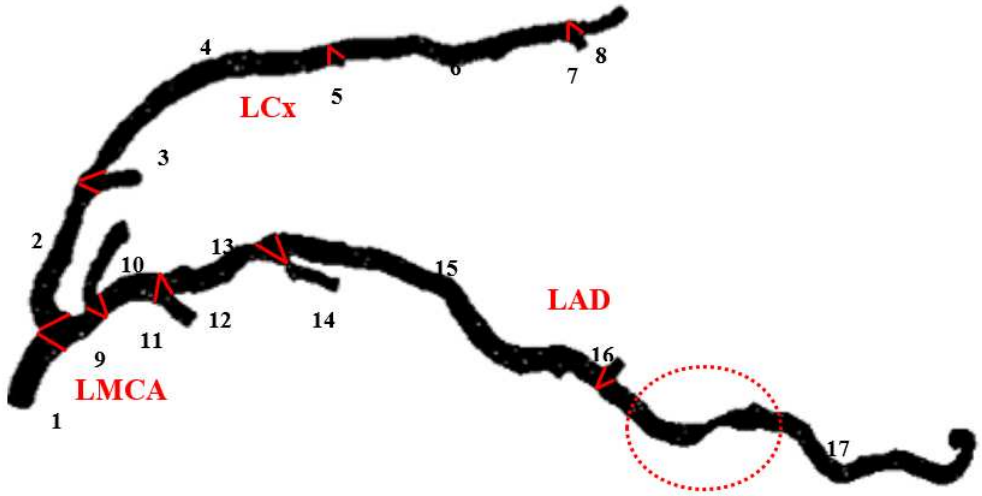

Figure 4.10 3D reconstructed LCA tree divided into branches

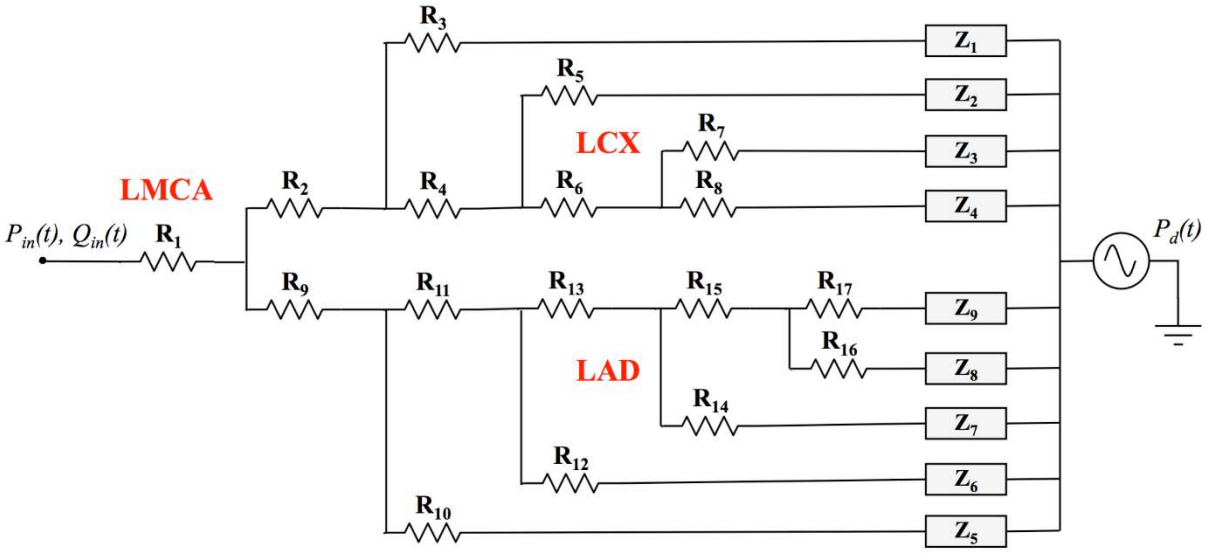

Figure 4.11 0D model of LCA with branches represented as resistance elements

Similarly to the equivalent 3D blood flow model (Section 3.4), the flow boundary condition at the artery tree inlet is assigned as the blood pressure from the root of the aorta $P_{in}(t)$ and the Z_i elements represent the downstream impedance of the peripheral vasculature for each of the branch outlets. The models of the peripheral vasculature are further coupled to the downstream pressure $P_d(t)$ that incorporates the intravascular pressure of the ventricle contraction. Table 4.1 presents the corresponding computed total resistance values R_i for each of the branches (4.1).

It can be observed that the flow resistances of the narrow side branches or the branches with stenosis are several times higher than that of the main branch segments. For instance, the

stenosed branch #17 considered in the previous section has a total resistance of $1.934 \cdot 10^9$ $kg/s \cdot m^4$, which is ten times higher than the rest of the vessel tree.

Table 4.1 Computed 0D resistances of the LCA tree branches

branch #	$R \cdot 10^9$ [kg/s·m^4]		branch #	$R \cdot 10^9$ [kg/s·m^4]		branch #	$R \cdot 10^9$ [kg/s·m^4]
1	0.011		7	0.120		13	0.079
2	0.163		8	0.323		14	0.646
3	0.310		9	0.036		15	0.185
4	0.262		10	0.277		16	0.194
5	0.113		11	0.022		**17**	**1.934**
6	0.257		12	0.055			

Table 4.2 presents the corresponding computed peripheral vasculature resistance values for each of the 9 outlets (see Section 3.4.3). The side branches with narrower outlet diameters have higher flow resistance of peripheral vasculature, thus preserving the required ratio between the flow rate and the outlet diameter.

Table 4.2 Computed 0D peripheral resistance for LCA tree outlets

outlet #	$Z \cdot 10^9$ [kg/s·m^4]		outlet #	$Z \cdot 10^9$ [kg/s·m^4]		outlet #	$Z \cdot 10^9$ [kg/s·m^4]
1	14.218		4	21.556		7	21.701
2	55.912		5	15.513		8	35.664
3	35.866		6	14.943		9	11.232

The blood flow model for this 0D vascular tree can also be easily defined through Ohm's law (4.4), especially when taking into account the absence of the nonlinear impact of C and L elements. However, in this case, the analysis of the computed blood flow will be less convenient with respect to spatial referencing to a specific location in multiple branches (e.g., specification of computed FFR in reference to a stenosis position along a branch). Therefore, it was proposed to implement complex 0D coronary blood flow models as a dynamic system in the MATLAB® Simulink with every branch represented by a separate block and the entire tree incorporated into the CVS loop as described in Section 4.6.

4.3 Incorporation of 0D Coronary Arterial Tree into 0D CVS Model

Due to the patient-specific variations and many interrelated factors between the heart rate, CO and pressure parameters of the CVS, the use of average flow waveforms as boundary conditions might lead to inaccuracies in the computed blood flow and potentially underestimation or overestimation of the FFR patterns. Since invasive measurements of the coronary blood flow are generally not available for blood flow simulation models, these flow

conditions can be generated by a model of the CVS that implements the functionality of the blood circulation system. Lumped parameter modelling is the classical approach for the definition of complex functionality of the integrated CVS components. Generally, CVS models comprise the major blocks of the systemic and pulmonary circulation loops, such as the left atrium and ventricle, the systemic vascular tree, the right heart and pulmonary vascular tree as shown in Figure 4.12 and therefore can approximate haemodynamics at any level of the CVS.

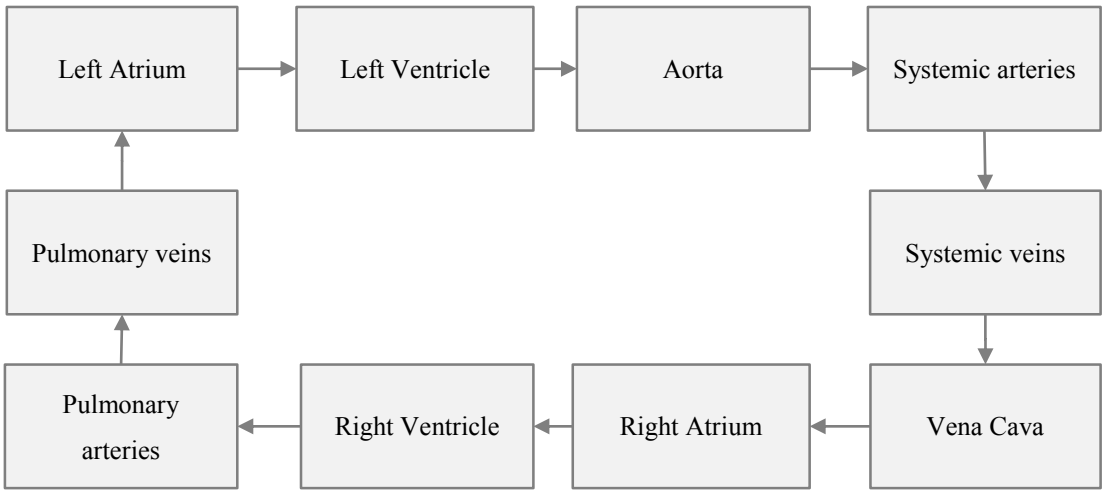

Figure 4.12 Structure of the CVS loop model

Since a 0D CVS model can be easily extended by a more detailed representation of any of its blocks, patient-specific coronary artery models (either 0D or 3D) can be directly incorporated into the 0D coronary circulation loop. This also provides the means for modelling of various physiological conditions and pathologies and analysis of their impact on the coronary blood flow features.

The scheme for incorporation of the coronary arterial tree model into a CVS loop is shown in Figure 4.13. Both coronary arteries originate from the root of the aorta and run along the pericardium surface. Thus, the coronary arterial tree inlet is connected to the root of the aorta 0D element after the aortic valve in the CVS loop. Next, the outlets are followed by the 0D peripheral vascular tree models (Section 3.4.3), which are coupled to the RV through the venous level of the coronary circulation. The impact of intravascular pressure of ventricle contraction is modelled as a pressure source coupled to the terminal level of peripheral vasculature. Either the RV or LV pressure is used depending on the location of the coronary artery.

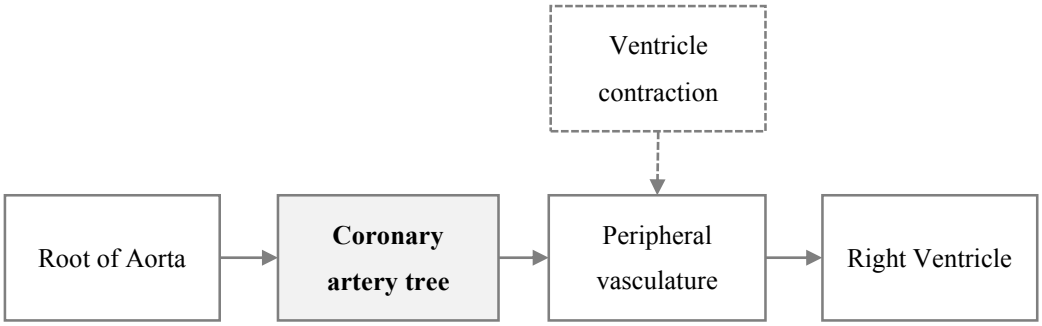

Figure 4.13 Incorporation of the coronary arterial tree model into the CVS loop

In other words, in the case when the 0D coronary tree model is fully incorporated into the CVS loop, the coronary blood flow is directly affected by such parameters as heart rate, CO, etc. These parameters can be defined to replicate a patient-specific case.

While the 0D tree model can be directly integrated into the 0D CVS loop, in the case of 3D modelling, the interpolated waveform of the measured central aortic blood pressure is used as the inlet pressure BC and the LV pressure waveform is coupled to the outlet BC models of the peripheral vasculature (Section 3.4).

4.4 0D Model of the Cardiovascular System

Lumped-parameter CVS models approximate the global characteristics of heart and blood circulation loops and are based on the 0D representation of hydraulic models through resistance, capacitance, inductance, and diode elements, with the corresponding time-varying ODEs governing the blood flow, pressure and volume relationships. They can also be employed to simulate various physiological conditions, including exercise induced changes in heart rate, cardiac output or hyperaemia.

The proposed 0D CVS is based on the classical 0D heart compartment model and the uncontrolled CVS loop model proposed by Rideout [83]. The corresponding electrical circuit of the model is shown in Figure 4.14, comprising of the left ventricle, systemic vascular tree, right ventricle, and pulmonary vascular tree components. The left heart (LH) model extending the basic 0D heart compartment model consists of the left atrial resistance R_{LA}, compliance C_{LA} and atrio-ventricular inertia $L_{LA,}$ connected though the mitral valve-diode to the left ventricular resistance R_{LV} and varying compliance $C_{LV}(t)$ that defines the ventricle contractility followed by the ventriculo-arterial valvular flow resistance R_{AW}. The systemic and pulmonary tree functional levels are modelled through a series of Windkessel models with the 0D

parameter values representing their respective physical properties. For instance, the 3-element Windkessel with the R_{A1}, C_{A1} and L_{A1} elements define the function of the A1 level of the arterial system, including the aorta and large arteries, while the 2-element Windkessel models of the A2 and A3 levels represent the arterial branches followed by microcirculation. The structure of the 0D models of the systemic and pulmonary circulation loops is identical, however, operating at low pressures, the right heart (RH) model is characterised by a lower flow resistance of the vascular tree and higher RA compliance values in order to accommodate the same blood flow volume per unit time as the systemic circulation loop.

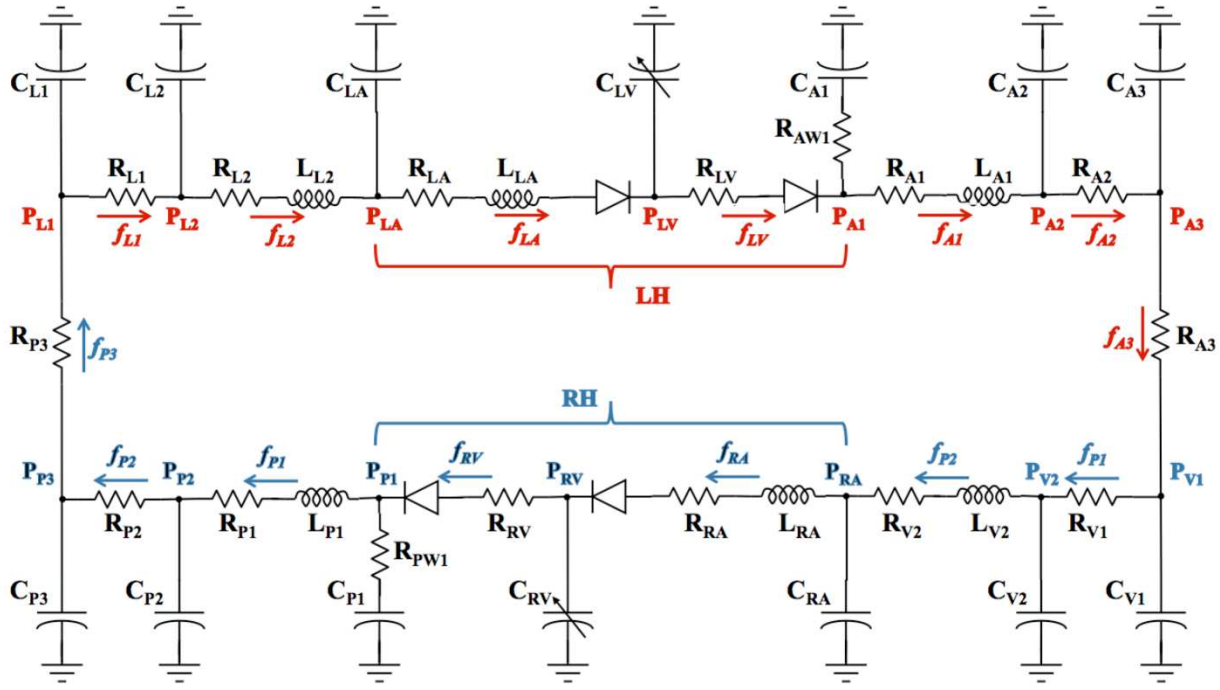

Figure 4.14 Electrical circuit representation of a 0D CVS model

The relaxation, filling, contraction and ejection phases of the heart cycle are simulated with time-varying elastance functions for $C_{LV}(t) = 1/E_{LV}(t)$ and $C_{RV}(t) = E_{RV}(t)$ in the 0D elements defining the ventricular blood pressure-volume relationship in time. In order to achieve physiologically realistic blood flow waveforms, in the proposed model, the ventricular elastance functions were derived from the LV and RV pressure-volume loops interpolated from average interpatient values [142]. Trigonometric polynomial interpolation was employed to preserve the periodic nature of the function and allow dynamic adjustment of the ventricle contractility function characteristics and heart rate.

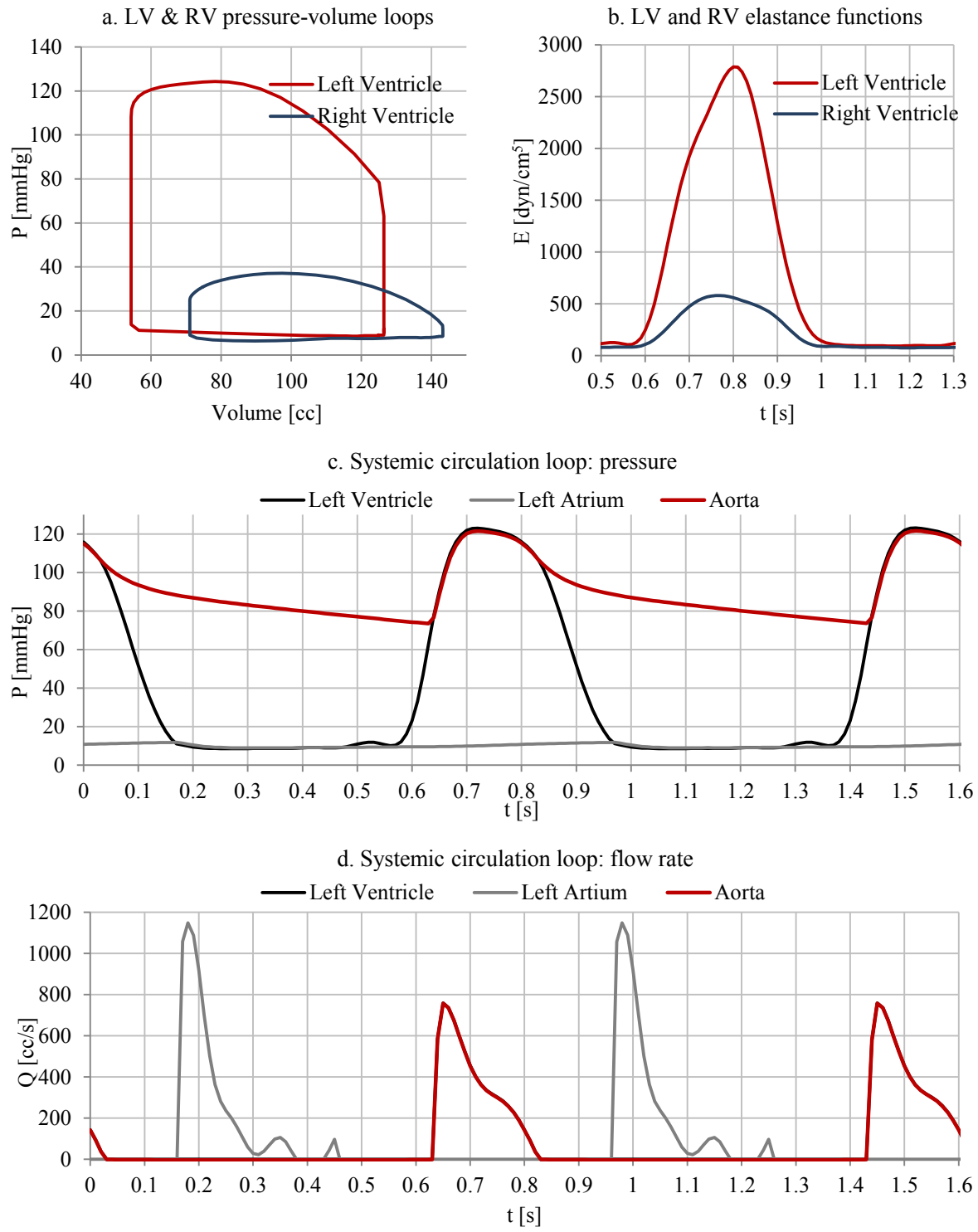

Figure 4.15 Haemodynamic characteristics of the implemented 0D CVS model

The main input parameter of the model is the heart rate (HR) which controls the CVS functionality in the time domain through the ventricle elastance function:

$$E(t)=A_0+E_{max}\cdot(A_1\cdot\sin(2\cdot\pi\cdot w\cdot t)+B_1\cdot\cos(2\cdot\pi\cdot w\cdot t)+A_2\cdot\sin(2\cdot\pi\cdot 2\cdot w\cdot t)+$$
$$+B_2\cdot\cos(2\cdot\pi\cdot 2\cdot w\cdot t)+A_3\cdot\sin(2\cdot\pi\cdot 3\cdot w\cdot t)+B_3\cdot\cos(2\cdot\pi\cdot 3\cdot w\cdot t)+ \quad (4.5)$$

$$A_3 \cdot \sin(2\cdot\pi\cdot3\cdot w\cdot t) + B_3 \cdot \cos(2\cdot\pi\cdot3\cdot w\cdot t) + A_4 \cdot \sin(2\cdot\pi\cdot4\cdot w\cdot t) + B_4 \cdot \cos(2\cdot\pi\cdot4\cdot w\cdot t) +$$
$$+A_5 \cdot \sin(2\cdot\pi\cdot5\cdot w\cdot t) + B_5 \cdot \cos(2\cdot\pi\cdot5\cdot w\cdot t) + A_6 \cdot \sin(2\cdot\pi\cdot6\cdot w\cdot t) + B_6 \cdot \cos(2\cdot\pi\cdot6\cdot w\cdot t) +$$
$$+A_7 \cdot \sin(2\cdot\pi\cdot7\cdot w\cdot t) + B_7 \cdot \cos(2\cdot\pi\cdot7\cdot w\cdot t),$$

where A_i and B_i are the interpolation coefficients, the frequency w_0 is adjusted with respect to the heart rate as $w_0 = w\cdot60/HR$, w is the frequency of the interpolated function, t is the simulation time, and E_{max} is the scaling parameter for additional adjustment of the strength of ventricle contraction (e.g., in the case of modelling of myocardial infarction).

In addition, the model is extended with the baroreflex mechanism for the external control of the system parameters, such as ventricle elastance and the systemic artery tree resistance [83].

An example of the CVS simulation results is given in Figures 4.15.a-b with the elastance functions and pressure-volume loops for the left and right ventricle models under the resting physiological condition. The corresponding heart rate is 75 beat/min (0.8 heart pulse duration) and the values of the cardiac output (CO) and stroke volume (SV) parameters correspond to the CVS circulation characteristics of a healthy adult [1,2,83]. The CO derived from the LV pressure-volume loop is 5.5 L/min with the SV being 73 ml and 57% ejection fraction.

The choice of the numerical values of the 0D model parameters is defined by the various physical parameters of the hemodynamic system. Apart from the elastance function, the identified optimal 0D circuit element values given in Table 4.3 are mainly based on the parameters from the models proposed by Rideout and Heldt [83,141,143]. Some of the essential outputs of the implemented 0D CVS model including the pressure and flow rate in the left atrium, ventricle and aorta are shown in Figure 4.15.c with the corresponding amplitude values and shape characteristics lying within the physiological range of the CVS hemodynamics of a healthy subject [1,2].

Table 4.3 0D CVS loop parameters as per the 0D CVS electrical circuit in Figure 4.14

Suffix	**Anatomy**	**Resistance R [g/s·cm^4]**	**Inertance L [cm^4·s^2/g]**	**Compliance C 10^6 · [g/s^2·cm^4]**
P1	Pulmonary Arteries 1	10	1	100
P2	Pulmonary Arteries 2	40	-	300
P3	Pulmonary Arteries 3	80	-	2700
L1	Pulmonary Veins 1	30	-	1000
L2	Pulmonary Veins 2	10	1	1000
LA	Left Atrium	5	1	11760

LV	Left Ventricle	5	1	variable
A1	Systemic Arteries 1	10	1	180
A2	Systemic Arteries 2	160	-	230
A3	Systemic Arteries 3	1000	-	1820
V1	Systemic Veins 1	90	-	21000
V2	Systemic Veins 2	10	1	45000
RA	Right Atrium	5	1	45000
RV	Right Ventricle	5	1	variable

4.5 Modelling assumptions

A classical 0D vessel blood flow model is defined through the application of electrical–hydraulic system analogy. The flow rate and pressure are represented through the current and voltage variables and the vascular geometry hydraulic components are defined with their electrical equivalents.

As previously mentioned, the main aim of this research is the development of a novel spatially extended 0D blood flow modelling approach for computation of virtual FFR in patient-specific coronary arteries. Taking into account the fact that the implemented 0D model has to be comparable with its 3D equivalent model for validation purposes, many of the specified 3D modelling assumptions (Section 3.3) have to be adopted in the equivalent 0D model. The following list summarises the modelling assumptions and requirements identified as appropriate for this research:

- Blood is assumed to be a Newtonian fluid with average values for density of 1060 kg/m^3 and dynamic viscosity of $3.5 \cdot 10^{-3}$ kg/m·s [130]. Blood flow is assumed incompressible and laminar. Vessel wall is assumed to be rigid (non-deformable) and immovable under the impact of ventricle contraction. Consequently, only the resistance elements are used in the 0D representation of vascular geometries.
- The 0D model is incorporated into the 0D blood circulation loop based on the classical CVS model [83,141] that generates cardiovascular haemodynamics within the average physiological value range corresponding to a healthy adult.
- The coronary tree inlet is coupled to the root of the aorta of the 0D CVS model. The 0D BC models coupled to the outlets replicate the models of peripheral resistance used in the 3D blood flow models including the R, RCR, and RCRCR models (Section 3.4.2) together with the method for approximation of peripheral vascular resistance and compliance values.

Hyperaemia in the coronary arteries is modelled by vasodilation of the peripheral vasculature models to 0.2-0.25 of the resting state resistance [44,138].

At the next step, the defined 0D coronary blood flow model incorporated into the CVS loop is implemented in Simulink for modelling of electromechanical and electrical systems. The model implemented through the elements of SimElectronics® library. The settings for the numerical solution of the system of PDEs defining the haemodynamics of the CVS are described in Section 4.6.

4.6 Implementation of 0D Coronary Blood Flow Model

The 0D model of the CVS loop with the incorporated coronary arterial tree defined in Sections 4.2-4 was implemented in MATLAB® Simulink based on the SimElectronics toolbox elements. A specific 0D blood flow modelling library consisting of individual blocks representing the essential CVS elements was developed following the modelling approach originally proposed by Barnea [86]. The advantage of using a graphical modelling environment and representing the CVS through interconnected blocks instead of the classical modelling approach describing the CVS functionality through a system of PDEs [83] is that it provides direct control over the individual system components and allows for straightforward connections between the elements transferring pressure and flow data. It is especially convenient in the case of varying structures of patient-specific 0D coronary artery models that can be easily extended with an additional vessel branch block.

During the model implementation process, the elastance function defining the left ventricle contraction formed the basis of the implemented model, which was further extended with the rest of the CVS model components. Next, the patient-specific 0D coronary arterial tree model was incorporated into the CVS loop in accordance with the coronary circulation loop physiology (Section 4.3). The resulting model consists of more than 50 blocks constructed from more than 200 basic SimElectronics toolbox elements. The implemented 0D library includes the models of heart ventricle and atrium, valves, RLC, RC and R 0D vascular trees, 0D BC peripheral vasculature, baroreflex and ANS (Autonomic Nervous System) control mechanisms, SN (Sinoatrial Node) pulse generator, Ventricular Pressure Generator (VPG), and additional pressure and flow measurement blocks. The description of these elements is presented in Section 4.6.1.

The diagram of the implemented 0D CVS loop model extended with the patient specific coronary arterial tree is given in Figure 4.16. The connectors between the elements represent the blood flow transfer. Beginning from the left atrium (LA) the oxygenated blood flow through the mitral valve (diode) to the left ventricle (LV), which is the central part of the system since it defines the pulsatile nature of the blood circulation. The LV contraction mechanism is defined through the elastance function (Elastance LV), which is one of the inputs of the LV. Next, under the pressure of LV contraction, the blood is pumped through the aortic valve to the aorta (A1) and the rest of the systemic arterial tree (A2-A4). Through the capillary bed incorporated into the A4 element, the blood flows into the systemic venous tree (V1-V2) and to the right atrium (RA). The deoxygenated blood is transferred to the right ventricle (RV) through the tricuspid valve. Next, the blood is pumped into the pulmonary arterial tree (P1-P3) through the pulmonary valve. From the pulmonary venous tree (L1-L2) the oxygenated blood flows into the left atrium (LA). The pulse generation controlling the elastance function (4.5) is performed in the sinoatrial node (SA) element, which generates the sawtooth wave signal defining the duration of a heart cycle with respect to the set HR value. The ANS block controls the short-term vasodilation/vasoconstriction of systemic arterial tree with respect to the changes in the AP detected by the baroreceptor element (BaroReceptor). The input of the 0D coronary artery element is connected to the root of the aorta element (A1) and the output in the form of the total coronary flow rate is coupled to the right atrium (RA). In accordance with the definition formalised in Section 4.2.2, the 0D blood flow model for the left coronary artery was represented through the resistance elements and simple resistance 0D downstream BC models, as shown in Figure 4.17. Each of the 17 branches were represented through the R1-17 “Artery” 0D element (Figure 4.21) with the resistance values derived from the 3D lumen dimensions (Table 4.1). In this particular case, simple resistance 0D R BC models were assigned to the nine outlets ($Z_{out1} - Z_{out9}$). The vasodilation/vasoconstriction is controlled from the ANS 1 input through the scaling of the resistance. The mechanism for local simulation of hyperaemia is implemented through the user-defined vasodilation degree of peripheral vascular resistance at the ANS 2. The impact of the myocardial contraction of the coronary arteries is modelled in the CVS VPG block as scaled LV pressure (or RV pressure in the case of RCA) and assigned as the input to the coronary artery element. The flow rate and pressure are measured at the outlets of every branch with the PressureMeter and FlowMeter elements and stored in the corresponding files for further processing.

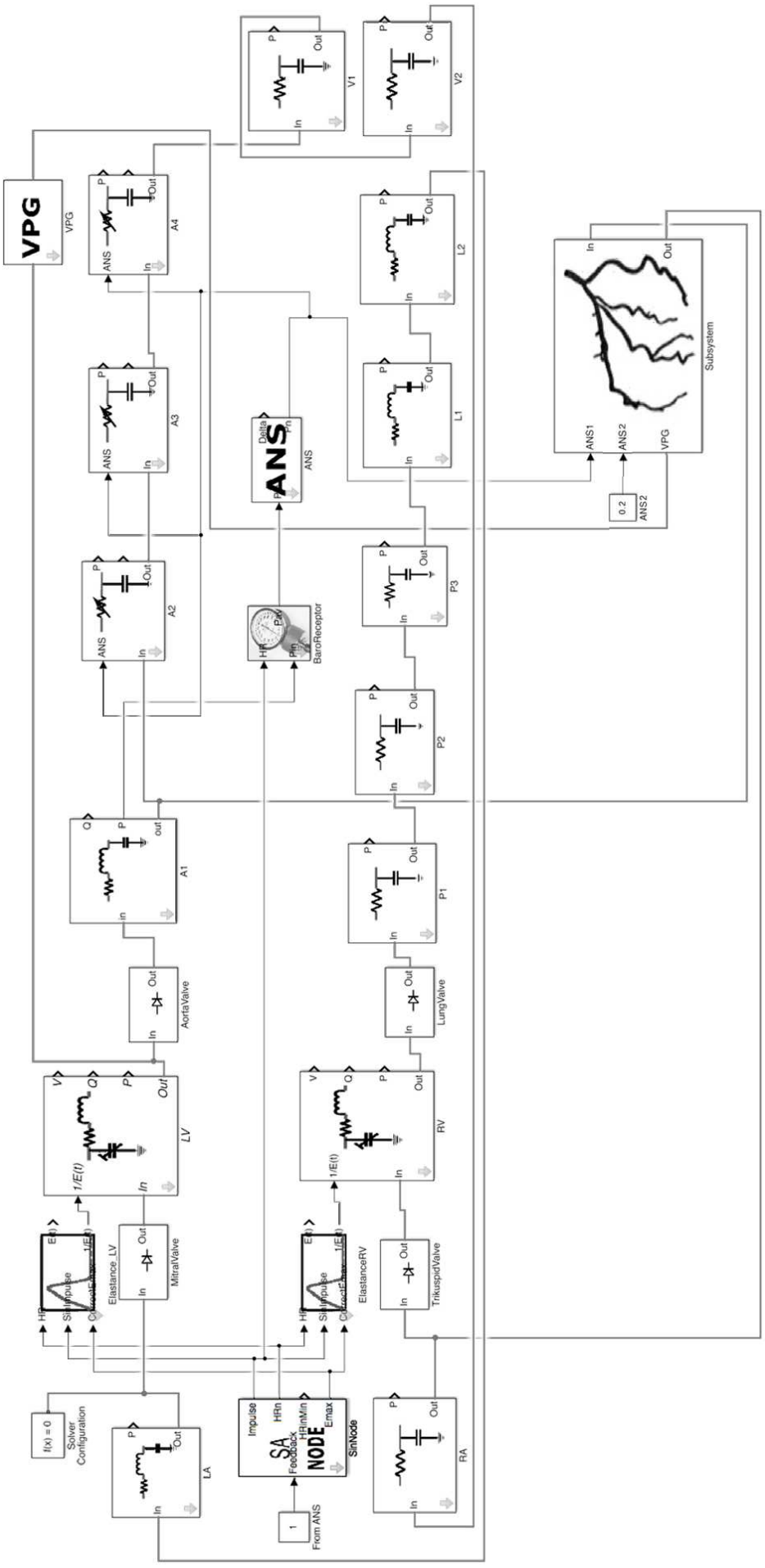

Figure 4.16 0D model of the CVS implemented in MATLAB® Simulink

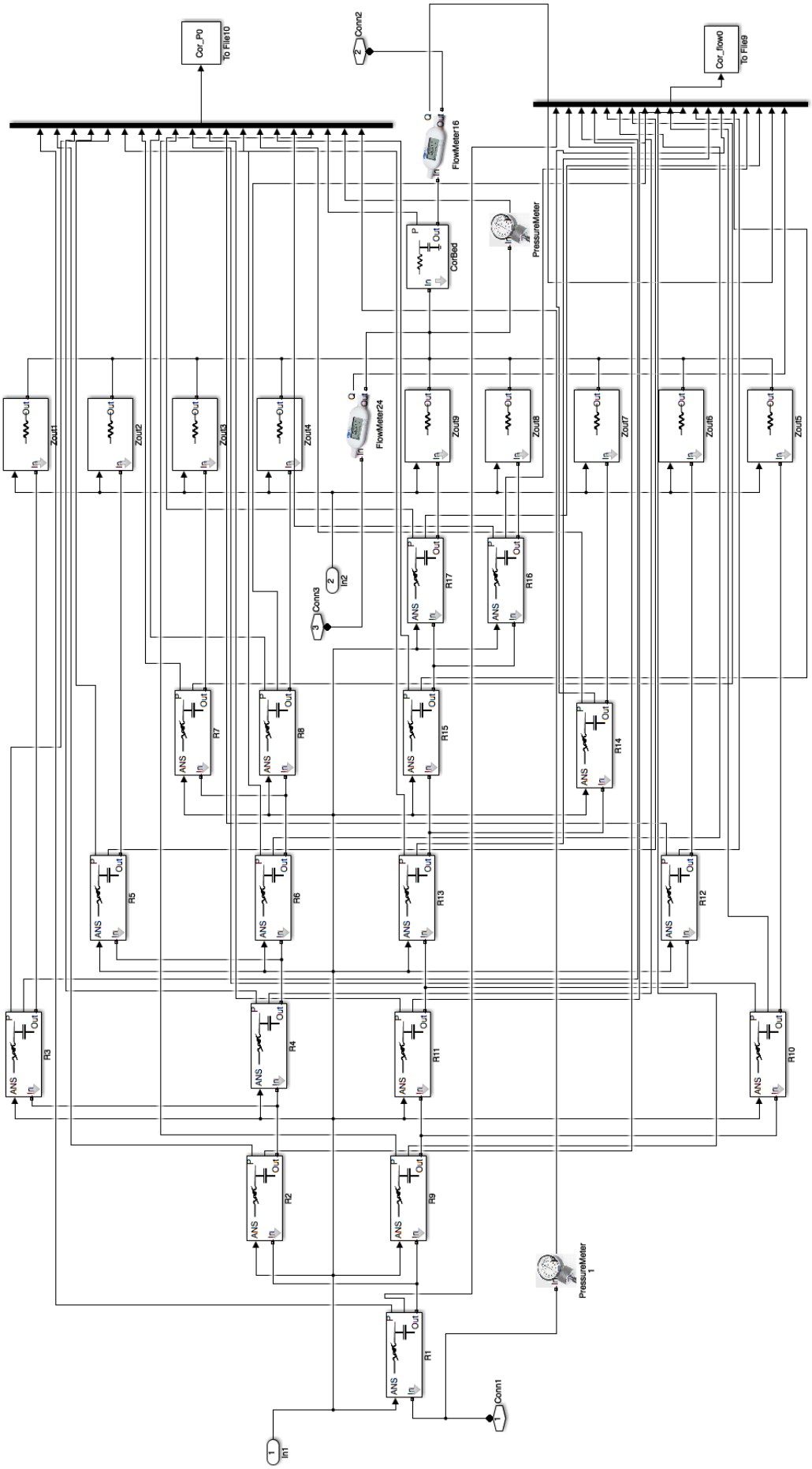

Figure 4.17 0D model of the LCA tree implemented in MATLAB® Simulink

4.6.1 0D CVS Library Components

As mentioned above, the structure and function of the implemented CVS elements is based on the original 0D CVS loop model from [83] with the identified optimal parameter values given in Table 4.3. It is further extended with the set of element for modeling the individual vessel branches and coronary artery tree.

The model of the left ventricle shown in Figure 4.18 is based on the RLC circuit with a variable capacitor controlled with the ventricle stiffness function.

<u>0D Left Ventricle model</u>

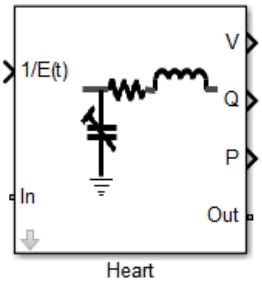

<u>Inputs:</u>

- 1/E(t): control signal Stiffness
- In: input blood flow

<u>Outputs:</u>

- V: blood volume integral signal [ml]
- Q: measured flow rate [cc/s]
- P: measured pressure [mmHg]
- Out: output blood flow

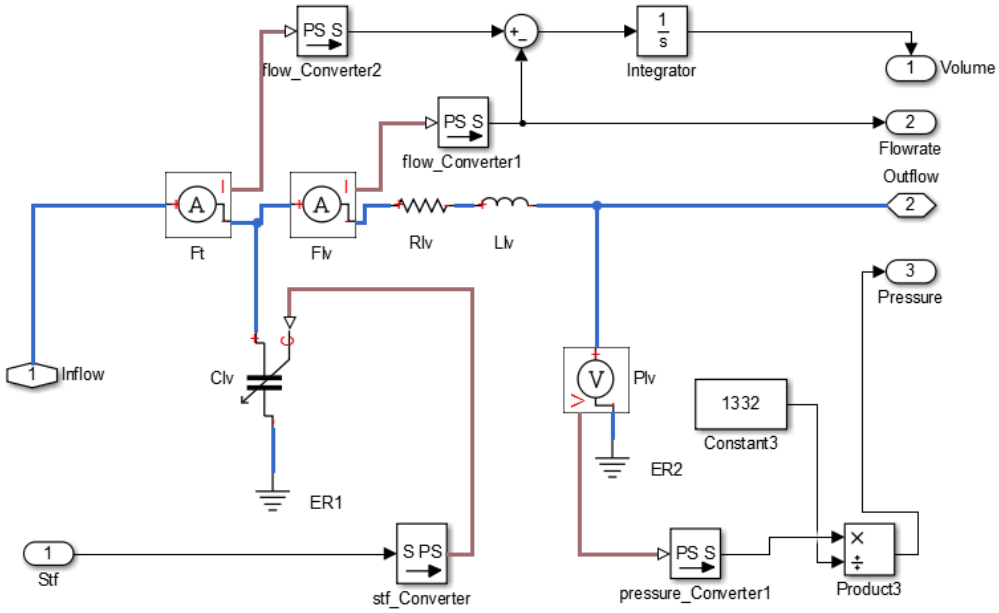

Figure 4.18 0D model of the "Left Ventricle" element implemented in MATLAB® Simulink

The input blood flow signal form the left atrium at the inlet "Inflow" ("In") is measured by the ammeter "F_t". The signal representing ventricular stiffness inversely proportional to the ventricle elastance function (C(t) = 1/E(t)) is measured at the input "1/E(t)". It is applied to the variable capacitor C_{lv}, which defines the ventricular pressure as P(t) =

$E(t)\cdot(V(t)-V_0)$, where $V(t)$ is the ventricular volume and V_0 is is a constant correction volume, which is recovered when the ventricle is unloaded. Next, the blood flows though the resistor R_{lv} and inductor L_{lv} to the "Outflow" output. After the L_{lv} block, the blood pressure is measured by the voltmeter P_{lv} and is divided by 1332 constant in order to convert the units from [V] to [mmHg] and assigned to the output "Pressure" ("P"). The ventricular volume is computed as $V(t) = \int (F_t - F_{lv})\cdot dt$, where F_t and F_{lv} are the flow values measured by the ammeters F_t and F_{lv} at the inlet and after the C_{lv} capacitor. The measured blood volume is then assigned to the "Volume" outlet ("V") and is used for CO calculation and plotting of the Pressure-Volume loop. The flow rate measured by the ammeter F_{lv} is assigned to the "Flowrate" outlet ("Q"). The PS-S converters "flow_Converter" and "pressure_Converter" are used for conversion of a physical signal into a MATLAB® Simulink output signal.

The waveforms of the corresponding LV elastance and stiffness functions are generated in the "Elastance" block shown in Figure 4.19, which implements the 7th order Fourier polynomial defined in (4.5). The inputs that control the E(t) function are the heart rate HR and impulse from the sinoatrial node indicating beginning of a heartbeat. The "CorrectEmax" parameter for scaling of E(t) providing means for simulation of such pathologies as myocardial infarction corresponding to lower elastance magnitude.

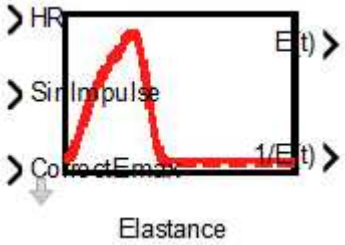

Inputs:

- HR: heart rate
- SNimpulse: sinoatrial node impulse
- CorrectEmax: scaling of elastance

Outputs:

- E(t): ventricular elastance
- 1/E(t): ventricular stiffness

Figure 4.19 0D model of the "Elastance" element implemented in MATLAB® Simulink

Next, Figure 4.20 present the model of the aorta element based on the WK RLC circuit. At the inlet "Inflow", the blood flow rate is measured by an ammeter element "Fao" and is then assigned to the output "Flowrate" ("Q") through the "flow_Converter". Next, the blood flows through the RLC circuit with resistance "Rao", inductance "Lao" and "Cao" elements to the output "Outflow" ("Out"). The capacitor "Cao" is connected between the main inlet and the electrical reference port "ER1". Measurement of the pressure after the circuit is

performed by the voltmeter "Pao". The measured pressure is then divided by 1332 constant in order to convert the units from [V] to [mmHg] and assigned to the output "Pressure" (“P”).

0D Aorta model

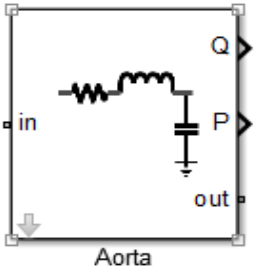

Inputs:

- In: input blood flow

Outputs:

- Q: measured flow rate [cc/s]
- P: measured pressure [mmHg]
- Out: output blood flow

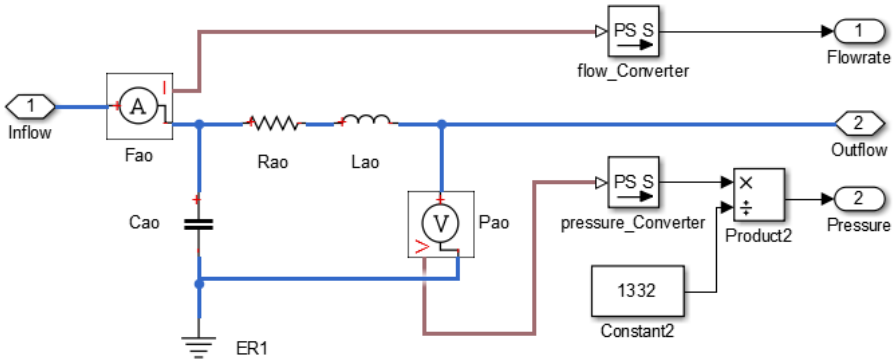

Figure 4.20 0D model of the “Aorta” element implemented in MATLAB® Simulink

The 0D Artery element used for modelling of the segments of the systemic arterial tree is based on the 2-element RC WK model with varying resistance. As can be seen in Figure 4.21, the general structure is similar to the Aorta element except for the varying resistor Ra with the resistance value controlled by the signal from the ANS block through the scaling of the default value. It can be used for simulation of either vasodilation or vasoconstriction in response to the baroreflex signal. The inputs of the block include the inlet blood flow “In” and the “ANS” signal. The outputs are the outlet flow rate “Out” and the measured pressure and flow rate “P” and “Q”.

0D Artery model

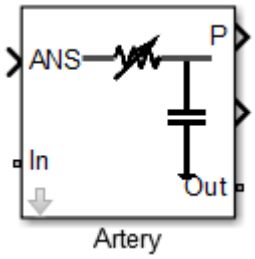

Inputs:

- In: input blood flow
- ANS: signal from the ANS block

Outputs:

- P: measured pressure [mmHg]
- Q: measured flow rate [cc/s]
- Out: output blood flow

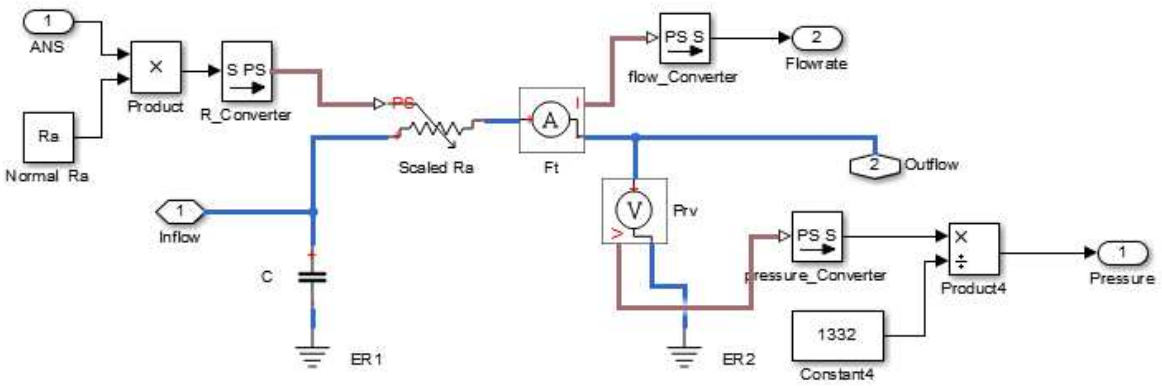

Figure 4.21 0D model of the "Artery" element implemented in MATLAB® Simulink

Similarly, the elements of the venous tree are represented as 2-element RC WK with the difference that their resistance is static and not controlled by the ANS, since venous resistance is not significantly altered under various physiological conditions. It has one input for the inlet blood flow "In" and three outputs including the outlet blood flow "Out" and the measured pressure and flow rate "P" and "Q" (Figure 4.22).

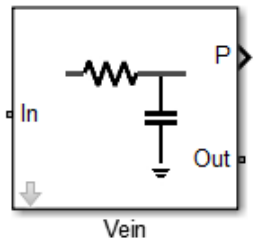

0D Vein model

Inputs:

- In: input blood flow

Outputs:

- P: measured pressure [mmHg]
- Q: measured flow rate [cc/s]
- Out: output blood flow

Figure 4.22 0D model of the "Vein" element implemented in MATLAB® Simulink

As shown in Figure 4.23, the element representing the 0D model of the left coronary arterial tree (see the scheme in Figure 4.17) has four inputs including: "In", "ANS 1" representing the standard signal from ANS for regulation of the CVS function, "ANS 2" used defined signal representing the degree of vasodilation the peripheral vasculature for simulation of hyperaemia, and "VPG" extravascular pressure of LV contraction. Since the coronary artery has multiple outlets, which are merged into the capillary bed, there is only one output "Out" representing the total coronary flow and the simulation results in terms of the coronary pressure and flow rate measured at the individual branches are stored in the output files for further processing. The individual vessel tree branches of the LCA tree are implemented through the "Artery" elements.

0D Left Coronary Artery model

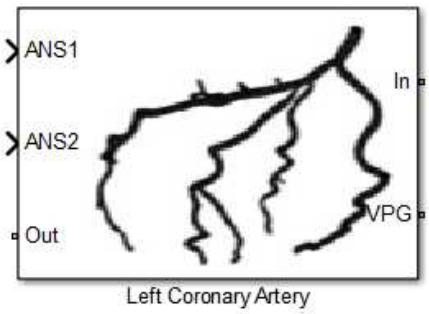

Inputs:

- In: input blood flow
- ANS 1: signal from the ANS block
- ANS 2: user defined degree of vasodilation the downstream vasculature for simulation of hyperaemia
- VPG: extravascular pressure of LV contraction

Outputs:

- P: measured pressure [mmHg]
- Q: measured flow rate [cc/s]
- Out: output blood flow

Figure 4.23 0D model of the "LAD" element implemented in MATLAB® Simulink

The 0D R, RCR and RCRCR models of the peripheral coronary vasculature for the individual outlets have the similar set of inlet/outlets with the difference in the electrical circuit structure and the approach for incorporation of the "VPG" extravascular pressure of LV contraction.

0D R peripheral coronary vasculature model

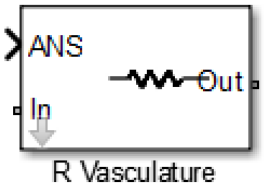

Inputs:

- In: input blood flow
- ANS: combined signal from the ANS block and user defined peripheral vasodilation degree

Outputs:

- P: measured pressure [mmHg]
- Out: output blood flow

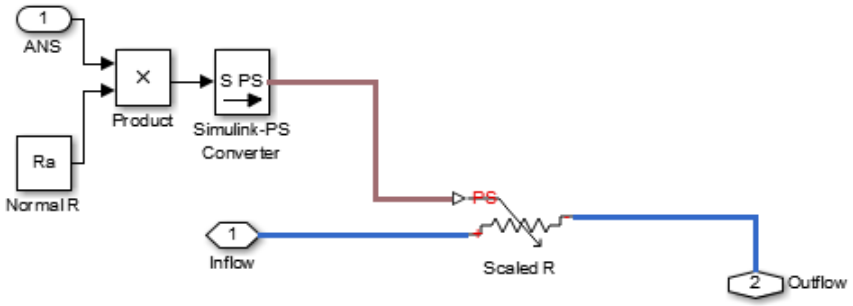

Figure 4.24 0D model of the "R peripheral coronary vasculature" element implemented in MATLAB® Simulink

Figure 4.24 shows the implemented simple 0D R model. If this type of BC model is used, the VPG pressure is connected directly into the merging point of the peripheral vasculature models for all branches (see Figure 4.17). The element inputs include the inlet

blood flow "In", the "ANS" combined signal from the ANS block and the user defined peripheral vasodilation degree. The output is the outlet blood flow "Out". The peripheral resistance R is scaled by the ANS signal. As can be seen in Figure 4.26, in the case of the 0D RCRCR model, the scaled "VPG" pressure of the myocardium contraction is coupled to the circuit through the C_{im} capacitor (the corresponding derived resistance and capacitance values together with the algorithm for their assessment can be found in Section 3.4.3). The resistances R_a and R_{am} are controlled by the ANS signal.

0D RCRCR peripheral coronary vasculature model

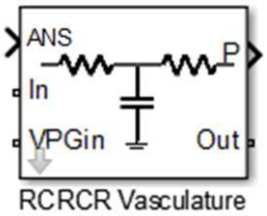

Inputs:

- In: input blood flow
- ANS: combined signal from the ANS block and user defined peripheral vasodilation degree
- VPG: extravascular pressure of LV contraction

Outputs:

- P: measured pressure [mmHg]
- Out: output blood flow

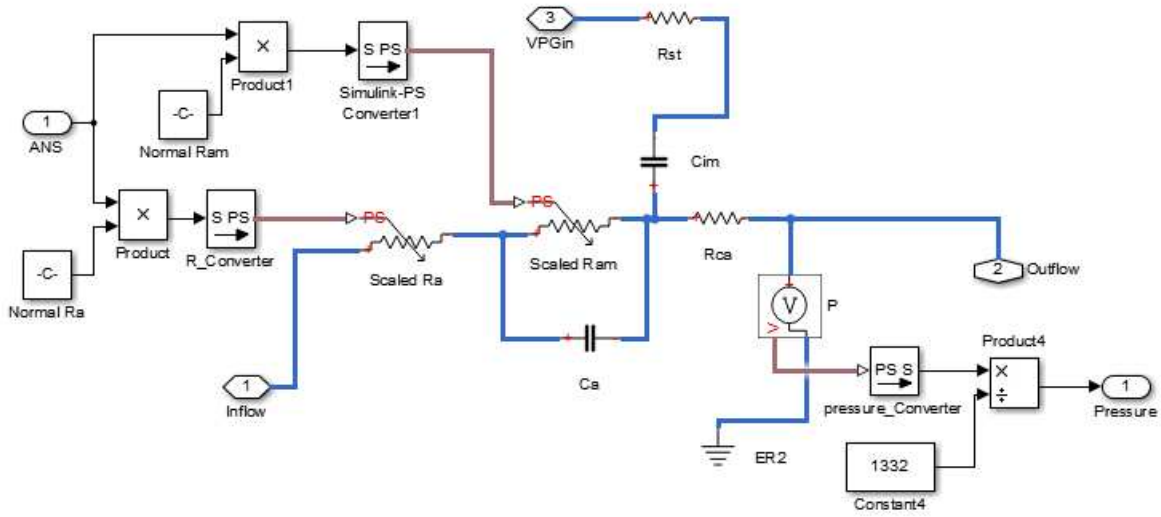

Figure 4.25 0D model of the "RCRCR peripheral coronary vasculature" element implemented in MATLAB® Simulink

4.6.2 0D Blood Flow Simulation

In MATLAB® Simulink, every implemented block in the library is defined through the system of PDEs with the blood flow simulation involving the numerical solution of the global system. The standard ode23t solver settings were chosen as optimal for this problem domain. Normally, a 0D blood flow simulation for 30 heart cycles with a 0.01s timestep does

not take more than 2 minutes on a standard workstation, while if the objective was simulations of higher accuracy for 200 heart cycles would not exceed a run time of 15 minutes.

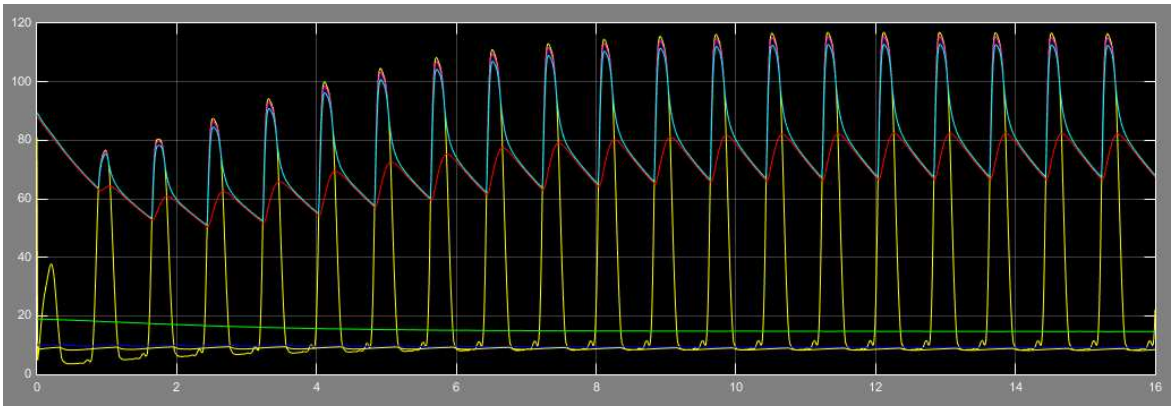

Figure 4.26 Real-time monitoring of the computed systemic loop blood pressure during 0D blood flow simulation

In addition, the MATLAB® Simulink functionality provides the means for monitoring and analysis of the block outputs during the transient simulations. An example of a systemic circulation loop pressure monitor is given in Figure 4.26. It also can be observed that the convergence of the solution with respect to the stabilisation of 0D CVS blood circulation took approximately 10 s (e.g., 13 heart cycles). The simulation results in the form of flow rate and pressure after every block are stored in files, which are used for further analysis of the results and extraction of haemodynamic parameters such as FFR (Section 4.7).

4.7 Extraction and Analysis of the Computed Blood Flow Fields

As already mentioned in Section 3.5, the results of blood flow simulations are generally analysed for evaluation of changes in haemodynamic variables in response to variations in vascular geometries, such as atherosclerotic plaques, aneurisms, and stents. In 0D domain, the computed blood flow variables include only pressure, volume, flow rate, and FFR.

In the proposed modelling approach, the simulation results are visualised as waveforms of the computed blood flow measured either at the inlet and outlet boundaries or along a specific vessel branch. For instance, Figure 4.27 demonstrates the simulation results for the 0D blood flow LCA model defined in Section 4.2.2 (Figures 4.10-11) under hyperaemia including flow rate, pressure, flow distribution between the outlets and FFR for two heart cycles. It can be observed, that the FFR at the outlet # 9 of the stenosed branch is considerably lower than the rest of the coronary tree with an average value of 0.76 being on the border of the critical 0.75 threshold. The spatial distribution of the computed FFR along the

corresponding stenosed branch # 17 is given in Figure 4.28. In addition, the 0D CVS model also provides information on the global CVS characteristics such as systemic pressure and flow rate (e.g., LV pressure and flow rate shown in Figure 4.15) for the specified input values such as CO and SV defining the global circulation of the CVS loop.

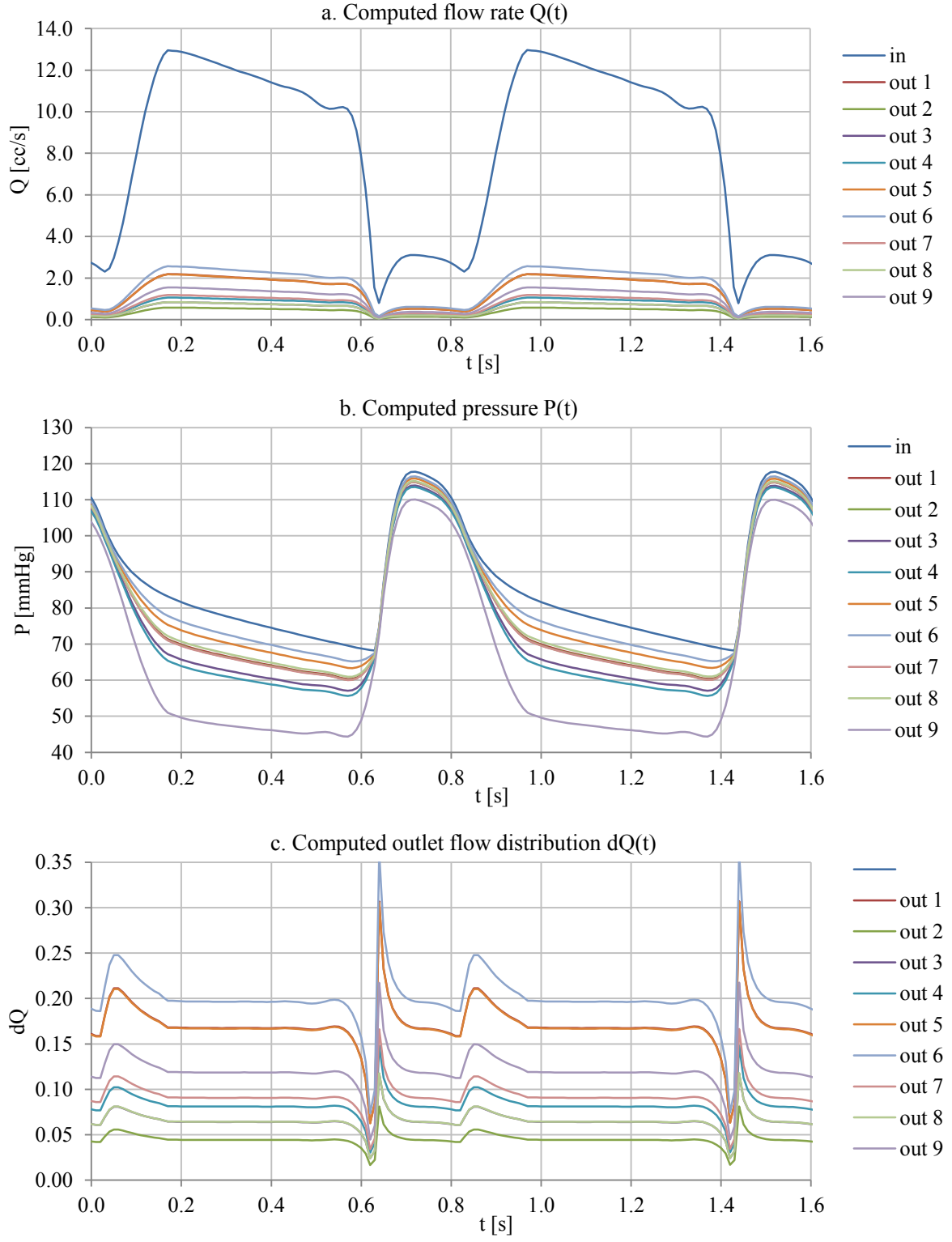

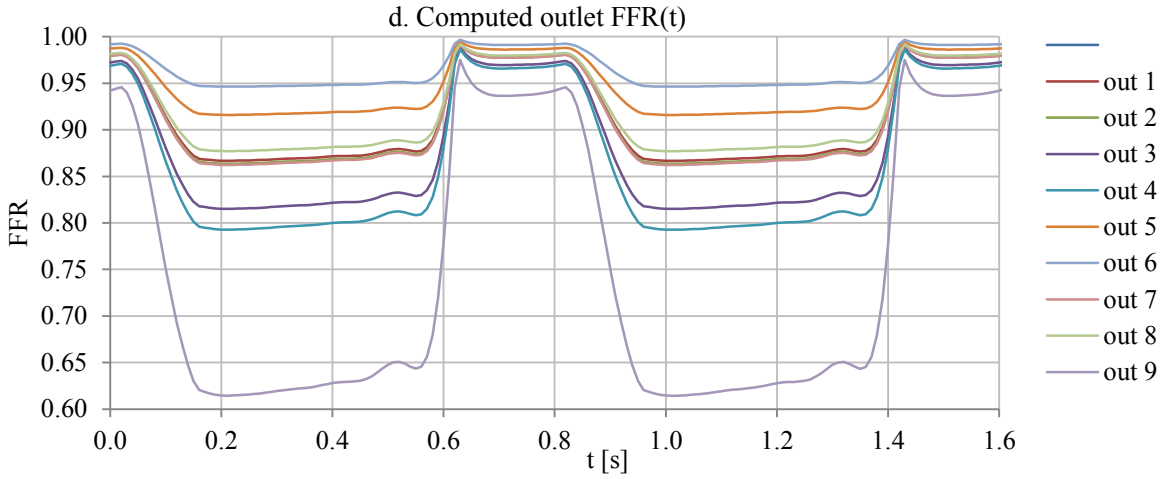

Figure 4.27 Waveforms of the computed blood flow at the inlet and outlet boundaries of the 0D LCA model

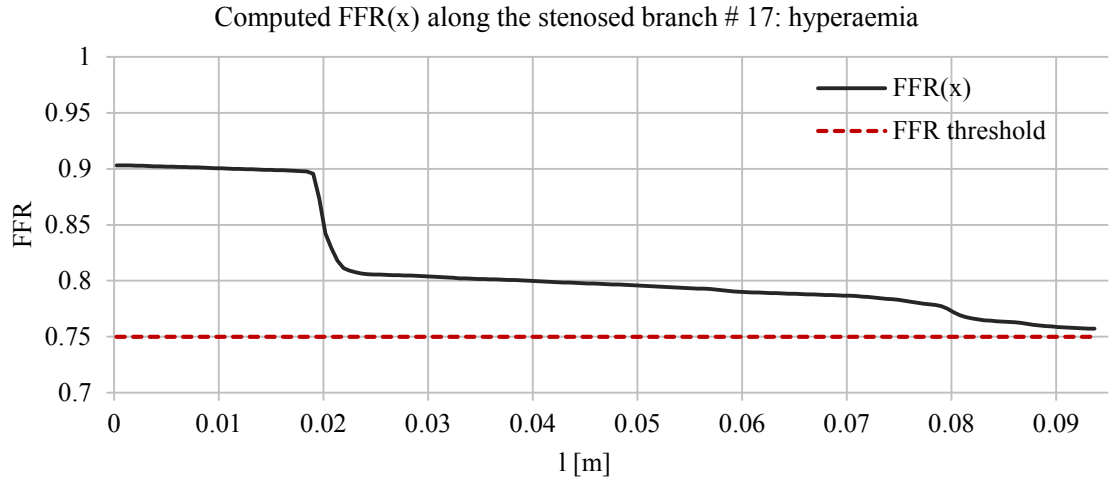

Figure 4.28 Waveform of the computed FFR along a branch of 0D LCA tree model

4.8 Limitations and Future Research Directions

Although the major advantage of the application of the lumped-parameter approach is the significantly lower computational costs in comparison to the classical 3D blood flow models, in the existing research works, the 0D simplification comes at the price of a lack of spatial characteristics of the computed flow fields. The proposed solution addressed this limitation by allowing the correlation of the computed flow fields with the location in the 3D lumen up to a specified level of accuracy (Figure 4.28). Yet, the employed methods for the extraction of vascular geometry information for further conversion into 0D elements are sensitive to lumen surface irregularities and segmentation quality. Similarly to the 3D domain case, this directly affects the computed flow fields and physiological accuracy of the results in the 0D domain. Therefore, further optimisation of the proposed methodology for automated

and accurate extraction of the vascular tree branches is required together with the corresponding validation of vessel segmentation accuracy.

Other limitations of the 0D blood flow modelling replicate those listed for the 3D model (Section 3.6) such as the accuracy of vessel segmentation, further geometric processing such as side branch truncation and the level of smoothing, and the requirement for the adjustment of the downstream BC parameter values. Apart from the investigation of the impact of these parameters, a thorough validation with invasively measured blood flow data other blood flow models will be required in order to establish a reliable modelling approach.

At the present stage of the research, the implementation of a 0D model requires manual input during both the extraction of the 0D parameters from the segment lumen and the construction of the coronary arterial tree from predefined blocks in the MATLAB® Simulink environment. Although being significantly less time consuming than the preparation of the 3D computation domain (Section 3.2), this introduces the possibility of the operator-related errors. For instance, the vessel segmentation and the corresponding construction of a 0D tree might take up to two hours versus 3-6 hours for the preparation and generation of a 3D volume mesh, depending on the level of experience. On the other hand, after the performed preparations, a 0D blood flow simulation itself requires only several minutes for the solution, while the duration of the equivalent 3D transient CFD simulation might last for approximately 8 to 30 hours (Section 3.4). However, since the 0D blood flow simulation results show high correlation with the computed 3D flow fields (Section 5.4), the developed 0D blood flow modelling framework can be further extended with a user interface for a more time-efficient solution. Due to the fact that both stages of the 0D blood flow model development use the MATLAB® framework, a direct data transition between them can be implemented relatively easy.

4.9 Conclusions

This chapter described the design of the proposed novel method for patient-specific 0D coronary blood flow modelling and the corresponding framework for implementation of this model. Like in the case of the 3D CFD model presented in Chapter 3, the main purpose of the 0D coronary blood flow simulations is the assessment of haemodynamic stenosis severity in the form of virtual FFR. The steps of the 0D coronary blood flow model development can be summarised as follows:

- Following the reconstruction of the coronary artery lumen from the CCTA volume, it is divided into branches based on the estimated centreline. Next, the arterial tree branches are subdivided into 3D elementary segments and the corresponding 0D RC elements are derived from their geometries.
- The 0D arterial tree is constructed as an electrical circuit with its branches represented through a series of elementary 0D circuit blocks. It is then incorporated into the 0D CVS loop model that generates physiologically realistic haemodynamics and can be adjusted with patient-specific data such as the CO and heart rate. The 0D BC models of the impedance of the peripheral vasculature are coupled to the tree outlets with the corresponding R and C values derived from the impedance of 1D idealised vascular trees generated from the outlet diameters.
- Both 0D CVS and coronary artery models are implemented in the MATLAB® Simulink through the set of blocks of the developed 0D blood flow simulation library based on the SimElectronics® toolbox. The blood flow model is established through the PDEs defining the current-voltage relationship in the corresponding electrical circuit network under the specified modelling assumptions.
- The solved blood flow model results include computed pressure, flow rate and FFR at the model outlets and along the arterial tree branches (under the rest and hyperaemia conditions) that can be used for the detection and assessment of haemodynamic severity of the stenoses in the vessel tree branches.

The implemented 0D modelling approach provides a solid foundation for further research in the area of 0D blood flow simulations in patient-specific vascular geometries. It overcomes the limitation of the lack of spatial information in the classical 0D blood flow models and has a significant advantage in comparison to 3D simulations in terms of significantly lower computational costs.

Chapter 5

Experiments and Discussion

5.1 Introduction

The emerging modern technologies in CFD modelling and extraction of vascular geometries from medical image volumes make the development of patient-specific blood flow models a relatively straightforward task. However, as discussed in Chapter 2, there are multiple interrelated factors that define complex flow fields and various modelling assumptions for approximation of physiological processes may significantly alter the simulation results. The main aim of blood flow modelling is the computation of flow patterns that are physiologically realistic (i.e., the obtained flow parameters are within a defined interpatient range) and accurate for a particular patient taking into account the corresponding individual CVS characteristics. The computational resources required for blood flow simulations also have to be taken into account since the numerical solution of the underlying flow governing equations is significantly time consuming and increases with the increased model complexity.

With respect to blood flow simulations in 3D patient-specific coronary arteries, the general level of model complexity is also increased by the number of unknown parameters, such as the flow conditions at the boundaries of a coronary vessel tree that represent the function of the remaining parts of the cardiovascular system. These flow conditions, as well as the precise geometry of the entire vascular tree are generally unknown inputs for blood flow simulations due to the lack of invasive coronary blood flow measurements and the resolution-related limitations of medical images. The essential modelling assumptions include the type of inlet and outlet BC models, the choice of rigid vs. compliant vessel wall model and the blood rheology model. In addition, since the computed blood flow is directly defined by the lumen geometry, the accuracy of reconstruction of the coronary vessel tree from CCTA or ICA also plays a major role. Although during the past decade a number of coronary blood flow models were implemented with the major progress achieved in the HeartFlow® project for non-invasive assessment of FFR [43,44], currently there are no general guidelines for coronary blood flow model development with respect to the factors that can potentially lead to inaccurate or erroneous flow patterns.

In accordance with the modelling approaches defined in Chapters 3-4, 3D CFD and 0D blood flow models were implemented for a patient-specific 3D LCA model extracted from a coronary CTA .dcm volume. The CCTA volume was acquired at the Department of Cardiology, St Thomas' Hospital, London from a patient with signs of ischemia. A medium severity 50-75% stenosis with full perfusion was diagnosed in the LAD, 50% stenosis in the LCx and one high severity 90% stenosis in the RCA. Further assessment of CAD severity performed with invasive FFR measurements showed the FFR values being 0.72 after the LAD stenosis and 0.83 after the LCx stenosis. Consequently, the LAD and RCA stenoses were diagnosed as critical and requiring surgical intervention. Taking into account that the case of multiple intermediate severity stenoses is more relevant for the assessment of blood flow model accuracy and sensitivity to various modelling assumptions, only the LCA geometry was used for blood flow simulations.

Following the implementation of the 3D and the 0D modelling approaches for patient-specific coronary blood flow simulations, this chapter investigates the influence of the various modelling assumptions and parameters on the computed blood flow. The qualitative impact of the introduced changes on the computed flow patterns is assessed through the derived FFR and TAWSS parameters (Figure 5.1) since both of them are employed in CAD diagnosis. Virtual FFR is used in the diagnosis of haemodynamic stenosis severity, while TAWSS patterns are associated with the mechanisms of atherosclerotic plaque formation and localisation (Sections 1.1.2-3).

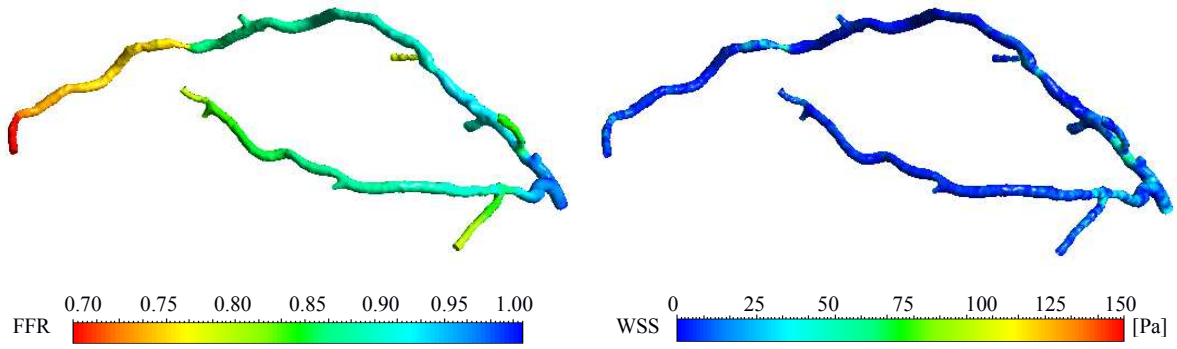

Figure 5.1 Computed FFR and TAWSS in the patient-specific LCA for CAD diagnosis

The plan for the performed set of experiments for the investigation of the impact of various modelling parameters is given in Figure 5.2. It includes the comparison of the outlet 0D BC model types generally employed in coronary blood flow simulations together with the

validation of the approach for the calculation and adjustment of the corresponding parameters that replicate the impedance of peripheral vasculature.

Next, Section 5.2 investigates the difference between the results of transient and steady state simulations and the impact of regulation of peripheral resistance for modelling of the hyperaemia condition induced by vasodilation. The influence of variations in the vessel tree lumen geometry reconstruction parameters such as the blood segmentation threshold, the side branch truncation levels, and the degree of surface smoothing is analysed in Section 5.3. This is followed by the assessment of the impact of interpatient variations in the model parameter values such as viscosity, aortic and LV pressure, and the geometry of the peripheral vascular tree.

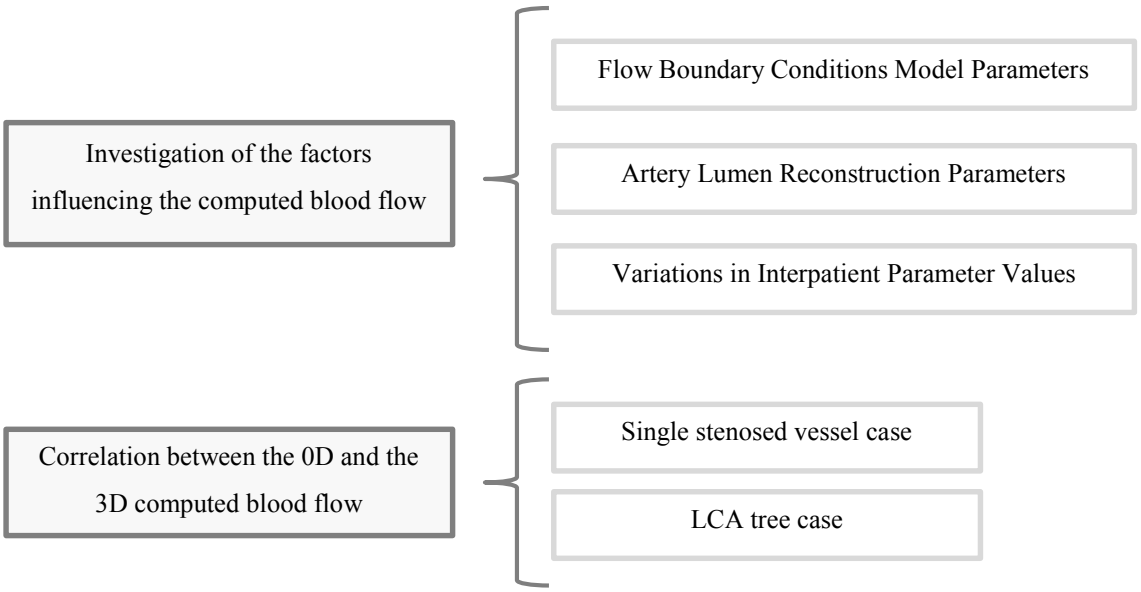

Figure 5.2 Blood flow simulations: experimental framework

Analysis of the correlations between the computed blood flow in the 0D and the 3D domains is presented in Section 5.4, thus validating the novel approach for the extraction of 0D flow resistance from vascular geometries and the extension of the classical lumped-parameter modelling with spatially distributed characteristics of computed blood flow such as FFR. Finally, Section 5.5 summaries the outcomes of the performed parametric study and comparison of the 0D and 3D models in the form of the modelling guidelines.

As explained in Chapters 3-4, the LCA tree geometry was reconstructed from CCTA with the set of functions for semi-automatic vessel segmentation implemented in MATLAB®. The 3D CFD model was defined in the ANSYS® Fluent CFD Solver and the 0D BC models were implemented as .c UDFs and implicitly coupled to the 3D model outlets. The 0D lumped-

parameter model of the CVS extended with the LCA was implemented in SIMULINK®. The characteristics of the baseline case of the 3D and 0D LCA blood flow models were defined based on the average interpatient CVS parameter values and include the following:

- General modelling assumptions: (i) simple R resistance 0D outlet BC model; (ii) steady-state blood flow simulation; (iii) dR = 0.2 vasodilation degree for simulation of hyperaemia; (iv) no additional adjustment of downstream BC parameters;
- Vessel lumen geometry extraction parameters: (i) 350 HU blood segmentation threshold; (ii) moderate volume-preserving smoothing; (iii) truncation of side branches at 2 mm level;
- General interpatient CVS parameter values: (i) 0.0035 Pa·s blood viscosity; (ii) 1060 kg/m^3 blood density; (iii) 75 beat/s heart rate corresponding to 0.8s cardiac cycle duration; (iii) mean LMCA pressure 90.5 mmHg; (iii) 52.5 mmHg mean downstream intravascular pressure of LV contraction; (iv) 2.75 cc/s mean LCA flow rate derived as 2.8% of 5.85 L/min CO; (iv) l/d = 20, $\xi = 3$ and $\alpha = 0.9$ / $\beta = 0.6$ default scaling parameters of the peripheral vascular tree for the approximation of 0D R and C values.

The blood flow simulation cases were compared either through the difference in the computed FFR and TAWSS patterns on the 3D artery surface or through the computed inlet flow rate, outlet FFR and flow distribution measured at the boundaries of the vessel tree. Since the flow-limiting impact of a stenosis is emphasised under higher flow rates and due to the general variations in interpatient flow resistance characteristics corresponding to hyperaemia condition, the degree of vasodilation dR varying between 1.0 and 0.0 was considered.

5.2 Investigation of the Impact of 3D Blood Flow Models Parameters

The results of blood flow simulations are highly sensitive to the choice of the models representing the flow conditions on the inlet and outlet boundaries of the vessel tree along with the employed approach for approximation of their parameters that replicate the functionality of the remaining parts of the cardiovascular system. This section investigates the impact of the type of 0D downstream BC model, the difference between the transient and steady-state flow simulation results, the approach for the simulation of hyperaemia, and the influence of adjustments on the downstream BC model parameter values.

5.2.1 Type of 0D BC Model

As described in Section 3.3.1, the optimal type of outlet boundary conditions for accurate assessment of pressure fields is the implicitly coupled lumped-parameter models representing the impedance of peripheral vasculature. There are three types of 0D models employed in blood flow modelling: (i) the simple resistance R; (ii) the 3-element Windkessel model RCR; and (iii) the coronary peripheral vasculature model RCRCR. The R model has a straightforward solution, since it does not contain the nonlinear transient elements. Both the RCR and the RCRCR models incorporate the impact of vascular compliance of the peripheral vessel tree and the myocardial wall, thus they produce more physiologically realistic flow waveform solutions. The parameter values for these models are derived from the outlet geometries (Section 3.3.2).

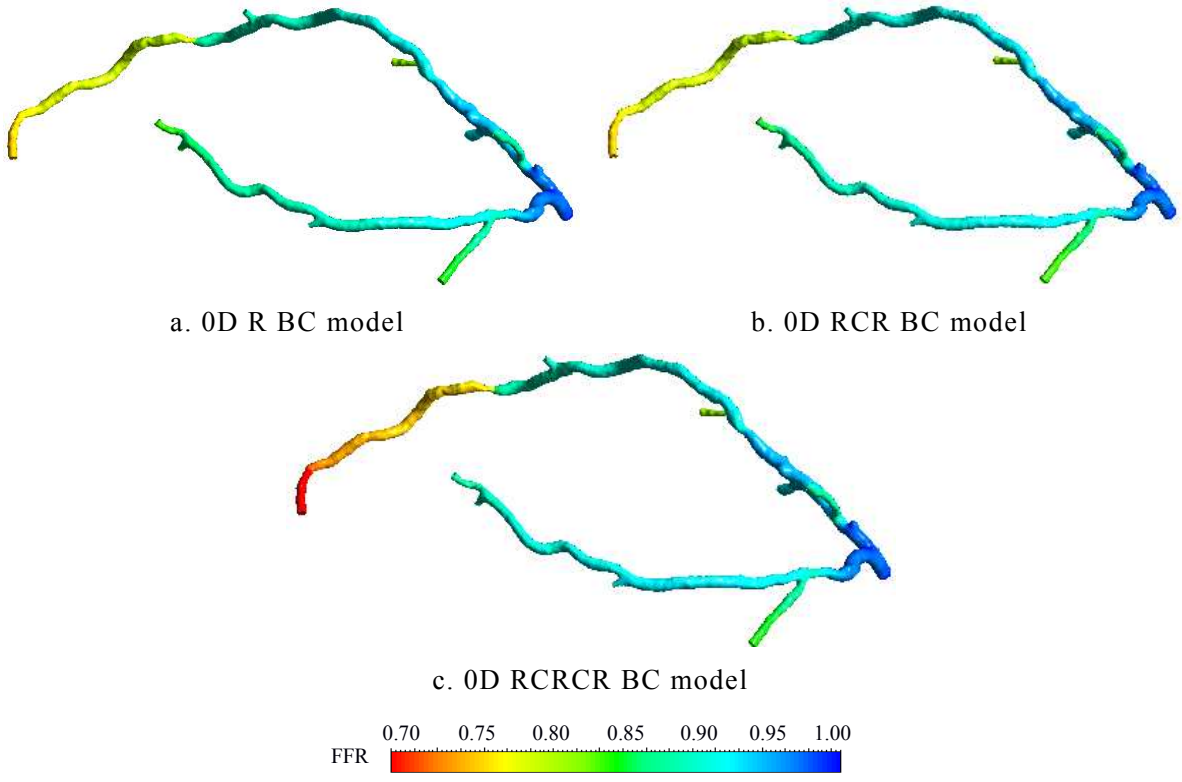

Figure 5.3 Computed FFR for the three types of 0D BC models (dR = 0.2)

Figure 5.3 shows the computed FFR results of transient blood flow simulations under the hyperaemia condition (dR = 0.2) for these three different types of 0D downstream BC models, with their parameter values derived from the structure of the generated 1D peripheral vascular tree (Section 3.4.3). It can be observed that in the R and the RCR BC cases, the FFR patterns closely resemble each other except for the slight deviation in the LCx branch and the slightly lower FFR values in the stenosed branch. At the same time, there is a pronounced

difference in the computed FFR in the stenosed branch in the RCRCR BC model case, since unlike the previous two cases, its value falls below the critical 0.75 threshold.

The difference is also noticeable in the computed flow rate distribution between the outlets dQ (Figure 5.4.a). While the dQ in the majority of the outlets is similar in all cases with the difference not exceeding +/- 5%, the flow rate in the stenosed branch (outlet #13) is significantly higher in the RCRCR case, i.e., it is 0.165 instead of ≈0.125 for the R and the RCR cases. This is caused by the presence of the C_{im} capacitance element, which represents the compliance of the myocardial wall through which the pressure of ventricle contraction is incorporated into the circuit (Figure 3.12). This emphasises the influence of the pressure difference caused by the stenosis leading to the higher flow rate to this branch, which, in its turn, results in the higher FFR drop, with the RCRCR FFR reaching the value of 0.711 versus the values of 0.758 and 0.755 for R and RCR cases, respectively (Figure 5.4.b).

a. Computed outlet flow distribution dQ (dR = 0.2)

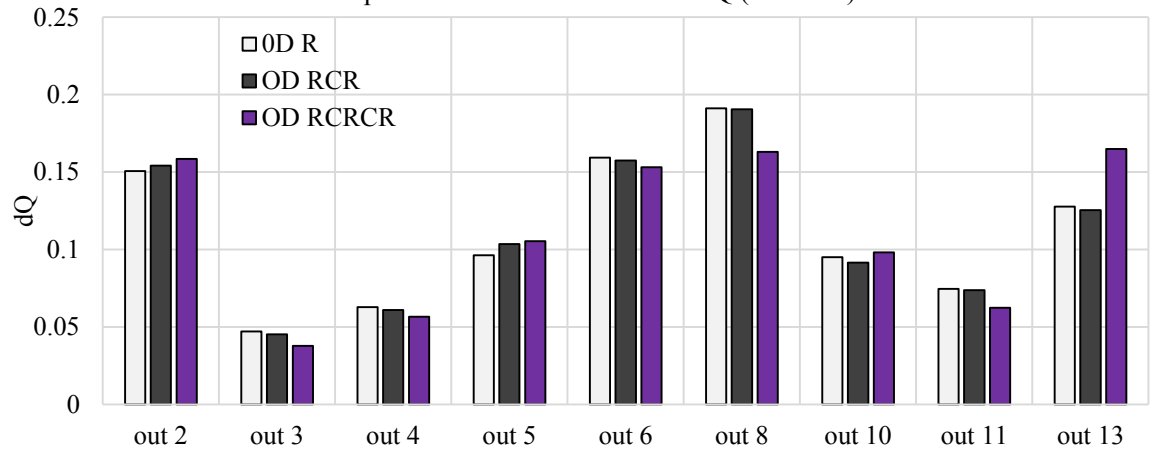

b. Computed outlet FFR (dR = 0.2)

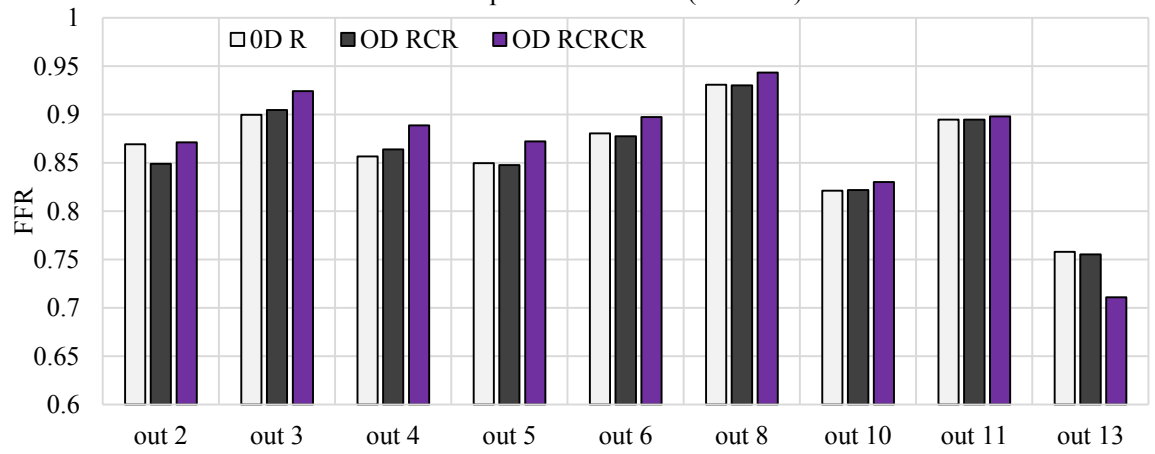

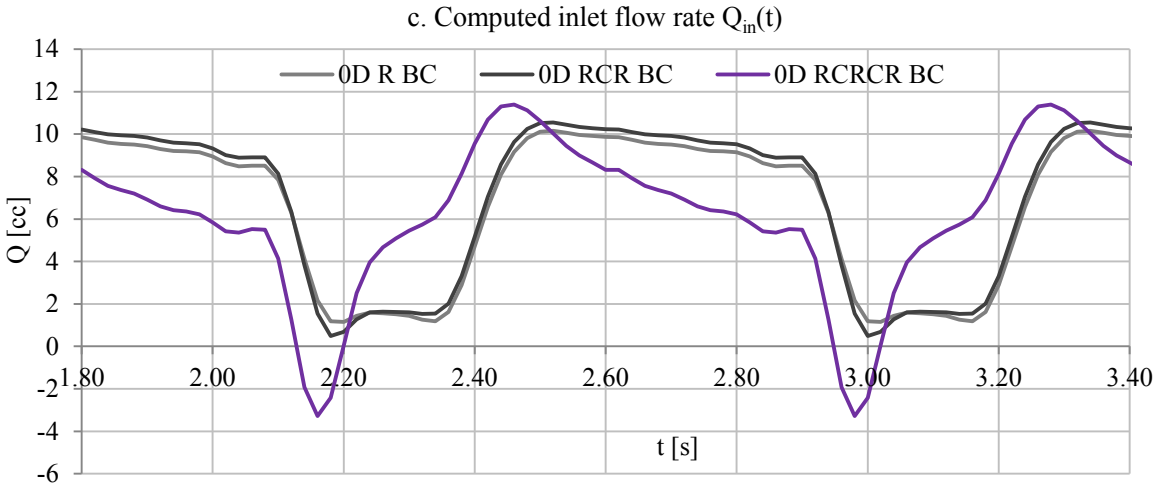

Figure 5.4 Computed FFR and dQ in the outlet #13 of the stenosed branch and inlet flow rate $Q_{in}(t)$ for the three types of 0D BC models (dR = 0.2)

The difference between these models is also clearly observed in the shape of the flow rate waveform (Figure 5.4.c). All three cases have the phase of the flow rate shifted with respect to the impact of the pressure of ventricle contraction. The fact that the difference between the R and the RCR BC results is relatively small is explained by the low compliance value because of the narrow diameters of the peripheral coronary vasculature (Table 3.3). On the other hand, the presence of the myocardial wall compliance C_{im} changes both the shape and the magnitude of the flow rate waveform, resulting in a non-linearly shifted phase of the flow rate with respect to the pressure waveform and a backflow during the systole, when the downstream pressure becomes higher than the inlet pressure.

The FFR and dQ waveforms presented in Figures 5.5-6 also replicate the inlet flow shape. In all downstream BC model types, the computed FFR drop in the stenosed branch (out #13) is considerably higher and falling below the critical threshold than in the healthy branch (outlet #6). At the same time, in the stenosed branch, the RCRCR-computed dQ is higher than the R and the RCR cases during the diastole, but in the healthy branch the dQ is nearly the same for all cases. Therefore, it can be concluded that while all these BC models result in the expected presence of a pressure drop after a stenosis, the non-linear characteristics of the RCRCR model enhance the haemodynamical impact of the stenosed regions by higher flow rates.

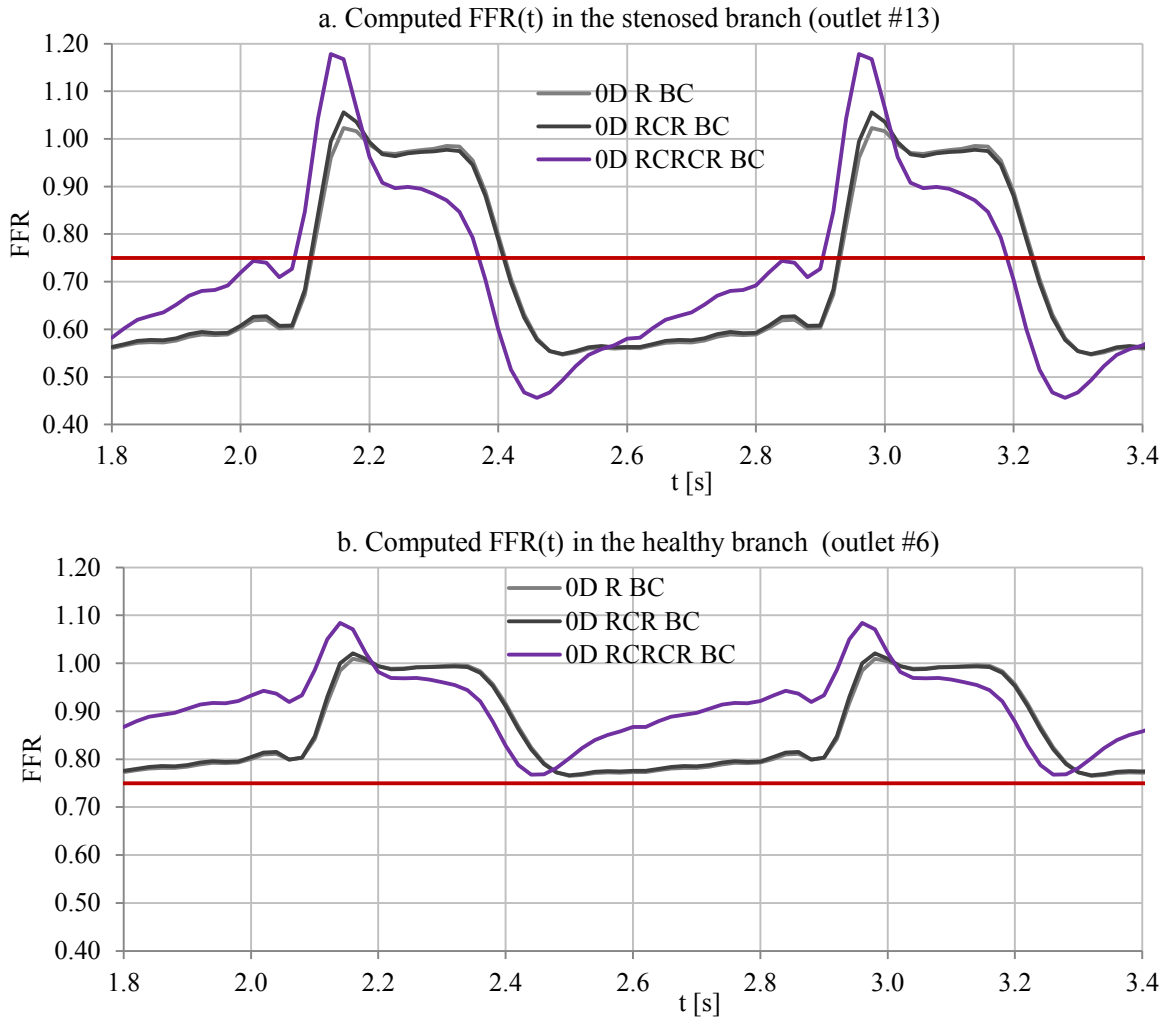

Figure 5.5 Computed FFR(t) in the stenosed and healthy branches for the three types of 0D BC models (dR = 0.2)

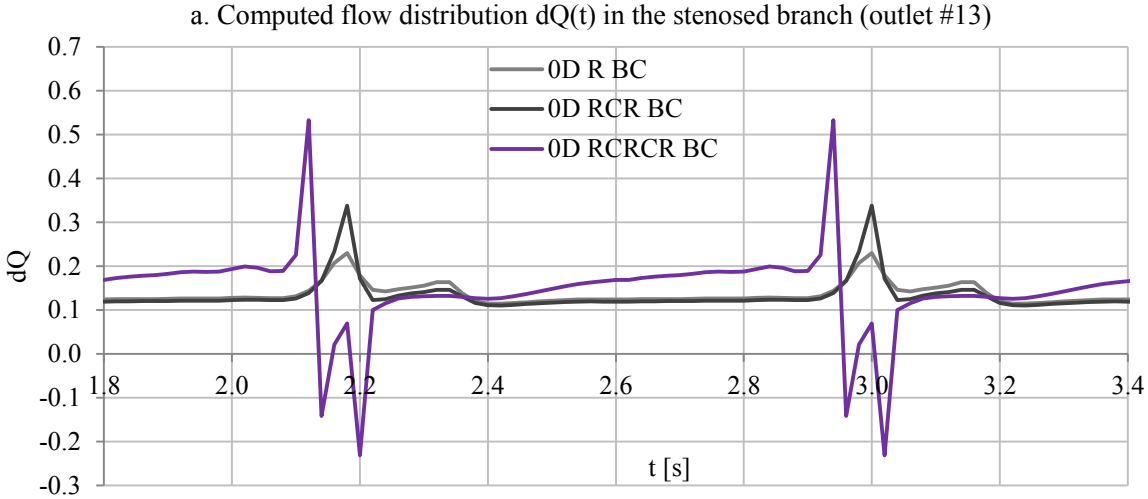

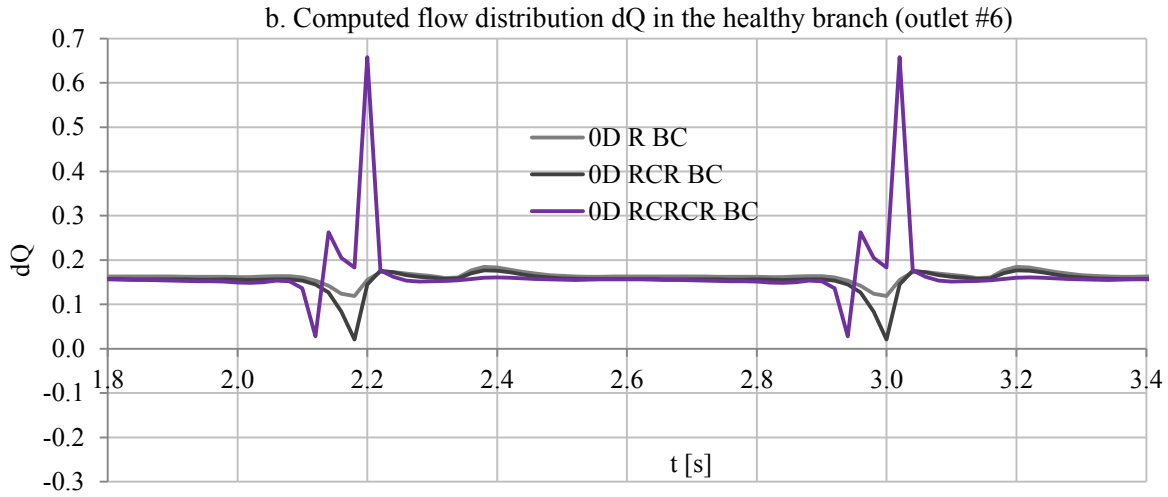

Figure 5.6 Computed dQ(t) in the stenosed and healthy branches for the three types of 0D BC models (dR = 0.2)

In other words, the RCRCR BC model produces more physiologically realistic results and as such it is the optimal choice in coronary blood flow simulations. Still, one of the major drawbacks of this BC model is that the solution of blood flow models with incorporated RCRCR BC models requires simulation times to be at least 3 times longer (see Section 3.5) in order to achieve solution convergence. In addition, apart from the peripheral vascular resistance, the RCRCR-based simulation results are also highly sensitive to the choice of C_{im} values, which can be only derived experimentally.

Hereafter, the steady-state simulation settings with the R 0D downstream BC are used as the baseline case in the further investigations of the impact of various modelling assumptions on the computed flow fields. The main underlying reasons of this choice are the simplicity of the R BC models and the faster numerical solution together with the possibility to employ the steady-state simulation option.

5.2.2 Transient vs. Steady-State CFD Simulations

This subsection investigates the differences between the transient and steady-state simulation results under the simple resistance R BC modelling assumption. Under this type of 0D BC model, the use of steady-state simulations is appropriate since it does not contain any nonlinear time-dependent elements (Section 3.3.2). Heart-cycle averaged values of aortic and scaled LV pressure waveforms are used in the inlet and the outlet BC models (Figure 5.7.a). At the same time, since the FFR and the TAWSS are computed as average values over a heart cycle, it is reasonable to assume that blood flow simulations with heart-cycle averaged pressure

values assigned to the BC models will result in similar FFR patterns. The main advantage of the steady-state simulation approach is that it significantly decreases the required simulation time from 2 heart cycles with 80 timesteps each to a single solution. In addition, it also eliminates any potential inaccuracies and backflow in the solved blood flow patterns during the systolic part of the heart cycle, when the inlet flow rate is close to zero due to the pressure of ventricle contraction.

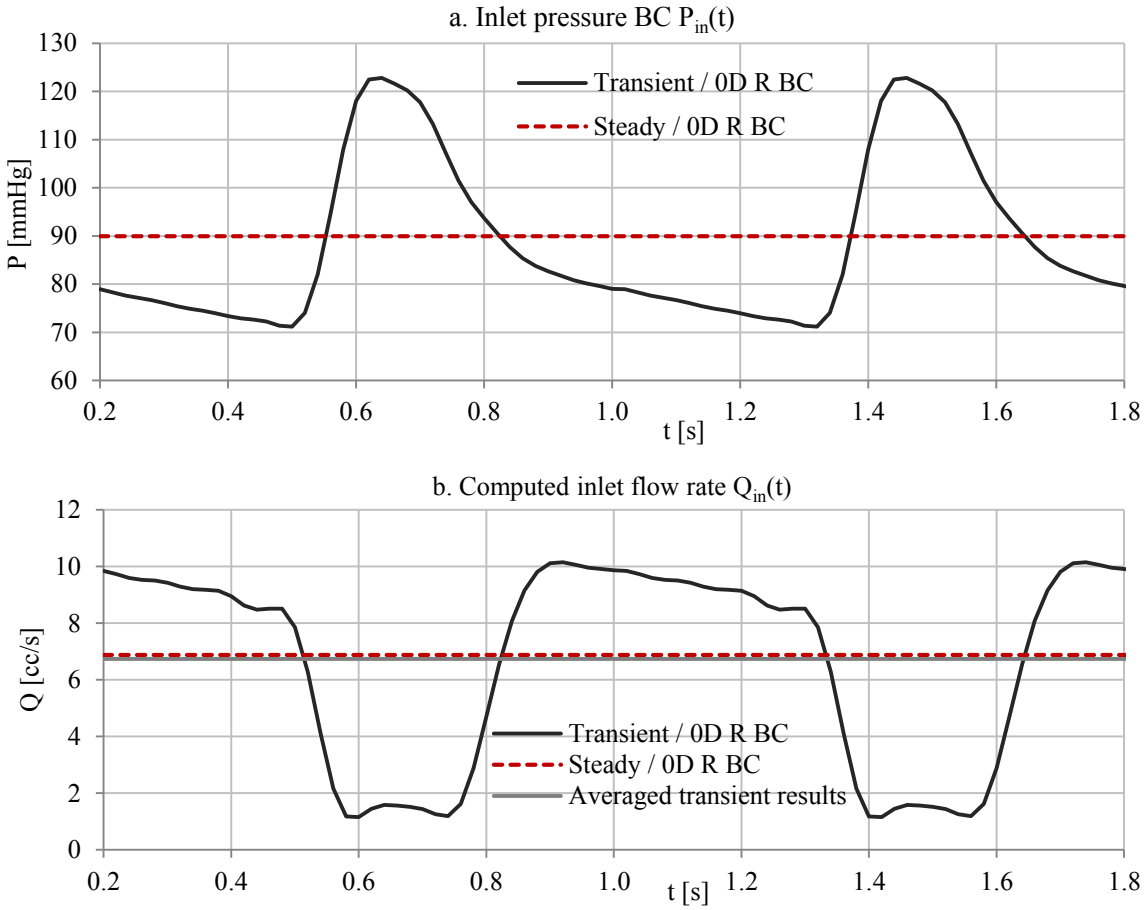

Figure 5.7 Inlet pressure BC and computed inlet flow rate and FFR and dQ in the stenosed branch (outlet #13) for the transient and the steady-state cases (dR = 0.2)

The comparison between the computed blood flow under hyperaemia with the steady-state and transient cases is given in Figures 5.7-8 The computed average inlet flow rate as well as the FFR and dQ in the stenosed branch (outlet #13) show a high degree of similarity with the difference caused primarily by the flow distribution variations during the systole (Figure 5.8.a).

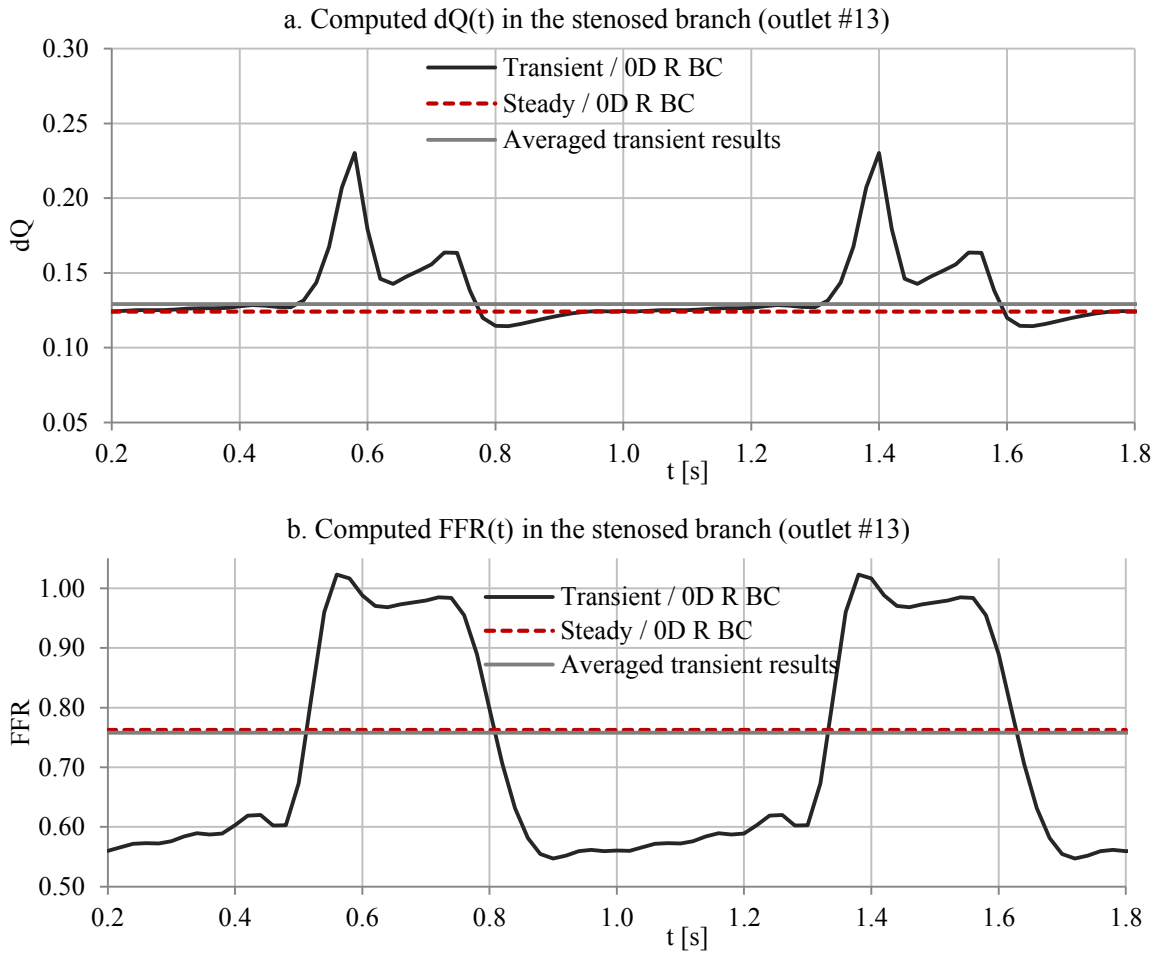

Figure 5.8 Computed FFR and dQ in the stenosed branch (outlet #13) for the transient and the steady-state cases (dR = 0.2)

The transient simulations in general showed a tendency to result in slightly lower FFR values for all outlets together with the variations in flow rate distribution (Figure 5.9). However, the difference between the values measured at the outlets does not exceed 2% for the FFR and 4% for the flow rate distribution. Accordingly, it can be concluded that, in the case of the chosen 0D resistance downstream BC model, the use of steady-state flow simulation mode is feasible for FFR assessment. Although not being the gold standard with respect to the "physiological accuracy" of the solution in general, this simulation mode is optimal for the purpose of the parametric study, since it allows to exclude the nonlinear impact of the RCRCR parameters and provides more than 100 times faster solution in comparison to the equivalent simulation in the transient-state mode.

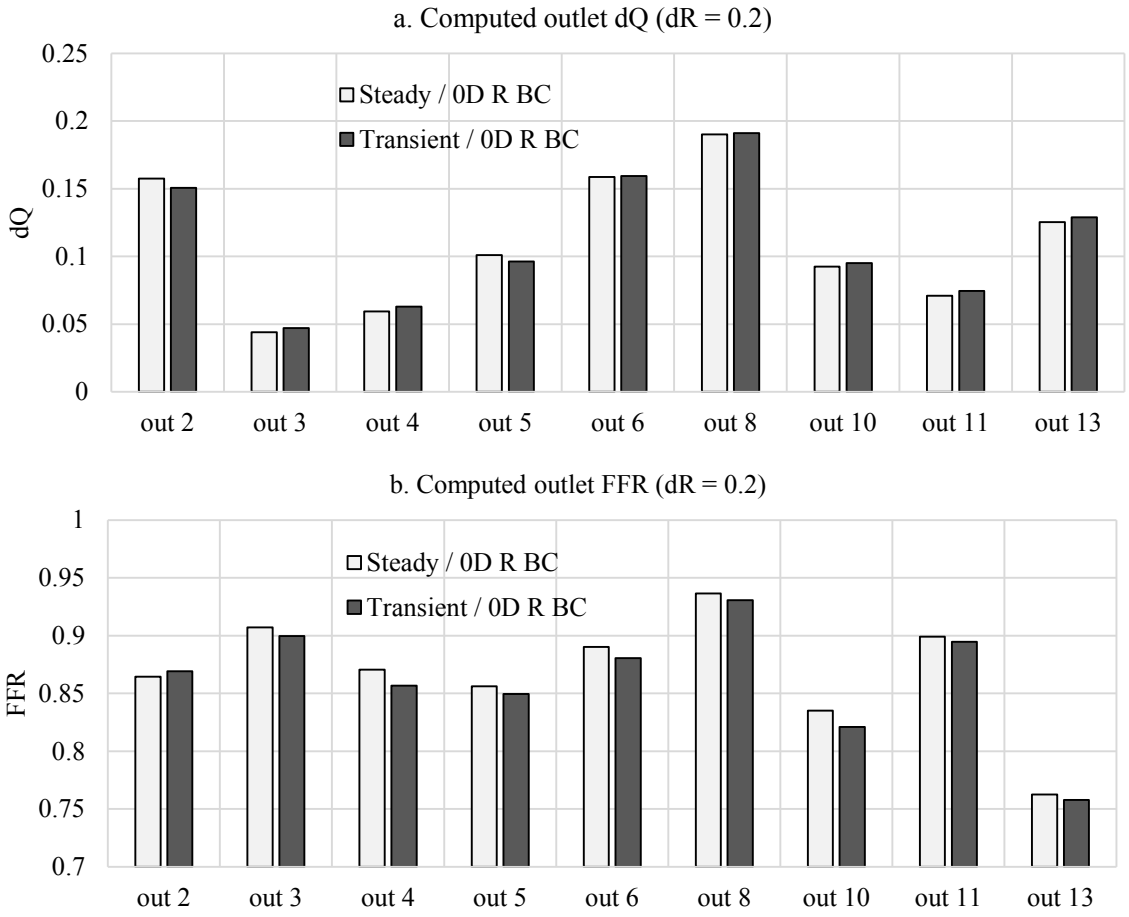

Figure 5.9 Difference in FFR and dQ for transient and steady cases (dR = 0.2)

The difference in the computed FFR and TAWSS 3D patterns between the transient and steady cases is presented in Figure 5.10. It can be observed that there is no significant deviation in the computed FFR with the maximum variation being +/-0.008 and the difference in the TAWSS does not exceed 13% in terms of variations in magnitude with the original patterns being preserved.

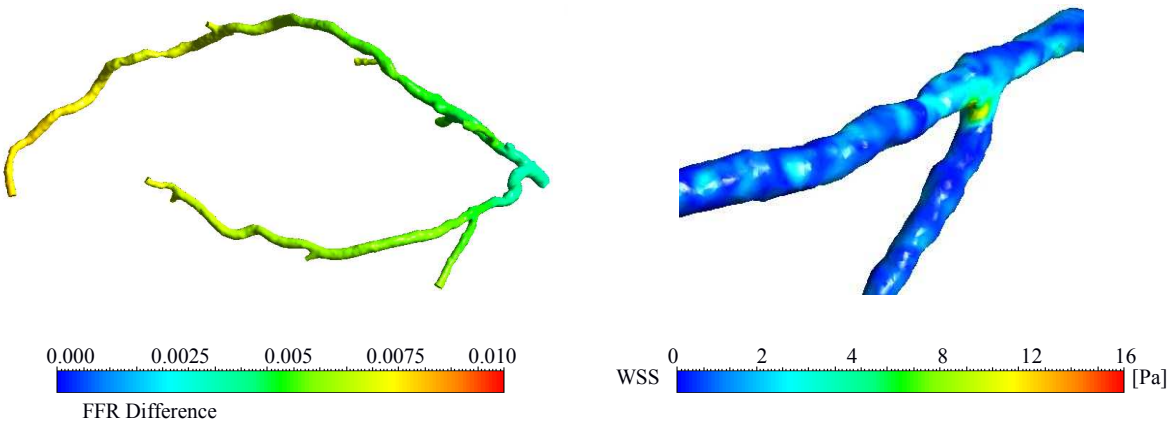

Figure 5.10 Difference in the computed FFR and dQ for transient and steady-state cases (dR = 0.2)

5.2.3 Simulation of Hyperaemia for FFR Assessment

As described in Section 3.4.4, pharmacologically induced hyperaemic condition is achieved by the reduction of the flow resistance of the peripheral vasculature up to the maximal vasodilation level achieved by adenosine administration. In the majority of the research works devoted to virtual FFR assessment, this condition corresponds to 0.2-0.25 of the original downstream resistance R_d value based on average physiological measurements [19]. A stenosis or a series of stenoses is considered critical if the value of FFR drops lower than the 0.75 threshold under the condition of hyperaemia.

Figure 5.11 shows the computed FFR for the initial dR = 1.0 of resting state and dR = {0.10, 0.18, 0.20, 0.25} corresponding to a hyperaemia-related condition. In this particular case, the FFR in the stenosed branch (outlet #13) does not drop below the critical threshold, and is equal to 0.763 under dR = 0.2. However, this is highly dependent on many aspects of the choice and adjustment of the BC model parameter values as will be discussed in the following sections. For instance, vasodilation to 0.1 of the original R_d shows a pronounced FFR drop to the critical value of 0.73 immediately after the stenosis, while the remaining branches remain in the "healthy" FFR range. This together with the FFR value of 0.83 in the LCx correlate with the invasive FFR measurements.

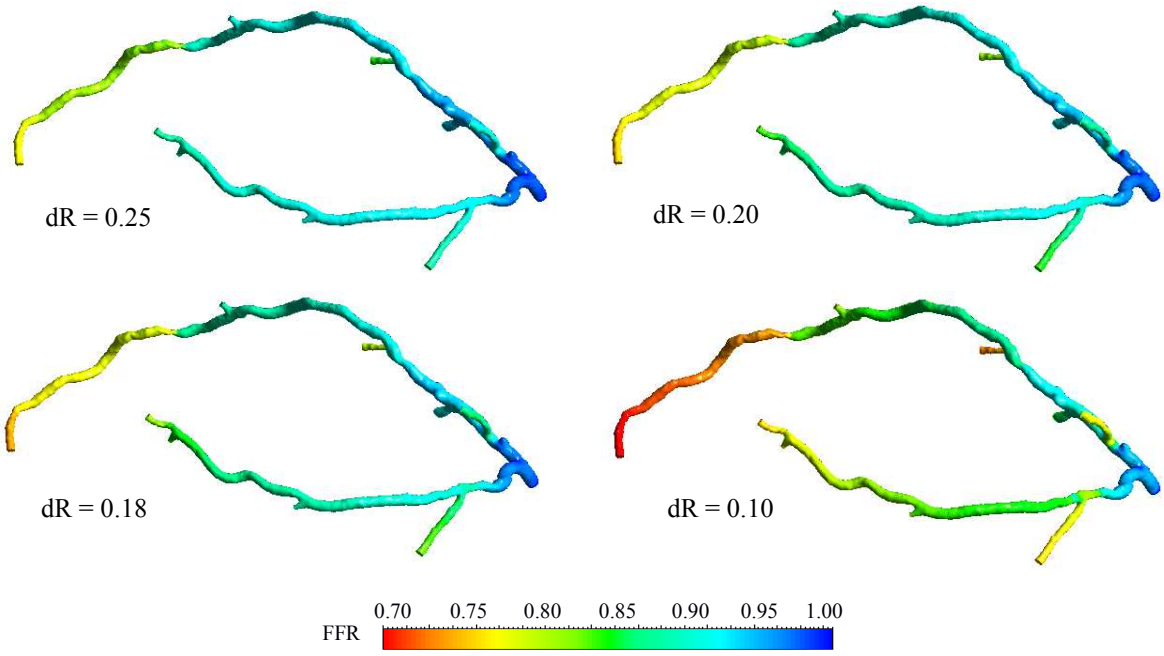

Figure 5.11 Computed FFR under varying degrees of vasodilation dR of the peripheral resistance

Gradual decreasing of the peripheral resistance from the originally approximated value to zero increases the inlet flow rate, consequently emphasizing the flow limiting impact of the stenoses (Figure 5.12). It can be observed that the slope of FFR vs. dR is significantly steeper for the stenosed branch than for the normal branch with the difference reaching the value of 0.12 in the 0.2-0.25 "hyperaemia range". This means that this stenosis causes 12% higher pressure drop versus the case of normal circulation.

As demonstrated in Figure 5.12, this difference is also replicated in the change of flow distribution between the branches as dR decreases ($dQ = Q_{out}/Q_{in}$). The flow rate distribution to the stenosed branch (outlet #13) drops by 32% from 0.185 to 0.125 when dR reaches 0.2, while there are no significant changes in dQ in the remaining branches until dR = 0.1. Since the healthy branch with outlet #8 has a flow lower resistance, the flow rate from the stenosed branch (outlet #13) is redirected there. Under dR = 1.0, the FFR values in all branches lie above 0.9, demonstrating only an insignificant pressure drop. In the idealised case of the total absence of peripheral resistance (dR = 0.0), the FFR values for all outlets meet at the 0.64 value corresponding to $FFR = P_{in}/P_d$, where P_{in} and P_d are the mean LMCA inlet pressure and the mean intravascular pressure of ventricle contraction, respectively. Therefore, the modelling assumption of approximating these parameter values also affects the magnitude of the computed FFR.

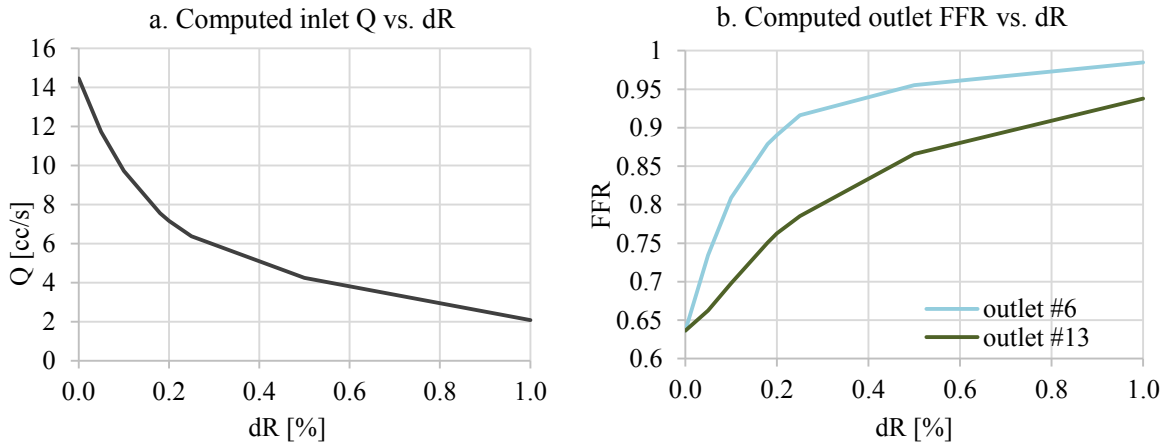

Figure 5.12 Computed inlet flow rate and FFR in the stenosed and healthy branches vs. dR (dR = 0.0:1.0)

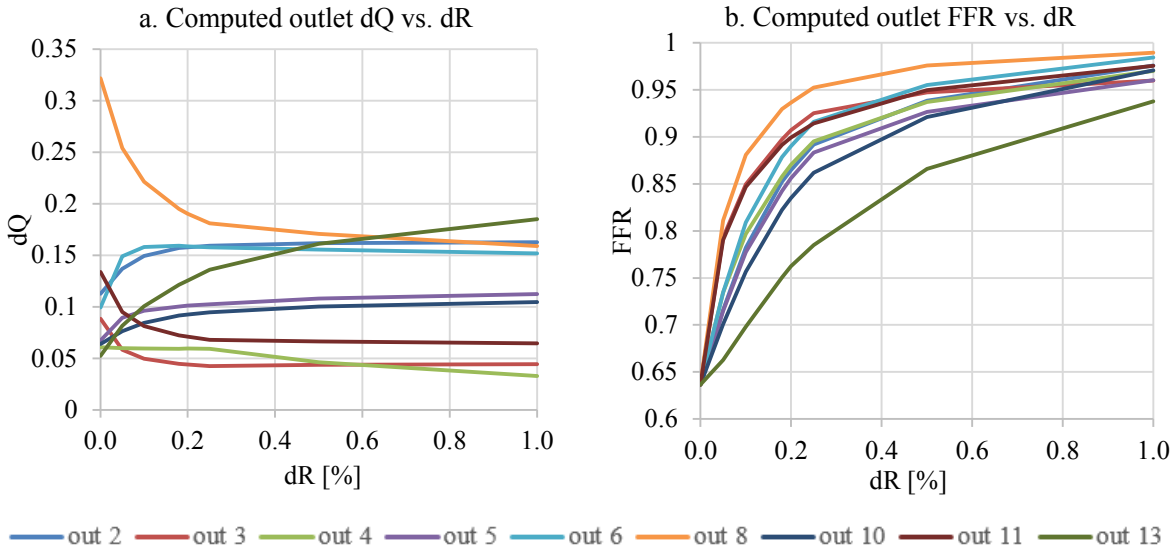

Figure 5.13 Computed outlet FFR and dQ vs. dR for the baseline LCA case (dR = 0.0:1.0)

Ideally, the choice of the optimal degree of vasodilation as well as the majority of the model parameters should be patient-specific (especially when considering the case of patients with vasoconstriction-related pathologies). As shown in Figure 5.13, even a small variation in dR can lead to different FFR and dQ values since they replicate variations in vessel geometry under higher/lower flow rates. At the same time, since the patient-specific degree of vasodilation for hyperaemia is generally unknown, the modelling assumption of dR being within the range of [0.2, 0.25] is reasonable based on the experimental study of Gould et al. [19]. This also emphasises the importance of the control of the originally derived R_d values corresponding to the peripheral vascular resistance under the resting condition so that further modelling of vasodilation will result in the correctly simulated state of hyperaemia. In other words, the computed flow under the resting state has to abide to the specified requirements to the inlet flow rate and the flow rate distribution between the outlets.

5.2.4 Adjustment of 0D Downstream Model Parameters

As described in Section 3.3.4, although the parameters for the 0D models representing the vasculature distal to 3D artery outlets are not known and cannot be estimated from medical images, they can be indirectly derived from the requirements for coronary blood flow. These requirements include the specific value for the inlet flow rate (the total coronary flow being assumed to be approximately 4% of the CO) and the $dQ_{out}^3 \sim d_{out}$ relation between the flow rate distribution between the vessel tree branches and the outlet diameters derived from the Poiseuille's solution. While the mean inlet flow rate Q_{in} requirement is extracted from the

measured patient-specific CO value [44,110], the proposed approach for the estimation of the downstream 0D BC model parameter values is based on the generation of idealised 1D vascular trees that represent the peripheral vascular tree for each of the outlets and further deriving the corresponding total resistance and capacitance values. Based on the defined scaling laws of vessel branching [77], one of the advantages of the proposed method is that it directly results in the computed dQ to be proportional to the outlet diameters of the healthy artery cases with the Q_{in} also being within the physiologically relevant range.

However, in the case of the presence of stenosed branches, the peripheral vasculature is affected due to the long-term autoregulation process, which adjusts the downstream resistance values to achieve optimal perfusion. Consequently, this requires the tuning of the 0D BC model parameters. The corresponding procedure involves the adjustment of the peripheral resistance based on the difference between the required Q_{in} and dQ_{out} and the preliminary simulation results (Section 3.3.4). Scaling of the total peripheral resistance R_d for all outlets will increase/decrease the inlet flow rate while the adjustment of the individual peripheral resistance values will update the computed flow rate distribution.

The results of the performed adjustment of peripheral resistance versus the initially computed flow fields under hyperaemia (dR = 0.2) are presented in Figure 5.14. A significant difference in FFR can be observed in the stenosed LAD branch together with an increased TAWSS magnitude in the stenosis and bifurcation areas, which is associated with higher velocities (Figures 5.14.e-f).

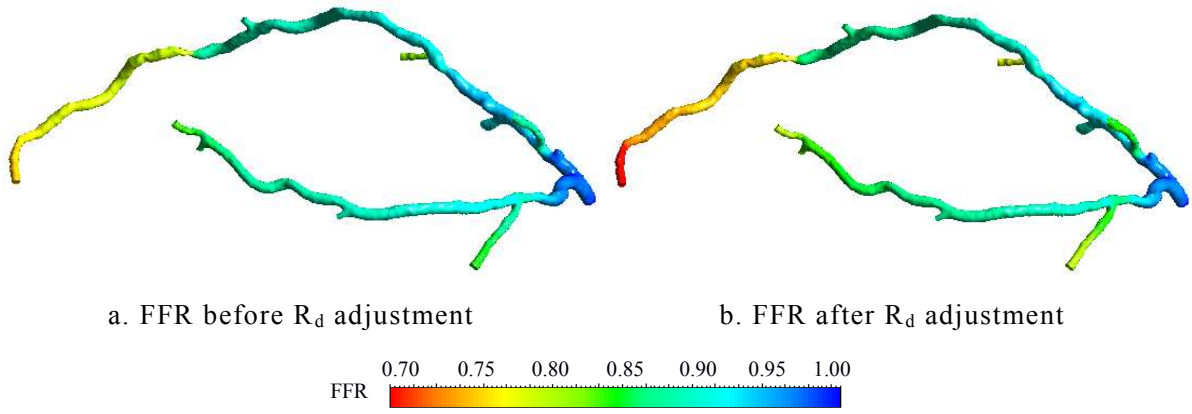

a. FFR before R_d adjustment b. FFR after R_d adjustment

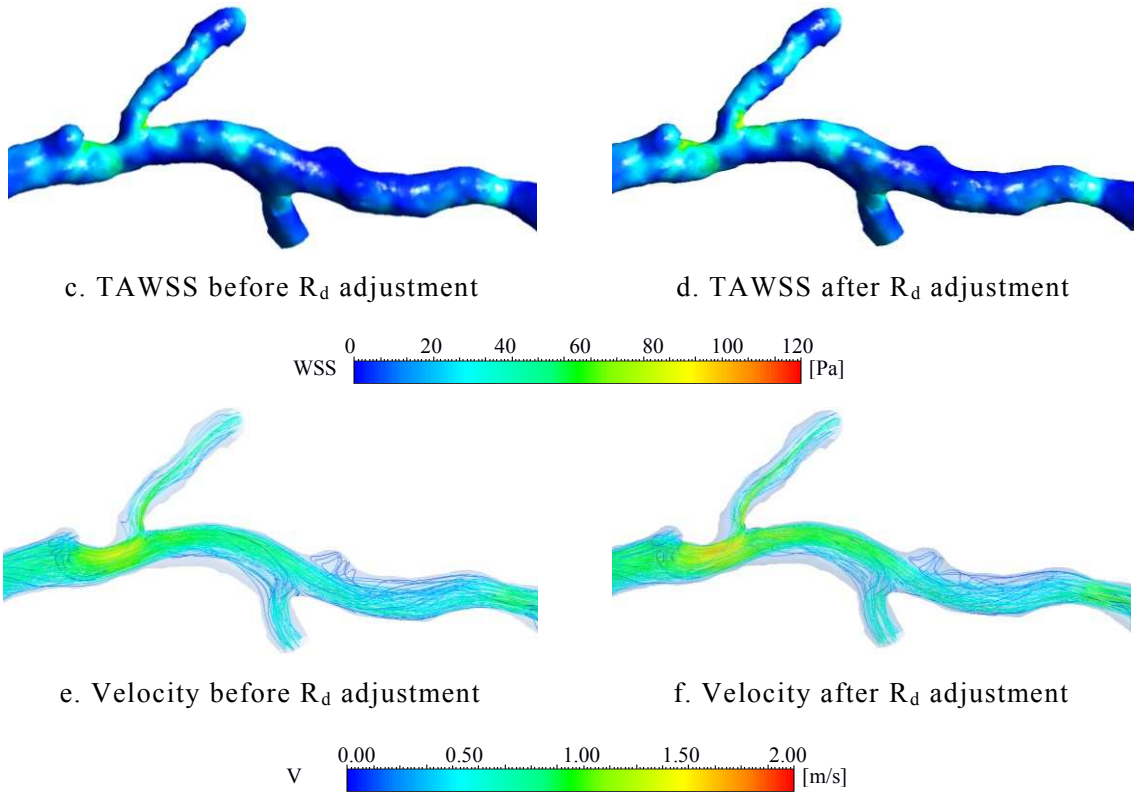

Figure 5.14 Computed FFR and TAWSS patterns and velocity streamlines before and after adjustment of R_d (dR = 0.2)

As shown in Figure 5.15.a, due to the difference between the required geometry derived dQ_{out} = 0.211 and the originally computed dQ_{out}* = 0.185 under dR = 1.0 in the outlet of the stenosed branch (outlet #13), the corresponding R_d was decreased to 0.88 of the original value, which resulted in a higher flow rate to this branch in the second simulation round with dQ_{out}* = 0.210. The corresponding FFR computed under dR = 0.2 dropped to 0.714, compared to 0.763 before the adjustment (Figure 5.15.b).

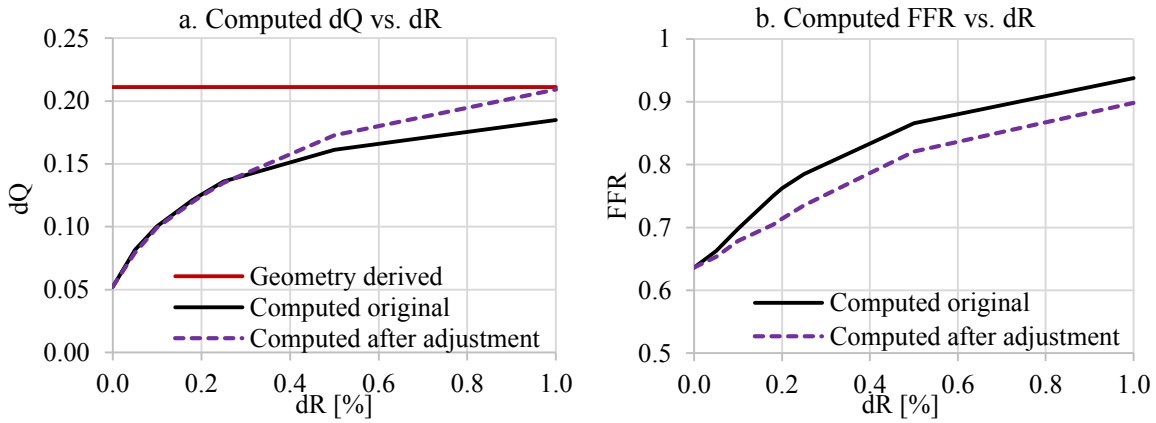

Figure 5.15 Computed FFR and dQ at the outlet #13 before and after adjustment of R_d (dR = 0.0:1.0)

The 25% difference between the originally computed and geometry-derived inlet flow rates (Q_{in} = 2.75 cc/s) required the scaling of the R_d value for all 0D BC outlet models by 0.75. Besides further decreasing the value of FFR downstream the LAD stenosis (Figure 5.17.a), the impact of the higher flow rate can be also observed in the difference in the TAWSS pattern magnitudes with the difference reaching a maximum value of 16% in the bifurcation area and in the presence of low severity stenosis narrowing of the branches, as shown in Figure 5.17.b.

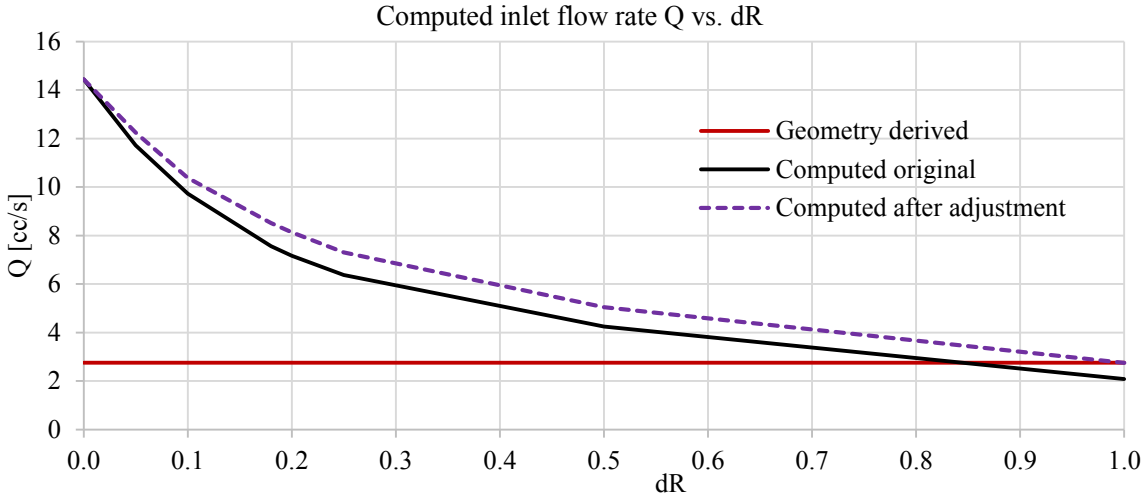

Figure 5.16 Computed inlet flow rate before and after adjustment of R_d (dR = 0.0:1.0)

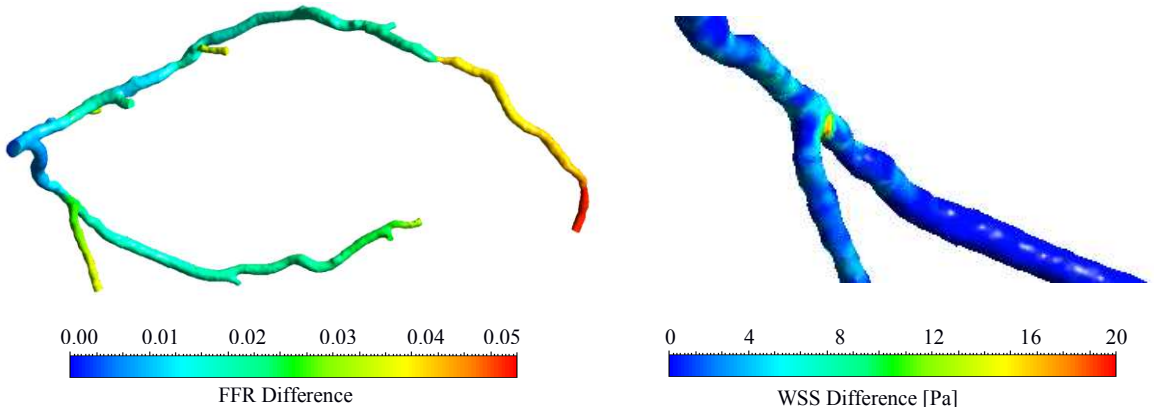

Figure 5.17 Computed difference in FFR and TAWSS before and after adjustment of R_d (dR = 0.2)

The results of adjustment of the peripheral resistance for the remaining outlet branches are given in Figure 5.18. Even before the adjustment, the difference between the geometry derived and computed dQ did not exceed +/- 0.02 of the total inlet flow rate. Thus, it validates the effectiveness of the proposed approach for calculation of the peripheral resistance. As

expected, the changes in total and individual outlet R_d values are replicated in the computed FFR being lower with respect to the degree of adjustment.

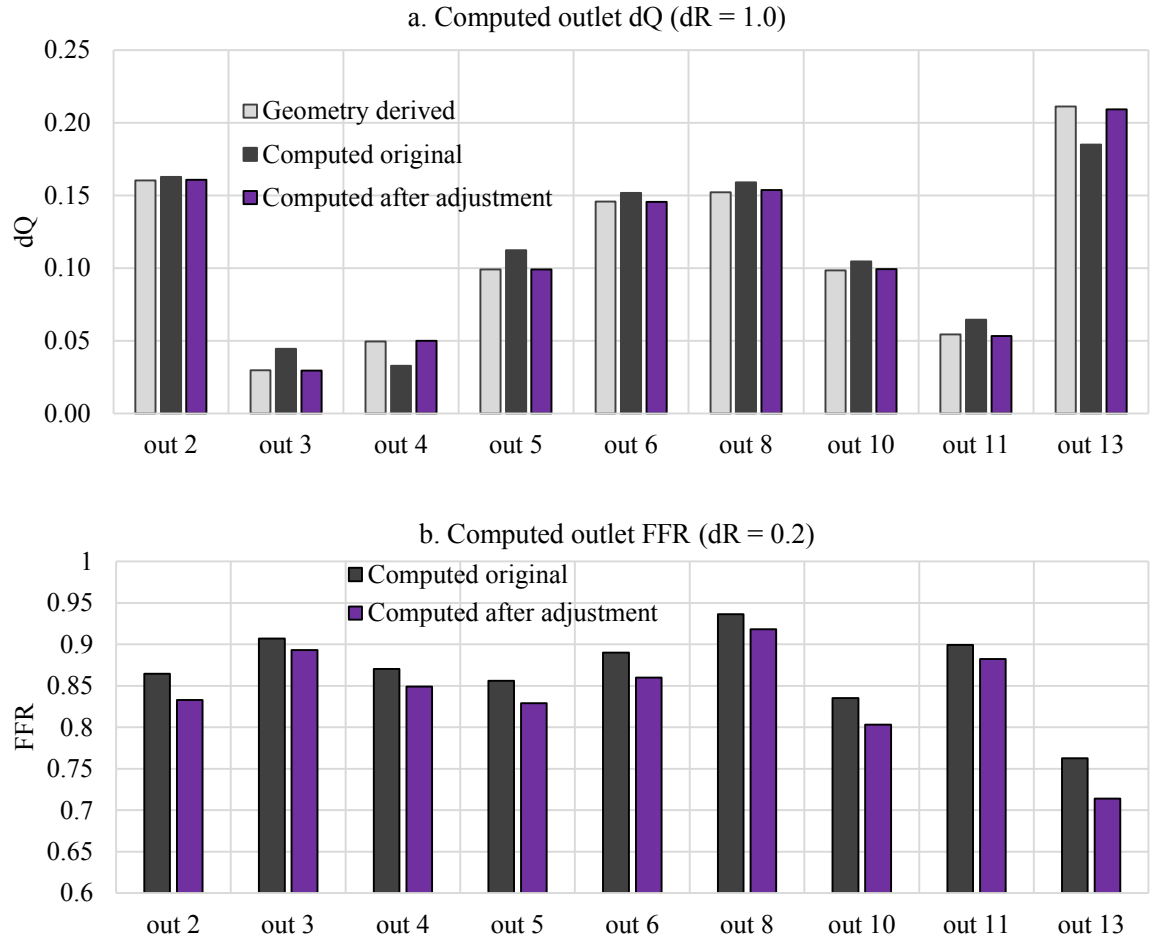

Figure 5.18 Computed outlet FFR and dQ before and after adjustment of Rd

Figure 5.19 shows the computed dQ and FFR for all outlets versus dR before and after adjustment of peripheral vasodilation. The R_d adjustment resulted in a significantly steeper slope in dQ and lower FFR values in the stenosed branch (outlet #13), thus emphasising the flow-limiting impact of the stenosis in comparison to the healthy branches. Therefore, it can be concluded that the computed FFR or TAWSS fields directly depend on the employed strategy for the choice of downstream BC model parameters. In addition, the control of the blood flow model compliance with the geometry-derived flow requirements is essential for accurate assessment of CAD-related computed flow patterns.

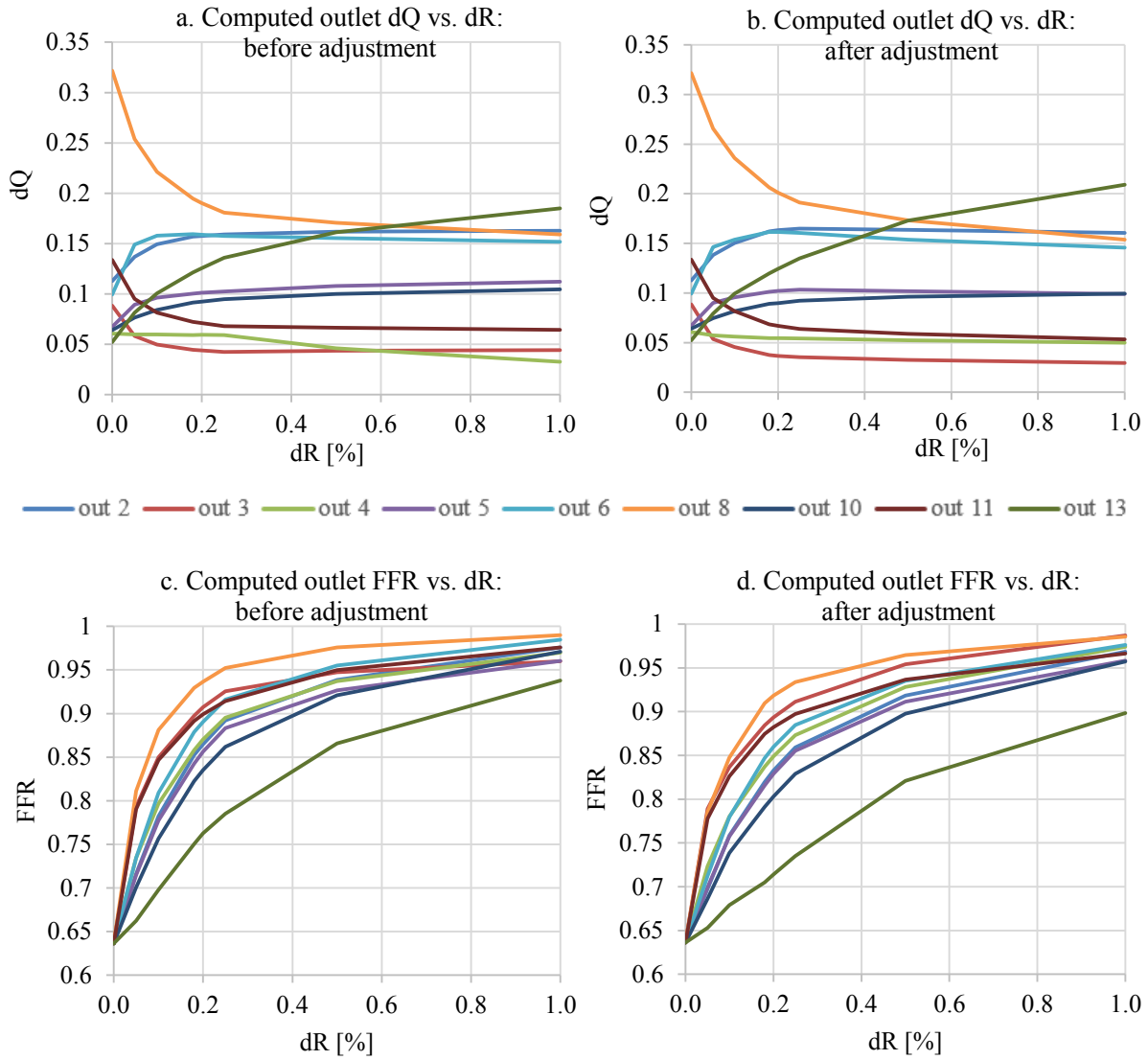

Figure 5.19 Computed FFR and flow distribution at the outlets before and after adjustment of Rd (dR = 0.0:1.0)

5.2.5 Variations in 0D Downstream Model Parameters

In accordance with the method for approximation of the 0D BC model parameters defined in Section 3.3.3, the geometry of the generated 1D peripheral vascular tree indirectly affects the 3D simulation results with respect to the derived flow resistance and compliance. In other words, morphometry law parameters such as the flow-diameter scaling factor, the length/diameter ratio and the bifurcation asymmetry ratio will change the magnitude of resistance and capacitance values and will thus affect the magnitudes of the computed pressure and velocity along with the total flow rate.

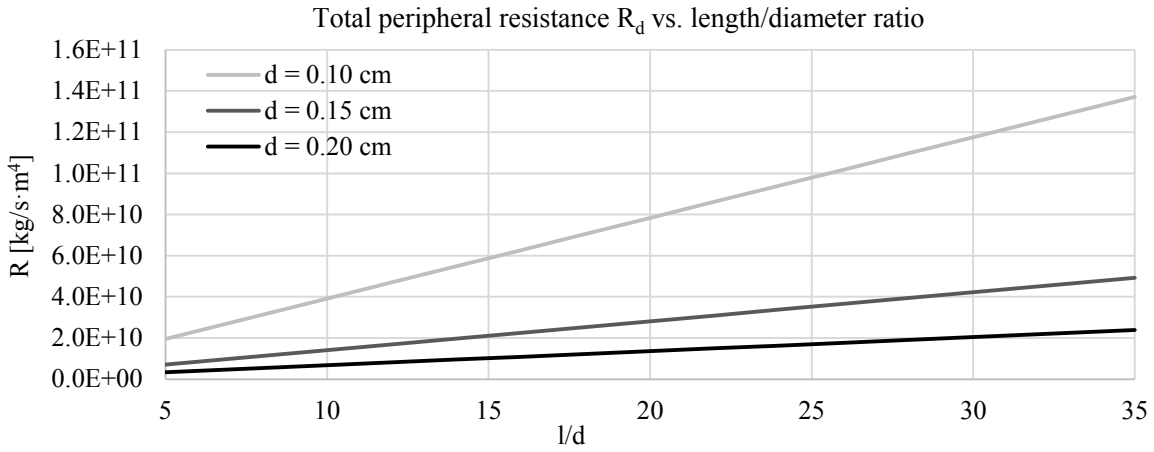

Figure 5.20 Computed downstream resistance for an outlet vs. length/diameter ratio of the 1D peripheral tree for three d_{out} cases

As was discussed in the previous section, the reduction of downstream resistance is used for modelling of hyperaemic blood flow but incorrectly estimated initial values can both underestimate or overestimate the stenosis severity (FFR). Due to the fact that it is not possible to measure the geometric parameters of the downstream vasculature, the actual values for the downstream flow resistance are unknown and modelling assumptions have to be applied. The relevance of these assumptions and associated approximations can be estimated only indirectly through the comparison of the computed blood flow features and magnitude with the known physiologically realistic range.

Figures 5.21 demonstrates the impact of the variations in the length/diameter ratio of the 1D tree branching morphology on the derived peripheral resistance, FFR and dQ under hyperaemia. The l/d = {15; 20; 25} values were considered based on the average physiologically derived values used in modelling of 1D vascular trees [77]. Similarly to the computed R_d vs. l/d graphs given in Figure 5.20, it can be observed that the change in l/d acts as a linear scaling factor of the resistance with higher l/d values corresponding to a higher R_d. Therefore, the computed flow rate will be lower and a higher degree of adjustment of the peripheral 0D BC parameter will be required. It was identified that the l/d = 20 assumption generally produces optimal resistance values and in turn results to physiologically realistic flow patterns.

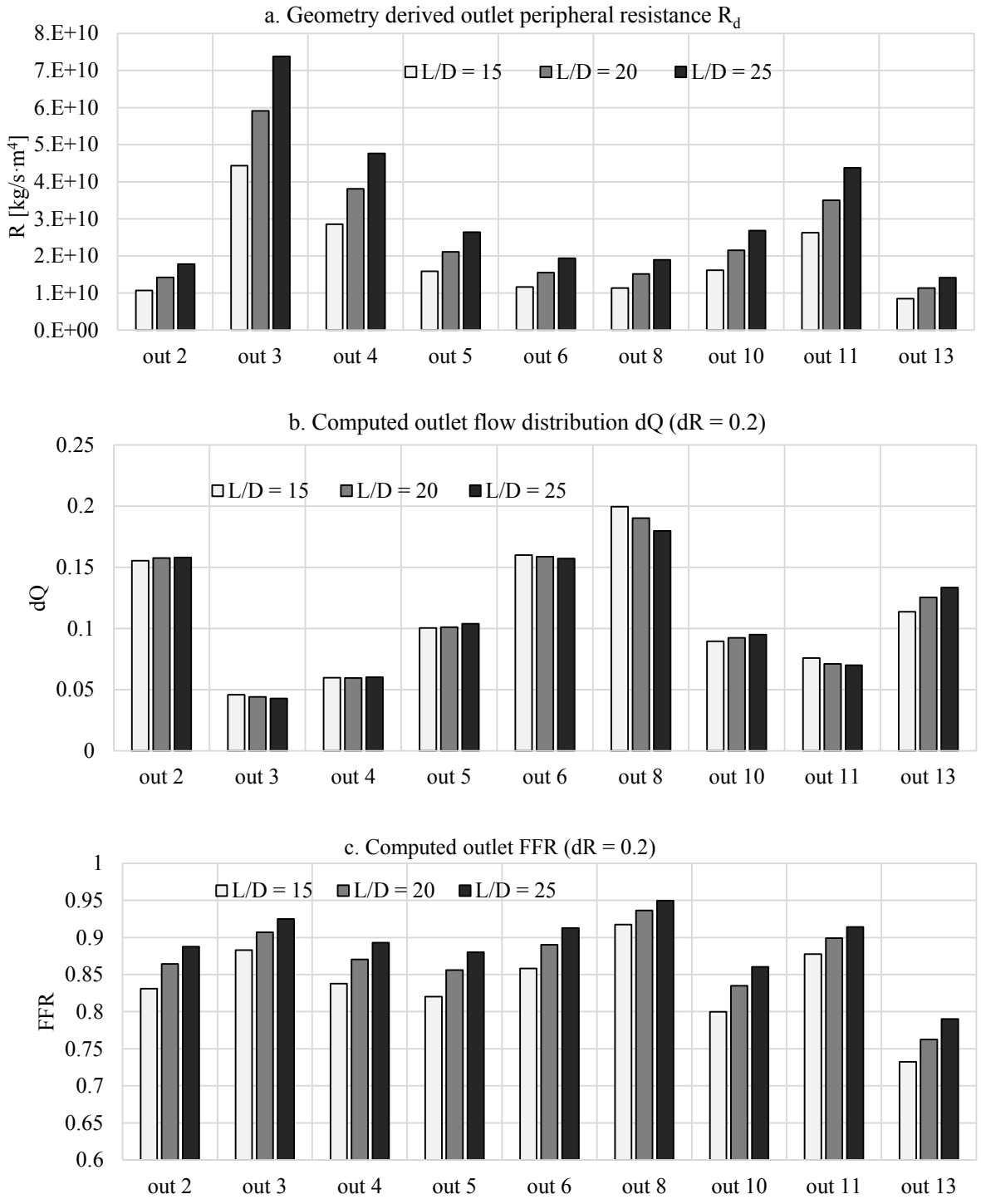

Figure 5.21 Computed outlet FFR, dQ and R_d for three cases of l/d ratio of 1D peripheral tree (dR = 0.2)

Other 1D scaling parameters also affect the approximated peripheral tree parameters such as the morphometric exponent ξ (flow-diameter scaling factor) that defines the bifurcation asymmetry ratio of the 1D tree (Section 3.3.3). The corresponding coefficients defining the r_{d1} and r_{d2} radii ratio with respect to r_p are α and β and are derived with respect to the required ξ value. This is derived from a power law based on the principle of minimum work given by r_p^{ξ}

$= r_{d1}^{\xi} + r_{d1}^{\xi}$ [77], where r_p , r_{d1} and r_{d2} are the radii of the parent and the two daughter branches. According to [77], $\xi = 3.0$ corresponds to laminar flow and $\xi = 2.33$ corresponds to turbulent flow, while a value of 2.76 is assumed to be optimal for narrow diameter peripheral vascular structures.

In the baseline case, ξ was chosen to be equal to 2.76 taking into account the dimensions of coronary vasculature, which correspond to $\alpha = 0.9$ and $\beta = 0.6$. However, for $\xi = 3$, these values will be {0.95; 0.52} and for $\xi = 2.33$, they will be {0.90; 0.52}. Figure 5.22 presents the derived peripheral resistance values for these three cases of the 1D tree structure for the baseline LCA tree and the computed outlet dQ and FFR under these 0D BC parameter values (under dR = 0.2). The computed downstream resistance decreases as ξ becomes closer to 3.0, derived from the Murray's law. Consequently, this affects the computed inlet flow rate, which becomes lower for higher peripheral resistances with Q_{in} = {4.6; 7.1; 8.4} cc/s for ξ = {2.33; 2.76; 3.00}, respectively. Therefore, this results in the difference in flow distribution between the branches with lower dQ in outlet #13, caused by the emphasised flow limiting impact of the stenosis. Similarly, FFR values will be higher for $\xi = 2.33$ because of the lower pressure drop under the lower flow rates.

a. Geometry derived outlet peripheral resistance R_d

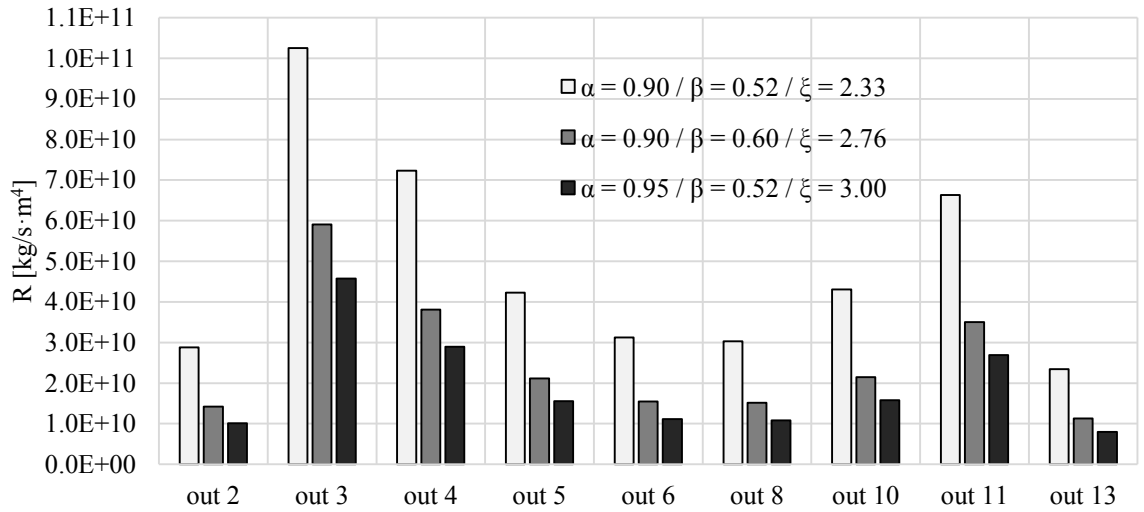

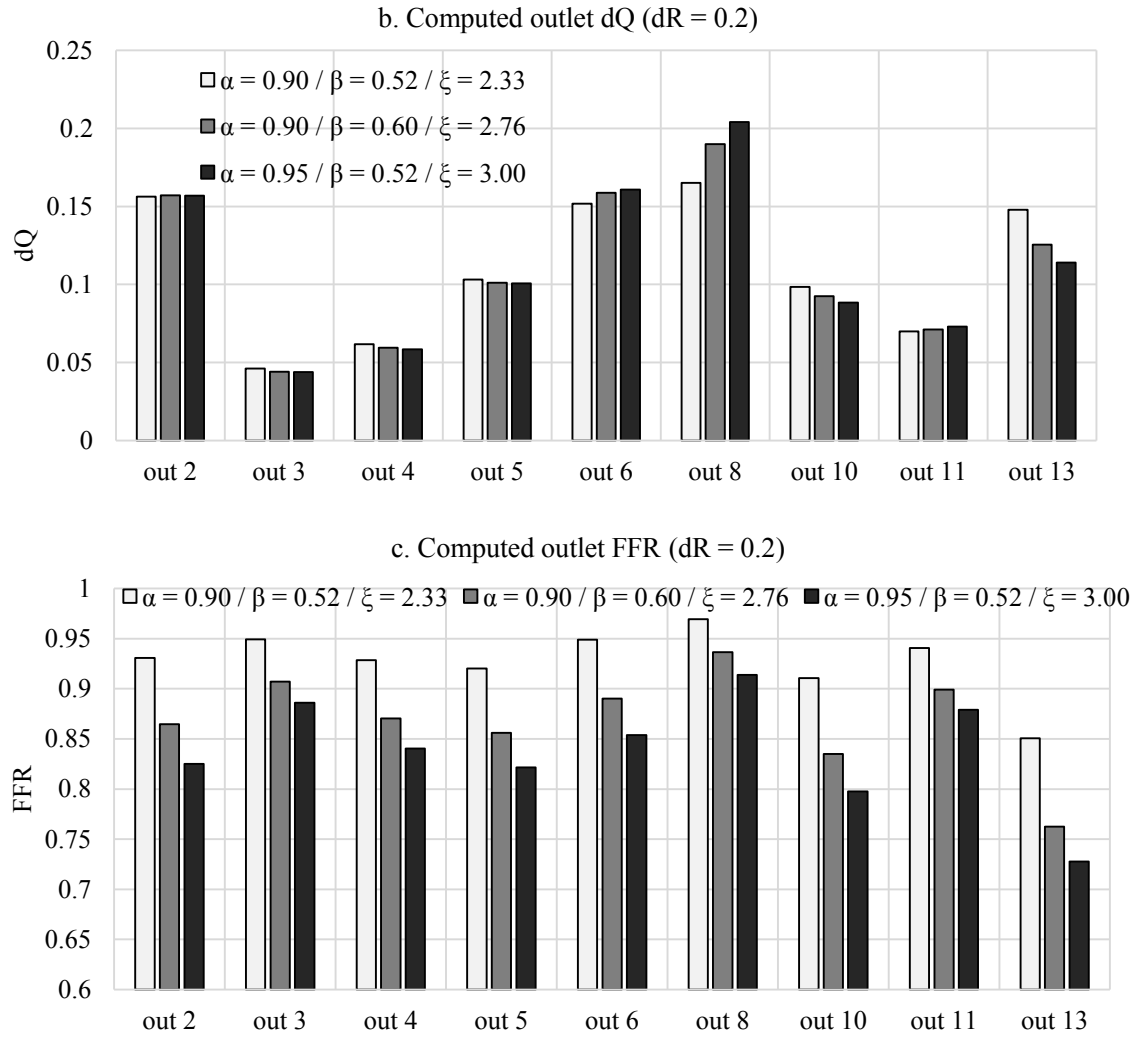

Figure 5.22 Computed outlet FFR, dQ and R_d for three cases of the morphometric exponent ξ of the 1D peripheral vascular tree (dR = 0.2)

As mentioned in Section 5.4.2, one of the advantages of the proposed method for extraction of the peripheral vascular tree parameters is that it straightforwardly produces the computed flow rate distribution to be proportional to its diameter in accordance with Murray's law, together with physiologically realistic pressure and flow rate magnitudes. At the same time, as was demonstrated above, even a small variation in the morphology of the 1D peripheral tree will produce a change on the computed flow patterns. This, however, can be controlled by the application of the procedure of the adjustment of the 0D BC model parameter values in accordance with the geometry-derived dQ and Q_{in} requirements (Section 3.3.4).

5.2.6 Impact of Interpatient Variations in Blood Flow Model Parameter Values

This section investigates the impact of modelling assumptions with respect to interpatient variations in physiological parameters such as inlet coronary flow rate, inlet pressure, downstream pressure, and blood viscosity.

The total coronary inlet flow rate under the resting condition is derived as 4-5% of the CO computed as the product of the heart rate and the stroke volume [110]. In addition, with respect to the arterial location, i.e., left or right, the coronary flow rate portion is assumed to be 6% or 4% [2]. Although it was not incorporated in the BC models, the inlet flow requirement is employed in the process of adjustment of the BC model parameters, thus indirectly controlling the vasodilation of peripheral resistance. Therefore, since the flow rate magnitude is directly related to the stenosis induced pressure drop, the initial assumption of a lower or higher flow rate will define the computed FFR though the dR value. For instance, Figure 5.23 shows the computed FFR under hyperaemia for two cases with the resting inlet flow rate being Q_{in} = {2.01; 2.75} cc/s before and after the performed adjustment of dR. The FFR drop in the stenosed branch is considerably higher in the second case and reaches the critical threshold.

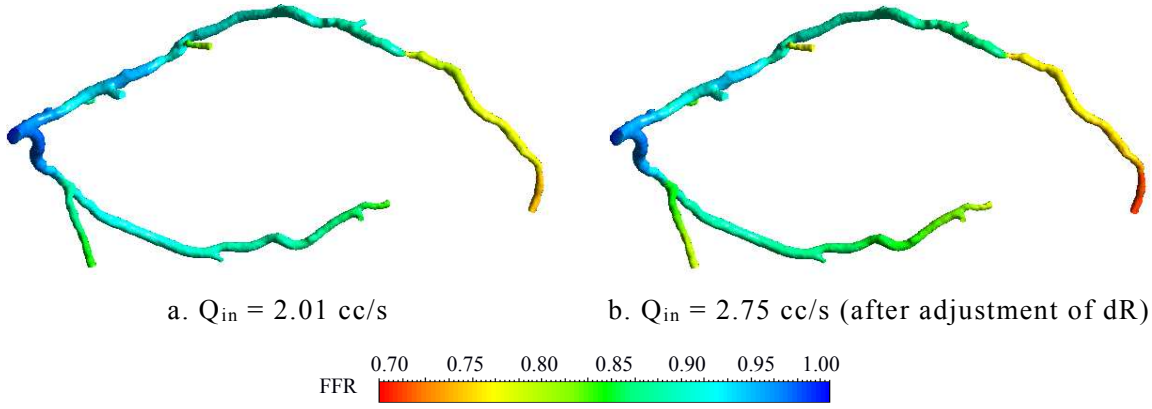

Figure 5.23 Computed FFR vs. inlet flow rate value (dR = 0.2)

The values of the pressure at the inlet of the coronary artery P_{in} and the downstream pressure P_d at the capillary level are the necessary inputs in the BC models and significantly affect the computed flow fields, with the main controlling factors being the difference between these pressures $\Delta P = (P_{in} - P_d)$ and their ratio $dP = P_d/P_{in}$. The pressure difference ΔP controls the computed inlet flow rate and P_d/P_{in} defines the magnitude of the pressure drop along the vascular tree, since it represents the minimum FFR for all branches under dR = 0.0 (i.e., the case of idealised vasodilation, when there is no resistance in the peripheral vascular tree).

The patient-specific P_{in} being equal to the central aortic pressure can be non-invasively measured by radial artery applanation tonometry [144]. At the same time, the approximation of the downstream pressure is a more difficult task since it is the product of the capillary level pressure and the intravascular pressure of ventricle contraction. An assumption of the P_d value being equal to the left ventricular pressure will lead to the computed backflow in the LCA, since the LV pressure is higher than the aortic pressure during the systole. This, however, is not in agreement with the physiological measurements, where the coronary flow rate is positive during both systole and diastole. In addition, the downstream pressure has to incorporate the resistance of the myocardium tissue and the capillary pressure. Consequently, the P_d value should be approximated as the sum of a scaled P_{LV} and the capillary level pressure P_{CA}. In the baseline case of the LCA blood flow, P_d is defined as $(0.75\% \cdot P_{LV} + P_{CA})$ mmHg, where a 75% reduction of P_{LV} accounts for the resistance of myocardium and P_{CA} = 15 mmHg is the approximated capillary level pressure (both P_{LV} and P_{ca} were measured in the 0D CVS model described in Chapter 4). These values were optimised for this particular case with the resulting computed flow chacteristics lying within the healthy physiological range and the computed FFR drop being in the agreement with the invasively measured value of 0.72 in the LAD and 0.83 in the LCx (Section 5.1). However, as it can be observed in Figures 5.24-6, variations in both P_{in} and P_d values produce significant differences in the computed FFR patterns. Table 5.1 specifies the P_{in} and P_d values for three cases with variations from the baseline (P_{in} = 90.80 mmHg and P_d = 52.50 mmHg) under the constant difference ΔP (Case I), the constant ratio dP (Case II), and the constant inlet pressure (Case III).

Table 5.1 Variations in inlet and downstream pressure in the BC models: case study

[mmHg]	**Case I: constant ΔP**				**Case II: constant dP**				**Case III: constant P_{in}**		
P_{in}	85.35	90.80	96.95		85.35	90.80	96.95		**90.80**	**90.80**	**90.80**
P_d	47.05	52.50	58.65		49.35	52.50	56.06		42.50	52.50	62.50
ΔP	**38.30**	**38.30**	**38.30**		36.00	38.30	40.89		48.30	38.30	28.30
dP	0.55	0.58	0.61		**0.58**	**0.58**	**0.58**		0.47	0.58	0.69

In the case of the constant ΔP value with the $P_{in} \approx$ +/- 6% and $P_d \approx$ +/- 10% varying from the baseline, the inlet flow rate Q_{in} remains the same under the changing dR (Figure 5.24.a) as well as the flow distribution between the outlets (Figure 5.24.b). This is in agreement with the hydraulic analogy of Ohm's law with $P_{in} - P_d = Q_{in} \cdot R_{total}$, where R_{total} is the total resistance of the vascular tree including the coronary tree itself and the peripheral resistance. At the same time, a constant difference between these cases can be observed in the computed

pressure P_{out} at the outlet of the stenosed branch (outlet#13), which is also in accordance with the expected flow solution results (Figure 5.23.b). However, since FFR is computed as P_{out}/P_{in} and is equal to P_d/P_{in} under dR = 0.0, there is an expected difference between these cases with FFR varying +/- 0.02 (Figure 5.23.c), which is significant with respect to the accuracy of FFR assessment (Figure 5.25.b). Since lower or higher FFR values correspond to the lower or higher dP = P_{in}/P_d ratio, respectively, further increasing or decreasing of the P_{in} and P_d values will affect the computed FFR patterns.

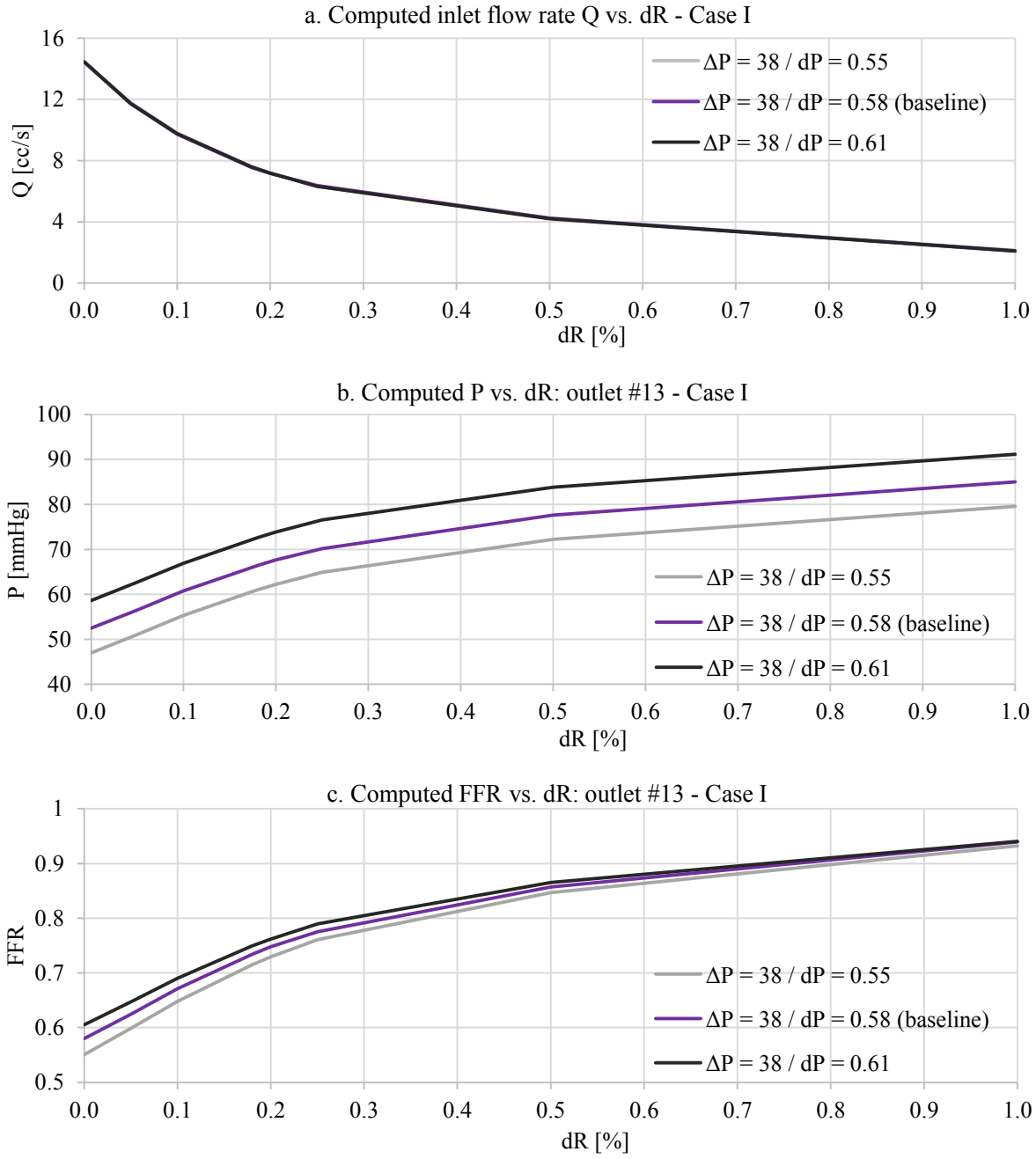

Figure 5.24 Computed inlet flow rate Q_{in} and P_{out} and FFR in the stenosed branch (outlet #13) vs. BC pressure condition with constant ΔP / Case I (dR = 0.2)

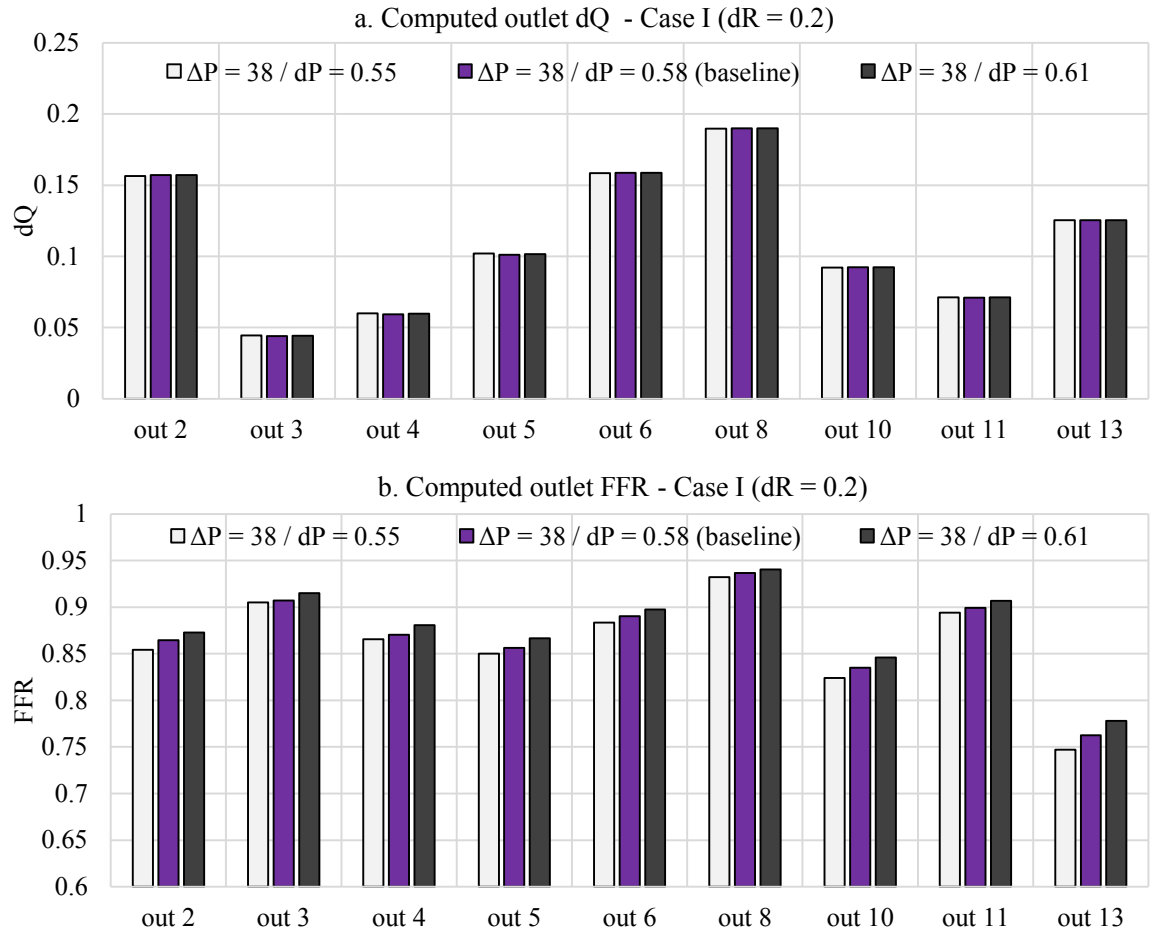

Figure 5.25 Computed outlet FFR and dQ vs. BC pressure condition with constant ΔP / Case I (dR = 0.2)

In Case II, the P_{in} values remain the same as in Case I, while P_d is changed so as to preserve the constant dP ratio. This means that this will change the inlet flow rate, which increases with an increased ΔP. Consequently, this will affect the pressure drop caused by a stenosis (which is increasing under higher flow rates, as well as the flow distribution in general). However, as can be observed in Figure 2.26, this does not produce such a major change as the variations in dP. Under the same P_d/P_{in} ratio set to 0.58, the +/- 2 mmHg difference in ΔP (with P_{in} = {85.35; 90.80; 96.95} mmHg) produced +/- 0.4 cc/s difference in the mean inlet flow rate with only slight changes in the flow rate distribution and a maximum difference of 0.006 in FFR. Furthermore, Figure 2.27 demonstrates how the inlet flow rate and dQ and FFR in the stenosed vessel change with ΔP varying within the 20-50 mmHg range, under the constant dP = 0.28. Even with the inlet pressure rising from 47 to 120 mmHg and the associated increase in flow rate from 4 to 9 cc/s, the difference in FFR did not exceed 0.034 with the flow distribution to this branch dropping by 0.012 with respect to the total flow, which was caused by the higher Q_{in}.

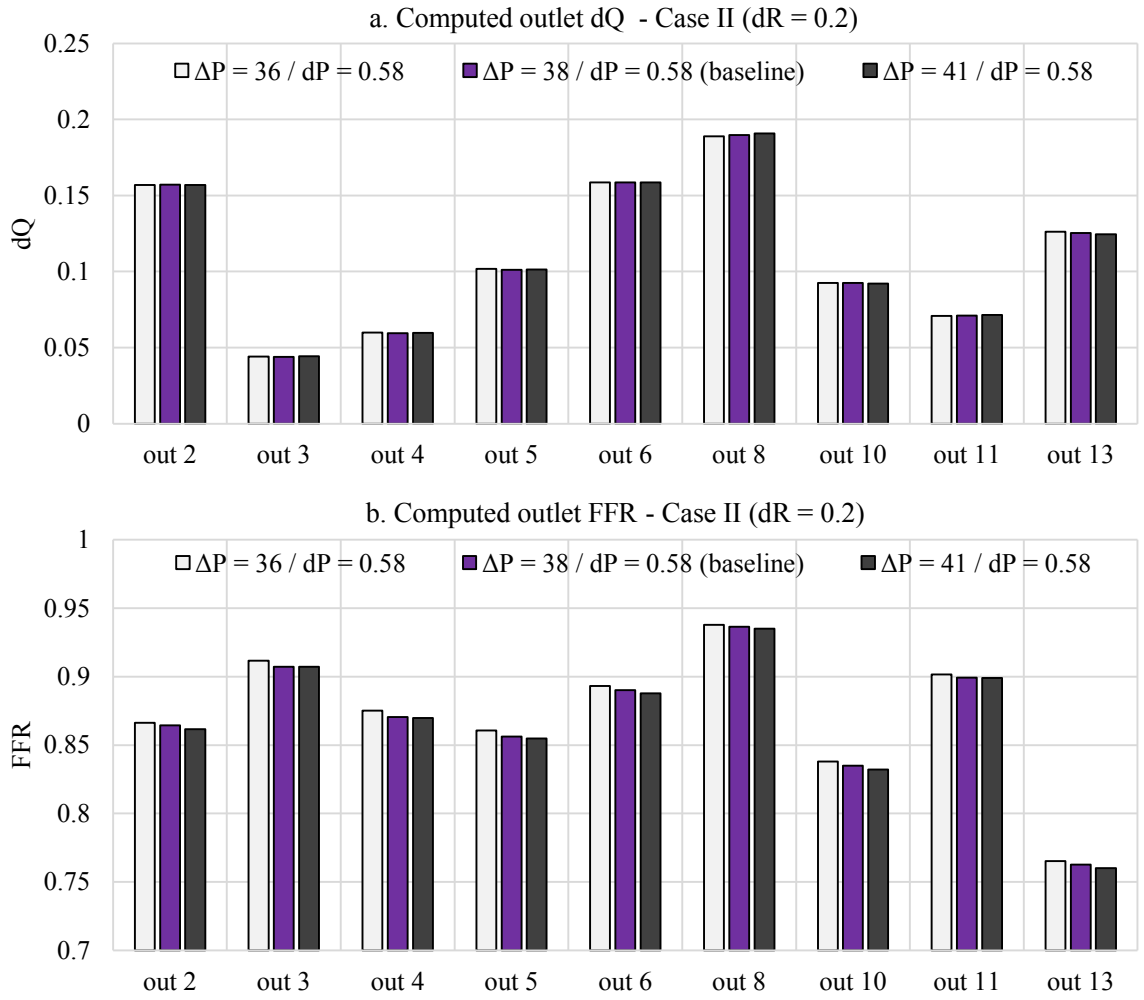

Figure 5.26 Computed inlet flow rate Q_{in} and P_{out} and FFR in the stenosed branch (outlet #13) vs. BC pressure condition with constant dP / Case II (dR = 0.2)

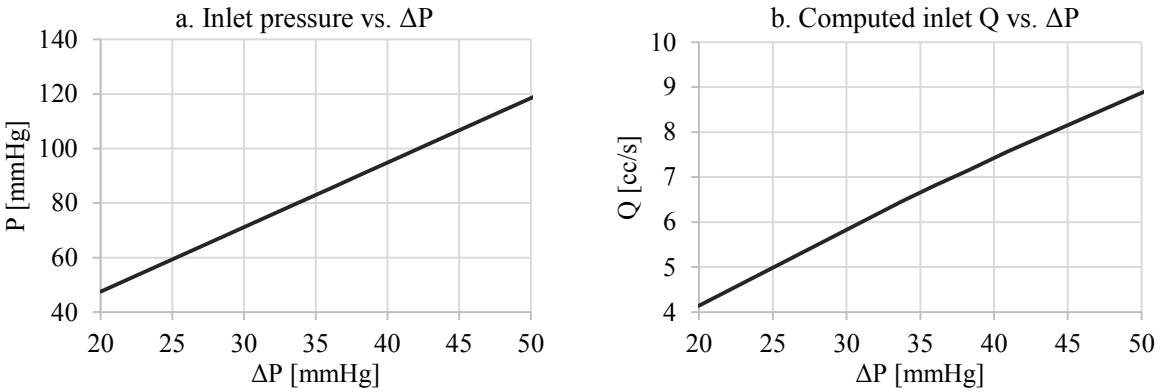

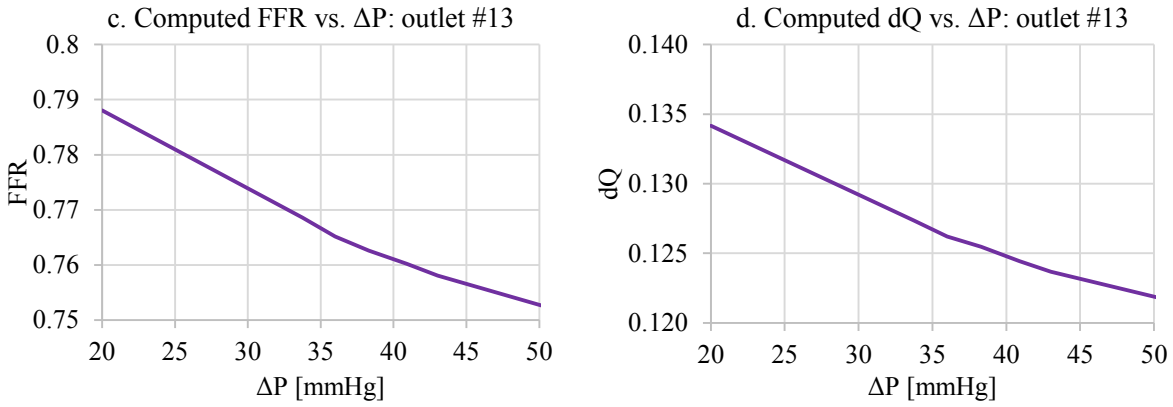

Figure 5.27 Computed inlet flow rate Qin and Pout and FFR in the stenosed branch (outlet #13) vs. ΔP under constant dP / Case II (dR = 0.2)

Figure 5.28 presents the results of Case III, where the downstream pressure changes with the constant inlet pressure P_{in} = 90.80 mmHg for the three cases of P_d = {42.50; 52.50; 62.50} mmHg. The corresponding changes in the computed flow rate and pressure fields are a combination of the impact of changes in ΔP and dP and therefore this will involve deviations in both FFR and dQ. In agreement with the hydraulic analogy to Ohm's law, higher magnitudes of the downstream pressure (under the same P_{in}) will cause lower inlet flow rates and lower pressure drop at the outlets. Consequently, the assessment of the accuracy and appropriateness of the approximation of P_d has to be performed through the validation of the model performance on the invasive measurements for several sets of clinical cases. Otherwise, similarly to variations in other modelling assumptions, this might lead to either overestimation or underestimation of FFR patterns.

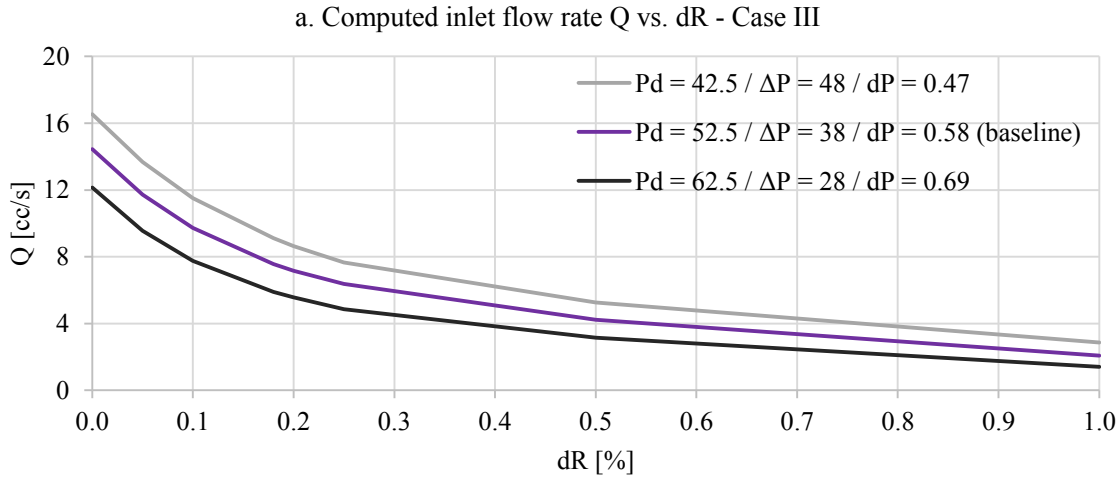

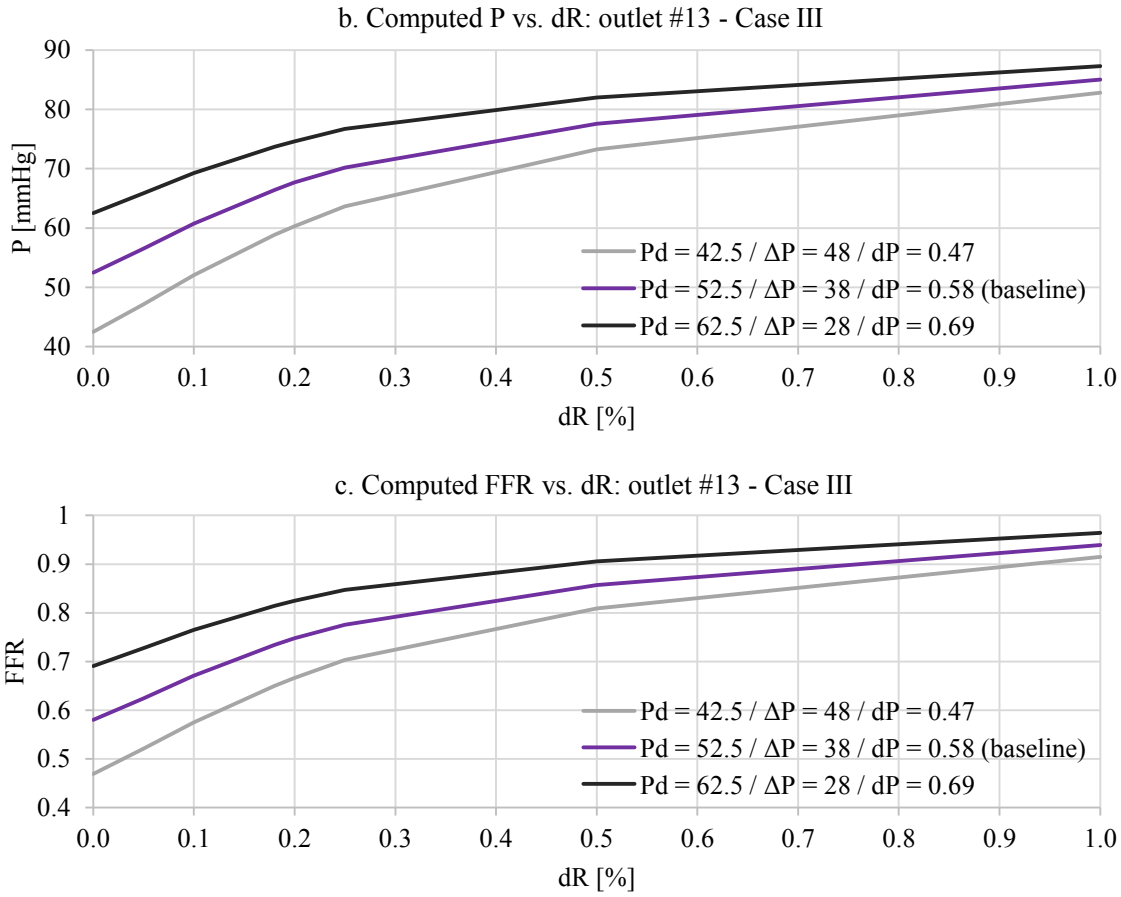

Figure 5.28 Computed inlet flow rate Q_{in} and P_{out} and FFR in the stenosed branch (outlet #13) vs. dR under constant P_{in} / Case III (dR = 0.0:1.0)

The value of blood viscosity depends on the red blood cell concentration, which increases when blood is more haemo-concentrated and decreases in the case of more haemo-diluted blood. The performed blood flow simulations under the blood viscosity value μ varying within the average physiological normal range at 37 °C of 0.0030 - 0.0040 Pa·s [2] showed that higher viscosity values lead to a higher pressure drop after the stenosis, since the blood flow resistance is proportional to the viscosity μ (4.1). For instance, as demonstrated in Figure 5.29.a, in two cases with μ = {0.0035; 0.0040} Pa·s, the difference in the computed FFR patterns is not critical (not exceeding 0.8%) and the difference in the TAWSS pattern magnitudes is around 4-8% on average, with a maximum value of 13%. Further increase of the viscosity value will lead to higher flow resistance of the vessel tree and higher pressure drop as shown in Figure 5.29.b with the difference between the two μ = {0.0035; 0.0055} Pa·s cases reaching 0.03 in FFR (0.763 vs. 0.733) in the stenosed vessel branch and more than 15% in the TAWSS patterns.

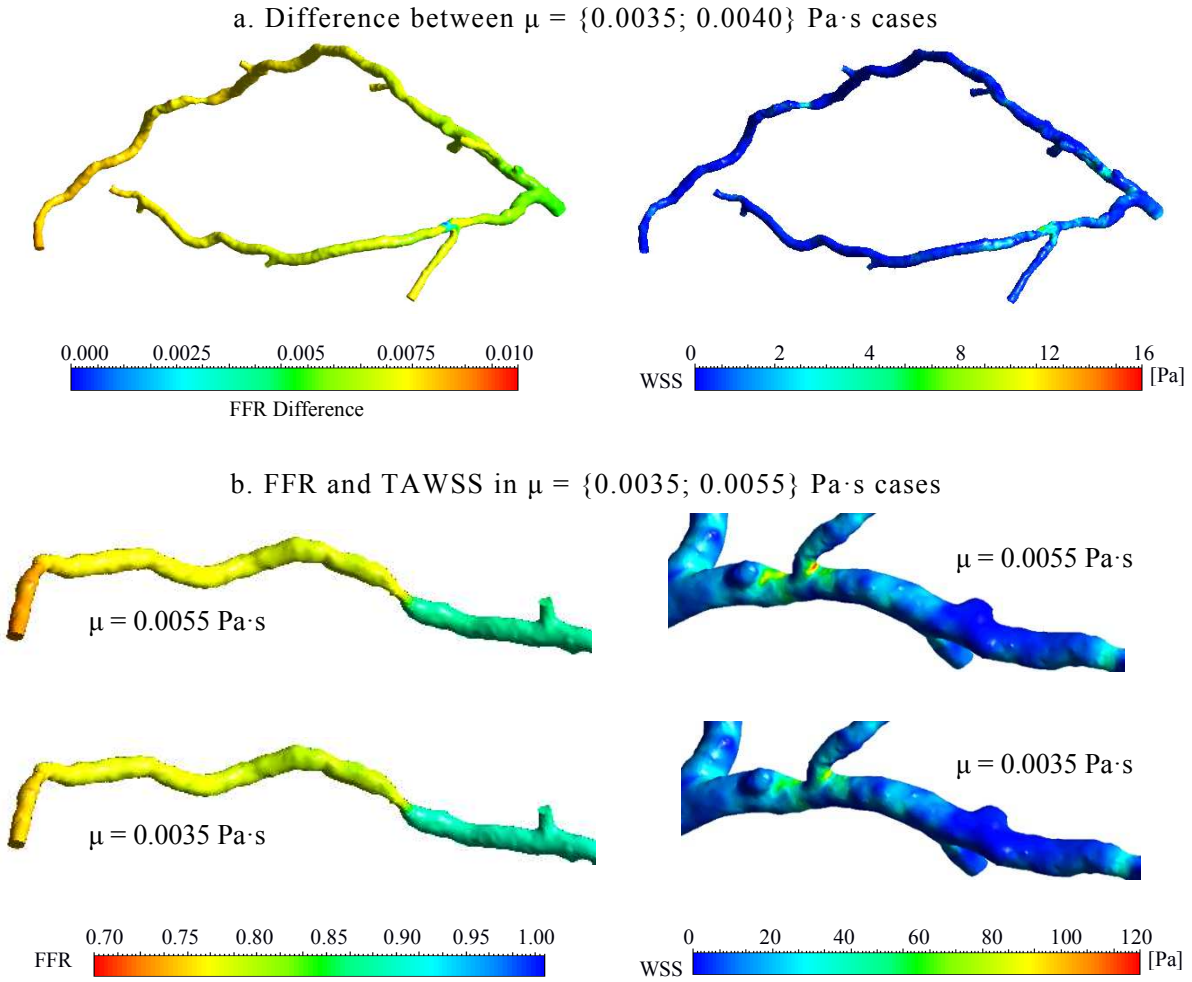

Figure 5.29 Difference in FFR and TAWSS in the stenosed branch vs. blood viscosity μ = {0.0035; 0.0040; 0.0055} Pa·s values (dR = 0.2)

Accordingly, it can be concluded that in the case of any known rheology-related pathologies (e.g., anaemia or hyperviscosity syndrome) patient-specific measured μ values have to be used in simulations for FFR assessment, while the use of average values can be considered as acceptable in normal blood condition cases. However, with respect to the assessment of CAD-associated TAWSS patterns or other WSS-derived parameters, the use of patient-specific values for blood viscosity is essential as it can affect simulation results and lead to a less accurate analysis. Other research works devoted entirely to the investigation of the influence of different blood viscoelasticity models [130] also demonstrated that deviations in μ values and the use of non-Newtonian models can significantly change the computed WSS patterns.

5.3 Investigation of the Impact of Coronary Artery Lumen Reconstruction Parameters

Since the vessel tree lumen boundary defines the 3D computational domain for blood flow models, the computed flow patterns directly depend on the parameters of the vessel tree geometry reconstruction method. This section investigates the influence of such parameters as the lumen segmentation threshold, the side branch truncation level, and the degree of surface smoothing on the computed FFR and TAWSS patterns. The choice of these parameter values varies depending on the patient-specific nature of the coronary artery geometry, vessel segmentation software settings, and the employed strategy for preparation of volume mesh.

5.3.1 Vessel Segmentation Blood Threshold

As described in Section 3.2.1, during the segmentation of the vascular tree from a CCTA volume, the choice of contrast blood segmentation threshold can significantly affect the accuracy of lumen reconstruction, since it may vary within the 200 – 400 HU range [134], depending on patient-specific and acquisition procedure related factors. Consequently, it is reasonable to investigate the impact of the segmentation threshold value on the computed flow fields in order to emphasise the importance of thorough assessment of the vessel reconstruction results before proceeding with blood flow simulations. In this case study, the LCA tree is reconstructed from the CCTA volume under three threshold values {210; 270; 350} HU for the contrast enhanced blood, with 350 HU being used for the baseline case, since it was identified as being the optimal in comparison with the manual segmentation results. For each of these cases, the FFR and TAWSS values computed under hyperaemia are presented in Figure 5.30. The increased threshold value “revealed” the LAD stenosis through a diameter reduction from 15% to 70-75% for the two values of 210 and 350 HU, respectively. Therefore, while the two cases of 210 and 270 HU do not show the presence of stenosis with FFR being ≈ 0.83 and above the critical threshold of 0.75, the computed FFR for the 350 HU case with 70-75% stenosis is 0.763. The wall shear stress patterns are also affected as can be observed in the computed TAWSS in the LCx bifurcation. TAWSS replicates the “revealed” internal vessel lumen with all irregularities present due to the atherosclerotic lesions along the vessel branch.

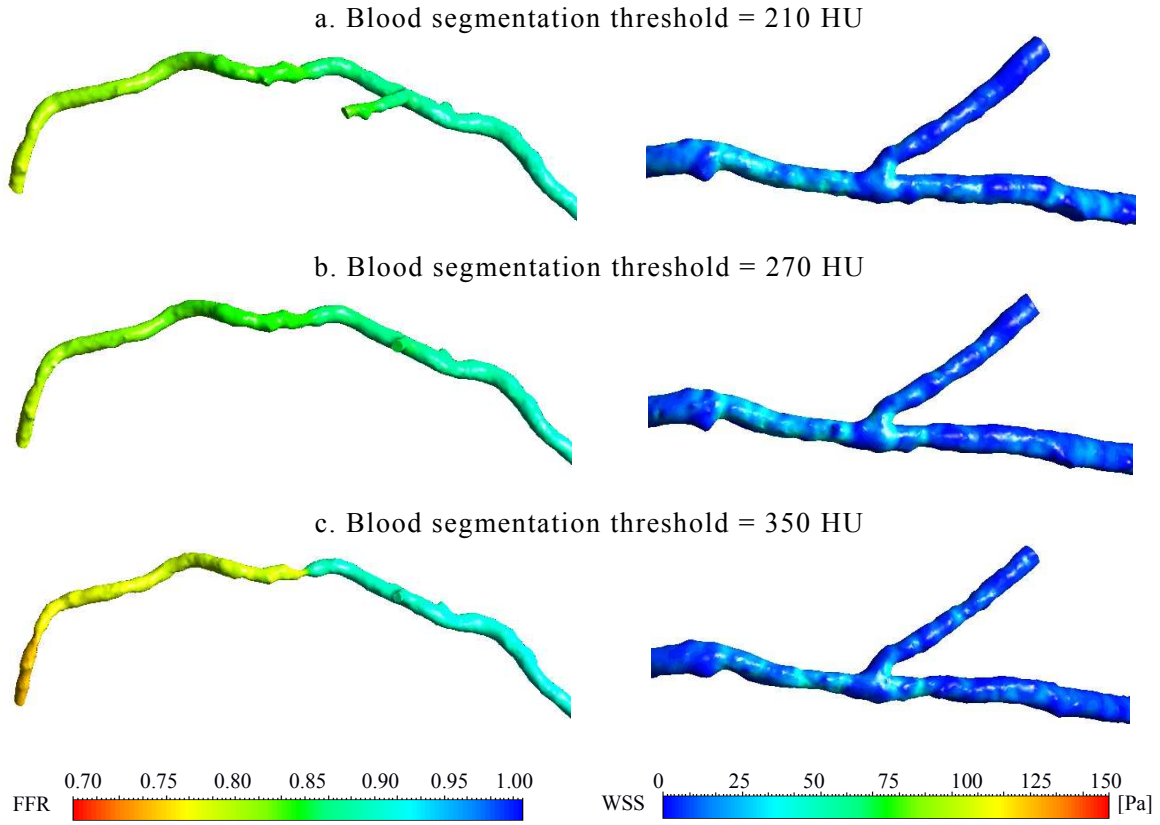

Figure 5.30 Computed 3D FFR in the stenosed LAD branch and TAWSS in the LCx bifurcation vs. blood segmentation threshold (dR = 0.2)

In addition, since of the vessel diameter is generally narrower under the higher threshold as well as the presence of stenoses, this resulted in the lower inlet flow for the 350 HU case. Even after the adjustment of peripheral resistance, in the 350 HU case, the flow rate is approximately 20% lower for dR values below 0.20 (Figure 5.31).

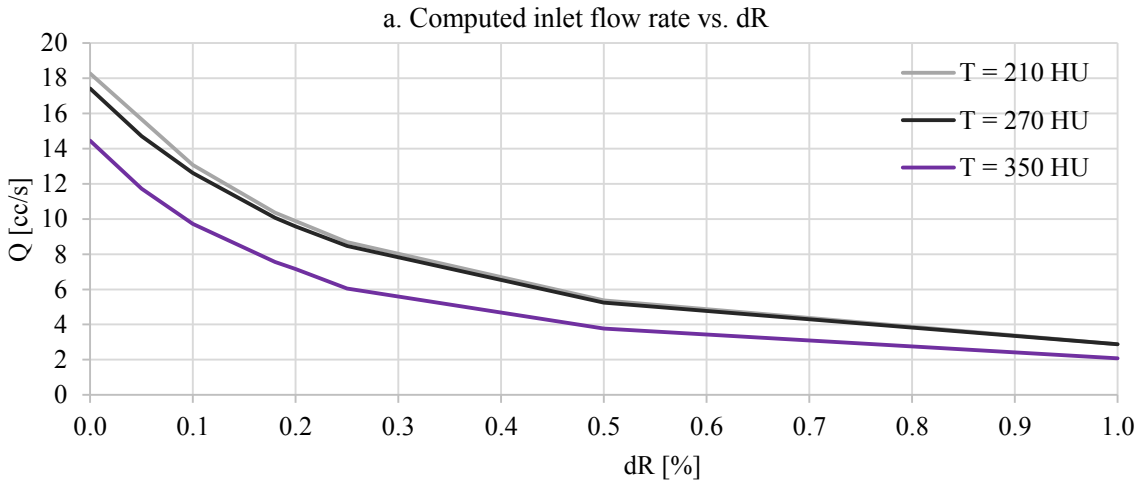

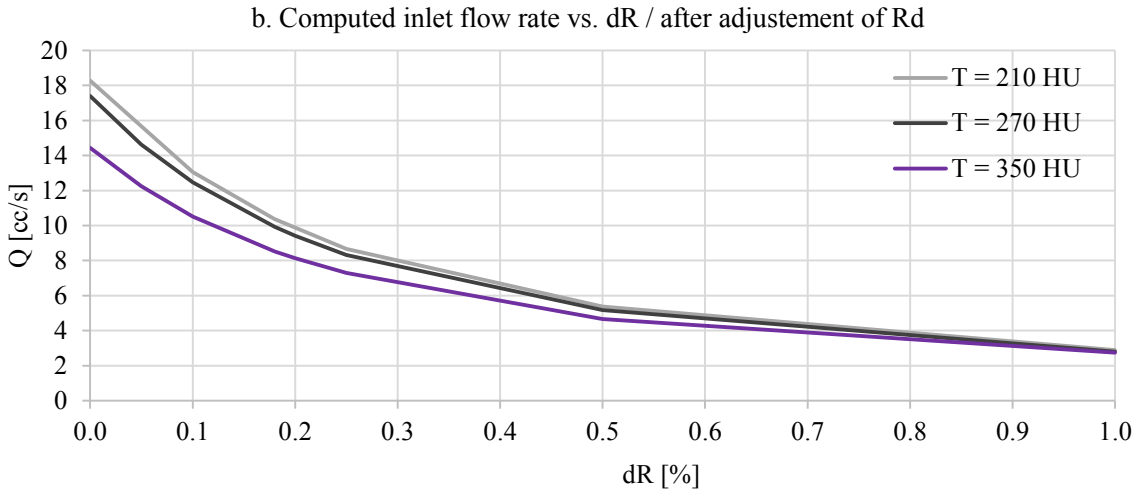

Figure 5.31 Computed inlet flow rate for three segmentation threshold cases before and after adjustment of peripheral resistance (dR = 0.0:1.0)

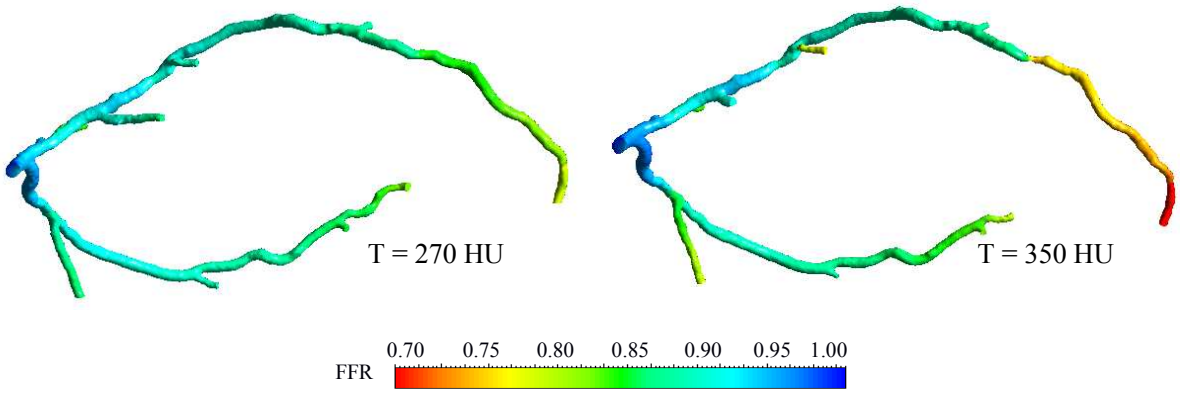

Figure 5.32 Computed 3D FFR for the 270 and 350 HU cases of the segmentation threshold after adjustment of peripheral resistance (dR = 0.2)

Figures 5.32-33 demonstrate the simulation results after the performed adjustment of peripheral resistance. It can be observed that in the stenosed LAD branch with outlet #13, the difference in FFR becomes significantly pronounced with a value of 0.83 for 270 HU case versus 0.714 for the 350 HU case. Since the segmentation threshold also affects the side branch outlet diameters, the general flow distribution patterns also change with respect to the average outlet diameter value. For instance, in outlet #6 the diameters for the 210, 270 and 350 HU cases are {195; 0.205; 191} cm respectively, while the derived dQ values are {0.110; 0.132; 0.146}, respectively (Figure 5.33.a). It also can observed that although, in theory, a threshold of 270 HU should result in a higher degree of LAD stenosis and a higher pressure drop in branch with outlet #13, respectively, the FFR for the 270 HU case is higher than in the 210 HU case due to the lower dQ to this branch.

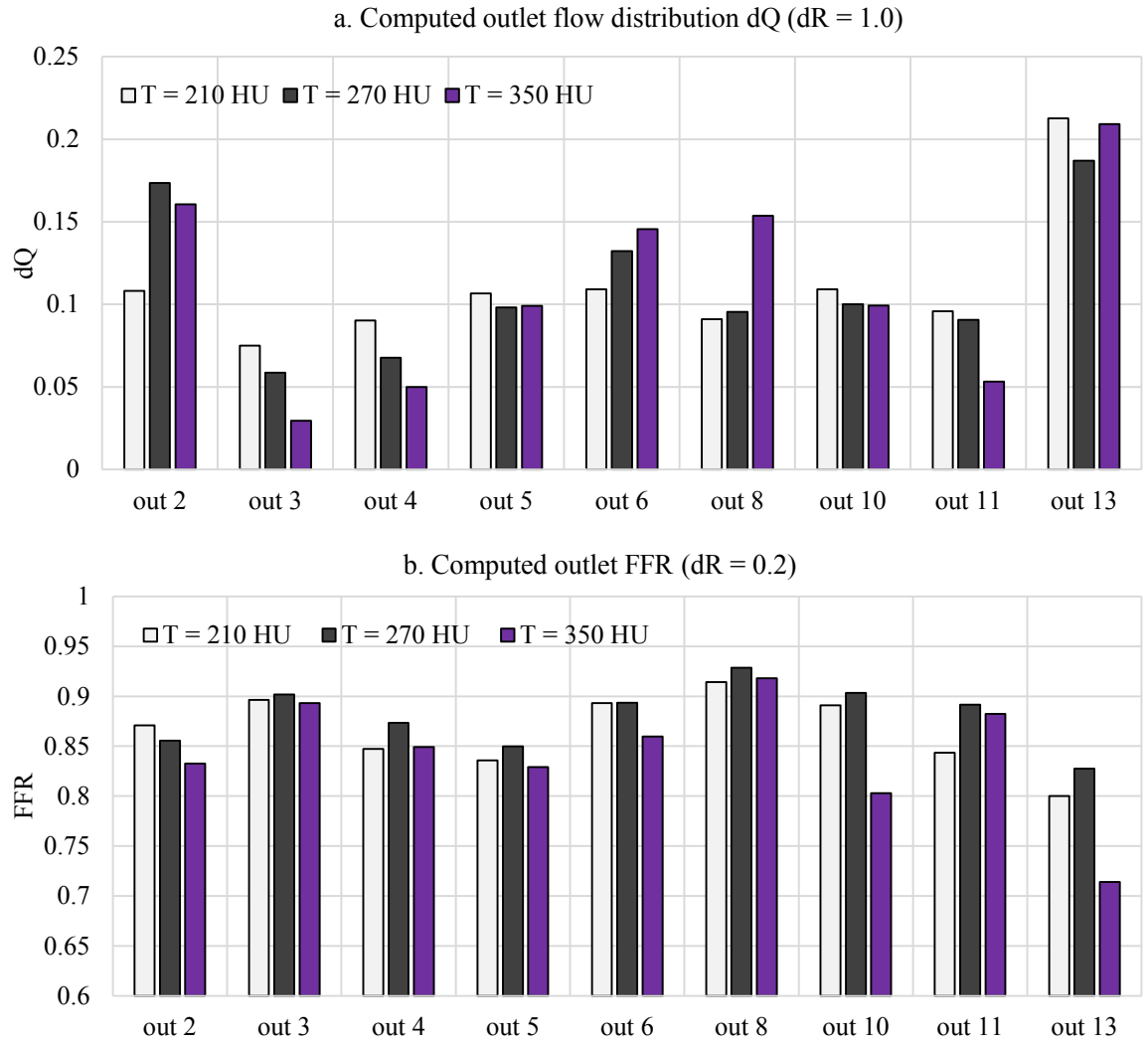

Figure 5.33 Computed outlet FFR and dQ for three different segmentation threshold cases after adjustment of BC parameters

In addition, Figure 5.34 presents the computed dQ and FFR at the outlet of the stenosed branch (outlet #13). As expected, the slopes of both dQ and FFR are significantly lower for the 350 HU case with the revealed stenosis. These results are also interesting from the point of view of comparison of the flow-limiting impact of the stenoses of various degree in the same geometries. Therefore, it can be concluded that the choice of the vessel segmentation parameter values is critical with respect to the accuracy of the simulation results. The corresponding general guidelines are to choose the segmentation threshold as high as possible in order to avoid inclusion of fibrous plaque and vessel wall components into the lumen surface. In addition, the verification of the 3D segmentation results for all branches of the coronary artery tree has to be performed before discretisation of the computational domain.

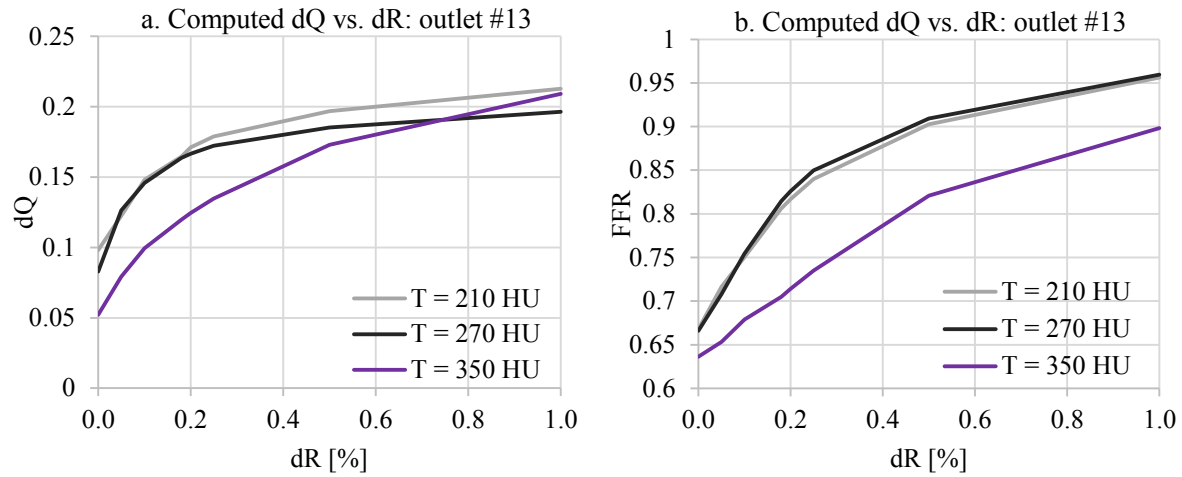

Figure 5.34 Computed FFR and dQ in the stenosed branch (outlet #13) for three different segmentation threshold cases after adjustment of BC parameters (dR = 0.0:1.0)

5.3.2 Side Branch Outlet Truncation Levels

The next aspect of the preparation of the vessel tree geometry for the computational domain is related to the level of outlet truncation for side branches, since in accordance with the BC requirements, the flow rate distribution for a particular branch is directly defined from the outlet diameter (Section 3.3.3). Higher flow rates produce a higher pressure drop along a stenosis and therefore it is logical to assume that in stenosed branches with wider outlets the pressure drop produced by the stenosis will be higher. However, at the present time, there are no clear guidelines regarding the optimal truncation level of vessel branches in coronary blood flow models and its influence on the computed pressure and flow pattern is not investigated.

According to the SCCT guidelines [16], it is the general practice that only branches with up to 2 mm diameter are analysed for the presence of CAD. At the same time, vessel segmentation methods imply a trade-off between the level of detail and the quality of lumen segmentation. This is particularly essential in the case of the presence of plaques with fibrous cap, due to the low HU contrast for soft tissues along with the relatively low CCTA resolution and dissipation of contrast agent in narrow branches. Consequently, this means that although it might be beneficial to incorporate as high as possible level of detail into the model, care should be taken regarding the reconstruction accuracy of narrow side branches. In theory, the accuracy of reconstruction can also be assessed by comparing the reconstructed geometry with the general vessel tree scaling laws [77] with the 0.95/0.52 average bifurcation diameter asymmetry scale and the 20-30 range for the branch length/diameter ratio.

Figures 5.35-36 present the FFR and TAWSS patterns computed under hyperaemia for two cases of LCA geometry reconstruction: (i) original LCA surface including all detected side branches; (ii) LCA surface with side branches truncated either up to ≈ 2 mm diameter or as close as possible to the main branch. Despite the difference in the flow rate distribution to the stenosed branch (outlet #13), both cases result in a similar pressure drop in the LAD artery with FFR ≈ 0.765. However, the computed FFR is different in the LCx branch (outlets #2-5) with ≈10% lower pressure drop for the LCA truncated case. Due to the higher flow rates, this difference is also prominent in the TAWSS magnitude in the LCx bifurcation.

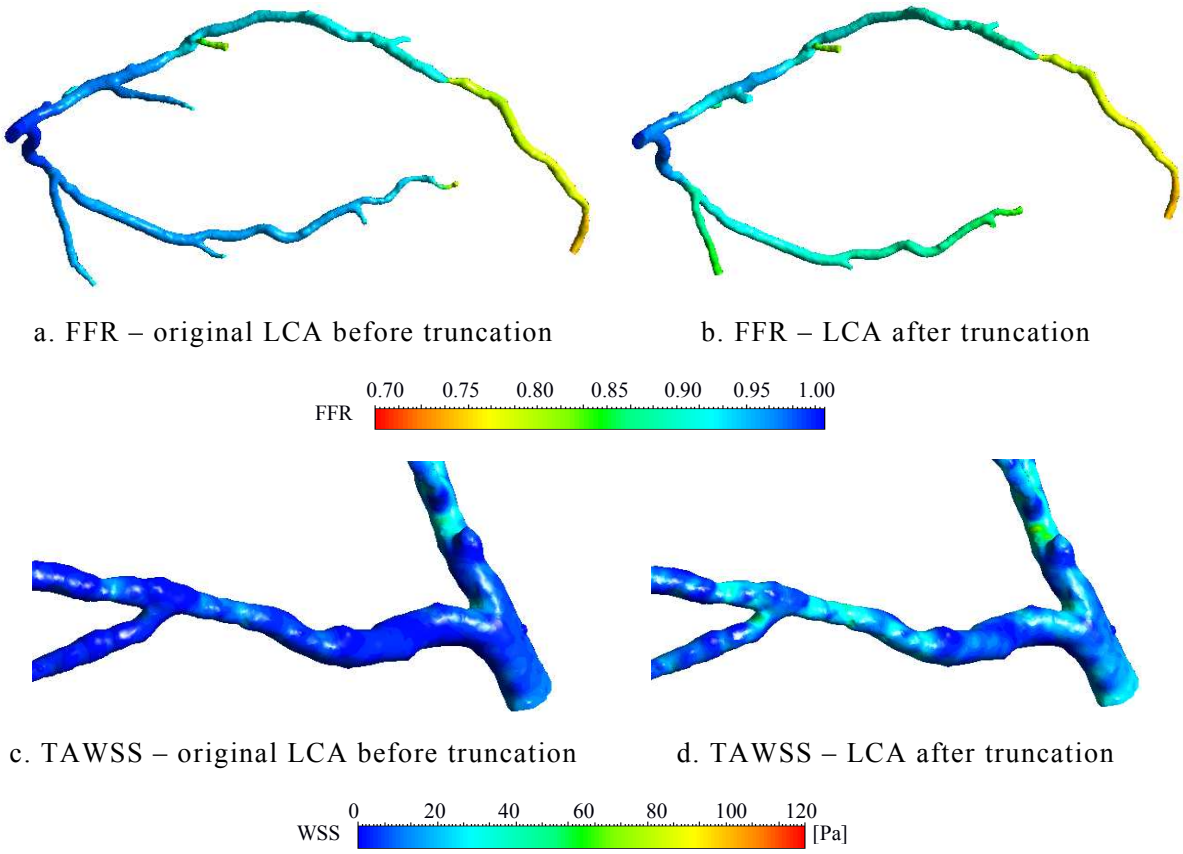

Figure 5.35 Computed 3D FFR and TAWSS before and after truncation of side branches up to ≈2 mm level (dR = 0.2)

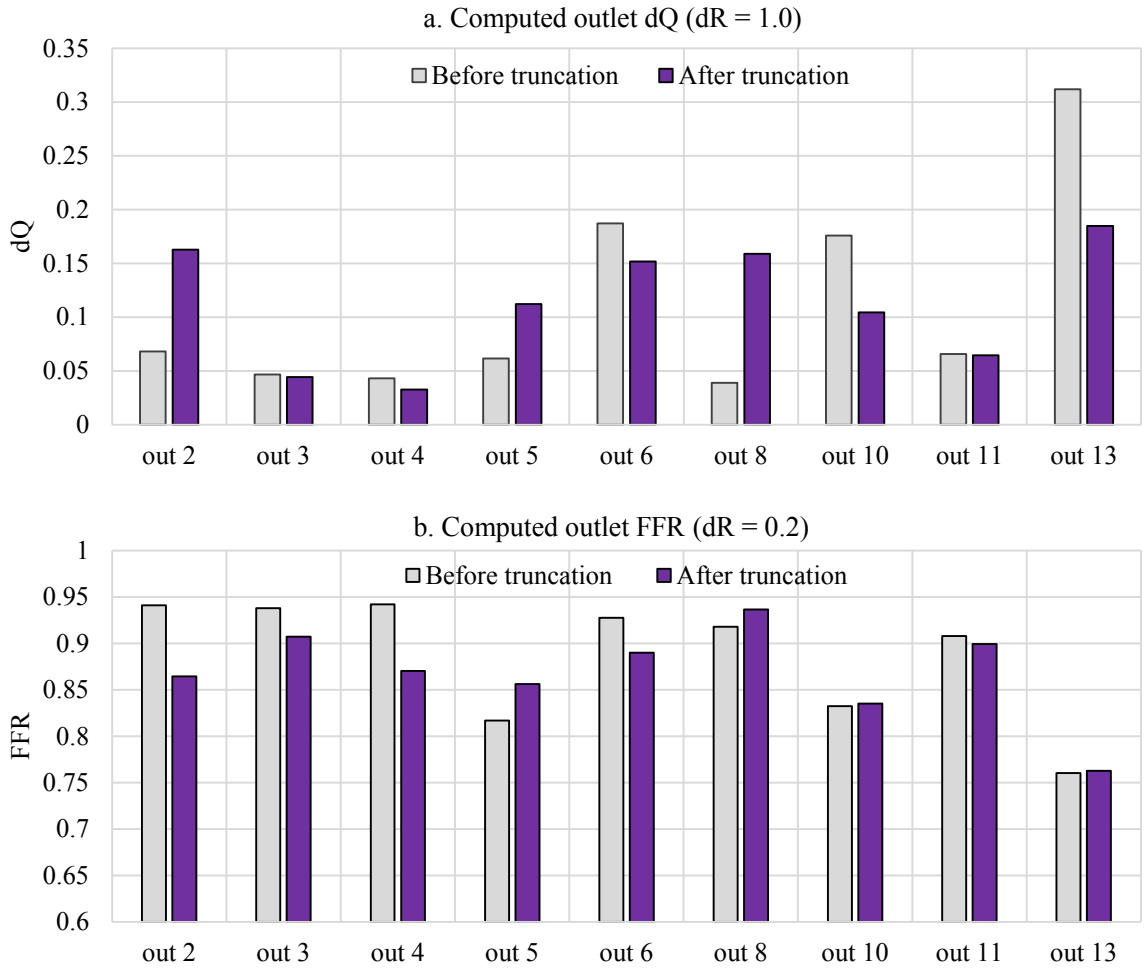

Figure 5.36 Computed outlet FFR and dQ before and after truncation of side branches (dR = 0.2)

In theory, the pressure and FFR in healthy branches should not be affected by the wider outlet diameter since it is computed as $P_{out}(t) = P_d(t) + R_d \cdot Q_{out}(t)$ (in the case of 0D R outlet BC model) and the lower peripheral resistance value will be compensated by the higher flow rate to this branch and the other way around for the narrower outlet. For instance, as shown in Table 5.2, after the truncation of the side branch at outlet #8 from 0.092 cm to 0.1933 cm diameter, the downstream resistance became approximately 9 times lower, with the corresponding flow rate distribution dQ to this branch increasing to 0.152 from 0.028. While the diameter of outlet #13 is the same in both cases (0.2161 cm), the derived dQ for this outlet is 0.3830 for the original LCA and 0.2111 for the truncated LCA. This difference is caused by the fact that the remaining branches in the original LCA have significantly narrower diameters and thus lower dQ.

Table 5.2 Outlet diameters and computed resistances for the original and truncated LCA

Original LCA volume			
out #	d [cm]	dQ^3	$R \cdot 10^5$ [dyn·s/cm^5]
1	0.0000	0.0000	0.0000
2	0.1127	0.0543	2.1110
3	0.0969	0.0345	8.3890
4	0.0956	0.0332	8.6540
5	0.1114	0.0525	5.9130
6	0.1687	0.1825	2.0740
7	0.0000	0.0000	0.0000
8	**0.0902**	**0.0278**	**10.1220**
9	0.0000	0.0000	0.0000
10	0.1676	0.1788	2.1110
11	0.1120	0.0534	5.9080
12	0.0000	0.0000	0.0000
13	0.2161	0.3830	1.1320

LCA volume after side branch truncation			
out #	d [cm]	dQ^3	$R \cdot 10^5$ [dyn·s/cm^5]
1	0.0000	0.0000	0.0000
2	0.1967	0.1603	1.4247
3	0.1120	0.0296	5.9084
4	0.1329	0.0494	3.8099
5	0.1676	0.0991	2.1115
6	0.1906	0.1457	1.5494
7	0.0000	0.0000	0.0000
8	**0.1933**	**0.1521**	**1.5137**
9	0.0000	0.0000	0.0000
10	0.1672	0.0983	2.1497
11	0.1372	0.0544	3.5026
12	0.0000	0.0000	0.0000
13	0.2156	0.2111	1.1323

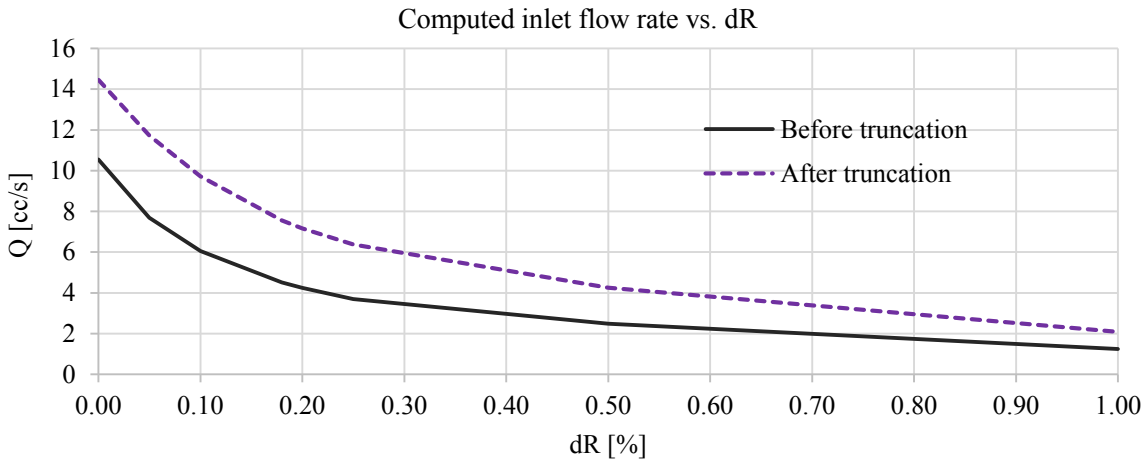

Figure 5.37 Computed inlet flow rate before / after side branch truncation (dR = 0.0:1.0)

However, for the cases with stenosed branches, the dQ values will affect the computed flow patterns since stenoses produce a higher pressure drop under higher flow rates and result in redistribution of flow between the branches. It also can be observed that for the original LCA case before truncation, the computed inlet flow rate is significantly lower with ≈ 25% difference caused by the higher peripheral resistance. This difference further increases under the higher degree of vasodilation (Figure 5.37).

The performed adjustment of R_d with respect to the computed inlet flow rate and outlet dQ requirements further enhances the difference between these two cases (as demonstrated in Figure 5.38). In the original LCA case, the flow to the LCx branch is significantly lower than in the truncated LCA due to the narrower outlet diameters. This leads to flow redistribution

with the higher flow rate in the LAD artery, which results in the higher pressure drop after the stenosis with the FFR value being equal to 0.66 compared to 0.714 prior to adjustment. Subsequently, this also causes the FFR in the LCx branch to be lower in the original case with a difference of up to 0.12, which is significant with respect to CAD severity assessment.

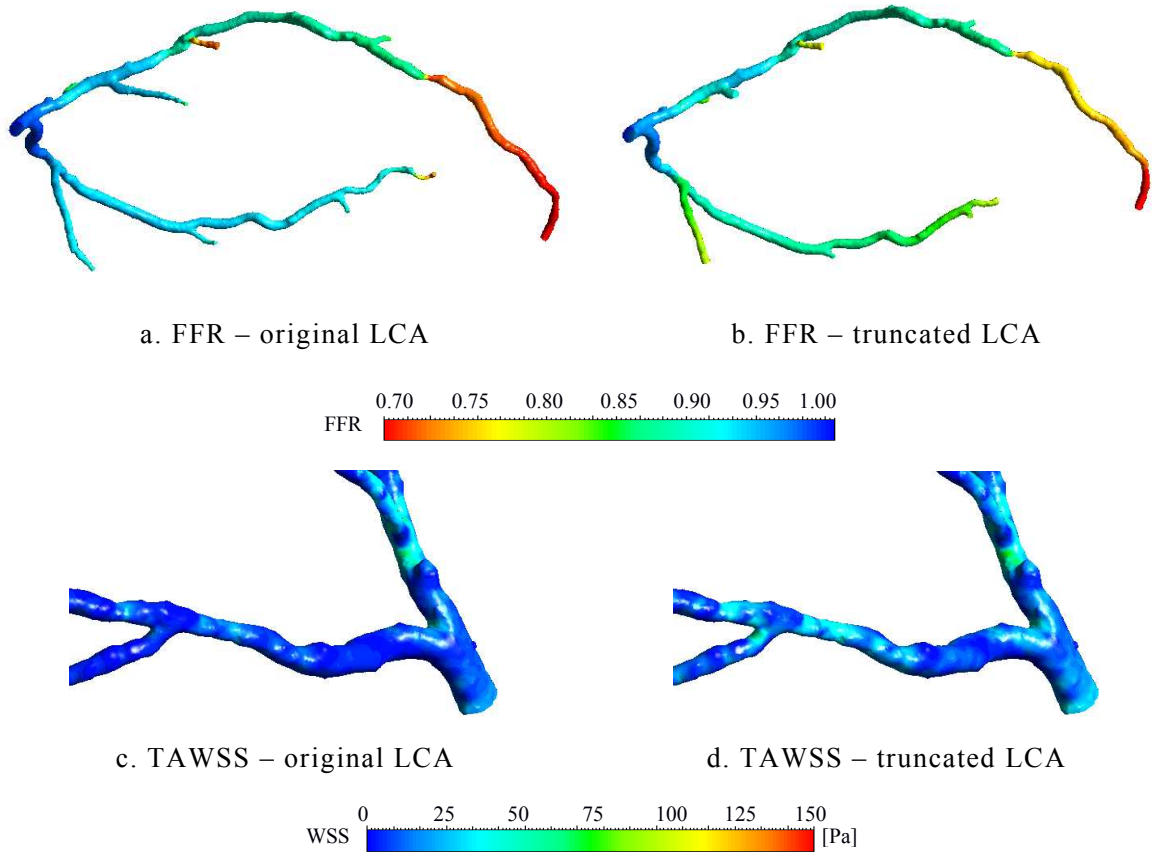

Figure 5.38 Computed 3D FFR and TAWSS before / after truncation of side branches after adjustment of peripheral resistance (dR = 0.2)

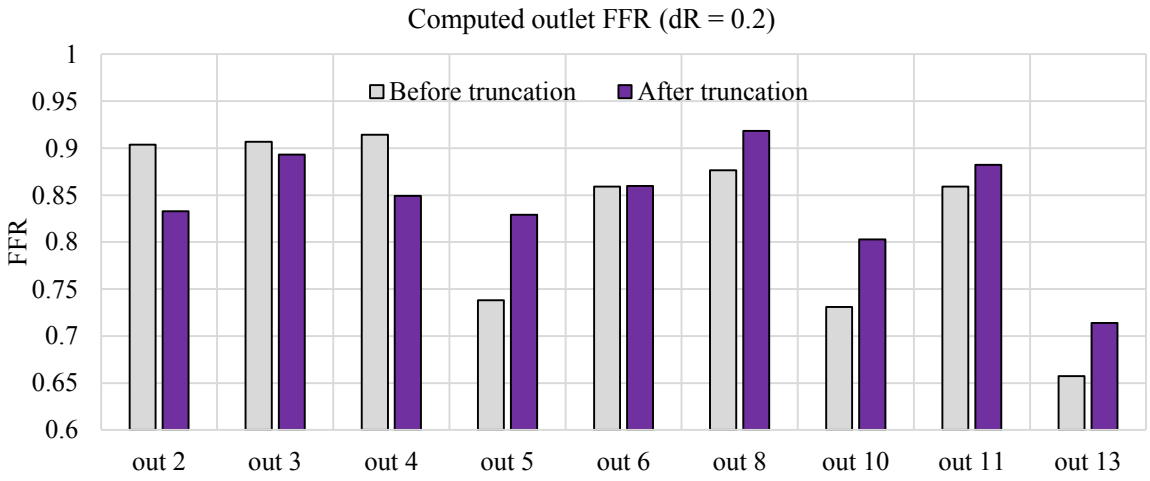

Figure 5.39 Computed outlet FFR before / after truncation of side branches after adjustment of peripheral resistance (dR = 0.2)

A similar situation is observed in the comparison of wall shear stress patterns with the computed TAWSS being significantly higher in the LCx bifurcation and the truncated LAD side branches. The difference between these two cases is shown in Figures 5.39-40 with the difference in FFR varying within +/- 12% range and the maximum change in TAWSS reaching 30%.

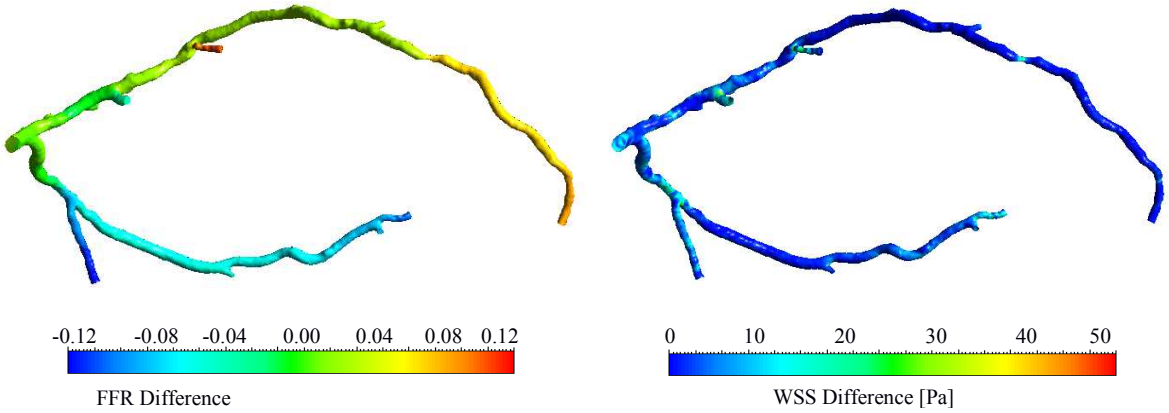

Figure 5.40 Difference in the computed 3D FFR and TAWSS before and after truncation of side branches with adjustment of peripheral resistance (dR = 0.2)

The results of a similar case study for the LCA volume reconstructed under a lower segmentation threshold (270 HU) and thus characterised by a lower LAD stenosis degree (Section 5.3.1) are shown in Figure 5.41. In the same manner, the difference in the computed FFR after the LAD stenosis and in the LCx branch originates from the different flow distribution patterns due to the geometry-derived dQ requirements for different outlet diameters. In other words, due the outlet #13 being wider than the rest of the outlets, the flow rate to the stenosed LAD branch is higher in the case before the side branch truncation, which emphasises the impact of the present stenoses.

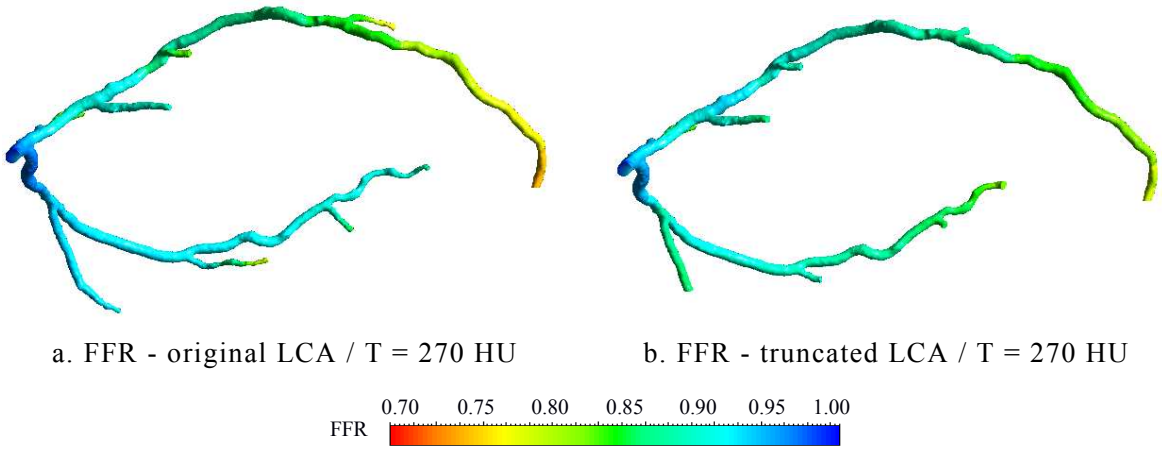

Figure 5.41 Computed FFR and before and after truncation of side branches with a lower segmentation threshold (270 HU) after adjustment of peripheral resistance (dR = 0.2)

In summary, it can be concluded that the results of the blood flow simulations and the assessment of both FFR and TAWSS are significantly affected by the choice of the side branch truncation level. This is caused by the requirement for the downstream BC models that defines the flow distribution with respect to the vessel tree outlet diameters. In addition, the CCTA resolution being generally insufficient for accurate reconstruction of narrow vessels together with the disadvantages of threshold-based segmentation may lead to erroneous estimation of the outlet diameters. Thus, if the extracted side branch diameter is lower than the actual vessel, the associated dQ will be lower and will also result to the lower flow rate in this branch. Consequently, the optimal strategy should be based on setting the truncation level to be above 2 mm or as close as possible to the main branch in the case of narrower side branches.

5.3.3 Degree of Lumen Surface Smoothing

The choice of the method and the degree of smoothing the surface mesh of the extracted vessel lumen also affects the blood flow simulation results. While being insignificant in the case in the volume-preserved smoothing methods are applied, this is especially pronounced in the case of the applied high degree Laplacian smoothing, since it changes the geometry by affecting the vessel diameter. However, smoothing is generally required in order to eliminate surface roughness caused by the insufficient resolution of CCTA and threshold based segmentation. Figure 5.42 presents the FFR values computed under hyperaemia for three cases of smoothing: (i) no smoothing; (ii) moderate smoothing; (iii) high degree Laplacian smoothing (6 iterations). While the global flow patterns remain similar with the FFR drop present after the stenosed regions in all cases, there is a difference in the magnitude of these changes. For instance, in the case of high Laplacian smoothing, the diameter of the LAD stenosis becomes narrower, thus resulting in lower FFR values after the stenosis region and generally lower computed inlet flow rates.

a. No smoothing

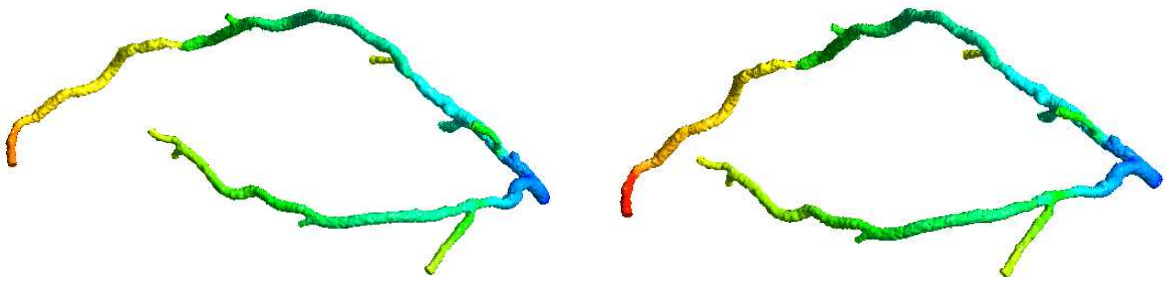

- before adjustment of R_d - after adjustment of R_d

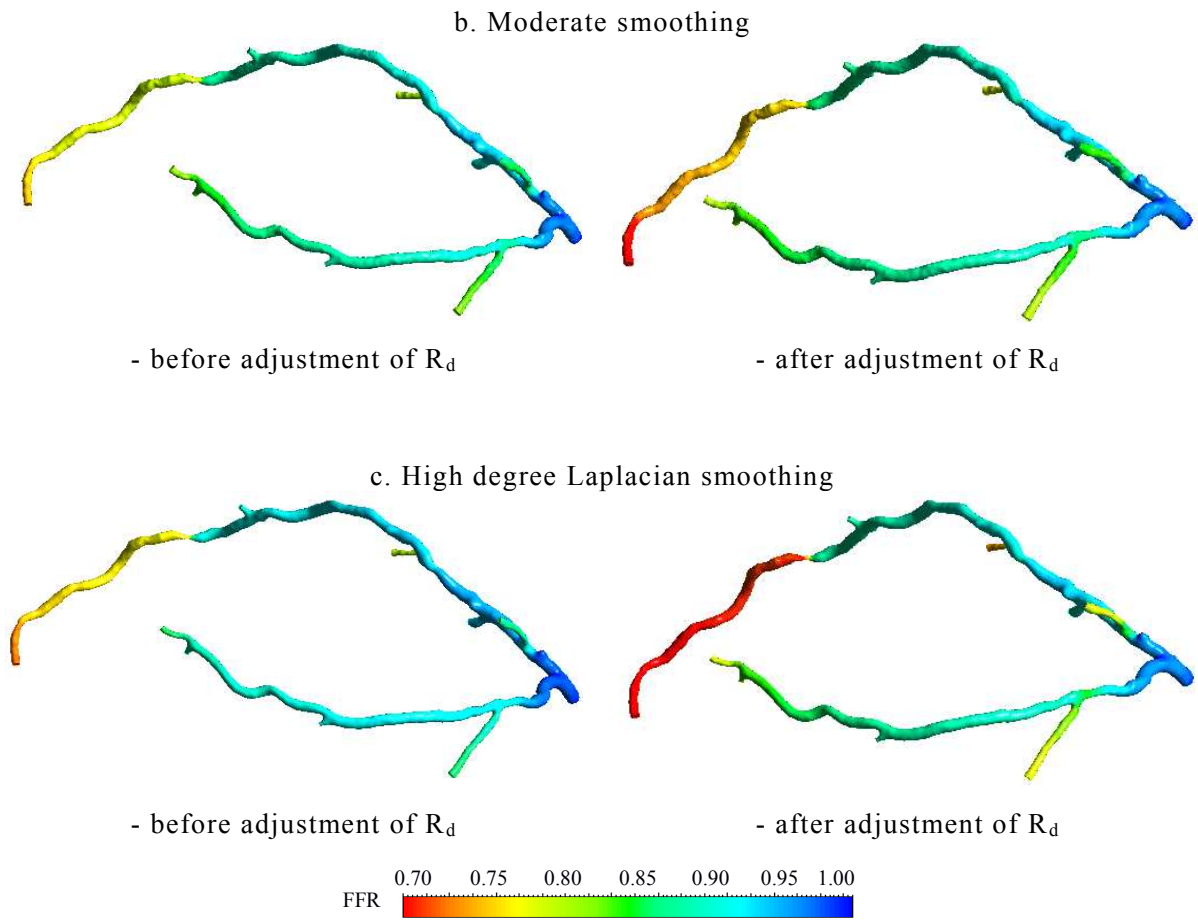

Figure 5.42 Computed FFR and TAWSS vs. degree of surface smoothing before and after adjustment of peripheral resistance (dR = 0.2)

In order to compare these cases under the same inlet flow conditions, the adjustment of the peripheral resistance was performed. It can be observed that while the original and moderately smoothed surface cases result in very similar FFR patterns, the FFR drop after the stenosis is significantly more prominent in the third case with the value of 0.673 compared to 0.715 for the other two cases. This is caused by the nonlinear relation between the flow resistance of vascular geometries and vessel diameter ($R \sim D^{-4}$). In other words, while not producing a significant influence on the blood flow computed in healthy vessel geometries, a high degree smoothing affects the results for complex geometries with stenoses or in the presence of narrow branches and can lead to overestimation of the FFR drop.

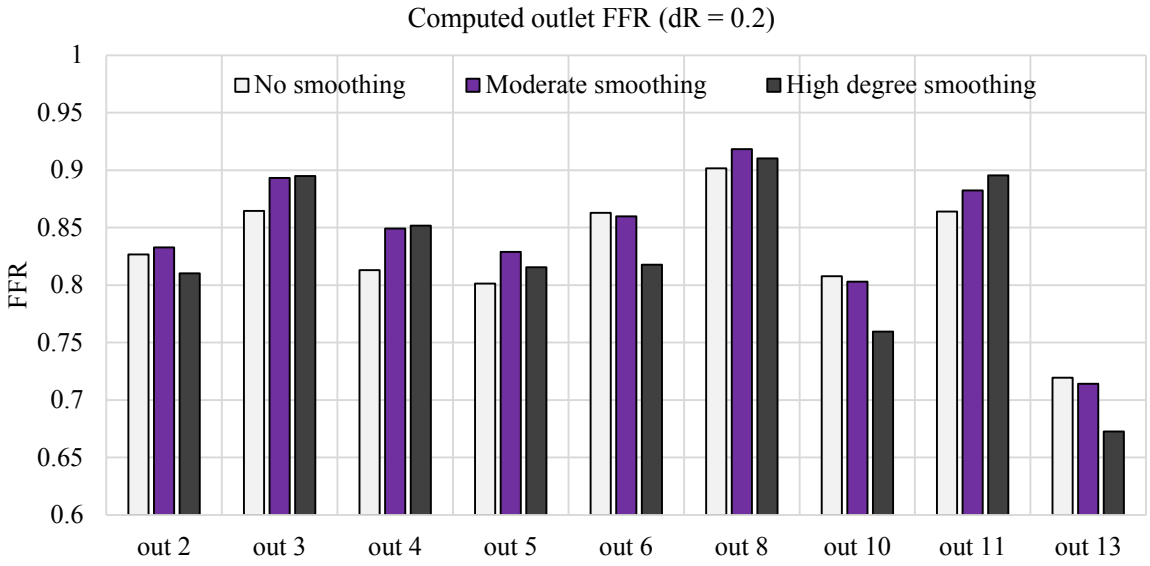

Figure 5.43 Computed outlet FFR for three cases of surface smoothing degree after adjustment of peripheral resistance (dR = 0.2)

This difference can also be clearly seen in the WSS patterns shown in Figure 5.44. Although, the computed TAWSS magnitude in the LAD bifurcation is higher in the smoothed geometry case due to the narrower vessel diameter, the TAWSS patterns remain similar replicating the variations in vascular structures. Subsequently, the choice of the degree of smoothing should be optimised in order to remove surface roughness, which is not present in the actual vessel lumen, being caused by imperfect segmentation, but, at the same time, the original geometry dimensions have to be preserved. This issue can be also be resolved by application of the volume-preserving smoothing methods [135].

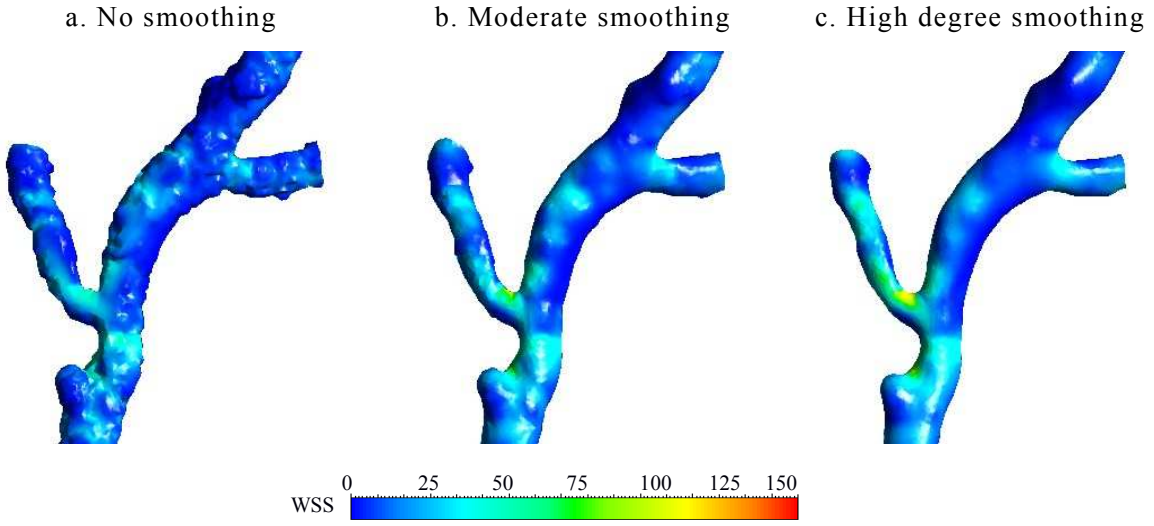

Figure 5.44 Computed TAWSS in the LAD bifurcation vs. degree of surface smoothing after adjustment of peripheral resistance (dR = 0.2)

5.4 Comparison of 0D and 3D Blood Flow Models

This section investigates the correlation between the computed 0D and 3D blood flow in patient-specific coronary arteries in order to assess the accuracy and applicability of 0D blood flow simulations and flow resistance in the assessment of functional stenosis severity. At first, the proposed novel approach for extension of lumped-parameter vascular models with spatial information is investigated in a single stenosed vessel branch case, modelled through a series of resistors, each corresponding to an elementary 3D vessel segment. The computed 0D and 3D blood flow fields are compared with respect to the FFR drop and flow rate. Next, the results of 0D and 3D blood flow simulations are compared for the baseline LCA geometry case under the similar 0D BC model parameters extracted from the 0D CVS.

5.4.1 Single LAD Branch Case

In accordance with the approach for extraction of 0D flow resistance from vascular geometries presented in Section 4.2.1, Figure 5.45 shows the measured diameter variations along the vessel centreline and the corresponding computed flow resistance for each of the elementary segments of the LAD branch of the LCA tree being analysed. The extracted LAD branch has a medium-to-high severity stenosis with a 70-75% maximum diameter reduction. The second stenosis, closer to the outlet, is of low severity with less than 50% narrowing. The fluctuations of the vessel diameter are mainly caused by the vessel lumen irregularities before surface smoothing. Flow resistance is highly sensitive to changes in vessel diameter with the prominent peaks in the stenosis areas being due to the $R \sim D^{-4}$ relation (4.1).

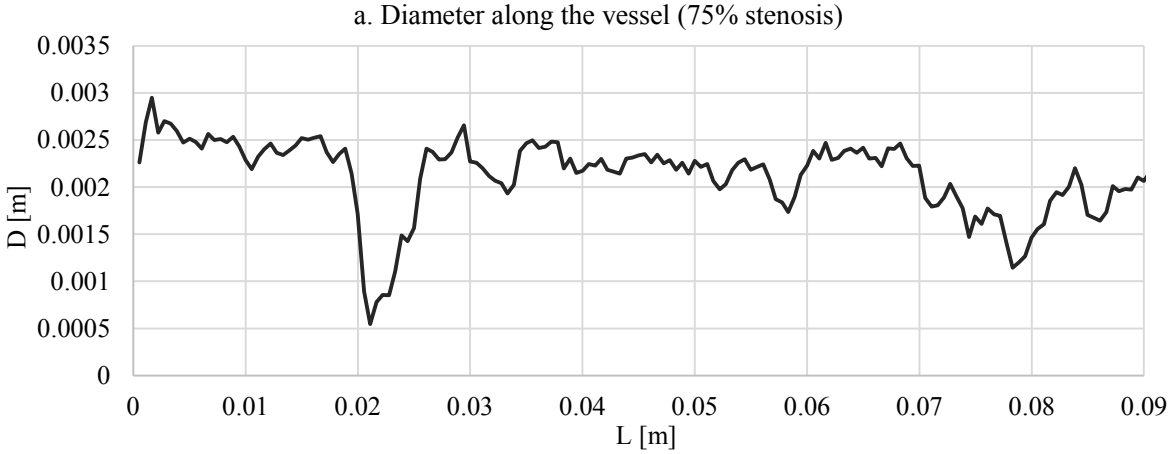

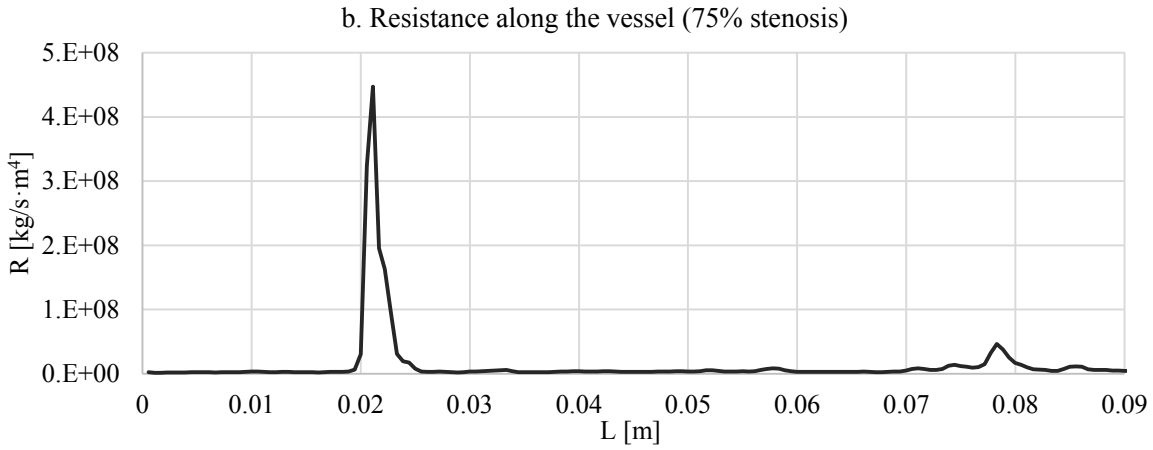

Figure 5.45 Extracted 0D flow resistance for 75% stenosis vessel case

Following the representation of the vessel through a series of resistors, the 0D blood flow model was solved under the specified flow boundary conditions ($P_{in}(t)$, $P_d(t)$, and R_d) for varying degrees of vasodilation (dR) of the downstream vasculature (Section 4.6.2). In order to validate the accuracy of the 0D model results, the equivalent 3D blood flow model for the same LAD branch was implemented and solved under the same BC model parameters.

Figure 5.46 presents a comparison of the results of 3D and 0D blood flow simulations for: dR = 1.0 (rest); dR = 0.2 (hyperaemia); and dR = 0.1 (idealised hyperaemia). In the 3D domain, the computed FFR does not go below 0.8 under hyperaemia (dR = 0.2), which means that in this case this stenosis is not haemodynamically significant. However, in the idealised case of a higher degree of vasodilation with dR = 0.1, the flow limiting impact of the series of stenoses is more pronounced. From the comparison with the computed FFR results in 0D, it can be observed that the impact produced by the stenoses on the pressure drop is similar in both domains. This is particularly clear for the hyperaemia cases with a “step” change in FFR after the first stenosis. Consequently, this verifies the suitability of employing both 0D blood flow simulations and flow resistance in the assessment of functional stenosis severity.

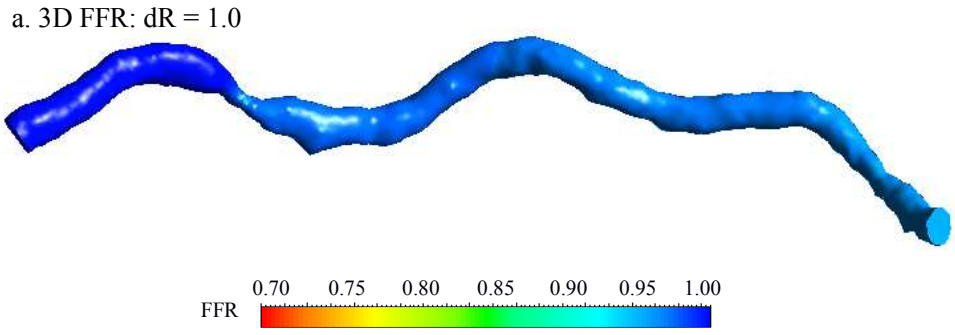

b. FFR along the vessel: dR = 1.00

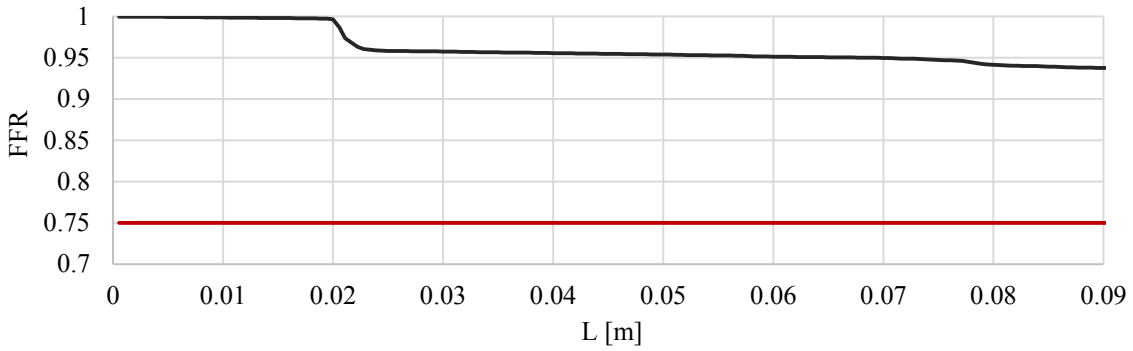

c. 3D FFR: dR = 0.2

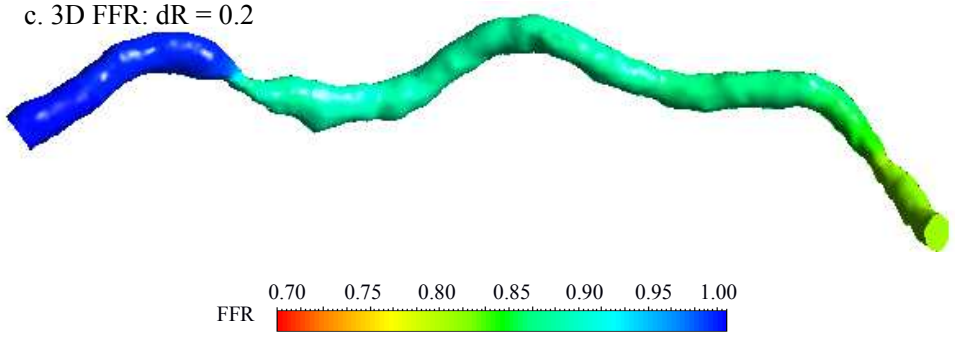

d. FFR along the vessel: dR = 0.20

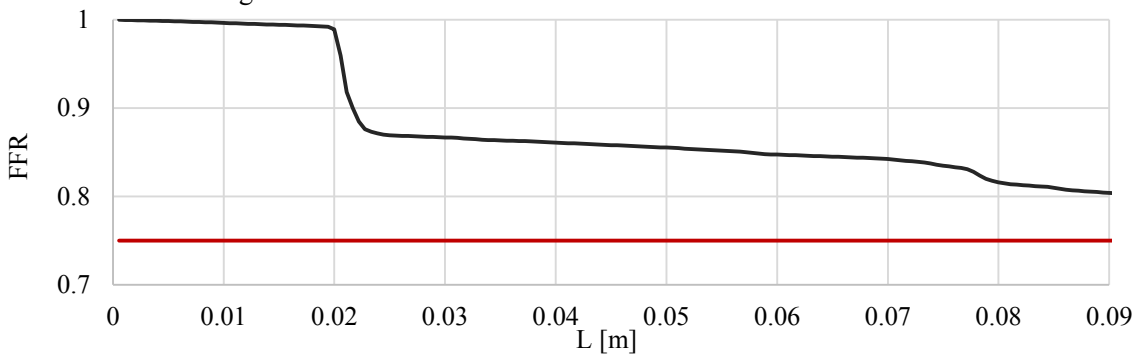

e. 3D FFR: dR = 0.10

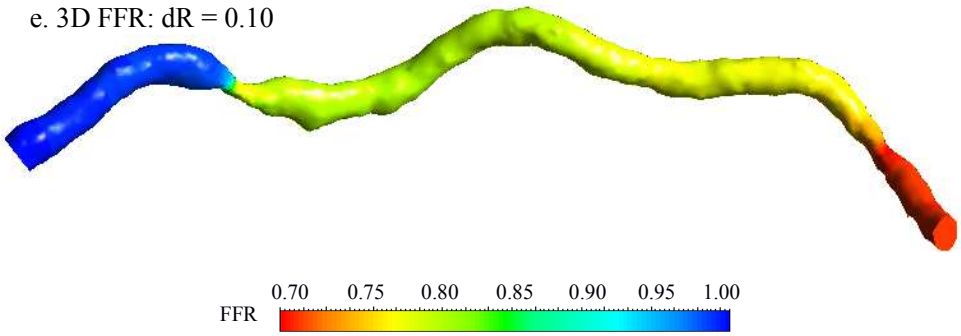

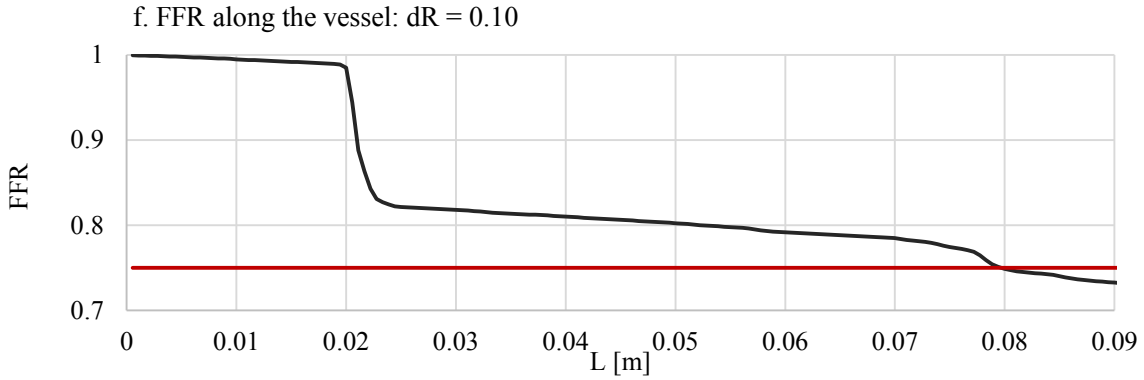

Figure 5.46 Computed FFR in 0D and 3D blood flow simulations in a vessel with 75% stenosis (dR = {1.0; 0.2; 0.1})

The comparison between the 0D and 3D computed inlet flow rate and outlet FFR under dR decreasing from 1.0 to 0.0 is shown in Figure 5.47. At the rest state, the computed FFR is close to a "healthy" value of 0.95 in both domains. Further decreasing of the peripheral resistance leads to an increased flow rate, which emphasises the impact of the stenosis resistance on the pressure drop. However, this particular series of stenoses (under the specified BC) does not result in a critical blood flow limiting condition with the outlet FFR being 0.8-0.85 within the dR = 0.2-0.25 hyperaemia range. At the same time, while the difference in the computed 0D and 3D FFR does not exceed +/- 2.5%, a considerable difference is observed in the computed inlet flow rate for dR values below 0.2.

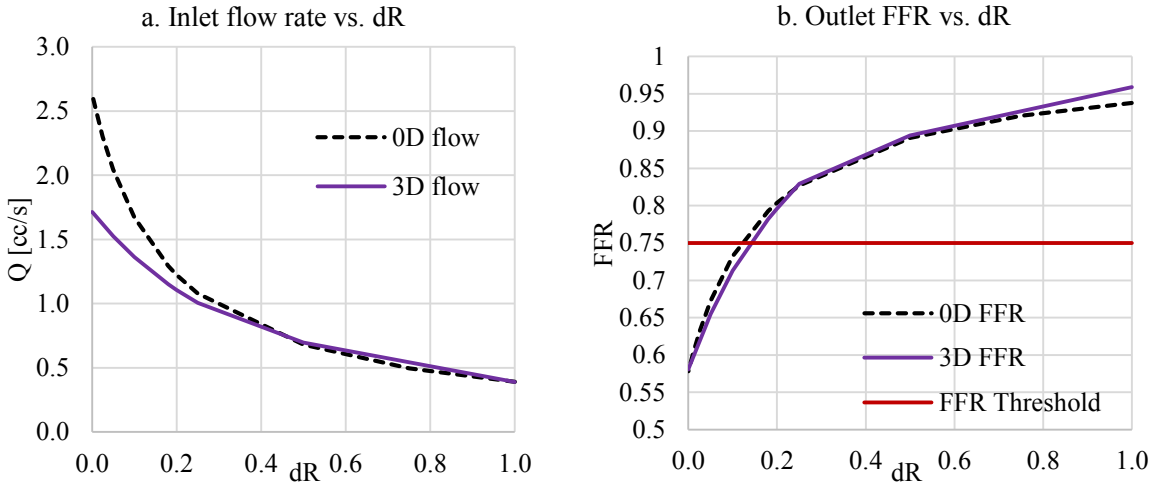

Figure 5.47 Computed inlet flow rate and outlet FFR in 0D and 3D blood flow simulations in 75% stenosis vessel (dR = 1.0:0.0)

This difference in the 0D and 3D flow rate is explained by the complex flow resistance in the 3D flow domain, which, unlike the constant resistance in the lumped-parameter 0D domain, is a product of viscous and flow separation losses and eddies at the site of the stenosis

and changes with the flow rate [146,147]. The result of the application of Ohm's law ($R = \Delta P/Q$) on the 3D computed flow is given in Figure 5.48. In can be observed that the R_{3D} resistance derived from the 3D simulation results increases with the inlet flow rate replicating the waveform shape. At the same time, the product of the inlet flow rate and the resistance $\Delta P=R\cdot Q$ defining the pressure drop along the vessel, shown in Figure 5.49, approximately coincides for both the 0D and 3D computed blood flow with the highest deviation occurring at dR = 1.0 (similarly to the difference in FFR). The average R_{3D} vessel resistance computed for this set of cases was found to be $2.23\cdot10^9$ kg/s·m^4, thus being in the range of the 0D total resistance $R_{0D} = 2.13\cdot10^9$ kg/s·m^4.

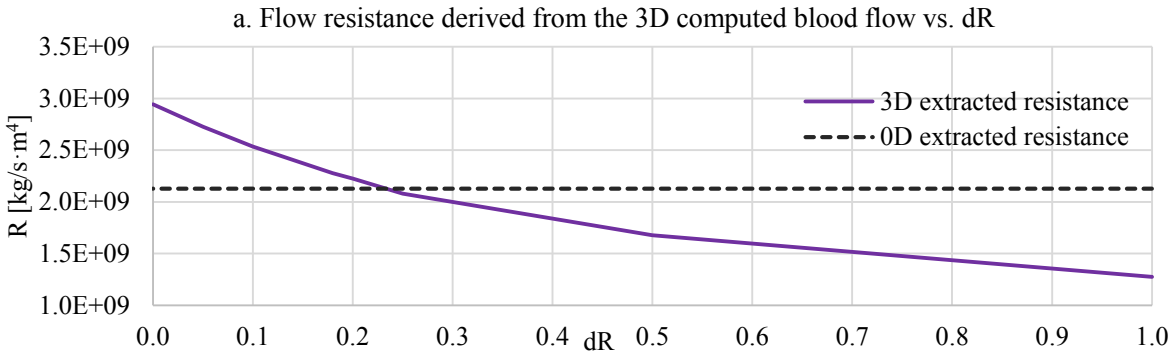

Figure 5.48 Flow resistance derived from the 3D computed blood flow in a vessel with a 75% stenosis (dR = 1.0:0.0)

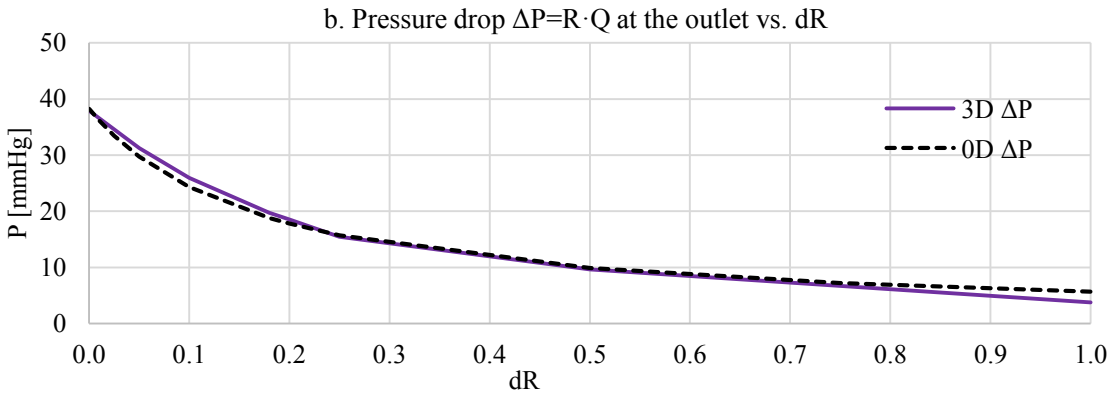

Figure 5.49 Computed ΔP in 0D and 3D blood flow simulations in a vessel with a 75% stenosis (dR = 1.0:0.0)

In other words, it was identified that the flow resistance of a vessel segment in 3D blood flow modelling derived as $R_{3D}=\Delta P/Q$ is defined only by the difference between its inlet and outlet pressure, irrespectively of the pressure magnitude.

Figure 5.50 shows the derived relationship between R_{3D} versus ΔP for the investigated 75% stenosed vessel branch and for the LAD branch segment of the same LCA volume, but reconstructed under a lower blood segmentation threshold (270 HU), thus resulting in a lower degree of stenosis (Section 5.3.1). As expected, the total flow resistance for the 75% stenosed vessel is significantly higher than in the 35% stenosed vessel case with an approximately constant difference of 41%.

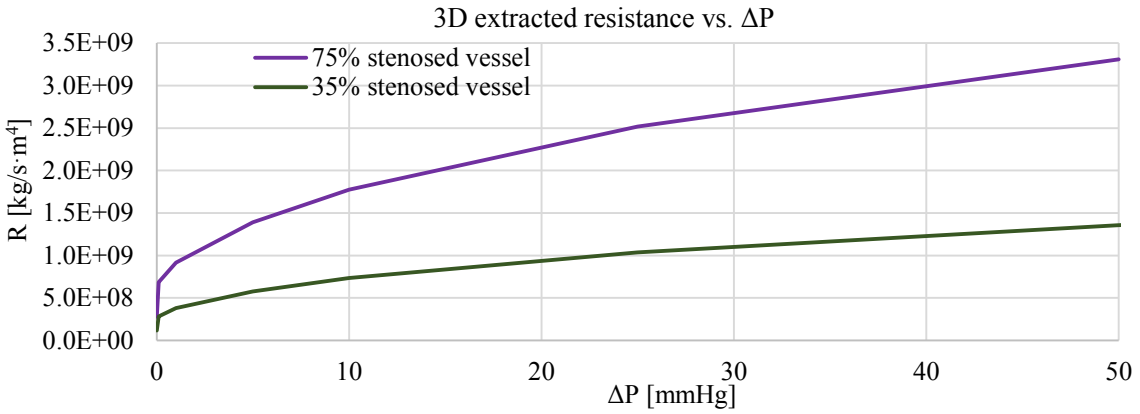

Figure 5.50 Flow resistance derived from 3D computed blood flow in vessels with a 35% and a 75% stenosis vs. ΔP

In order to verify these findings, the results of the 0D and 3D blood flow simulations for the 35% stenosed vessel case are presented in Figures 5.51-52. The drop in FFR in the stenosis regions is equivalent in both the 3D and 0D domains and, as expected, is significantly lower in comparison to the 75% stenosed case (i.e., a value of 0.82 compared to 0.73 under dR = 0.1). The total computed 0D vessel resistance is $7.28 \cdot 10^8$ kg/s·m^4, which is comparable to the average resistance value of $7.92 \cdot 10^8$ kg/s·m^4 derived from the 3D simulation results.

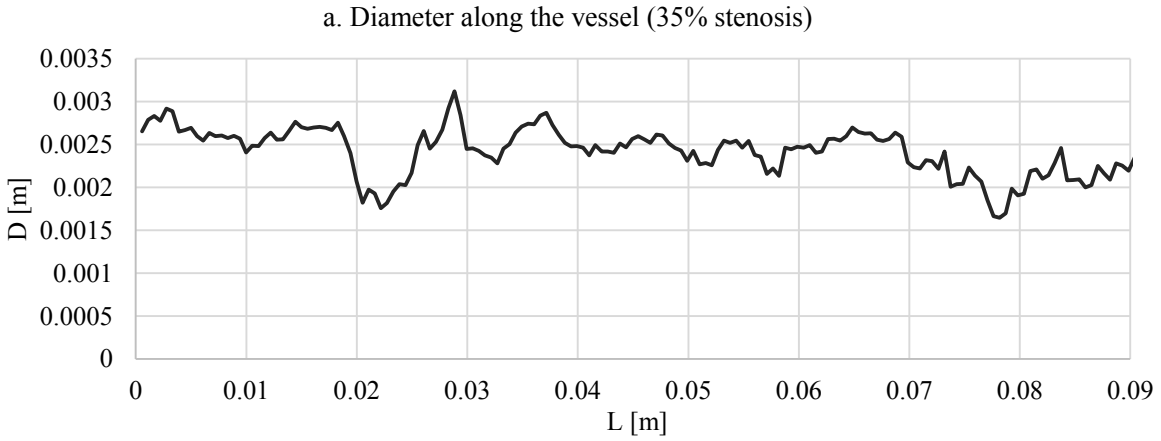

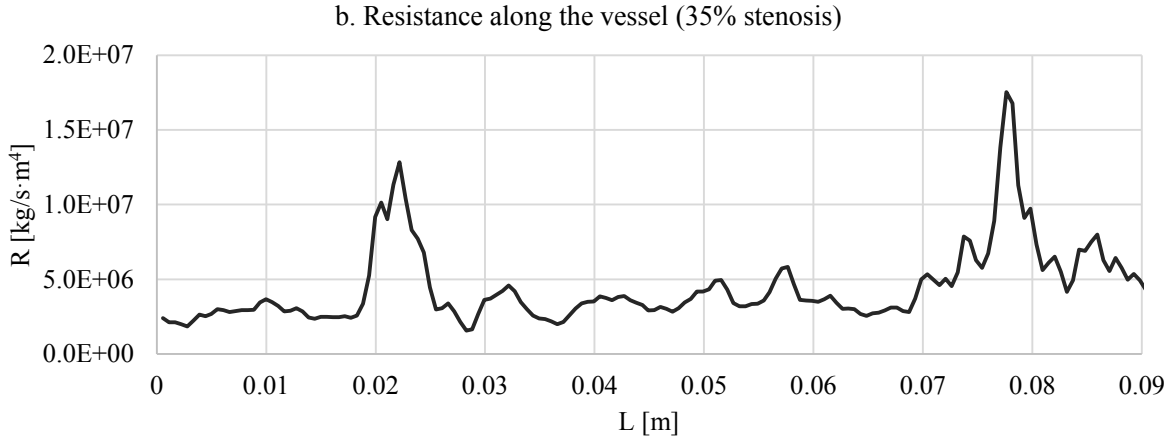

Figure 5.51 Extracted 0D flow resistance along 35% stenosis vessel case

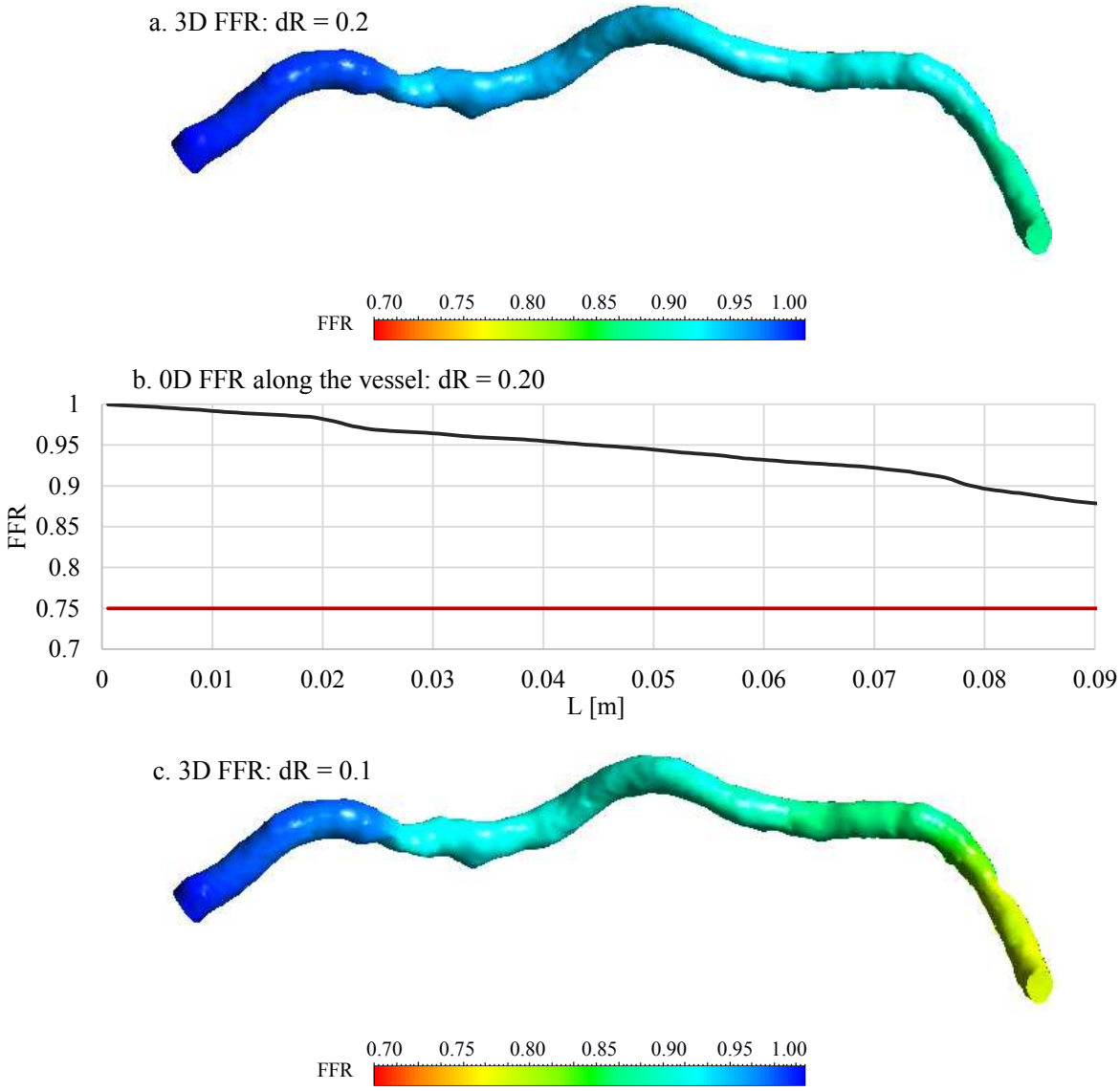

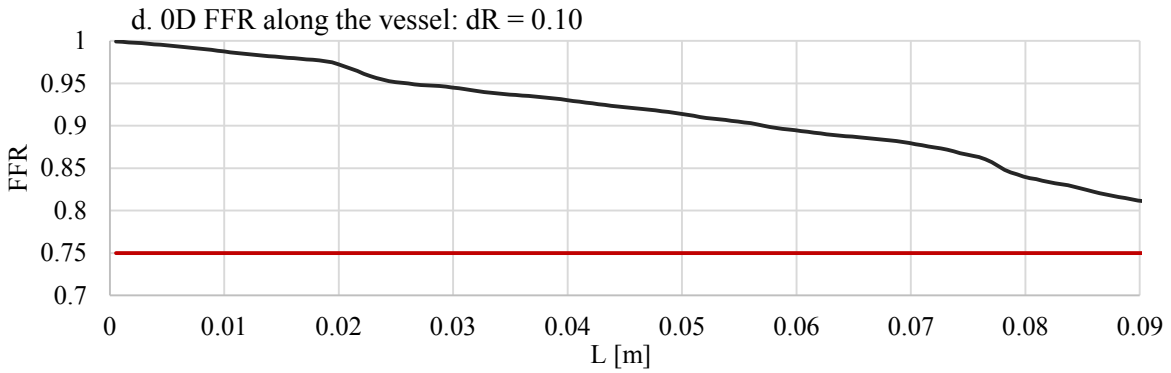

Figure 5.52 Computed FFR in 0D and 3D blood flow simulations in a vessel with 35% stenosis (dR = {0.2; 0.1})

Similarly to the 350 HU segmentation threshold case, the 3D-computed inlet flow rate is lower than in the 0D domain for the dR values below 0.2 along with the derived 3D flow resistance changing with respect to the flow rate. However, the computed FFR and ΔP are similar in the results of the 0D and 3D blood flow simulations.

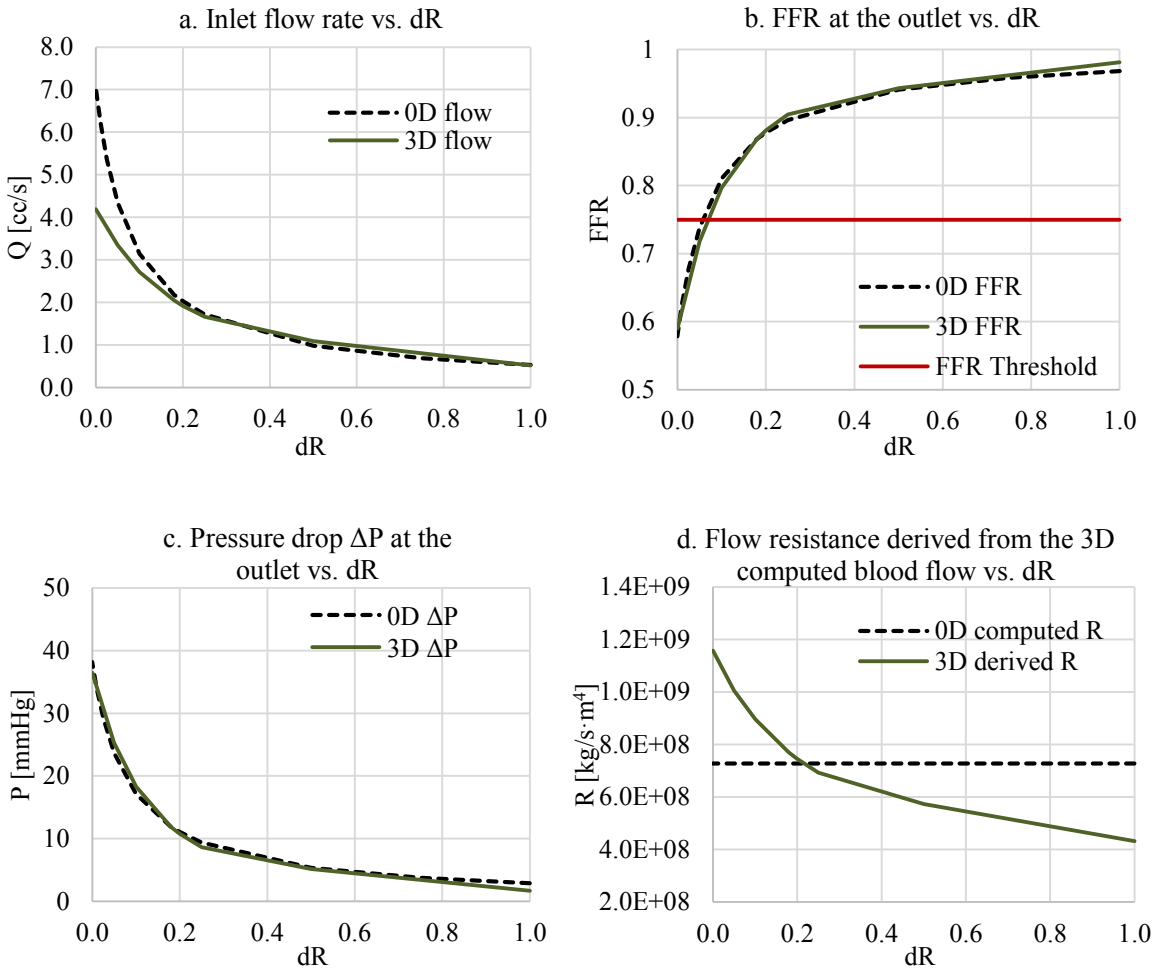

Figure 5.53 Computed inlet flow rate and outlet FFR and ΔP in 0D and 3D blood flow simulations in a vessel with 35% stenosis (dR = 1.0:0.0)

Based on the analysis of the obtained results, it can be concluded that the proposed methodology for extraction of flow resistance from coronary artery branches and associated 0D blood flow simulations is applicable in the diagnosis of functional stenosis severity through the assessment of FFR drop. This was verified by the fact that the results for the stenosis-related drops in FFR are proportional to the 3D CFD computed flow fields in terms of both FFR magnitude and location.

5.4.2 LCA Tree Case

Considering a more complex case of the entire LCA tree, which includes more than one branch, the associated solution and analysis become more complex taking into account the effect of flow distribution between the branches. As described in Section 4.2.2, the LCA geometry of the baseline case was converted into the 0D domain with the branches represented as a series of resistors under the rigid vessel wall assumption. The 0D LCA model was incorporated into the 0D CVS loop with the inlet connected to the root of the aorta and the 0D BC models were assigned at the outlets (the estimated peripheral resistance values Z_i are equivalent to the corresponding values in the 3D model). The downstream pressure, which is the product of the capillary level pressure and the pressure of ventricle construction, was approximated as $P_d(t) = 0.75 \cdot P_{LV}(t) + 15$ mmHg (Section 5.2.6). Figure 5.54 shows the notations of the LCA outlets in the 0D and 3D domains and the computed FFR for the baseline case. As can be observed, the single stenosed branch from the previous section is the LAD branch with outlet #13. The 0D simulations were run for 30 seconds to ensure the solution convergence. Similarly to the 3D domain, hyperaemia was modelled as vasodilation of the peripheral vasculature with dR = 0.2.

a. 0D LCA tree model (outlet number specification)

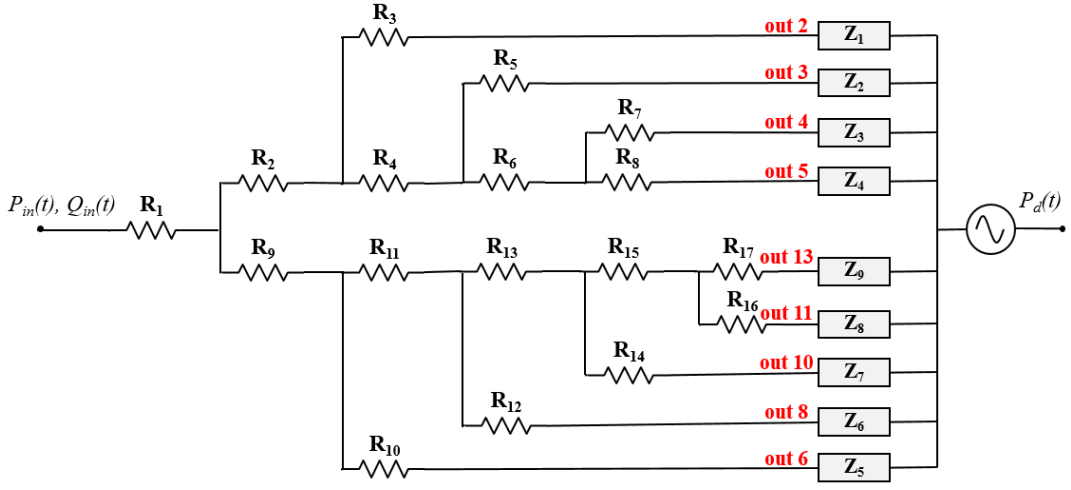

b. 3D LCA tree model (outlet number specification)

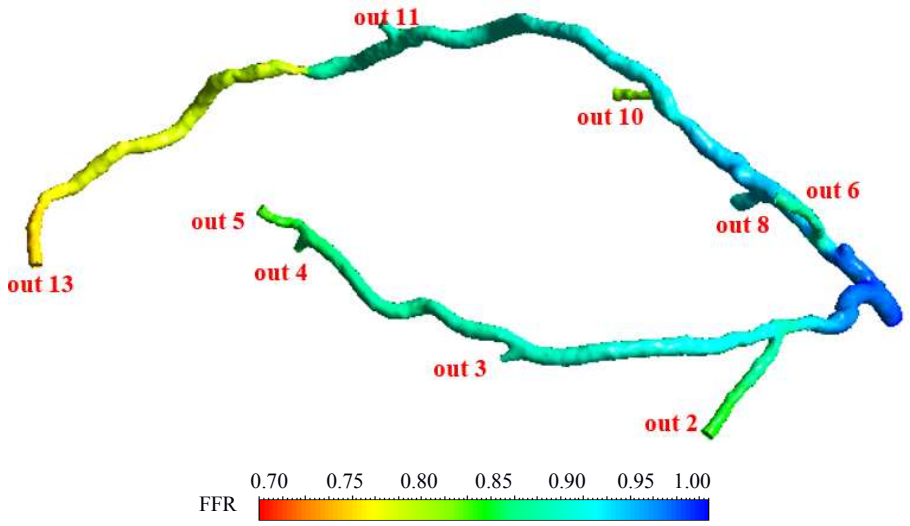

Figure 5.54 Equivalent 0D and 3D models of the baseline LCA case

An example of the 0D simulation results in the time domain is given in Figure 5.55, including the waveforms of the computed pressure, flow rate, dQ and FFR at the inlet and two of the outlets corresponding to a healthy and a stenosed branch, i.e., outlets #6 and #13, respectively. As can be observed, hyperaemia was modelled as a gradual decrease of the degree of vasodilation from dR = 1.0 to dR = 0.2 for a 10s period starting from 4s with the mean inlet flow rate increasing from 2.00 to 7.3 cc/s. Figures 5.46.b-c present the measured pressure at the inlet and outlets #6 and #13. During the 10s period of hyperaemia, the mean pressure in the healthy branch (outlet #6) decreased to 81 mmHg from the resting state of 90 mmHg, while in the stenosed branch (outlet #13), the pressure dropped from 82 to 66.7 mmHg. In addition, there is an approximate decrease of 4 mmHg in the mean inlet pressure, due to the decrease in the blood circulation loop resistance. A similar situation can also be observed in the real invasive pressure measurements for FFR assessment under pharmacologically induced hyperaemia (Figure 5.56).

The corresponding FFR (P_{out}/P_{in}) and mean dQ waveforms are shown in Figures 5.55.d-e. In the healthy branch, the mean FFR does not fall below 0.92, whereas the FFR value after the series of the stenoses in outlet #13 has a pronounced drop nearly reaching the critical 0.75 threshold. A similar behaviour can be observed in the flow rate distribution with dQ decreasing in the stenosed branch due to the high flow resistance, which subsequently leads to the redistribution of flow to the healthy branch outlets.

a. Computed inlet flow rate (hyperaemia 4-14 s)

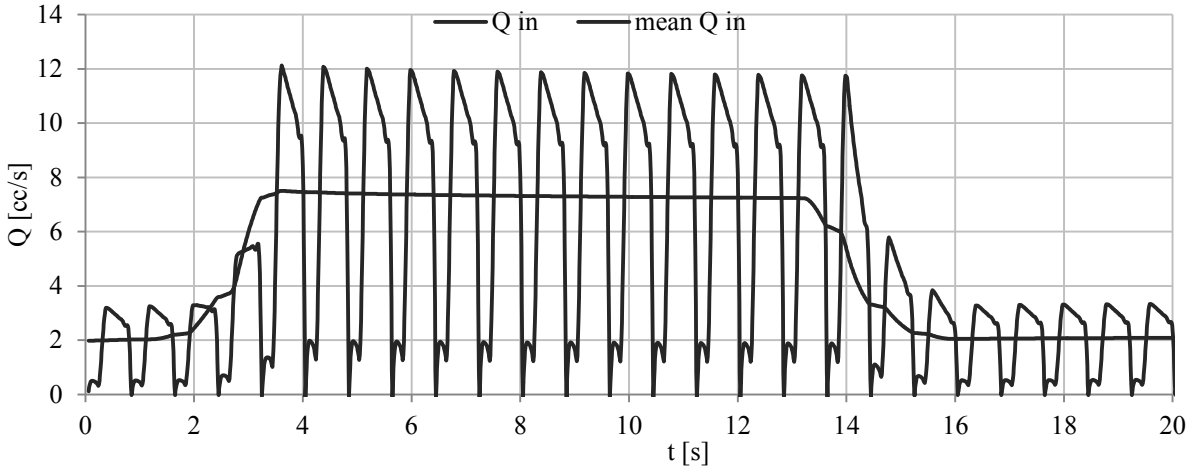

b. Computed pressure (hyperaemia 4-14 s): healthy branch (outlet#6)

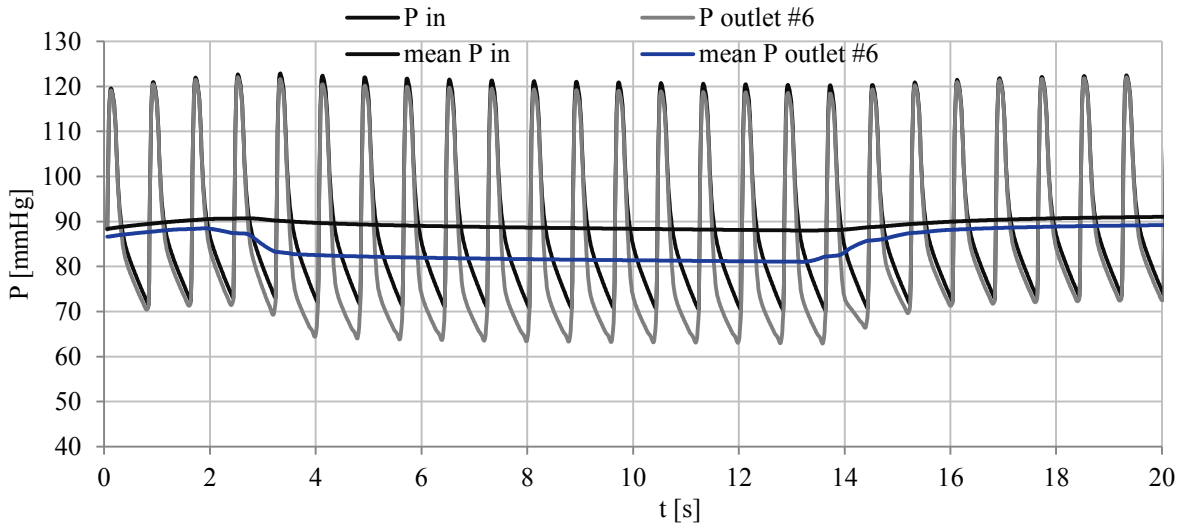

c. Computed pressure (hyperaemia 4-14 s) : stenosed branch (outlet #13)

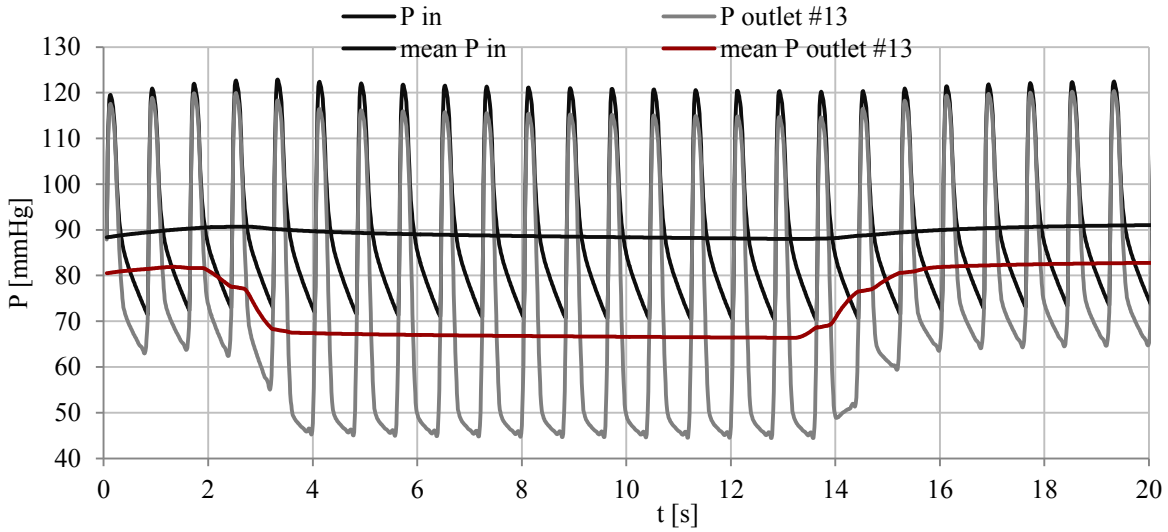

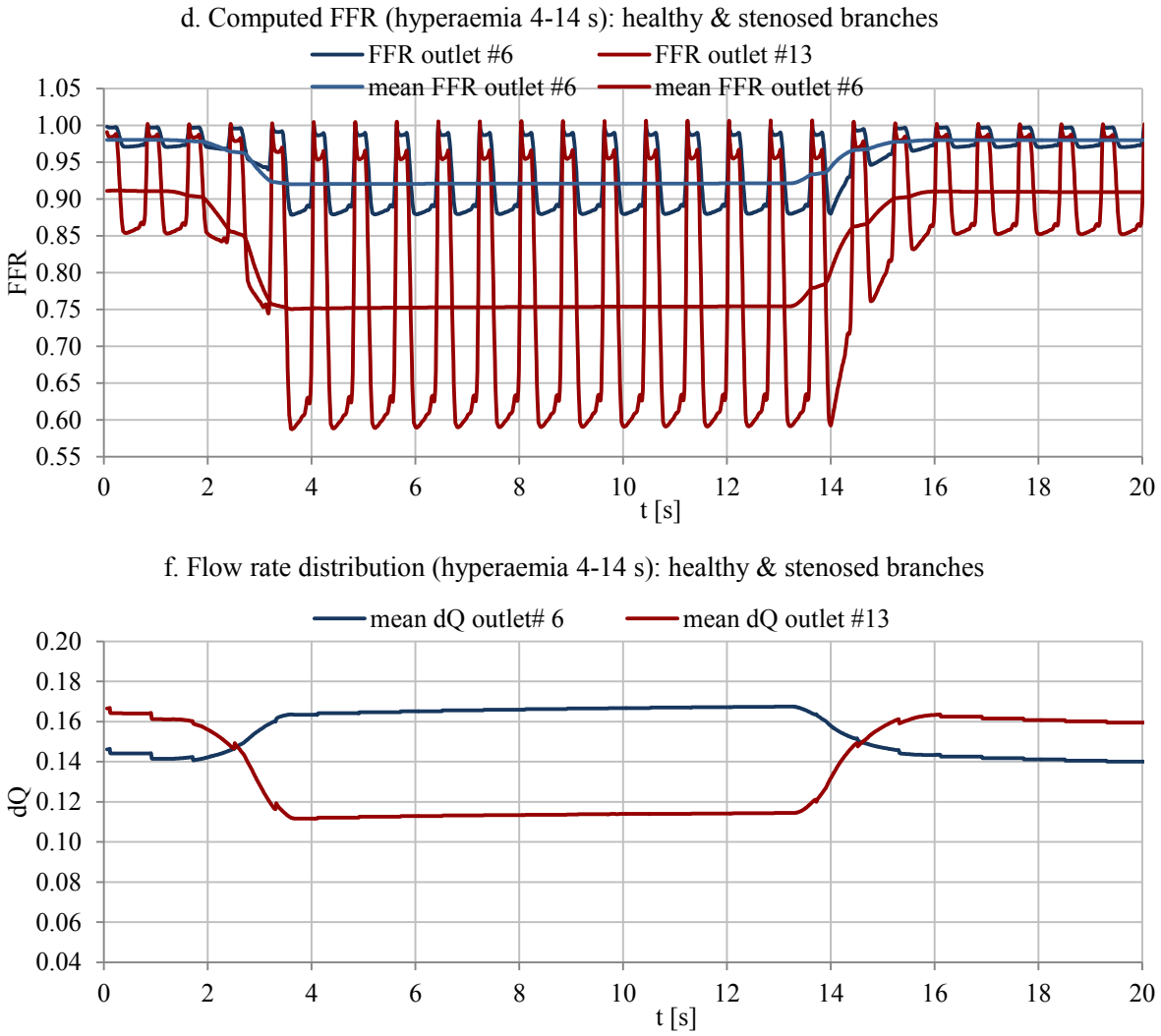

Figure 5.55 Computed Q(t), P(t), FFR(t) and dQ(t) during simulated hyperaemia in the interval between 4-14 s in the 0D domain for the LCA (dR = {1.0; 0.2})

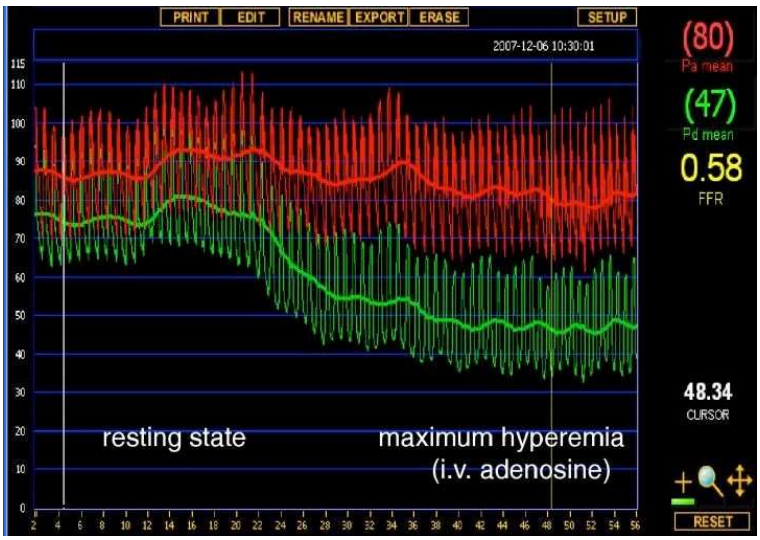

Figure 5.56 An example of invasively measured pressure in coronary arteries after adenosine administration for inducing of hyperaemia during FFR evaluation [145]

Comparison of the computed 0D and 3D flow patterns shows relatively strong correlation in terms of the mean FFR and dQ with the difference not exceeding 0.02 for the FFR and 0.01 for the dQ (Figure 5.57). In general, the values of both the FFR and dQ in the 0D domain are lower for the majority of the LCx outlets {2; 3; 4; 5} and higher or close to the 3D results in the LAD outlets {6; 8; 10; 11; 13}.

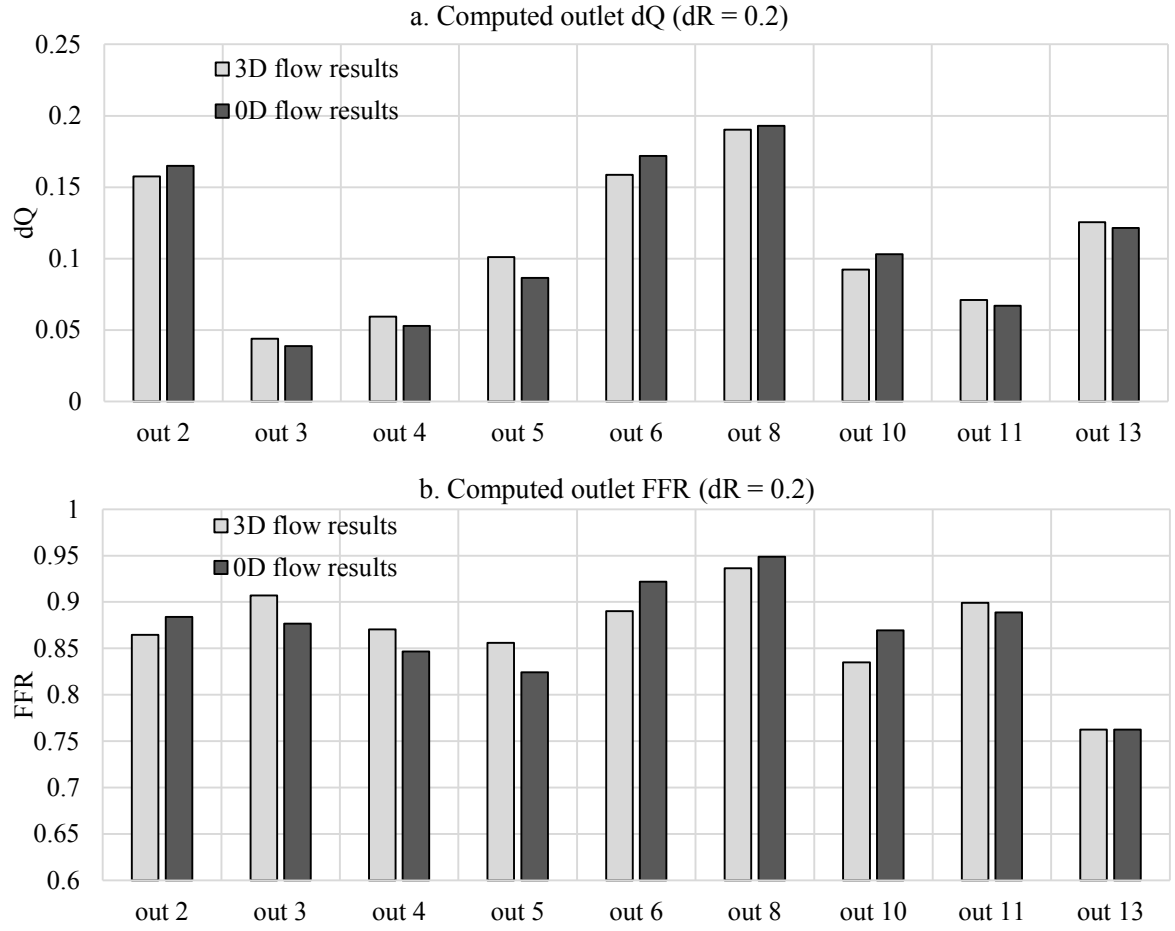

Figure 5.57 0D and 3D computed outlet FFR and dQ for the baseline LCA case (dR = {0.2; 1.0})

Besides the probable inaccuracies associated with the extraction of flow resistance from patient-specific geometries, the difference can be explained from the analysis of the FFR(t) and dQ(t) waveforms given in Figure 5.58. The noticeable difference is related to the backflow periods present during systole, when $P_d(t)$ is higher than $P_{in}(t)$, which cause significant redistribution in the flow patterns (Figure 5.58.d), thus changing the FFR as well. This, however, occurs to a lower extent in the 3D computed flow (Figure 5.58.c), since the 3D BC models employ interpolated versions of pressure waveforms measured in the 0D domain with a "smoothed" low $P_{in}(t)$ region in the beginning of the system. Consequently, the rational

solution to this issue is to use lower downstream pressure values, while preserving similar dP = P_d/P_{in} and $\Delta P = (P_{in} - P_d)$ (Section 5.2.6).

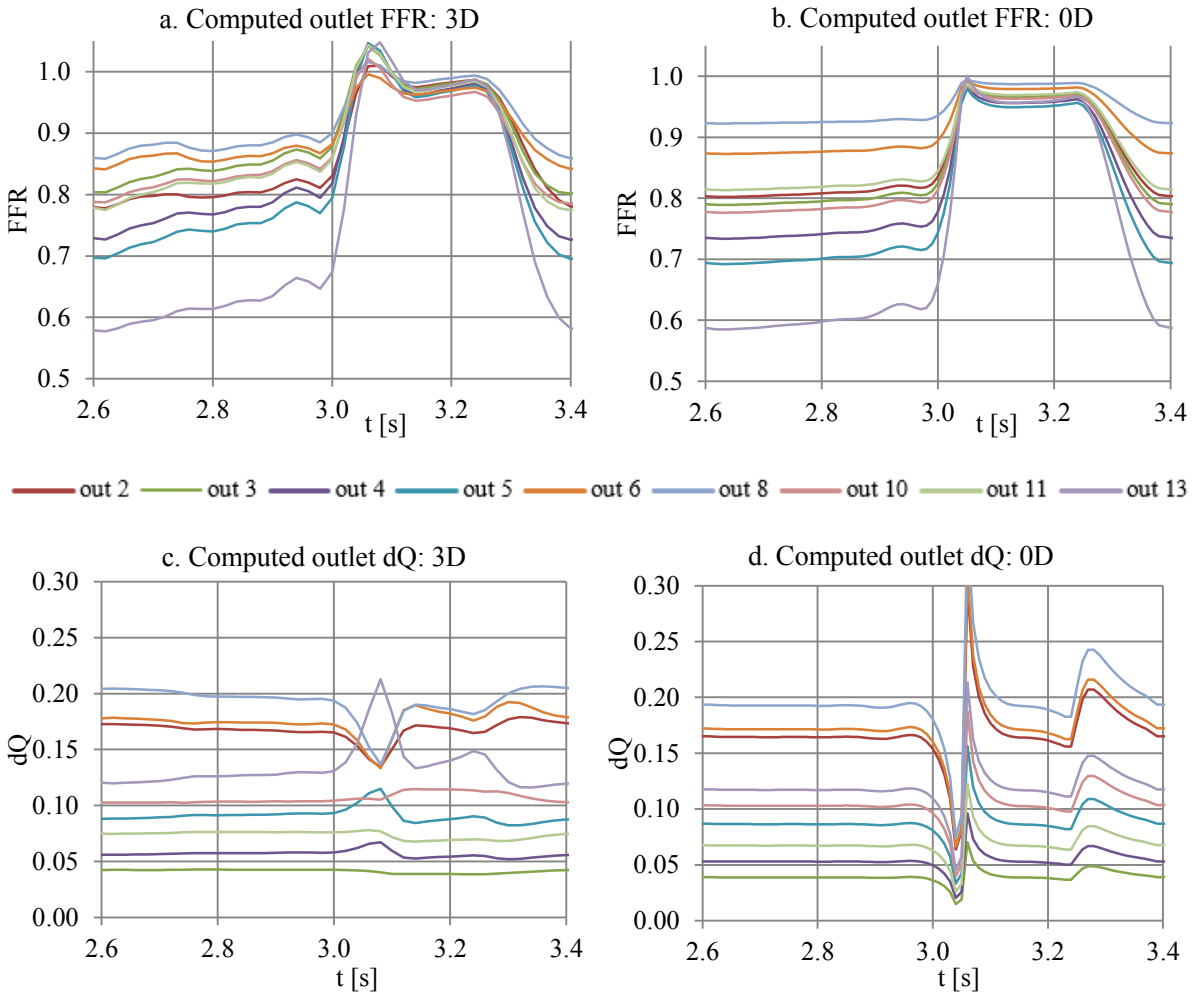

Figure 5.58 0D and 3D computed transient outlet FFR(t) and dQ(t) for the baseline LCA case (dR = 0.2)

Since, as was explained in Section 5.2.6, even a relatively small variation in the BC model values of the inlet and downstream pressures through dP=P_d/P_{in} or $\Delta P=P_{in}-P_d$ may lead to a different flow solution, it is reasonable to investigate how changes in the 0D CVS model parameters affect the results. The results of a series of equivalent 0D and 3D simulations performed under various degrees of vasodilation are presented in Figures 5.59-60. Due to the fact that the implemented 0D CVS model is a dynamic system, a decrease in the total resistance of the coronary circulation loop element under the same flow rate in the aorta will lead to a lower pressure in the aorta and the left ventricle in accordance with the Ohm's law. Therefore, this will change the boundary conditions for the coronary tree with lower P_{in} and P_d magnitudes. Figure 5.59.a shows how the inlet pressure $P_{in}(t)$ and the downstream pressure $P_d(t)$ change depending on the degree of vasodilation with the difference becoming more pronounced from

dR = 0.5. The corresponding differences between the 0D and 3D BC pressure values in terms of dP and ΔP are given in Figures 5.59.b-c. In the 3D domain, the inlet pressure also decreases but $P_d(t)$ remains constant. Consequently, the difference in the computed flow when dR = 0.2 can be partially explained by the changes in ΔP and dP. In addition, the fact that the critical drop in the aortic and LV pressure values occurs for dR < 0.15 indirectly proves the concept of the 0.2-0.25 range corresponding to the maximum physiologically achievable vasodilation degree, since a higher vasodilation of the coronary vasculature will lead to a significant disruption in CVS functionality.

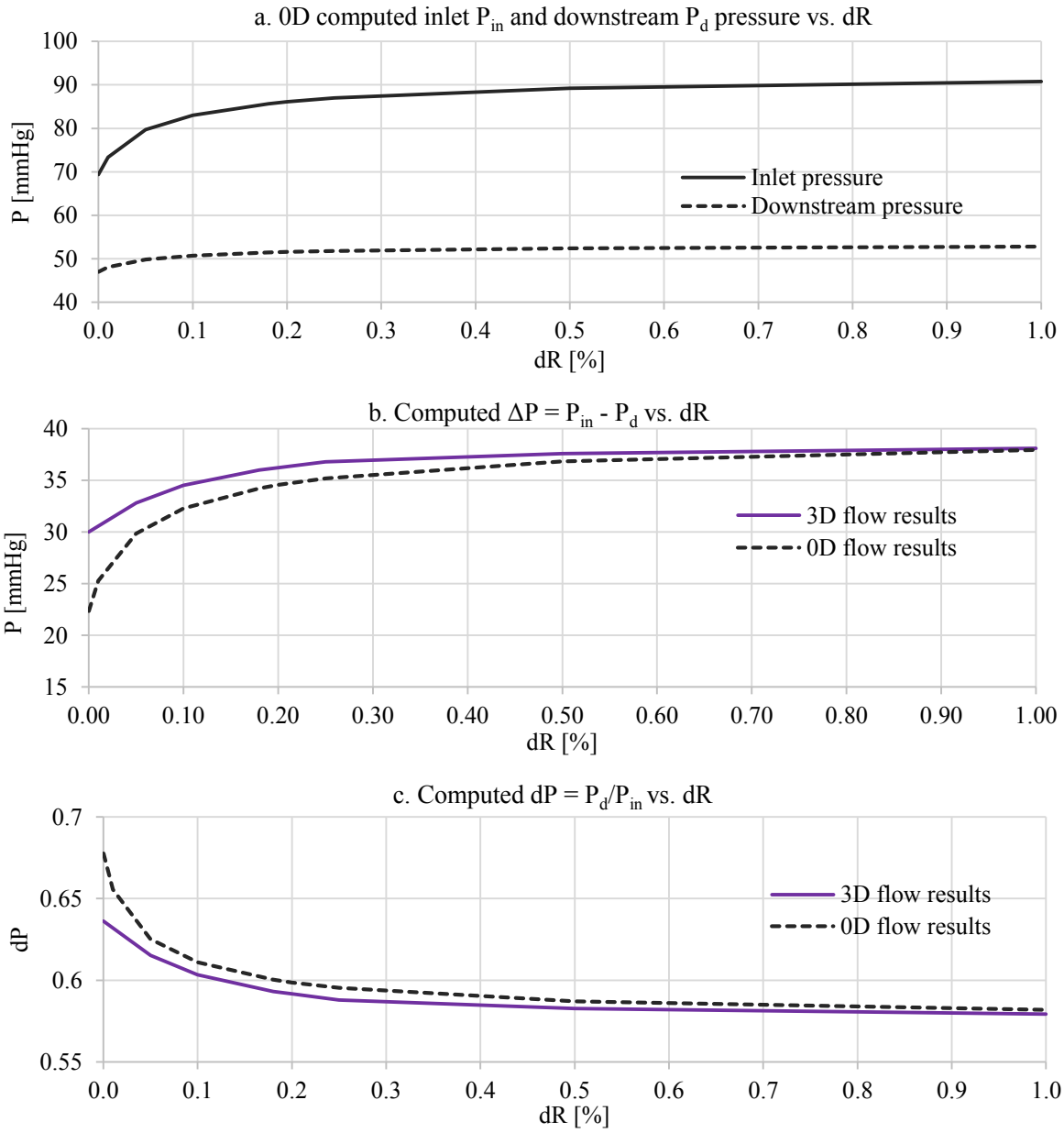

Figure 5.59 0D and 3D computed inlet and downstream pressures for the baseline LCA case (dR = 0.0:1.0)

Similarly to the single vessel case, while remaining approximately equal within the dR = 1.0-0.2 physiological range, the 0D computed inlet flow rate becomes higher than in the 3D case under dR lower than 0.1 (Figure 5.60.a). As discussed in the previous section, this is caused by the complex flow resistance in the 3D domain being a product of viscous and flow separation forces and changing with respect to the flow rate magnitude [146,147]. In the stenosed branch (outlet #13), both the 0D computed dQ and FFR are lower when dR = 1.0 (Figures 5.60.b-d). The difference between the 3D and 0D results is 0.0133, 0.028 and 2.53 mmHg for dQ, FFR and ΔP_{out}, respectively. This means that in this particular case, the 0D model overestimates the stenosis severity in comparison to the 3D model, since when dR = 1.0, both dP and $\Delta P = P$ are the same in the 3D and 0D cases. With the decreasing of dR up to 0.1, the 3D-0D difference in dQ to outlet #13 remains approximately the same but the FFR in the 0D domain becomes higher due to the higher general dP (Figure 5.59.c) and therefore closer to the 3D results. For dR values below 0.1, the critical change in the inlet and downstream pressure in the 0D domain (Figure 5.50.a) leads to an expected higher deviation between the 3D and 0D results in FFR, dQ and ΔP_{out}.

a. Computed inlet flow rate vs. dR

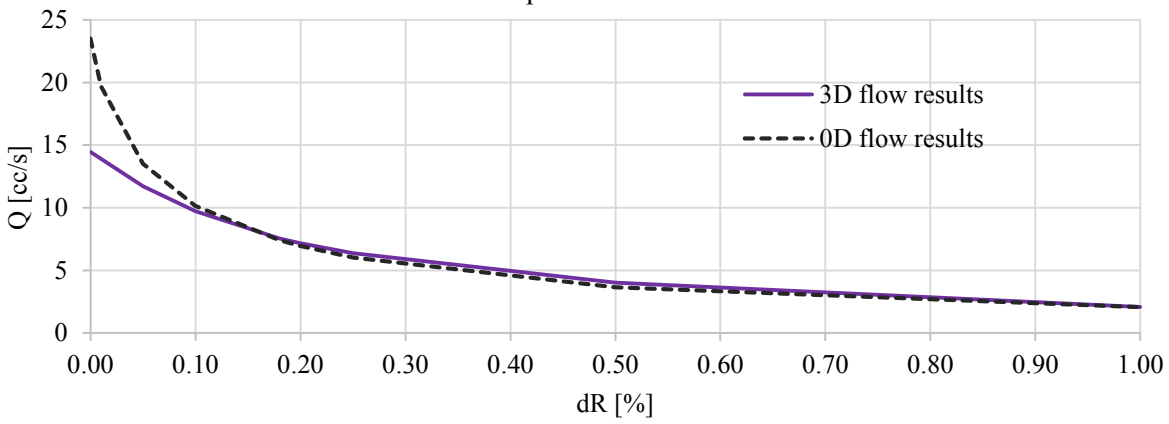

b. Computed dQ vs. dR: stenosed branch (outlet #13)

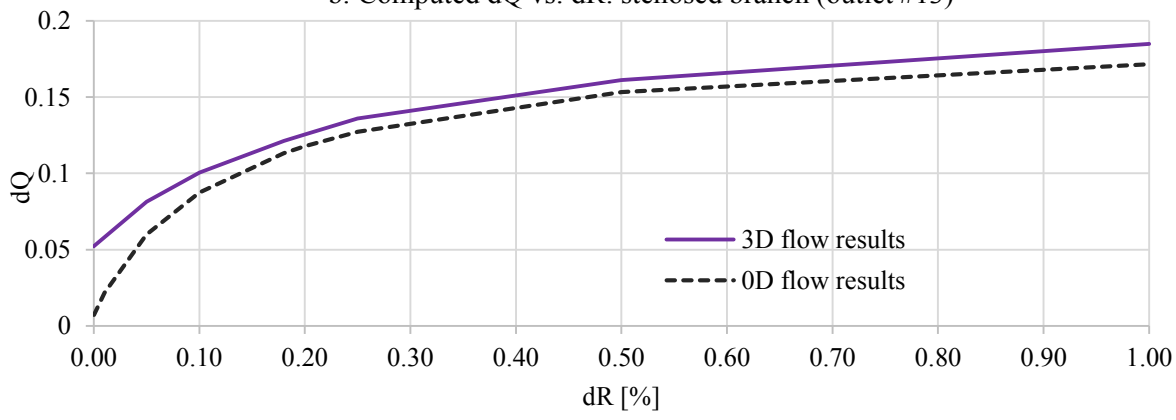

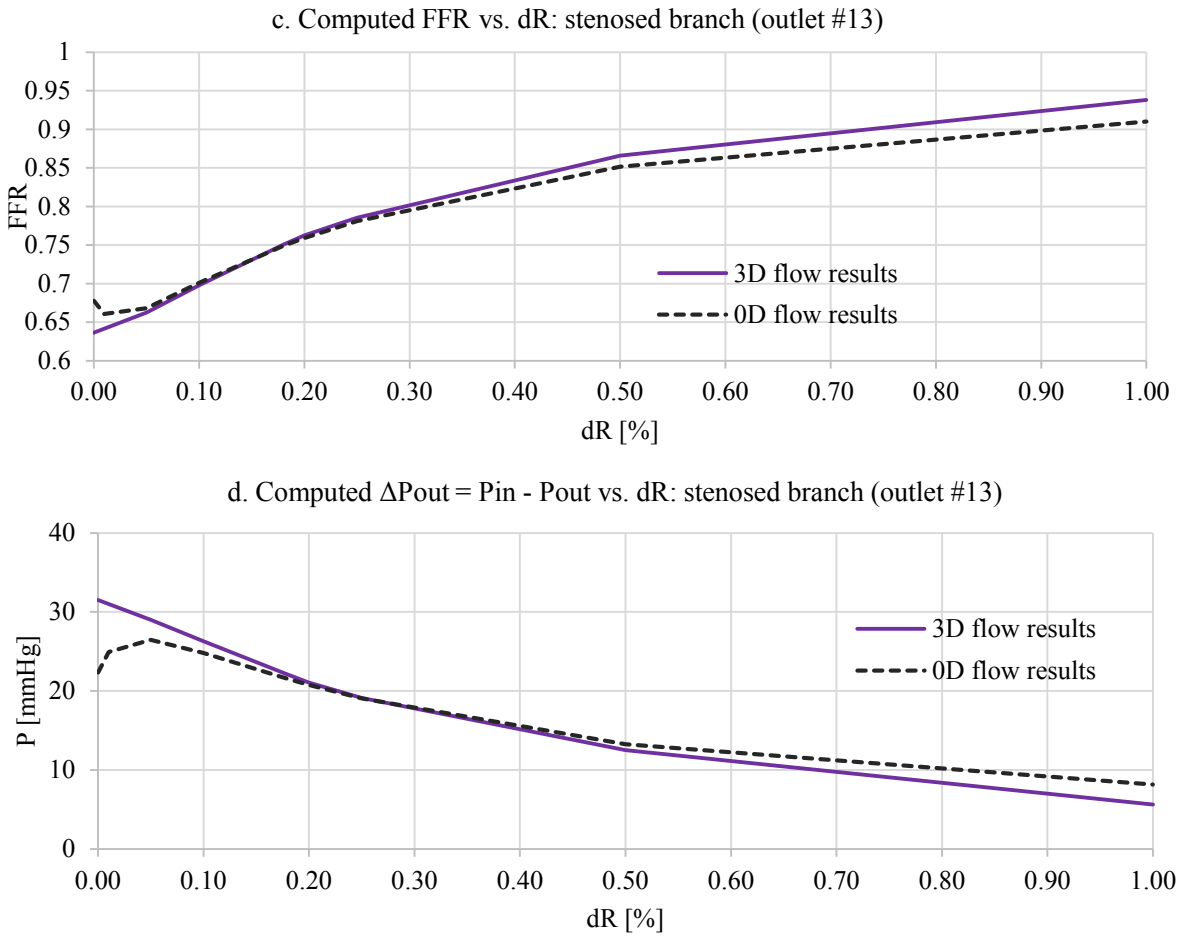

Figure 5.60 0D and 3D computed inlet flow rate and dQ, FFR and ΔP in the stenosed branch (outlet #13) for the baseline LCA case (dR = 0.0:1.0)

The results for the healthy branch with outlet #6 are given in Figure 5.61. While showing a high correlation in the range dR = 1.0-0.5, the 0D results begin to deviate from the 3D computed flow for dR below 0.5 along with the corresponding change in the inlet and downstream pressure and redistribution of the flow to the branches with lower resistance.

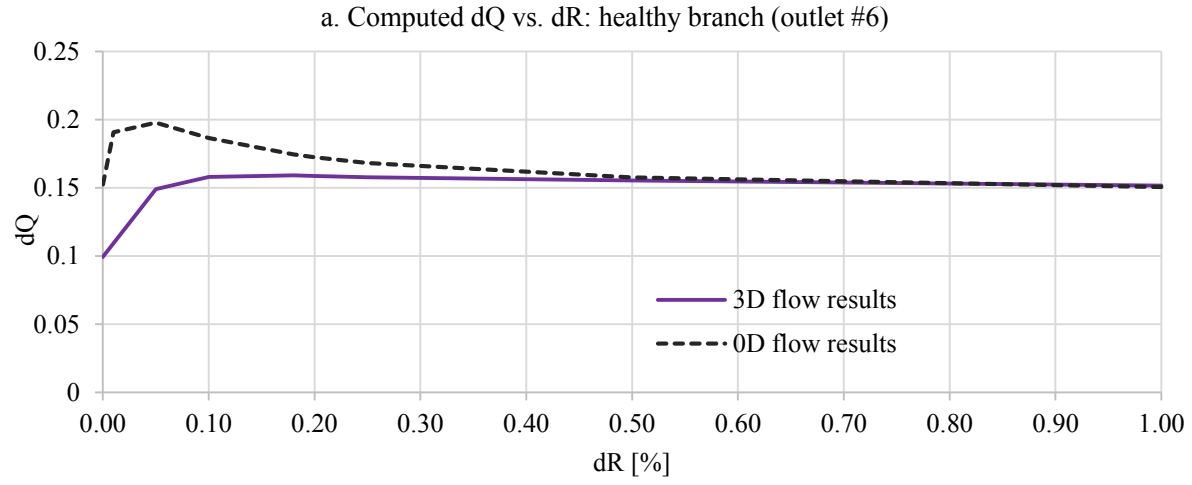

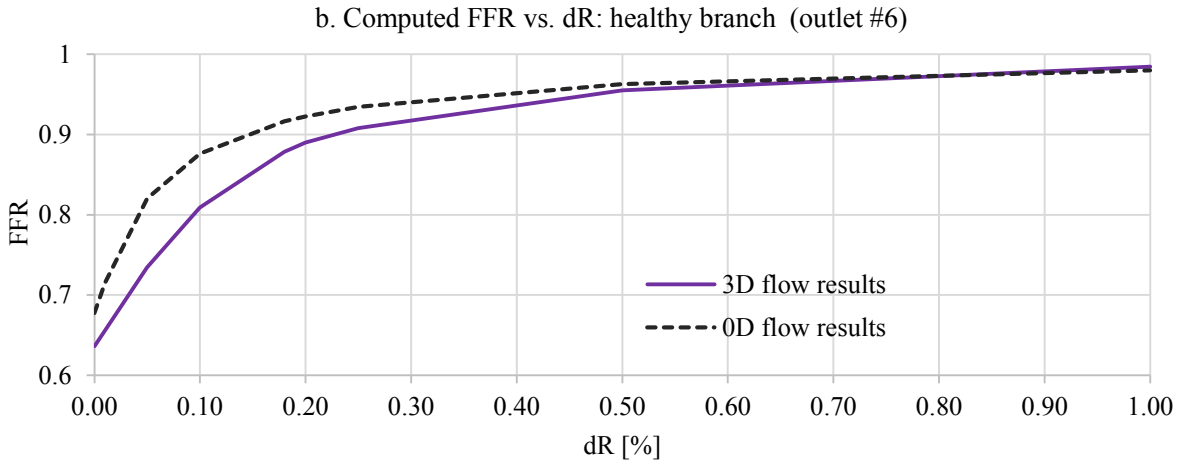

Figure 5.61 0D and 3D computed dQ and FFR in a healthy branch (outlet #6) for the baseline LCA case (dR = 0.0:1.0)

Another factor that directly defines the accuracy of the 0D computed flow is the quality of assessment of flow resistance from 3D geometries. This includes such aspects as the extraction of cross-sectional area, the resolution defined by the length of the elementary segments, and the algorithm for the assessment of total resistance for a segment (Section 4.2.1). In order to investigate how the flow resistance of a specific branch affects the computed flow, a gradual change in the total resistance of the stenosed branch $1.93 \cdot 10^9$ kg/s·m^4 by +/- 60% was performed. The corresponding computed dQ and FFR for this branch (outlet #13) versus % of R total branch resistance are shown in Figure 5.62. As expected, an increase in the branch resistance leads to the lower FFR and dQ, while the alignment of the 0D computed flow with the corresponding 3D results is achieved when the branch resistance is 85-90% of the originally computed value. Therefore, further qualitative assessment of the accuracy of extraction of 0D resistance values is essential for validation of the model performance.

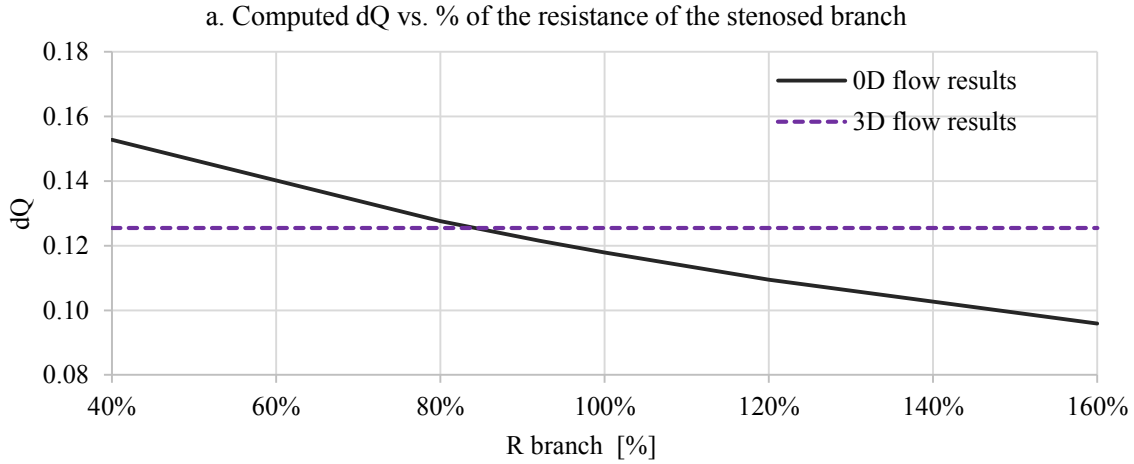

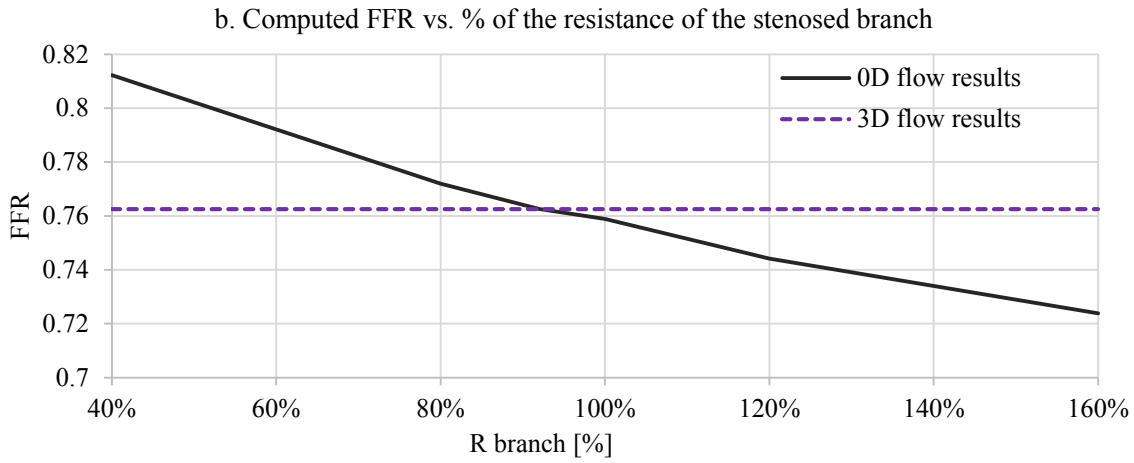

Figure 5.62 0D computed dQ and FFR in a stenosed branch (outlet #13) for the baseline LCA case vs. total branch resistance % (dR = 0.2)

Figure 5.63 demonstrates the comparison of the 0D and 3D computed FFR along the stenosed branch with the spatially distributed 0D FFR(x) representation, where x is the location along the vessel centreline from the beginning of the branch. There is a strong correlation between the results, especially in the locations of the stenoses, which produced the pressure drops.

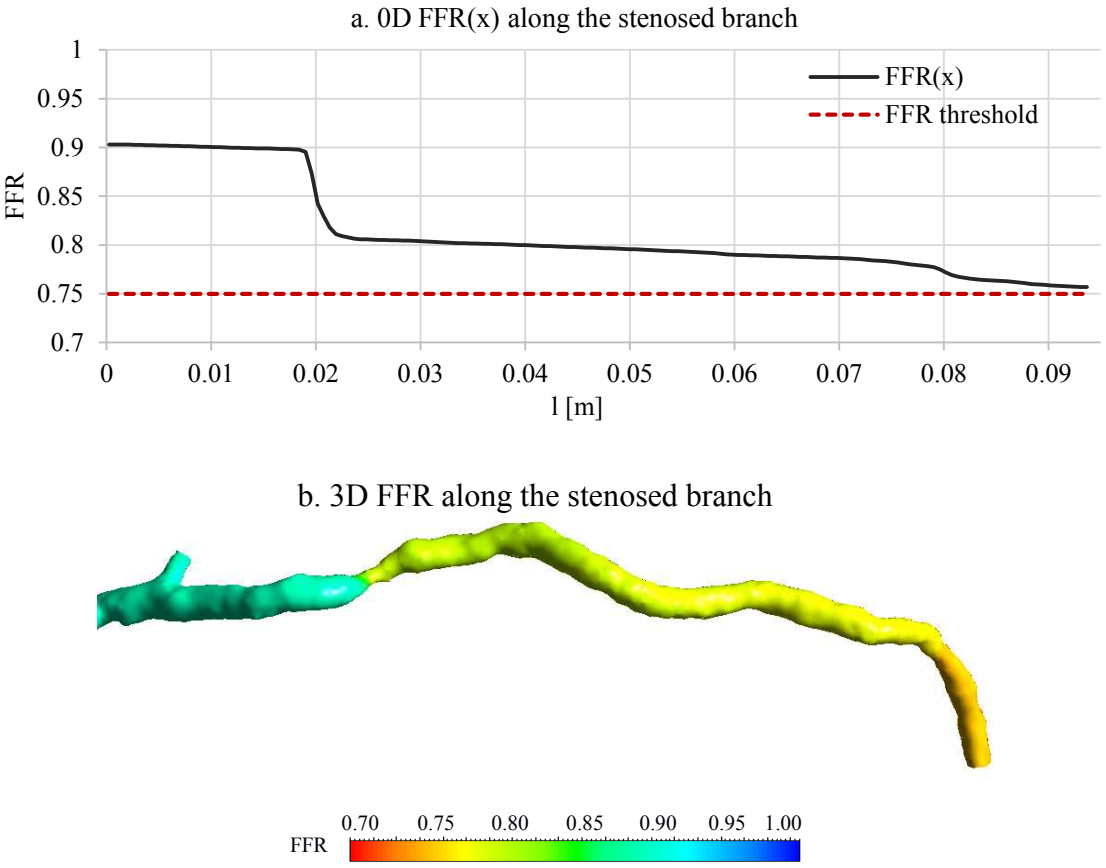

Figure 5.63 0D and 3D computed FFR along the stenosed branch for the baseline LCA case (dR =0.2)

In summary, the 0D model results showed high correlation with the equivalent 3D computed flow in FFR, pressure and dQ within the 0.1-1.0 peripheral vasodilation range. The slightly lower FFR and dQ values for the stenosed branch in the 0D simulations were due to the dynamic changes in ΔP and dP values at the boundaries of the coronary artery and the overestimated stenosis resistance. In addition, these findings indicate the importance of incorporating the 0D CVS model into the 3D coronary blood flow model in order to preserve physiologically accurate flow boundary conditions in terms of the inlet and downstream pressure, changing under different physiological conditions. When comparing these results with the single vessel case, it can be observed that the FFR drop in the stenosed LAD branch is lower if the entire LCA tree case is considered, since this is an accumulated product of a series of stenoses. Therefore, the accurate assessment of FFR requires blood flow simulations for the entire coronary arterial tree rather than individual branches.

5.5 Guidelines for Coronary Blood Flow Modelling

The accuracy of blood flow simulations in reconstructed vascular geometries is defined not only from the average range of physiological values but also by taking into account a list of patient-specific parameters. In coronary blood flow models, this includes such parameters of flow boundary conditions as pressure and flow rate at the inlet of the coronary artery and impedance from the peripheral vasculature. Other factors include the parameter settings in the methods used in the reconstruction of coronary arteries from CCTA data (or ICA) and blood rheology properties. Since, normally, the majority of these parameter values are not known due to risks related to performing invasive flow measurements, the set of modelling assumptions based on the average interpatient characteristics have to be employed in the model setup.

The baseline case for the performed qualitative comparison of the impact of variations in these modelling assumptions was the 3D blood flow model in the CCTA-reconstructed LCA with a series of stenoses with known invasively measured FFR values in the LAD and LCx branches, indicating a critical flow-limiting stenosis in the LAD artery. The computed flow patterns were assessed and compared with respect to the FFR values under hyperaemia (especially after the LAD stenosis), differences in the TAWSS patterns, and through the correspondence of the computed inlet flow rate and flow rate distribution between the branches with geometry-derived requirements.

Section 5.2 of this chapter presented the results of investigations of: (i) the difference in the computed flow produced by the three common 0D models of downstream vasculature; (ii) the relevance of employing steady-state simulations for assessment of heart-cycle averaged values, such as FFR and TAWSS; (iii) the choice of the vasodilation degree for modelling of maximum hyperaemia, required in the assessment of FFR; (iv) the results of the procedure of adjustment of the 0D BC model parameters with respect to the dQ and Q_{in} requirements; (v) variations in flow patterns produced by the different 1D peripheral tree morphology parameters; (vi) impact of interpatient variations in inlet and downstream coronary pressure, inlet flow rate and blood viscosity. In general, it can be concluded that the computed pressure fields and FFR are highly sensitive to the majority of these parameters, since they change the inlet flow rate and flow rate distribution between the branches, which are directly related to the magnitude of the pressure drop caused by a stenosis. Thus, incorporation of the C_{im} element, representing the myocardium wall compliance, into the 0D BC model will result in a higher flow rate to the stenosed branch in accordance with the geometry-derived dQ, which will subsequently lead to a lower FFR. In both the 0D resistance and Windkessel models, the flow distribution to the stenosed branch was lower and required additional adjustments of peripheral resistance values (Section 5.2.4). On the other hand, after the performed adjustment of the 0D R BC model parameters, the computed flow showed the same FFR drop after the stenosis. Consequently, it can be concluded that the main factor affecting the computed FFR is not the type of downstream BC model but the compliance with the requirements to the flow distribution and the inlet flow rate. These requirements are derived from the assumptions of the outlet flow–diameter relationship $Q \sim d^3$, known as the Murray's law and the total coronary inlet flow rate being 4-5% of the cardiac output [110] under the resting physiological condition. In addition, comparison of the results of steady-state and transient blood flow simulations demonstrated that the use of steady simulations with heart-cycle averaged values for the inlet and downstream pressure is relevant in the case of the 0D R BC model without the presence of nonlinear elements. The major advantage of using steady-state simulations is the significantly lower times required for the solution of the blood flow model. The choice of vasodilation threshold, which is equivalent to the maximum degree of decreasing of peripheral vascular resistance under hyperaemia is another modelling assumption that affects the magnitude of the computed FFR and consequently the diagnosis of the haemodynamic stenosis severity. Although this is generally assumed to lie within the 0.2-0.25 range, based on invasive measurements [44,138], it can vary depending on the interpatient characteristics, as well as in cases of patients with vasoconstriction-related pathologies. In theory and in combination with

other factors, the related difference in the computed FFR may exceed +/- 0.15, which is significant when compared to the fixed value of the 0.75 threshold. Analysis of the impact of interpatient variations on the computed flow fields showed that although the magnitude of inlet and downstream pressure used in the BC models does not affect the computed flow itself, the changes in their difference $\Delta P = P_{in} - P_d$ and ratio $dP = P_d/P_{in}$ directly define the inlet flow rate and FFR magnitudes. Whereas the inlet pressure represented by the aortic pressure can be noninvasively measured, it is essential to verify the approach for approximation of the downstream pressure of ventricle contraction. In general, the choice of lower P_d values results in higher flow rates and lower FFR values, however, if the dP ratio remains the same, even +/- 20 mmHg change in ΔP does not affect FFR and dQ for more than 5%. As mentioned above, the patient-specific value of the inlet flow rate indirectly affects the computed flow since it defines the process of BC model parameter adjustment and resistance of peripheral vasculature. Variations in blood viscosity within the healthy range do not produce any significant changes, however higher viscosity values result in higher flow resistance and higher pressure drop.

Investigation of the impact of the vessel segmentation accuracy and other aspects of preparation of the computational domain on the computed flow fields was presented in Section 5.3. This included variations in the choices for: (i) vessel segmentation blood threshold; (ii) side branch outlet truncation level; and (iii) degree of lumen surface smoothing. Due to the fact that contrast-enhanced blood intensity can vary within the 200 – 400 HU range together with the insufficiently high resolution of CCTA, automatic segmentation of coronary arteries with an inaccurately chosen segmentation threshold may result in a significant difference in the lumen diameter with the extracted lumen also including parts of the vessel wall and the fibrous cap of atherosclerotic plaques. A series of cases with the values of the segmentation threshold varying within the 210-350 HU range were considered for the same CCTA volume with the corresponding results demonstrating a 15% as compared to 75% maximum reduction in the LAD stenosed region for the two case of 210 and 350 HU values, respectively. Logically, this caused a significant difference in the FFR values derived from the computed flow fields being 0.83 compared to 0.71 after the adjustment of BC model parameters to the same flow boundary conditions. Another essential aspect of preparation of the geometry of the computational domain is the level at which the side branches are truncated for the definition of the outlets. Due to the limitations of CCTA resolution, narrow side branches generally cannot be reconstructed with the required level of accuracy, particularly when it comes to the dissipation of the contrast agent along the branch length. This, together with the variations of the blood

threshold, can potentially result in the branch outlets becoming narrower at distal locations constituting for erroneous segmentation results. At the same time, as described above, the flow distribution between the branches is derived from the outlet diameters and directly defines the computed flow fields and thus the truncation level will define the dQ to the branches. The corresponding blood flow simulation results showed a significant difference in the computed FFR and TAWSS fields for different truncation level cases (Section 5.3.2) with lower flow and pressure drop in branches with narrower outlets. It was identified that the optimal choice of truncation level is either 2 mm or as close as possible to the main branch. Next, the impact of the degree of smoothing of the artery lumen surface was investigated. The comparison of the computed FFR and TAWSS for three cases of the initial "rough" surface, moderately smoothed surface, and the lumen surface after the applied high-degree Laplacian smoothing confirmed that while moderate smoothing does not change the flow patterns and allows for removal of surface irregularities caused by limited CCTA resolution and suboptimal threshold-based segmentation, a high degree smoothing should be avoided since it modifies the vascular geometry and the stenosis diameter, thus leading to overestimation of the FFR drop.

Section 5.4 provided the results of the investigation of the correlation between the patient-specific 0D and 3D coronary blood flow models and the corresponding applicability of using the extracted 0D flow resistance as a characteristic of haemodynamic stenosis severity. The efficiency of the proposed novel approach for extension of the classical 0D models with spatial information was assessed through the comparison of the 0D and 3D computed flow in a single stenosed LAD branch. The results of the comparison demonstrated high correlation in the computed pressure and FFR along the vessel. On the other hand, the deviation in the computed flow rate occurring under a high degree of vasodilation was explained through the complex flow resistance in the 3D domain that varies depending on the flow rate [146,147]. However, since this does not produce the difference in the computed pressure with the pressure difference $\Delta P = P_{in} - P_{out}$ being preserved the same in both 0D and 3D domains, the relevance of using 0D blood flow simulations in the assessment of FFR was confirmed. In addition, the proposed modelling approach also provides spatial information on the FFR and pressure along a vessel branch, which so far was considered to be the main drawback of 0D blood flow simulations. In the case of the entire LCA tree model based on the baseline LCA case, the 0D and 3D results showed similar patterns in FFR, pressure and flow rate distributions within 0.1-1.0 vasodilation range. However, since the implemented 0D CVS is the dynamic system, decreasing of the total resistance of the coronary circulation loop leads to the changes in the

entire CVS loop. Consequently, this also changes the flow boundary conditions for the coronary artery tree model with the difference in lower P_{in} and P_d becoming critical beginning from dR = 0.1. In summary, 0D simulations resulted in a slightly higher pressure drop under hyperaemia for the stenosed LAD branch than produced by the 3D CFD model with the main factor being the corresponding changes in ΔP and dP BC model values. One of the other possible reasons for deviations between 0D and 3D results is the accuracy of calculation of resistance from vessel geometers in the stenosis area. This emphasises the need for future research to focus on the thorough investigation of the accuracy of the flow resistance extraction methodology as well as other aspects of 0D blood flow simulations in vessel structures with multiple outlets. Although, unlike 3D CFD models, 0D domain simulations do not provide detailed information on blood flow such as velocity and WSS, they are highly efficient with respect to time and computational resource requirements and can also be considered to have a more straightforward solution.

5.6 Conclusions

This chapter presented the results of a series of performed blood flow simulations in the both implemented 3D and 0D patient-specific coronary blood flow models with the overall purpose of analysis of the factors that may potentially affect the computed flow patterns.

The outcomes of this parametric study formalised the basis for development of the guidelines for high accuracy 3D coronary blood flow simulations. This is especially critical since the analysis of the impact of various modelling assumptions is essential in establishing a reliable blood flow modelling approach in real world applications, such as virtual FFR assessment. In addition, the new concept of spatially extended 0D blood flow models showed the potential to become a useful tool in the assessment of the flow-limiting impact of a series of stenoses though the extraction of the flow resistance along vessel branches.

Chapter 6

Conclusions and Future Work

The final chapter of this thesis concludes the current research and makes recommendations regarding possible extensions and future directions.

The goal of this project has been to develop a methodology for implementation of patient-specific blood flow simulations in coronary arteries reconstructed from CCTA datasets, which would assist clinicians in the diagnosis of coronary artery disease by the assessment of functional stenosis severity in the form of the virtual FFR clinical index. The computed FFR patterns increase the diagnostic value of CCTA through the additional information of changes in coronary haemodynamics under the hyperaemia condition with respect to the anatomical characteristics of arterial trees, which is particularly relevant in the case of multivessel CAD disease. Formalisation of the methodology for implementation of the multiscale blood flow models and investigation of the essential parameters through a parametric study is especially relevant with respect to the physiological accuracy of the computed blood flow, since there is a significant lack of general guidelines on developing patient-specific coronary blood flow simulations.

The conclusions related to the design, implementation and analysis of the multiscale 3D and 0D patient-specific coronary blood flow models described in Chapters 3-5 are presented in Section 6.1. And, based on the analysis of the achieved results, the possible extensions and recommendations for future research are given in Section 6.2.

6.1 Multidomain Patient-Specific Coronary Blood Flow Modelling

Despite of the reported high correlation between the computed virtual and invasively measured FFR patterns in a series of clinical studies, the majority of the implemented coronary blood flow modelling approaches are generally characterised by high levels of uncertainty. This is caused by the highly patient-specific nature of the problem domain together with the lack of guidelines defining the optimal modelling parameters and requirements for computation of physiologically accurate flow fields. The diversity of the methods that can be employed at the various stages of model implementation as well as the general lack of the validation data also play an important role. The accuracy of blood flow simulations in reconstructed vascular

geometries is defined not only from the average range of physiological values but also by taking into account a list of patient-specific parameters and the associated modelling assumptions. In coronary blood flow models, this includes of flow boundary conditions as pressure and flow rate at the inlet of the coronary artery and impedance from the peripheral vasculature. Other factors include the parameter settings in the methods used in reconstruction of coronary arteries from CCTA data (or ICA) and blood rheology model type. Since, normally, the majority of these parameter values are not available as inputs for the simulation or validation due to the risks related to invasive flow measurements, a set of modelling assumptions based on the average interpatient characteristics have to be employed in the model setup.

Following the outcomes of the extensive background research on the requirements, limitations and potential uncertainties of the existing blood flow modelling methods presented in Chapter 2, a systematic approach for the design of 3D patient-specific coronary blood flow models was proposed. Implementation of a blood flow model begins from the reconstruction of the coronary artery lumen geometry from a CCTA volume, which is then pre-processed and the blood volume within the lumen is discretised into the computational domain. Next, the formalised blood flow model is defined in a professional CFD solver, including the modelling assumptions and the specification of the flow boundary conditions on the inlet and outlets of the coronary artery tree. Taking into account that the computed blood flow fields are directly defined by the BC, the downstream impedance representing the response of the peripheral vasculature is implemented as 0D models implicitly coupled at the outlets. The corresponding resistance and capacitance values are computed from the patient-specific 1D tree impedance, derived from the classical morphometric law defining vascular structures. The computed 0D model parameters are further adjusted in order to achieve an appropriate flow rate distribution between the vascular branches proportional to the outlet diameters. Following the numerical solution of the model with the classical CFD methods, the haemodynamic parameters including pressure, flow rate, wall shear stress and FFR are extracted from the computed flow for the analysis of the global patterns, detection of CAD lesions and interpretation of stenosis severity.

Based on the specified baseline case of the blood flow in the left coronary artery with a series of stenoses, a large spectre of simulations was performed for the investigation of the sensitivity of the blood flow solution to variations in the modelling assumptions and parameters. The analysis of the results formalised the foundation for the guidelines in coronary blood flow modelling including the aspects of: (i) vessel segmentation in CCTA datasets; (ii) definition of the boundaries of the 3D computational domain; (iii) blood flow modelling

assumptions; (iv) boundary condition model type; (v) approximation of the downstream vascular impedance; (vi) tuning of the BC model parameters; (vii) simulation of vasodilation induced hyperaemia condition; (viii) interpatient variations in BC model parameters. In addition to the computed FFR, the 3D model results were also analysed with respect to the variation in TAWSS patterns, which are considered to be linked to the underlying mechanisms of atherogenesis. These results demonstrated that the computed flow fields are highly sensitive to the influence of the adjustment of the 0D BC model parameters that replicate the impedance of peripheral vasculature as well as the interpatient variation of the CVS flow patterns, such as the inlet coronary flow rate, aortic and LV pressure. The performed investigations of the impact of variations in the vessel tree lumen geometry reconstruction parameters such as blood segmentation threshold, side branch truncation level, and degree of surface smoothing also showed a significant influence on the computed FFR and TAWSS patterns. The corresponding findings were summaries in the form of a set of guidelines for optimisation of the coronary blood flow model development.

Taking into account the fact that one of the major limitations of CFD blood flow modelling is related to the high computational costs and the long times required for one simulation, the feasibility of the application of reduced order models was investigated, since they are significantly more time-efficient. A novel approach for the implementation of spatially extended patient-specific 0D blood flow models was proposed. While the classical 0D models based on the electrical–hydraulic analogy use the lumped-parameter representation of major vessel tree structures and are thus characterised by limited spatial characteristics, the proposed method for modelling of individual vessel tree branches through a series of 0D elements provides the means for correlation of the computed flow with the precise location along a vessel. The corresponding flow resistance values are extracted from the vessel lumen geometry reconstructed from the CCTA dataset. Therefore, this extends the applicability of 0D modelling in patient-specific blood flow simulations for FFR assessment.

Following the reconstruction of the coronary artery lumen from the CCTA volume, it is divided into branches based on the estimated centreline. Next, the arterial tree branches are subdivided into 3D elementary segments and the corresponding 0D flow resistance and capacitance elements are derived from their geometries. The 0D arterial tree is constructed as an electrical circuit with its branches represented through a series of elementary 0D blocks. The 0D model of the left coronary artery was developed and implemented together with the 0D model of the CVS, which is required for the modelling of physiologically realistic flow

boundary conditions. The haemodynamics of the 0D CVS loop model can be adjusted with respect to patient-specific data, such as CO and heart rate. The blood flow model is established through the PDEs defining the current-voltage relationship in the corresponding electrical circuit network, under the specified modelling assumptions. The outcomes of the transient solution of the blood flow model include the computed pressure, flow rate and FFR at the model outlets and along the arterial tree branches that can be used for the assessment of the haemodynamic severity of the stenoses.

The performed series of experiments showed high correlation between the equivalent 0D and 3D computed flow models of the patient-specific coronary artery under both the rest and hyperaemia conditions, thus confirming the general applicability of 0D blood flow modelling in the task of FFR assessment. In addition, this also validated the proposed approach for extraction of flow resistance from vascular geometries and the extension of the classical 0D modelling for computation of spatially distributed characteristics of computed blood flow.

The implemented library of 0D CVS and coronary tree elements was integrated into the MATLAB SIMULINK® environment, which provides a means for straightforward construction of patient-specific coronary artery trees for performing coronary blood flow simulations.

6.2 Recommendations for Future Work

6.2.1 Improvements Regarding 3D Coronary Blood Flow Modelling

Based on the developed 3D blood flow modelling approach and the performed analysis of the factors affecting the computed flow patterns, future research will focus on the further optimisation of the model and the specification of the optimal range of 0D BC parameters though the analysis of the results for a larger set of coronary artery geometries.

At first, verification of the outcomes of the study of the influence of modelling assumptions should be performed based on the model validation in the interpatient case study. This will also involve the definition of the optimal value ranges for the model parameters. The general validation of the model performance in FFR assessment on a larger dataset with both invasive measurements and results from the HeartFlow® FFR_{CT} tool [44] is planned to be performed on a series of FFR/CCTA/FFR_{CT} cases. In addition, the comparison of the model

performance with the other existing frameworks for virtual FFR assessment such as cFFR by Siemens Healthcare [55] might also be considered.

Further development of the model will focus on the analysis of the difference between the transient downstream 0D BC model types is required with qualitative investigation of the impact of variations in the myocardium wall compliance values and optimisation of the solution strategy in order to decrease the simulation times. Since, so far, the impact of vessel wall compliance on the computed FFR was considered negligible and was not investigated, the extension of the model with vessel wall compliance will be performed through FSI. This will also extend the scale of the model applicability for blood flow simulations in stented arteries and in CABG cases. Taking into account the significant amount of user input required for the implementation of blood flow models in professional CFD solvers, the strategy for automation and optimisation of the methodology for the blood flow model setup and preparation of the computational domain should be investigated.

Planning of the investigation of various physiological factors and pathologies affecting the simulation results (e.g., diastole duration, arterial stiffness, aortic stenosis, cardiac arrhythmia, myocardial infarction, etc.) should also be in the close correlation with the 0D simulations, since it is based on modification of the related CVS characteristics in the BC model parameters. It can be relatively easy performed in the implemented 0D CVS model, since it provides the means for straightforward modelling of cardiovascular pathologies by adjusting the associated 0D element parameters. Next, incorporation of the 0D heart model as the inlet BC should be considered in order to account for the dynamic changes in aortic and LV blood pressure under simulated hyperaemia for the comparison with the 0D CVS model results.

6.2.2 Improvements Regarding 0D Coronary Blood Flow Modelling

The results of the comparison between the 3D and 0D domains demonstrated high correlation in the computed pressure and FFR along the vessel. In the case of the entire LCA tree model based on the baseline LCA case, the 0D and 3D results showed similar patterns in FFR, pressure and flow rate distribution within the 0.1-1.0 dR vasodilation range. However, the divergence of the results for lower dR, caused by the change in the dynamics of 0D CVS, confirmed the importance of incorporating the full CVS loop into the model in order to preserve physiologically realistic flow patterns.

The 0D results also demonstrated a slightly higher pressure drop under hyperaemia for the stenosed LAD branch than the one produced by the 3D CFD model with one of the possible reasons for this deviation being the accuracy in calculating the resistance from the vessel geometry in the stenosis area. Consequently, this emphasises the need for future research to focus on the thorough investigation of the accuracy of the methodology for the extraction of spatially distributed flow resistance, the validation of the employed vessel segmentation methods with respect to the lumen extraction accuracy (similarly to the 3D model) as well as the further automation of the implemented framework. This should be indirectly achieved through the validation of the 0D model in comparison to 3D CFD results on a series of CCTA datasets with the presence of various atherosclerotic plaque types.

The next step will involve the incorporation of the vessel wall compliance feature for coronary vessel segments together with the automatic mechanism for the adjustment of the 0D downstream model parameters and an option for the setting of patient-specific CVS parameters such as diastole duration and CO. In addition, following the establishment of the foundation for 0D coronary blood flow modelling, the assessment of the applicability of using the extracted flow resistance and 0D modelling in CAD diagnosis by comparison with invasively measured FFR along a coronary artery should be performed.

Bibliography

[1] V. Fuster, R.W. Alexander, R.A. O'Rourke RA, “Hurst's The Heart,” 10th ed., New York: McGraw Hill Medical Publishing, 2001.

[2] A. J. Pappano and W.G. Wier, “Cardiovascular Physiology,” 10th Edition, Elsevier, 2013.

[3] Coronary Anatomy and Blood Flow, [Online]. Available: http://www.cvphysiology.com/Blood%20Flow/BF001.htm. [Accessed 01 July 2015].

[4] C. Berry, K. P. Balachandran, P. L. L’Allier, J. Lespérance, R. Bonan, K. G. Oldroyd, “Importance of collateral circulation in coronary heart disease,” Eur. Heart J., vol. 28, pp. 278–291, 2007.

[5] J.T. Dodge and B.G. Brown, E.L. Bolson, H.T. Dodge, “Lumen diameter of normal human coronary arteries influence of age , sex , anatomic variation , and left ventricular hypertrophy or dilation,” Circulation, vol 86, no 1, pp. 232–246, July 1992.

[6] M.D. Silver, A.I. Gotlieb, F.J. Schoen, “Cardiovascular pathology,” 3rd ed. New York: Churchill Livingstone, 2001.

[7] K. S. Cunningham and A. I. Gotlieb, “The role of shear stress in the pathogenesis of atherosclerosis,” Lab. Investig., vol. 85, no. 1, pp. 9–23, 2005.

[8] Wall Shear Stress and Arterial Wall Remodeling, [Online]. Available: http://zarinslab.stanford.edu/research/wall_shear.html. [Accessed 01 July 2015].

[9] C.J.Pepine, "The effects of angiotensin-converting enzyme inhibition on endothelial dysfunction: Potential role in myocardial ischemia", The American Journal of Cardiology, vol. 82, no. 10, Supplement 1, pp. S23-S27, 1998.

[10] R. Virmani, F.D. Kolodgie, A.P. Burke, A. Farb, S.M. Schwartz, “Lessons from sudden coronary death: a comprehensive morphological classification scheme for atherosclerotic lesions,” Arterioscler Thromb Vasc Biol., vol. 20, no. 5, pp. 1262-75, 2000.

[11] M. Naghavi, et al. “From vulnerable plaque to vulnerable patient: a call for new definitions and risk assessment strategies: Part I,” Circulation, vol. 108, no. 14, pp. 1664–1672, 2003.

[12] P. Stenvinkel, R. Pecoits-filho, B. Lindholm, “Coronary artery disease in end-stage renal disease : no longer a simple plumbing problem,” J Am Soc Nephrol, vol. 14, pp. 1927–1939, 2003.

[13] A. Arbab-Zadeh, J. Hoe, “Quantification of coronary arterial stenoses by multidetector CT angiography in comparison with conventional angiography methods, caveats, and implications,” Journal of the American College of Cardiology, vol. 42, no. 2, pp. 191–202, 2011.

[14] J. Zhang, L. Zhong, B. Su, M. Wan, J. S. Yap, “Perspective on CFD studies of coronary artery disease lesions and hemodynamics : A review,” Numer. METHODS Biomed. Eng., vol. 30, no. January, pp. 659–680, 2014.

[15] M.C. Rosenberg, L.W. Klein, J.B. Agarwal, G. Stets, G.A. Hermann, and R.H. Helfant, “Quantification of absolute luminal diameter by computer-analyzed digital subtraction angiography: an assessment in human coronary arteries,” Circulation, vol. 77, no. 2, pp. 484–490, 1988.

[16] G. L. Raff, A. Abidov, S. Achenbach, D. S. Berman, L. M. Boxt, M. J. Budoff, V. Cheng, T. DeFrance, J. C. Hellinger, and R. P. Karlsberg, “SCCT guidelines for the interpretation and reporting of coronary computed tomographic angiography.,” J. Cardiovasc. Comput. Tomogr., vol. 3, no. 2, pp. 122–36, 2009.

[17] P. Pavone and R. Leo, “Coronary CT Angiography : evaluation of stenosis and occlusion.,” in CT Evaluation of Coronary Artery Disease, Springer-Verlag Italia, 2009.

[18] J.A.E. Spaan, J.J. Piek, J.I.E. Hoffman, M. Siebes, “Physiological basis of clinically used coronary hemodynamic indices.,” Circulation, vol. 113, no. 3, pp. 446–55, Jan. 2006.

[19] W.L. Gould, K. Lipscomb, G.W. Hamilton, “Physiologic basis for assessing critical coronary stenosis: instantaneous flow response and regional distribution during coronary hyperemia as measures of coronary flow reserve,” The American Journal of Cardiology, vol. 33, no. 1, pp. 87–94, 1974.

[20] N.P. Johnson, R.L. Kirkeeide, K.L. Gould, “Is discordance of coronary flow reserve and fractional flow reserve due to methodology or clinically relevant coronary pathophysiology?,” JACC Cardiovascular Imaging, vol. 5, no. 2, pp. 193–202, 2012.

[21] K.K. Kolli et al., “Diagnostic performance of pressure drop coefficient in relation to fractional flow reserve and coronary flow reserve,” J Invasive Cardiol., vol. 26, no. 5, pp. 188-195, 2014.

[22] K.L. Gould, N.P. Johnson, “Coronary artery disease: percent stenosis in CAD - a flaw in current practice,” Nature Reviews Cardiology, vol. 7, no. 9, pp. 482–484, 2010.

[23] V.J.E. Velzen, J.D. Schuijf, F.R. De Graaf, J.W. Jukema, A.D. Roos, L.J. Kroft, M.J. Schalij, J.H. Reiber, E.E. Van DerWall, J.J. Bax, “Imaging of atherosclerosis: invasive and noninvasive techniques,” Hellenic Journal of Cardiology, vol. 50, no. 4, pp. 245–263, 2009.

[24] M. Hamilos, A. Peace, G. Kochiadakis, E. Skalidis, A. Ntalianis, B. De Bruyne, P. Vardas, “Fractional flow reserve: an indispensable diagnostic tool in the cardiac catheterisation laboratory,” Hellenic Journal of Cardiology, vol. 51, pp. 133-141, 2010.

[25] N. H. J. Pijls, W. F. Fearon, P. L. Tonino, U. Siebert, F. Ikeno, B. Bornschein, M. Van’t Veer, V. Klauss, G. Manoharan, T. Engstrøm, K. G. Oldroyd, P. N. Ver Lee, P. MacCarthy, B. De Bruyne, “Fractional flow reserve versus angiography for guiding percutaneous coronary intervention in patients with multivessel coronary artery disease: 2-year follow-up of the FAME (Fractional Flow Reserve Versus Angiography for Multivessel Evaluation) study.,” J. Am. Coll. Cardiol., vol. 56, no. 3, pp. 177–84, Jul. 2010.

[26] V. Gorenoi, M. P. Schönermark, A. Hagen, “CT coronary angiography vs. invasive coronary angiography in CHD.,” GMS Health Technol. Assess., vol. 8, pp. 1-8, 2012.

[27] U. Olgac, D. Poulikakos, S. C. Saur, H. Alkadhi, V. Kurtcuoglu, “Patient-specific three-dimensional simulation of LDL accumulation in a human left coronary artery in its healthy and atherosclerotic states,” Am J Physiol Heart Circ Physiol, vol. 296, no. 6, pp. 1969–1981, 2009.

[28] U. Olgac, J. Knight, D. Poulikakos, S. C. Saur, H. Alkadhi, L. M. Desbiolles, P. C. Cattin, V. Kurtcuoglu, “Computed high concentrations of low-density lipoprotein correlate with plaque locations in human coronary arteries.,” Journal of biomechanics, vol. 44, no. 13, pp. 2466–71, Sep. 2011.

[29] J. Knight, U. Olgac, S. C. Saur, D. Poulikakos, W. Marshall, P. C. Cattin, H. Alkadhi, V. Kurtcuoglu, “Choosing the optimal wall shear parameter for the prediction of plaque location-A patient-specific computational study in human right coronary arteries.,” Atherosclerosis, vol. 211, no. 2, pp. 445–50, Aug. 2010.

[30] F. Rikhtegar, J. Knight, U. Olgac, S. C. Saur, D. Poulikakos, W. Marshall, P. C. Cattin, H. Alkadhi, V. Kurtcuoglu, “Choosing the optimal wall shear parameter for the prediction of plaque location: A patient-specific computational study in human left coronary arteries.,” Atherosclerosis, vol. 221, no. 2, pp. 432–7, Apr. 2012.

[31] P. H. Stone, A. U. Coskun, S. Kinlay, M. E. Clark, M. Sonka, A. Wahle, O. J. Ilegbusi, Y. Yeghiazarians, J. J. Popma, J. Orav, R. E. Kuntz, C. L. Feldman, “Effect of endothelial shear stress on the progression of coronary artery disease, vascular remodeling, and in-stent restenosis in humans: in vivo 6-month follow-up study.,” Circulation, vol. 108, no. 4, pp. 438–44, Jul. 2003.

[32] M. I. Papafaklis, S. Takahashi, A. P. Antoniadis, A. U. Coskun, M. Tsuda, S. Mizuno, I. Andreou, S. Nakamura, Y. Makita, A. Hirohata, S. Saito, C. L. Feldman, P. H. Stone, “Effect of the local hemodynamic environment on the de novo development and progression of eccentric coronary atherosclerosis in humans: Insights from PREDICTION.,” Atherosclerosis, vol. 240, no. 1, pp. 205–211, 2015.

[33] P. Eshtehardi, M. C. McDaniel, J. Suo, S. S. Dhawan, L. H. Timmins, J. N. G. Binongo, L. J. Golub, M. T. Corban, A. V Finn, J. N. Oshinski, A. Quyyumi, D. P. Giddens, H. Samady, “Association of coronary wall shear stress with atherosclerotic plaque burden, composition, and distribution in patients with coronary artery disease.,” Journal of the American Heart Association, vol. 1, no. 4, p. e002543, Aug. 2012.

[34] D. Sengupta, A. M. Kahn, J. C. Burns, S. Sankaran, S. C. Shadden, A. L. Marsden, “Image-based modeling of hemodynamics in coronary artery aneurysms caused by Kawasaki disease.,” Biomechanics and modeling in mechanobiology, vol. 11, no. 6, pp. 915–32, Jul. 2012.

[35] W.S. Nesbitt, E. Westein, F.J. Tovar-Lopez, E. Tolouei, A. Mitchell, J. Fu, J. Carberry, A. Fouras, S.P.A. Jackson, “Shear gradient-dependent platelet aggregation mechanism drives thrombus formation.,” Nature Medicine, no. 15, pp. 665 – 673, May 2009.

[36] D. Sengupta, “Risk Assessment using Image-Based Hemodynamic Modeling of Patients with Coronary Artery Aneurysms caused by Kawasaki Disease,” PhD Thesis, University of California, San Diego, 2013.

[37] D. Tang, Z. Teng, G. Canton, T. S. Hatsukami, L. Dong, X. Huang, C. Yuan, “Local critical stress correlates better than global maximum stress with plaque morphological features

linked to atherosclerotic plaque vulnerability: an in vivo multi-patient study.," Biomedical engineering online, vol. 8, p. 15, Jan. 2009.

[38] D. Tang, C. Yang, J. Zheng, P. K. Woodard, J. E. Saffitz, D. Joseph, G. A. Sicard, C. Yuan, "Local Maximal Stress Hypothesis and Computational Plaque Vulnerability Index for Atherosclerotic Plaque Assessment," Ann Biomed Eng., vol. 33, no. 12, pp. 1789–1801, 2006.

[39] X. Huang, C. Yang, J. Zheng, R. Bach, D. Muccigrosso, P. K. Woodard, D. Tang, "Higher critical plaque wall stress in patients who died of coronary artery disease compared with those who died of other causes: a 3D FSI study based on ex vivo MRI of coronary plaques.," Journal of biomechanics, vol. 47, no. 2, pp. 432–7, Jan. 2014.

[40] B. Liu, J. Zheng, R. Bach, D. Tang, "Correlations of coronary plaque wall thickness with wall pressure and wall pressure gradient: a representative case study.," Biomedical engineering online, vol. 11, no. 1, p. 43, Jan. 2012.

[41] R. Fan, D. Tang, C. Yang, J. Zheng, R. Bach, L. Wang, D. Muccigrosso, K. Billiar, J. Zhu, G. Ma, A. Maehara, G. S. Mintz, "Human coronary plaque wall thickness correlated positively with flow shear stress and negatively with plaque wall stress: an IVUS-based fluid-structure interaction multi-patient study.," Biomedical engineering online, vol. 13, no. 1, p. 32, Jan. 2014.

[42] S. H. Rambhia, X. Liang, M. Xenos, Y. Alemu, N. Maldonado, A. Kelly, S. Chakraborti, S. Weinbaum, L. Cardoso, S. Einav, D. Bluestein, "Microcalcifications increase coronary vulnerable plaque rupture potential: a patient-based micro-CT fluid-structure interaction study.," Annals of biomedical engineering, vol. 40, no. 7, pp. 1443–54, Jul. 2012.

[43] B. L. Nørgaard, J. Leipsic, S. Gaur, S. Seneviratne, B. S. Ko, H. Ito, J. M. Jensen, L. Mauri, B. De Bruyne, H. Bezerra, K. Osawa, M. Marwan, C. Naber, A. Erglis, S.-J. Park, E. H. Christiansen, A. Kaltoft, J. F. Lassen, H. E. Bøtker, S. Achenbach, "Diagnostic performance of noninvasive fractional flow reserve derived from coronary computed tomography angiography in suspected coronary artery disease: the NXT trial (Analysis of Coronary Blood Flow Using CT Angiography: Next Steps).," J. Am. Coll. Cardiol., vol. 63, no. 12, pp. 1145–55, Apr. 2014.

[44] C. A. Taylor, T. A. Fonte, J. K. Min, “Computational fluid dynamics applied to cardiac computed tomography for noninvasive quantification of fractional flow reserve: scientific basis.,” J. Am. Coll. Cardiol., vol. 61, no. 22, pp. 2233–41, Jun. 2013.

[45] J. K. Min, C. A. Taylor, S. Achenbach, B. K. Koo, J. Leipsic, B. L. Nørgaard, N. J. Pijls, B. De Bruyne, “Noninvasive fractional flow reserve derived from coronary CT angiography: Clinical data and scientific principles,” JACC Cardiovasc. Imaging, vol. 8, no. 10, pp. 1209–1222, 2015.

[46] A. D. Choi, J. M. Joly, M. Y. Chen, W. G. Weigold, “Physiologic evaluation of ischemia using cardiac CT: Current status of CT myocardial perfusion and CT fractional flow reserve.,” J. Cardiovasc. Comput. Tomogr., vol. 8, no. 4, pp. 272–281, 2014.

[47] J. Min, D. Berman, L. Shaw, L. Mauri, B.-K. Koo, A. Erglis, J. Leipsic, “TCT-19 Fractional Flow Reserved Derived From Computed Tomographic Angiography (FFRCT) for Intermediate Severity Coronary Lesions: Results from the DeFACTO Trial (Determination of Fractional Flow Reserve by Anatomic Computed TOmographic Angiography),” J. Am. Coll. Cardiol., vol. 60, no. 17, p. B6, Oct. 2012.

[48] S. Baumann, R. Wang, U. J. Schoepf, D. H. Steinberg, J. V Spearman, R. R. Bayer, C. W. Hamm, M. Renker, “Coronary CT angiography-derived fractional flow reserve correlated with invasive fractional flow reserve measurements - initial experience with a novel physician-driven algorithm.,” Eur. Radiol., pp. 1201–1207, Nov. 2014

[49] P. D. Morris, D. Ryan, A. C. Morton, R. Lycett, P. V. Lawford, D. R. Hose, J. P. Gunn, “Virtual fractional flow reserve from coronary angiography: modeling the significance of coronary lesions: results from the VIRTU-1 (VIRTUal Fractional Flow Reserve From Coronary Angiography) study.,” JACC. Cardiovascular interventions, vol. 6, no. 2, pp. 149–57, Feb. 2013.

[50] S. Tu, E. Barbato, Z. Köszegi, J. Yang, Z. Sun, N. R. Holm, B. Tar, Y. Li, D. Rusinaru, W. Wijns, J. H. C. Reiber, “Fractional Flow Reserve Calculation From 3-Dimensional Quantitative Coronary Angiography and TIMI Frame Count: A Fast Computer Model to Quantify the Functional Significance of Moderately Obstructed Coronary Arteries.,” JACC. Cardiovascular interventions, vol. 7, no. 7, pp. 768–77, Jul. 2014.

[51] J. Zhang, L. Zhong, T. Luo, Y. Huo, S. Y. Tan, A. S. L. Wong, B. Su, M. Wan, X. Zhao, G. S. Kassab, H. P. Lee, B. C. Khoo, C.-W. Kang, T. Ba, R. S. Tan, "Numerical simulation and clinical implications of stenosis in coronary blood flow.," Biomed Res. Int., vol. 2014, p. 514729, 2014.

[52] P. K. Siogkas, M. I. Papafaklis, A. I. Sakellarios, K. Stefanou, C. V Bourantas, L. M. Athanasiou, C. V Bellos, T. P. Exarchos, K. K. Naka, L. K. Michalis, O. Parodi, D. I. Fotiadis, "Computational assessment of the fractional flow reserve from intravascular ultrasound and coronary angiography data: a pilot study.," in 35th Annual International Conference of the IEEE EMBS, pp. 3885–8, Osaka, Japan, 3 - 7 July, 2013.

[53] S. Sankaran, L. Grady, C. A. Taylor, "Impact of geometric uncertainty on hemodynamic simulations using machine learning," Comput. Methods Appl. Mech. Eng., vol. 297, pp. 167–190, 2015.

[54] J. T. C. Schrauwen, J. J. Wentzel, F. W. van der Steen, F. J. H. Gijsen, "Geometry-based pressure drop prediction in mildly diseased human coronary arteries.," Journal of biomechanics, vol. 47, no. 8, pp. 1810–5, Jun. 2014.

[55] M. Renker, U. J. Schoepf, R. Wang, F. G. Meinel, J. D. Rier, R. R. Bayer, H. Möllmann, C. W. Hamm, D. H. Steinberg, S. Baumann, "Comparison of diagnostic value of a novel noninvasive coronary computed tomography angiography method versus standard coronary angiography for assessing fractional flow reserve.," Am. J. Cardiol., vol. 114, no. 9, pp. 1303–8, 2014.

[56] L. Itu, P. Sharma, V. Mihalef, A. Kamen, C. Suciu, D. Comaniciu, "A patient-specific reduced-order model for coronary circulation," in 9th IEEE International Symposium Biomedical Imaging (ISBI), Barcelona, pp. 832–835, May 2012.

[57] A. Uus, P. Liatsis, M. Jawaid, R. Rajani, E. Benderskaya, "Assessment of stenosis introduced flow resistance in CCTA-reconstructed coronary arteries," in 2015 International Conference on Systems, Signals and Image Processing (IWSSIP), pp.313-320, 10-12 Sept. 2015.

[58] S. Sankaran, M. Esmaily Moghadam, A. M. Kahn, E. E. Tseng, J. M. Guccione, A. L. Marsden, "Patient-specific multiscale modeling of blood flow for coronary artery bypass graft surgery.," Annals of biomedical engineering, vol. 40, no. 10, pp. 2228–42, Oct. 2012.

[59] F. Kabinejadian and D. N. Ghista, “Compliant model of a coupled sequential coronary arterial bypass graft: effects of vessel wall elasticity and non-Newtonian rheology on blood flow regime and hemodynamic parameters distribution.,” Medical engineering & physics, vol. 34, no. 7, pp. 860–72, Sep. 2012.

[60] J. F. LaDisa, I. Guler, L. E. Olson, D. Hettrick, J. R. Kersten, D. C. Warltier, P. S. Pagel, “Three-Dimensional Computational Fluid Dynamics Modeling of Alterations in Coronary Wall Shear Stress Produced by Stent Implantation,” Annals of Biomedical Engineering, vol. 31, no. 8, pp. 972–980, Sep. 2003.

[61] L. M. Ellwein, H. Otake, T. J. Gundert, B. Koo, T. Shinke, Y. Honda, J. Shite, J. F. LaDisa, “Optical Coherence Tomography for Patient-specific 3D Artery Reconstruction and Evaluation of Wall Shear Stress in a Left Circumflex Coronary Artery,” Cardiovascular Engineering and Technology, vol. 2, no. 3, pp. 212–227, May 2011.

[62] V. Dehlaghi, M. T. Shadpoor, S. Najarian, “Analysis of wall shear stress in stented coronary artery using 3D computational fluid dynamics modeling,” Journal of Materials Processing Technology, vol. 197, no. 1–3, pp. 174–181, Feb. 2008.

[63] B. L. Nørgaard, S. Gaur, J. Leipsic, H. Ito, T. Miyoshi, S.-J. Park, L. Zvaigzne, N. Tzemos, J. M. Jensen, N. Hansson, B. Ko, H. Bezerra, E. H. Christiansen, A. Kaltoft, J. F. Lassen, H. E. Bøtker, S. Achenbach, “Influence of Coronary Calcification on the Diagnostic Performance of CT Angiography Derived FFR in Coronary Artery Disease,” JACC Cardiovasc. Imaging, vol. 8, no. 9, pp. 1045–1055, 2015.

[64] D. M. Martin, E. Murphy, F. J. Boyle, “Computational fluid dynamics analysis of balloon-expandable coronary stents: influence of stent and vessel deformation.,” Medical engineering & physics, vol. 36, no. 8, pp. 1047–56, Aug. 2014.

[65] K. Tanaka, H. Bezerra, H. E. Botker, B. Nørgaard, “TCT-318 Trans-lesional {FFRCT} gradient correlates with measured {FFR} gradient in vessels with serial coronary stenosis: role in stenting strategy.,” J. Am. Coll. Cardiol., vol. 64, no. 11, Supplement, pp. B91 – B92, 2014.

[66] C. Chiastra, F. Migliavacca, M. Á. Martínez, M. Malvè, “On the necessity of modelling fluid-structure interaction for stented coronary arteries.,” Journal of the mechanical behavior of biomedical materials, vol. 34, pp. 217–30, Jun. 2014.

[67] F. Migliavacca, R. Balossino, G. Pennati, G. Dubini, T.-Y. Hsia, M. R. de Leval, E. L. Bove, "Multiscale modelling in biofluidynamics: application to reconstructive paediatric cardiac surgery.," Journal of biomechanics, vol. 39, no. 6, pp. 1010–20, Jan. 2006.

[68] T.Y. Hsia, D. Cosentino, C. Corsini, G. Pennati, G. Dubini, F. Migliavacca, "Use of mathematical modeling to compare and predict hemodynamic effects between hybrid and surgical Norwood palliations for hypoplastic left heart syndrome.," Circulation, vol. 124, no. 11 Suppl, pp. S204–10, 2011.

[69] A. Baretta, C. Corsini, W. Yang, I. E. Vignon-Clementel, L. Marsden, J. Feinstein, T.-Y. Hsia, G. Dubini, F. Migliavacca, G. Pennati, "Virtual surgeries in patients with congenital heart disease: a multi-scale modelling test case.," Philos. Trans. A. Math. Phys. Eng. Sci., vol. 369, no. 1954, pp. 4316–30, 2011.

[70] J.H. Ferziger and M. Peric, "Computational Methods for Fluid Dynamics", Springer-Verlag, 2002.

[71] G. Arbia, C. Corsini, M. Esmaily Moghadam, A. L. Marsden, F. Migliavacca, G. Pennati, T.-Y. Hsia, I. E. Vignon-Clementel, "Numerical blood flow simulation in surgical corrections: what do we need for an accurate analysis?," The Journal of surgical research, vol. 186, no. 1, pp. 44–55, Jan. 2014.

[72] J. Ryval, A. G. Straatman, D. A. Steinman. "Two-equation turbulence modeling of pulsatile flow in a stenosed tube.," J. Biomech. Eng., vol. 126, pp. 625–635, 2004.

[73] M. Zamir, "Physics of coronary blood flow.," Springer, 2004.

[74] T.J.R. Hughes, W.K. Liu, T.K. Zimmermann, "Lagrangian–eulerian finite element formulation for incompressible viscous flows.," Comput Methods Appl Mech Engrg., vol. 29, pp. 329–349, 1981.

[75] C. Figueroa, I. Vignon-Clementel, K. Jansen, T. Hughes, C. Taylor, "A coupled momentum method for modeling blood flow in three-dimensional deformable arteries," Comput. Methods Appl. Mech. Eng., vol. 195, no. 41–43, pp. 5685–5706, Aug. 2006.

[76] C. A. Taylor and J. D. Humphey, "Open Problems in Computational Vascular Biomechanics: Hemodynamics and Arterial Wall Mechanics," Comput Methods Appl Mech Eng, vol. 198, pp. 3514–3523, 2010.

[77] J. T. Ottesen, M. S. Olufsen, J. K. Larsen, “Applied Mathematical Models in Human Physiology.,”, Roskilde University, Denmark, 2003.

[78] B. N. Steele, M. S. Olufsen, C. A. Taylor, “Fractal network model for simulating abdominal and lower extremity blood flow during resting and exercise conditions.,” Computer methods in biomechanics and biomedical engineering, vol. 10, no. 1, pp. 39–51, Feb. 2007.

[79] N. P. Smith, A. J. Pullan, P. J. Hunter, “Generation of an anatomically based geometric coronary model.,” Annals of biomedical engineering, vol. 28, no. 1, pp. 14–25, Jan. 2000.

[80] N. P. Smith, A. J. Pullan, P. J. Hunter, “An anatomically based model of transient coronary blood flow in the heart,” Society for Industrial and Applied Mathematics, vol. 62, no. 3, pp. 990–1018, 2002.

[81] F. Liang, S. Takagi, R. Himeno, H. Liu, “Multi-scale modeling of the human cardiovascular system with applications to aortic valvular and arterial stenoses.,” Medical & biological engineering & computing, vol. 47, no. 7, pp. 743–55, Jul. 2009.

[82] N. Mittal, Y. Zhou, C. Linares, S. Ung, B. Kaimovitz, S. Molloi, G. S. Kassab, “Analysis of blood flow in the entire coronary arterial tree,” Am J Physiol Heart Circ Physiol, vol. 289, pp. 439–446, 2005.

[83] V.C. Rideout, “Mathematical computer modeling of physiological systems.,” Prentice Hall, Englewood Cliffs, NJ, 1991.

[84] L. M. Ellwein, H. T. Tran, C. Zapata, V. Novak, M. S. Olufsen, “Sensitivity analysis and model assessment: mathematical models for arterial blood flow and blood pressure.,” Cardiovascular engineering, vol. 8, no. 2, pp. 94–108, Jun. 2008.

[85] J. F. de Canete, P. del Saz-Orozco, D. Moreno-Boza, E. Duran-Venegas, “Object-oriented modeling and simulation of the closed loop cardiovascular system by using SIMSCAPE.,” Computers in biology and medicine, vol. 43, no. 4, pp. 323–33, May 2013.

[86] O. Barnea, “Open-Source Programming of Cardiovascular Pressure-Flow Dynamics Using SimPower Toolbox in Matlab and Simulink.,”, The Open Pacing, Electrophysiology & Therapy Journal, vol. 3, pp. 55–59, 2010.

[87] N. Westerhof, J. Lankhaar, B. E. Westerhof, “The arterial Windkessel.,” Medical & biological engineering & computing, vol. 47, no. 2, pp. 131–41, Feb. 2009.

[88] S. Mantero, R. Pietrabissa, R. Fumero, “The coronary bed and its role in the cardiovascular system: a review and an introductory single-branch model.,” Journal of biomedical engineering, vol. 14, no. 2, pp. 109–16, Mar. 1992.

[89] R. Pietrabissa, S. Mantero, T. Marotta, L. Menicanti, “A lumped parameter model to evaluate the fluid dynamics of different coronary bypasses.,” Med. Eng. Phys., vol. 18, no. 6, pp. 477–84, Sep. 1996.

[90] M. Maasrani, “Patients’ specific simulations of coronary fluxes in case of three-vessel disease,” J. Biomed. Sci. Eng., vol. 04, no. 01, pp. 34–45, 2011.

[91] R. Rajani, Y. Wang, A. Uus, D. Perera, S. R. Redwood, M. R. Thomas, J. B. Chambers, R. Preston, G. S. Carr-White, P. Liatsis, “Virtual fractional flow reserve by coronary computed tomography - hope or hype?,” EuroIntervention, vol. 9, no. 2, pp. 277–284, Jun. 2013.

[92] P.H.M. Bovendeerd, P. Borsje, T. Arts, F. N. van De Vosse, “Dependence of intramyocardial pressure and coronary flow on ventricular loading and contractility: a model study.,” Ann. Biomed. Eng., vol. 34, no. 12, pp. 1833–45, Dec. 2006.

[93] M. Verburg, “A lumped parameter model of coronary flow to analyze time intensity curves extracted from angiograms.,” Report number: BMTE 07.36, Eindhoven University of Technology, 2007.

[94] H. Nickisch, Y. Lamash, S. Prevrhal, M. Freiman, M. Vembar, L. Goshen, and H. Schmitt, “Learning Patient-Specific Lumped Models for Interactive Coronary Blood Flow Simulations.,”, Medical Image Computing and Computer-Assisted Intervention – MICCAI 2015, pp. 433–441, 2015.

[95] I. Larrabide, P. J. Blanco, S. Urquiza, E. Dari, M. J. Vénere, N. de Souza e Silva, R. Feijóo, “HeMoLab--Hemodynamics Modelling Laboratory: an application for modelling the human cardiovascular system.,” Computers in biology and medicine, vol. 42, no. 10, pp. 993–1004, Oct. 2012.

[96] S. Urquiza, P. J. Blanco, M. J. Vénere, R. Feijóo, “Multidimensional modelling for the carotid artery blood flow,” Computer Methods in Applied Mechanics and Engineering, vol. 195, no. 33–36, pp. 4002–4017, Jul. 2006.

[97] P. J. Blanco, P. R. Trenhago, L. G. Fernandes, R. A. Feijóo, “On the integration of the baroreflex control mechanism in a heterogeneous model of the cardiovascular system,” Int. J. Numer. Meth. Biomed. Engng, vol. 28, pp. 412–433, 2011.

[98] B. Berthier, R. Bouzerar, C. Legallais, “Blood flow patterns in an anatomically realistic coronary vessel: influence of three different reconstruction methods.,” J. Biomech., vol. 35, no. 10, pp. 1347–56, Oct. 2002.

[99] H. Kirişli, M. Schaap, C. T. Metz, A. S. Dharampal, W. B. Meijboom, S. L. Papadopoulou, A. Dedic, K. Nieman, M. de Graaf, M. F. L. Meijs, et al., “Standardized evaluation framework for evaluating coronary artery stenosis detection, stenosis quantification and lumen segmentation algorithms in computed tomography angiography,” Med. Image Anal., vol. 17, no. 8, pp. 859–876, 2013.

[100] O. Sahni, K. E. Jansen, C. Taylor, M. S. Shephard, “Automated adaptive cardiovascular flow simulations,” Engineering with Computers, vol. 25, no. 1, pp. 25–36, Oct. 2008.

[101] E. Wellnhofer, J. Osman, U. Kertzscher, K. Affeld, E. Fleck, L. Goubergrits, “Flow simulation studies in coronary arteries--impact of side-branches.,” Atherosclerosis, vol. 213, no. 2, pp. 475–81, Dec. 2010.

[102] T. Chaichana, Z. Sun, J. Jewkes, “Computation of hemodynamics in the left coronary artery with variable angulations.,” Journal of biomechanics, vol. 44, no. 10, pp. 1869–78, Jul. 2011.

[103] T. Chaichana, Z. Sun, J. Jewkes, “Hemodynamic impacts of various types of stenosis in the left coronary artery bifurcation: A patient-specific analysis,” Physica Medica, vol. 29, no. 5, pp. 447–452, 2013.

[104] B. Su, Y. Huo, G. S. Kassab, F. Kabinejadian, S. Kim, H. L. Leo, L. Zhong, “Numerical investigation of blood flow in three-dimensional porcine left anterior descending artery with various stenoses.,” Computers in biology and medicine, vol. 47, pp. 130–8, Apr. 2014.

[105] X. Xie, Y. Wang, H. Zhou, “Impact of coronary tortuosity on the coronary blood flow: a 3D computational study.,” Journal of biomechanics, vol. 46, no. 11, pp. 1833–41, Jul. 2013.

[106] Y. Li, C. Shen, Y. Ji, Y. Feng, G. Ma, N. Liu, “Clinical Implication of Coronary Tortuosity in Patients with Coronary Artery Disease.,” PLoS ONE , vol. 6, no. 8, : e24232, Aug. 2011.

[107] T. Frauenfelder, E. Boutsianis, T. Schertler, L. Husmann, S. Leschka, D. Poulikakos, B. Marincek, H. Alkadhi, “In-vivo flow simulation in coronary arteries based on computed tomography datasets: feasibility and initial results.,” European radiology, vol. 17, no. 5, pp. 1291–300, May 2007

[108] I.E. Vignon-Clementel, C.A. Figueroa, K. Jansen, C. Taylor, “Outflow boundary conditions for three-dimensional finite element modeling of blood flow and pressure in arteries,” Comput. Methods Appl. Mech. Eng., vol. 195, no. 29–32, pp. 3776–3796, Jun. 2006.

[109] L. Grinberg and G. E. Karniadakis, “Outflow boundary conditions for arterial networks with multiple outlets.,” Annals of biomedical engineering, vol. 36, no. 9, pp. 1496–514, Sep. 2008.

[110] H. J. Kim, I. E. Vignon-Clementel, J. S. Coogan, C. Figueroa, K. E. Jansen, C. Taylor, “Patient-specific modeling of blood flow and pressure in human coronary arteries.,” Ann. Biomed. Eng., vol. 38, no. 10, pp. 3195–209, Oct. 2010.

[111] A. G. van der Giessen, H. C. Groen, P.-A. Doriot, P. J. de Feyter, A. F. W. van der Steen, F. N. van de Vosse, J. J. Wentzel, F. J. H. Gijsen, “The influence of boundary conditions on wall shear stress distribution in patients specific coronary trees.,” Journal of biomechanics, vol. 44, no. 6, pp. 1089–95, Apr. 2011.

[112] M. E. Moghadam, I. E. Vignon-Clementel, R. Figliola, A. L. Marsden, “A modular numerical method for implicit 0D/3D coupling in cardiovascular finite element simulations,” Journal of Computational Physics, vol. 244, pp. 63–79, Jul. 2013.

[113] P. J. Blanco, J. S. Leiva, G. C. Buscaglia, “A black-box decomposition approach for coupling heterogeneous components in hemodynamics simulations,” Int. J. Numer. Meth. Biomed. Engng., vol. 29, pp. 408–427, 2012.

[114] M. S. Olufsen, “Structured tree outflow condition for blood flow in larger systemic arteries.,” The American journal of physiology, vol. 276, no. 45, pp. H257–68, Jan. 1999.

[115] M. S. Olufsen, C. S. Peskin, W. Y. Kim, E. M. Pedersen, A. Nadim, J. Larsen, "Numerical simulation and experimental validation of blood flow in arteries with structured-tree outflow conditions.," Annals of biomedical engineering, vol. 28, no. 11, pp. 1281–99, 2000.

[116] M. S. Olufsen and A. Nadim, "On deriving lumped models for blood flow and pressure in the systemic arteries," Mathematical Biosciences and Engineering, vol. 1, no. 1, pp. 61–80, 2004.

[117] K. Sommer, R. Schmidt, D. Graafen, H.-C. Breit, L. M. Schreiber, "Contrast agent bolus dispersion in a realistic coronary artery geometry: influence of outlet boundary conditions.," Annals of biomedical engineering, vol. 42, no. 4, pp. 787–96, Apr. 2014.

[118] N. Stergiopulos, J. J. Meister, N. Westerhof, "Simple and accurate way for estimating total and segmental arterial compliance: the pulse pressure method.," Annals of biomedical engineering, vol. 22, no. 4, pp. 392–7, 1994.

[119] N. Stergiopulos, P. Segers, N. Westerhof, "Use of pulse pressure method for estimating total arterial compliance in vivo," Am J Physiol Heart Circ Physiol 276, 1999.

[120] R. L. Spilker and C. A. Taylor, "Tuning multidomain hemodynamic simulations to match physiological measurements.," Annals of biomedical engineering, vol. 38, no. 8, pp. 2635–48, Aug. 2010.

[121] D. Zeng, Z. Ding, M. H. Friedman, C. R. Ethier, "Effects of Cardiac Motion on Right Coronary Artery Hemodynamics," Annals of Biomedical Engineering, vol. 31, no. 4, pp. 420–429, Apr. 2003.

[122] D. Zeng, E. Boutsianis, M. Ammann, K. Boomsma, S. Wildermuth, D. Poulikakos, "A study on the compliance of a right coronary artery and its impact on wall shear stress.," Journal of biomechanical engineering, vol. 130, no. 4, p. 041014, Aug. 2008.

[123] J. Dong, Z. Sun, K. Inthavong, J. Tu, "Fluid-structure Interaction Analysis of Representative Left Coronary Artery Models with Different.," Computing in Cardiology Conference (CinC), vol. 40, pp. 5–8,2013.

[124] A. Theodorakakos, M. Gavaises, A. Andriotis, A. Zifan, P. Liatsis, I. Pantos, D. Katritsis. "Simulation of cardiac motion on non-Newtonian, pulsating flow development in the human

left anterior descending coronary artery.," Physics in Medicine and Biology, vol. 53, no. 18, pp. 4875–4892, 2008.

[125] R. Torii, N. B. Wood, N. Hadjiloizou, A. W. Dowsey, A. R. Wright, A. D. Hughes, J. Davies, D. P. Francis, J. Mayet, G. Yang, S. A. M. Thom, X. Y. Xu, "Fluid – structure interaction analysis of a patient-specific right coronary artery with physiological velocity and pressure waveforms," Commun. Numer. Meth. Engng, vol. 25, pp. 565–580, Feb. 2009.

[126] R. Torii, J. Keegan, N. B. Wood, A. W. Dowsey, A. D. Hughes, G.-Z. Yang, D. N. Firmin, S. a M. Thom, X. Y. Xu, "MR image-based geometric and hemodynamic investigation of the right coronary artery with dynamic vessel motion.," Annals of biomedical engineering, vol. 38, no. 8, pp. 2606–20, Aug. 2010.

[127] E. Kung, A. S. Les, C. A. Figueroa, F. Medina, K. Arcaute, R. B. Wicker, M. V McConnell, C. Taylor, "In vitro validation of finite element analysis of blood flow in deformable models.," Annals of biomedical engineering, vol. 39, no. 7, pp. 1947–60, Jul. 2011.

[128] E. Kung, A. M. Kahn, J. C. Burns, A. Marsden, "In Vitro Validation of Patient-Specific Hemodynamic Simulations in Coronary Aneurysms Caused by Kawasaki Disease.," Cardiovascular engineering and technology, vol. 5, no. 2, pp. 189–201, Jun. 2014.

[129] J. V Soulis, G. D. Giannoglou, Y. S. Chatzizisis, K. V Seralidou, G. E. Parcharidis, G. E. Louridas, "Non-Newtonian models for molecular viscosity and wall shear stress in a 3D reconstructed human left coronary artery.," Medical engineering & physics, vol. 30, no. 1, pp. 9–19, Jan. 2008.

[130] B.M. Johnston, P.R. Johnston PR, S. Corney, D. Kilpatrick, "Non-Newtonian blood flow in human right coronary arteries: transient simulations.," Journal of Biomechanics, vol. 39, no. 6, pp. 1116–1128, 2006.

[131] H. J. Kim, K. E. Jansen, C. A. Taylor, "Incorporating autoregulatory mechanisms of the cardiovascular system in three-dimensional finite element models of arterial blood flow.," Ann. Biomed. Eng., vol. 38, no. 7, pp. 2314–30, Jul. 2010.

[132] Y. Wang and P. Liatsis, "Automatic Segmentation of Coronary Arteries in CT Imaging in the Presence of Kissing Vessel Artifacts.," IEEE Transactions on Information Technology in Biomedicine, vol. 16, no. 7, pp. 782-788, 2012.

[133] Y. Wang, X. Meng, D. Wang, "Automated Coronary Artery Analysis System in 3D CTA Images," 3rd International Conference on Biomedical Engineering and Informatics BMEI 2010, pp. 122-126, 2010.

[134] P.J. de Feyter Pim and G. P. Krestin, "Computed Tomography of the Coronary Arteries", 2nd edition, CRC Press, 2008.

[135] G. Xiong and C. A. Taylor, "Influence of vessel roughness on wall shear stress in image-based blood flow modeling," 2010 IEEE Int. Symp. Biomed. Imaging From Nano to Macro, pp. 33–36, 2010.

[136] J. Yang, L. X. Yu, M. Y. Rennie, J. G. Sled, and R. M. Henkelman, "Comparative structural and hemodynamic analysis of vascular trees.," Am. J. Physiol. Heart Circ. Physiol., vol. 298, no. 4, pp. H1249–H1259, 2010.

[137] R. Burattini, P. Sipkema, G. van Huis, N. Westerhof, "Identification of canine coronary resistance and intramy- ocardial compliance on the basis of the waterfall model.," Ann. Biomed. Eng., vol. 13, no. 5, pp. 385–404, 1985.

[138] K.L. Gould, K. Lipscomb, G.W. Hamilton, "Physiologic basis for assessing critical coronary stenosis. Instantaneous flow response and regional distribution during coronary hyperemia as measures of coronary flow reserve.," Am J Cardiol., vol. 33, pp. 87-94, 1974.

[139] ANSYS FLUENT 14.0 Documentation, [Online]. Available: http://www.ansys.com/Support/Documentation [Accessed 01 July 2015].

[140] J. A. Sethian, "A fast marching level set method for monotinically advancing fronts", in Proc. of Nat. Acad. of Sci., vol. 93, pp. 1591–1595, 1996.

[141] T. Heldt, Thomas, E. B. Shim, R. D. Kamm R. G. Mark, «Computational modeling of cardiovascular response to orthostatic stress.," J Appl Physiol., vol. 92, pp. 1239–1254, 2002.

[142] H. Senzaki, C. Chen, D. A. Kass, "Single beat estimation of end-systolic pressure-volume relations in humans.," Circulation, vol. 94, pp. 2497 – 2506, 1996.

[143] E. B. Shim, J. Y. Sah, C. H. Youn, "Mathematical Modeling of Cardiovascular System Dynamics Using a Lumped Parameter Method.," Japanese Journal of Physiology, vol. 54, No.6, pp. 545-553, 2005.

[144] M. R. Nelson, J. Stepanek, M. Cevette, M. Covalciuc, R. T. Hurst, A. J. Tajik, "Noninvasive measurement of central vascular pressures with arterial tonometry: clinical revival of the pulse pressure waveform?," Mayo Clin. Proc., vol. 85, no. 5, pp. 460–472, 2010.

[145] N. H. Pijls and J.-W. Sels, "Functional Measurement of Coronary Stenosis," J. Am. Coll. Cardiol., vol. 59, no. 12, pp. 1045–1057, 2012.

[146] M. Siebes, B.J. Verhoeff, M. Meuwissen, R.J. de Winter, J.A.E. Spaan, J.J. Piek, "Single-Wire Pressure and Flow Velocity Measurement to Quantify Coronary Stenosis Hemodynamics and Effects of Percutaneous Interventions," Circulation, vol. 109, no. 6, pp. 756–762, 2004.

[147] M. J. Kern, A. Lerman, J.-W. Bech, B. De Bruyne, E. Eeckhout, W. F. Fearon, S. T. Higano, M. J. Lim, M. Meuwissen, J. J. Piek, N. H. J. Pijls, M. Siebes, J. E. Spaan, "Physiological assessment of coronary artery disease in the cardiac catheterization laboratory: a scientific statement from the American Heart Association Committee on Diagnostic and Interventional Cardiac Catheterization, Council on Clinical Cardiology.," Circulation, vol. 114, no. 12, pp. 1321–1341, 2006.